Magnetohydrodynamic Processes and Polarized Emission in AGN Jets

INAUGURAL-DISSERTATION

zur

Erlangung des Doktorgrades

der Mathematisch-Naturwissenschaftlichen Fakultät

der Universität zu Köln

vorgelegt von

Joana Anna Höllmer, geb. Kramer

aus Oberhausen, Deutschland

Köln 2023

Berichterstatter: Prof. Dr. J. Anton Zensus

Prof. Dr. Andreas Eckart

Tag der letzten mündlichen Prüfung: 16.10.2023

Eidesstattliche Erklärung

Hiermit versichere ich an Eides statt, dass ich die vorliegende Dissertation selbstständig und ohne die Benutzung anderer als der angegebenen Hilfsmittel und Literatur angefertigt habe. Alle Stellen, die wörtlich oder sinngemäß aus veröffentlichten und nicht veröffentlichten Werken dem Wortlaut oder dem Sinn nach entnommen wurden, sind als solche kenntlich gemacht. Ich versichere an Eides statt, dass diese Dissertation noch keiner anderen Fakultät oder Universität zur Prüfung vorgelegen hat; dass sie - abgesehen von unten angegebenen Teilpublikationen und eingebundenen Artikeln und Manuskripten - noch nicht veröffentlicht worden ist sowie, dass ich eine Veröffentlichung der Dissertation vor Abschluss der Promotion nicht ohne Genehmigung des Promotionsausschusses vornehmen werde. Die Bestimmungen dieser Ordnung sind mir bekannt. Darüber hinaus erkläre ich hiermit, dass ich die Ordnung zur Sicherung guter wissenschaftlicher Praxis und zum Umgang mit wissenschaftlichem Fehlverhalten der Universität zu Köln gelesen und sie bei der Durchführung der Dissertation zugrundeliegenden Arbeiten und der schriftlich verfassten Dissertation beachtet habe und verpflichte mich hiermit, die dort genannten Vorgaben bei allen wissenschaftlichen Tätigkeiten zu beachten und umzusetzen. Ich versichere, dass die eingereichte elektronische Fassung der eingereichten Druckfassung vollständig entspricht.

Joana Anna Höllmer

Köln, den 14.08.2023

Zur Doktorarbeit **relevante** Teilpublikationen

Publikationen:

1 **Kramer, J. A.** and MacDonald, N. R. (2021), *Ray-tracing in relativistic jet simulations: A polarimetric study of magnetic field morphology and electron scaling relations*, Astronomy and Astrophysics, 656, A143, 15, `doi:10.1051/0004-6361/202141454`.

Manuskripte:

2 **Kramer, J. A.**, Müller, H., Röder, J., and Ros, E. (est. 2023), *Probing circular polarization and magnetic field structure in AGN*, eingereicht bei Astronomy and Astrophysics, AA/2023/47707.

3 **Kramer, J. A.** and MacDonald, N. R. et al. (est. 2023), *3D Hybrid fluid-particle jet simulations and the importance of synchrotron radiative losses*.

Darüber hinaus habe ich während meiner Promotionszeit zu folgenden Veröffentlichungen beigetragen

1 Abe, H. et al. (2023), *Multimessenger Characterization of Markarian 501 during Historically Low X-Ray and γ-Ray Activity*, Astrophysical Journal, Supplement, 266, 2, `doi:10.3847/1538-4365/acc181`.

2 Emami, R. et al. (2023), *Probing Plasma Composition with the Next Generation Event Horizon Telescope (ngEHT)*, Galaxies, 11 (1), 11, `doi:10.3390/galaxies11010011`.

3 Escudero, J. et al. (est. 2023), *The repeating flaring activity of blazar AO 0235+164*, eingereicht bei Astronomy and Astrophysics, AA/2023/46885.

4 Event Horizon Telescope Collaboration (est. 2023), *First M87 Event Horizon Telescope Results IX: Detection of Near-Horizon Circular Polarization*, eingereicht bei Astrophysical Journal Letters.

5 Event Horizon Telescope Collaboration (est. 2023), *First Sagittarius A* Event Horizon Telescope Results. VIII.: Physical interpretation of the polarized ring*, Manuskript.

Abstract

Active galactic nuclei (AGN) stand out as some of the most powerful entities in the universe. At their core lies a supermassive black hole (SMBH) with a mass ranging up to several billion times the mass of the Sun, surrounded by an accretion disk that feeds the system. As matter falls toward the black hole, a portion of it is expelled perpendicularly to the accretion disk, forming what we call jets. These relativistic flows are highly collimated and can travel enormous distances up to kiloparsecs away from the central engine. The radiation emitted by AGN jets display significant features in structure across the electromagnetic spectrum and in polarized emission, reflecting changes in intrinsic parameters, such as the magnetic field and the rest-mass density.

It is essential to understand how magnetic properties of the relativistic plasma impact the morphology of polarized synchrotron emission in jets. In order to study this, it is necessary to compare numerical simulations to the observed structure of the polarized radio signal in relativistic jets and to uncover the nature of the underlying physics.

To investigate the structural behaviour of polarized AGN jets, I employ a numerical laboratory using a three-dimensional relativistic magnetohydrodynamic (RMHD) module within the PLUTO code. I study how non-thermal synchrotron radiation, resulting from relativistic electrons spiraling around magnetic field lines, is affected by three primary factors: first, the implementation of various magnetic field morphologies, such as purely poloidal, helical, and purely toroidal; second, the application of different electron scaling relations to map non-thermal physics from the thermal parameters calculated in each simulation; and third, the requirement for a jet tracer to exclude the non-cooled ambient medium in RMHD codes. This study analyzes for the first time the polarized synthetic synchrotron emission in full Stokes. This results in major findings: The synthetic maps reveal that when the magnetic field is toroidal in nature, the emission from the jet is brighter at the jet sheath, that is, showing an edge-brightening. Conversely, an underlying purely poloidal magnetic field structure results in a brighter central spine. In the latter case, the emission concentrates in the recollimation shock, which is associated with the radio core in radio-wavelengths observations. Further, the circularly polarized emission shows both positive and negative signs for the toroidal magnetic field morphology over various types of AGN: radio galaxies, with a large viewing angle, and blazar sources, which show a jet structure emanating close to our line of sight. Finally, the emission from the relativistic jet remains largely unaltered by different emission scaling relations when the ambient medium is excluded.

To test the hypothesis, I compare archival very-long-baseline interferometric (VLBI) observations from the MOJAVE program at 15 GHz and recent, dedicated observations obtained from the Very Long Baseline Array (VLBA) at 15 GHz and 23 GHz with the

synthetic polarized synchrotron emission maps of blazars studied in this thesis. The archival observations extend over several years to decades. I analyze linear polarized emission and electric vector position angles, as well as circular polarization at 15 GHz and 23 GHz. The findings of the study are compared to previous reconstructions of these features, which confirms the robustness of electric vector position angles. This suggests the presence of a consistent magnetic field within the VLBI radio core over time. Further, the linear polarized emission structure is consistent with polarized signals observed in the past, that is, matching the total intensity peak in most blazar sources. Examining the circular polarization reveals a switch in sign when moving from 15 GHz to 23 GHz. This result is contextualized by discussing optical depth and Faraday screens.

The numerical study of AGN jets is improved by including particle physics into three-dimensional hybrid fluid-particle jet simulations. This is achieved by using a Lagrangian particle approach within the PLUTO code. I develop a specialized jet setup to accommodate Lagrangian particles with distinct physical parameters and power-law energy distributions. These particles are tracked via the underlying plasma flow. The non-thermal particle attributes are numerically updated over time. Particle physics allows to include radiative losses in numerical jet simulations which leads to cooling of the ambient medium and the backflow of the bow shock of the jet head. This provides an unobscured view of the polarized synchrotron emission of the relativistic jet. I specifically employ the example of the nearby radio galaxy Centaurus A to confirm the results of an edge-brightened jet with an underlying toroidal magnetic field configuration.

Zusammenfassung

Aktive galaktische Kerne (AGN) stechen als einige der hellsten Objekte im Kosmos hervor. In ihrem Zentrum befindet sich ein supermassives Schwarzes Loch (SMBH) mit einer Masse von mehreren Milliarden Sonnenmassen, umgeben von einer Akkretionsscheibe, die das System mit Materie versorgt. Wenn Materie durch Gravitation zum Schwarzen Loch angezogen wird, wird ein Teil davon senkrecht zur Akkretionsscheibe ausgestoßen und bildet sogenannte Jets. Diese relativistischen Strömungen sind stark zentrierte Strukturen und können weite Strecken zurücklegen, bis hin zu Kiloparsecs von der zentralen Antrieb entfernt. Die von Jets in AGN emittierte Strahlung zeigt bemerkenswerte Strukturmerkmale im elektromagnetischen Spektrum und in polarisierter Emission, die Veränderungen in intrinsischen Parametern wie dem Magnetfeld und der Teilchendichte widerspiegeln.

Das Verständnis, wie die magnetischen Eigenschaften des relativistischen Plasmas im Jet die Morphologie seiner polarisierten Synchrotronemission beeinflussen, ist entscheidend für den Vergleich von numerischen Simulationen mit der beobachtbaren Struktur und Polarisation des Lichts.

Um das Verhalten von Jets zu erforschen, verwende ich eine numerische Methode, welche ein dreidimensionales relativistisches magnetohydrodynamisches (RMHD) Modul innerhalb des PLUTO-Codes nutzt. Ich untersuche, wie die nicht-thermische Synchrotronstrahlung, die von relativistischen Elektronen, die um magnetische Felder kreisen, von drei Hauptfaktoren beeinflusst wird: Erstens die Implementierung verschiedener magnetischer Feldstrukturen wie rein poloidal, helikal und rein toroidal; zweitens die Anwendung diverser Skalierungsrelationen im Bezug auf nicht-thermische Teilchen, um nicht-thermische Physik aus den in den Simulationen berechneten thermischen Parametern abzubilden; und drittens die Notwendigkeit eines Jet Indikators, um das stark leuchtende Material um den Jet in RMHD-Codes auszuschließen. Erstmals wird die Analyse polarisierter synthetischer Synchrotronstrahlung in allen Polarisationsrichtungen durchgeführt. Dies führt zu bedeutenden Erkenntnissen. Die synthetischen Karten zeigen, dass bei einer toroidalen magnetischen Feldstruktur die Emission des Jets am Rande heller ist und zu einer Erhöhung der Helligkeit dieser äußeren Struktur führt, während eine rein poloidale Magnetfeldstruktur eine hellere zentrale Emission im Jet erzeugt. Im letzteren Fall konzentriert sich die emittierte Strahlung im Rekollimationsstoß, der bei Beobachtungen von Jets im Radio-Bereich mit dem Radiokern in Verbindung gebracht wird.

Weiterhin trägt die zirkular polarisierte Emission sowohl negative als auch positive Vorzeichen bei einer toroidalen magnetischen Feldstruktur in verschiedensten Arten von AGN: In Radiogalaxien mit einem großen Sichtwinkel und Blazaren, welche in einem kleinen Winkel zu unserer Beobachtungslinie ausgetoßen werden. Abschließend

ist die Emission des relativistischen Jets weitgehend unbeeinflusst von verschiedenen Elektronskalierungsrelationen, sofern das Umgebungsmedium aus den Berechnungen des Strahlungstransports ausgeschlossen wird.

Um diese These zu testen, vergleiche ich sehr langbasisinterferometrische (VLBI) Beobachtungen aus dem MOJAVE Archiv bei einer Frequenz von 15 GHz mit aktuellen, speziell gewonnenen Beobachtungen des Very Long Baseline Array (VLBA) bei einer Frequenz von 15 GHz und 23 GHz mit den synthetischen polarisierten Karten der Synchrotronstrahlung von Blazaren, die in dieser Arbeit vorgestellt werden. Die bisherigen Beobachtungen erstrecken sich über mehrere Jahre bis Jahrzehnte. Ich analysiere lineare polarisierte Emission und die Positionswinkel des elektrischen Vektors, sowie zirkulare Polarisation bei 15 GHz und 23 GHz. Die Ergebnisse der Studie werden mit früheren Rekonstruktionen dieser Merkmale verglichen, was zu einer Bestätigung der Robustheit der Positionswinkel des elektrischen Vektors führt. Dies deutet auf ein zeitlich konsistentes Magnetfeld im VLBI-Radiokern hin. Weiterhin stimmt die lineare polarisierte Struktur mit polarisierten Signalen aus der Vergangenheit überein, d.h., sie entspricht dem Peak der Gesamtintensität in den meisten Blazar-Quellen. Die Untersuchung der zirkularen Polarisation ergibt eine Änderung des Vorzeichens beim Wechsel von 15 GHz auf 23 GHz. Ich diskutiere dieses Ergebnis im Zusammenhang mit optischer Tiefe und Faraday-Schirmen.

Um die numerische Untersuchung von AGN-Jets zu verbessern, werden Ansätze von Teilchenphysik in einem hybriden Plasma-Teilchen-Ansatz innerhalb des PLUTO-Codes integriert. Ich habe ein spezielles Jet-Modul entwickelt, welches Lagrangesche Teilchen mit unterschiedlichen physikalischen Parametern und Energieverteilungen einbindet und diese während der Simulation verfolgt und aktualisiert. Die Teilchenphysik ermöglicht die Einbeziehung von Strahlungsverlusten in numerischen Jet-Simulationen, wodurch das Umgebungsmedium Energie verliert und der Rückfluss des Jets, der sich durch das thermische Plasma bewegt, ausgeschlossen wird. Dies zielt auf eine ungehinderte Sicht auf die Emission des Blazar-Jets ab. Ich verwende speziell das Beispiel von der Radiogalaxie Centaurus A, um die Ergebnisse eines Jets mit starker Emission am äußeren Rande mit einer darunter liegenden toroidalen magnetischen Feldkonfiguration zu präsentieren.

To those we have lost along the way

Contents

List of Figures

List of Abbreviations

AGN	Active Galactic Nuclei
BH	Black Hole
SMBH	Supermassive Black Hole
BLR	Broad Line Region
NLR	Narrow Line Region
FWHM	Full-Width Half Maximum
LINER	Low-Ionization Nuclear Emission Line Region
QSO	Quasi Stellar Object
LoS	Line of Sight
LERG	Low Emission Radio Galaxies
HERG	High Emission Radio Galaxies
FR I/II	Fanaroff-Riley I/II
FRSQ	Flat-Spectrum Radio Quasar
VLBI	Very-Long-Baseline Interferometry
VLBA	Very Long Baseline Array
EHT	Event Horizon Telescope
SED	Spectral Energy Distribution
CP	Circular Polarization
LP	Linear Polarization
EVPA	Electric Vector Position Angle
RCP	Right-handed Circular Polarization
LCP	Left-handed Circular Polarization
IF	Intermediate Frequency
RMHD	Relativistic Magnetohydrodynamics
BZ	Blandford & Znajek
BP	Blandford & Payne
NTP	Non-Thermal Particles

1 Introduction to active galactic nuclei

The study of black holes (BHs) is a topic that is closely connected to philosophy, mathematics, and (astro-)physics. In philosophy, questions related to the nature of space, time, and existence are fundamental to understand the concept of black holes. For instance, the idea that a black hole can distort spacetime to the extent that it becomes boundless raises important questions about the nature of space and time itself. Similarly, the concept of an event horizon, beyond which nothing can escape, raises questions about the limits of existence.

In physics, black holes are studied as objects that exhibit extreme gravitational fields that can distort the fabric of spacetime. The study of black holes and their environment involves a range of physical concepts, including thermodynamics, electromagnetism, and quantum mechanics. Astrophysics provides the observational and experimental data that allows us to test these models and theories. For example, astrophysics uses numerical simulations to study the behavior of gas and dust as it falls into a black hole and emits radiation. Active galactic nuclei (AGN) observations test theories of black hole physics, such as the No-Hair Theorem, which states that black holes can be characterized by only three parameters: mass, spin, and electric charge. The emitted radiation of AGN *jets* is a mystery itself, i.e., how jets are being launched and collimated, resulting in a luminous object that outshines its host galaxy. Jets are studied in numerous fields in astrophysics, for instance, *to* explain the star formation rate in galaxies, *to* study magnetic fields of AGN, or *to* unveil the origin of high energy neutrinos.

The interdisciplinary nature of black hole research demonstrates the connection of different fields of knowledge in expanding our understanding of the universe.

1.1 Albert Einstein's theory of general relativity and black holes

Einstein mathematically described the concept of spacetime, which is a four-dimensional construct consisting of three dimensional space and time as the fourth dimension. The Minkowski space considers space and time as two coordination points. Gravity can be interpreted as a distortion of spacetime. Gravitation is based on the curvature of spacetime, which in turn determines the trajectory of freely falling masses. Mass causes a distortion that determines the trajectory of objects in spacetime. The equivalence principle, as a basic assumption of the general theory of relativity, states that the effects of gravity correspond exactly to the effects of mass acceleration. Space is surrounded by a downward gravitational field. Gravity is based on two basic principles: First, higher mass at a certain distance means higher curvature. Second, density also affects curvature.

It follows logically that compressing more and more mass onto a constant radius distorts spacetime boundlessly. This results in a singularity, or in this context, in a BH. Physical objects that enter the BH's range are falling along the singularity to infinity and are being trapped since the escape speed is larger than the speed of light (the fastest velocity known). An approximation of the limit of this is the event horizon. Supposedly, events within the event horizon can no longer affect the universe.

The mathematical concept of the BH was first described by John Michell and Pierre-Simon Laplace in the 18th century (Montgomery et al., 2009). They stated that an object's escape velocity depends only on its mass and size. For very compact and massive objects, the escape velocity is greater than the speed of light. Albert Einstein then showed that the gravity of objects can become so great that not even light can escape (Einstein, 1916). John Wheeler popularized the term 'black holes' in his scientific talks in the 1960's (Thorne, 2009).

The spatial size of a BH is described by its event horizon, which is represented as a radius. This radius, called the Schwarzschild radius, is as a function of the BH mass (Schwarzschild, 1999, see description of Schwarzschild back holes in Section 1.3.1 in this thesis). Mass is one of the three fundamental properties of BHs. The second property is electric charge, and the third is angular momentum. Spiraling BHs are defined as Kerr black holes (Kerr, 1963, see Section 1.3.1 in this thesis).

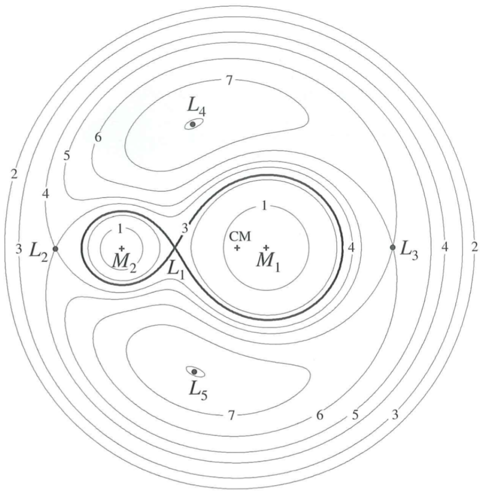

Figure 1.1: The equipotential lines of the Roche potential depict the regions of equal gravitational potential within a binary system. The center of mass (CM) indicates the point around which the masses of the two companions, M1 and M2, are balanced. The Lagrange points, labeled L1, L2, L3, L4, and L5, represent specific points in the system where the gravitational forces from both companions and the centrifugal force are in equilibrium. Figure taken from Frank et al. (2002).

1.2 From stellar mass black holes to supermassive black holes

Stellar mass BHs are formed from the gravitational collapse of massive stars. When a massive star has exhausted its nuclear fuel, the inward force of gravity exceeds the outward force of radiation pressure, and the star collapses in itself. The collapse continues until the star becomes so dense that not even light can escape its gravitational pull, resulting in a BH.

Microquasars are a type of compact object binary systems that includes a BH or neutron star as compact object and a companion star. They are similar to quasars, which are extremely luminous and distant active galactic nuclei, but mircroquasars are much smaller in size. Given this scaling, only objects of this kind in the Milky Way have been studied to far. In microquasars, material from the companion star is transferred onto the compact object by filling its Roche Lobe until the Lagrangian point L1, creating an accretion disk that emits intense radiation, including high-energetic X-rays (see Figure 1.1). The intense radiation and jets that are ejected from microquasars can be measured observationally. Matter is attracted by the strong gravitational force around the compact object, however, a stable accretion disk can form due to conversation of the matter's angular momentum. The matter in the accretion disk reaches centrifugal equilibrium and has to be disturbed in order to fall into the compact object. Two physical mechanisms causing this process are, for instance: (i) energy and angular

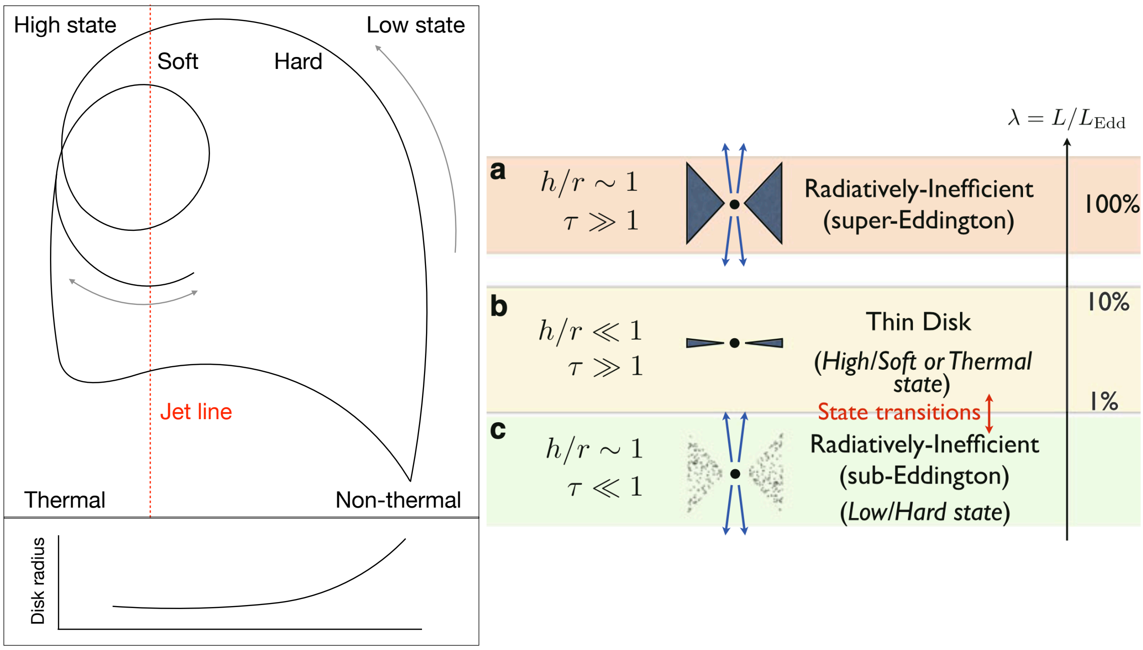

Figure 1.2: Spectral hardness diagram showing accretion states of microquasars. The diagram (on the **left**) depicts the relationship between hardness, i.e., non-thermal vs. thermal emission, and intensity/jetted and non-jetted jets. It includes schematic representations of the inflow/outflow configuration corresponding to each state. The diagram specifically focuses on the two canonical states, namely the hard state and the soft state. The corresponding disk configurations are listed on the **right**. Figure adapted from Contopoulos et al. (2015).

momentum transfer by colliding material in a turbulent environment, or (ii) magnetic fields extracting both energy and angular momentum from the gas. If the structures of jets and accretion disks exhibit self-similarity across the vast range of mass and power observed in compact objects, then it is expected that all black holes, when adjusted for mass, would display a similar relationship between X-ray and radio luminosity with respect to the relative accretion rate and jet behavior (Merloni et al., 2003; Falcke et al., 2004). Both groups, employing different approaches, discovered that such a correlation indeed appears to extend to AGN. This is based on their argument that a scale-invariant framework can be applied to all disk-jet systems (see further Körding et al., 2008). A study prove similarities in the systems by deriving both the accretion rate and the jet power from either the core (radio) luminosity or the extended (low-frequency radio) luminosity for AGN and microquasars (based on Körding et al., 2006; Willott et al., 1999).

The hardness-intensity diagram is a representation of the X-ray emission behavior observed from microquasars (Figure 1.2). Spectral hardness refers to the ratio of the X-ray flux at higher energies to that at lower energies. The diagram is divided into different regions or tracks that correspond to specific X-ray states of the microquasar. The X-ray states observed in microquasars are categorized based on the variability and hardness of their X-ray emission (Esin et al., 1997). These states are often referred to as the low/hard state, intermediate states, and high/soft state (see Figure 1.2):

1. Low/Hard state: In this state, microquasars exhibit relatively low X-ray intensity and high spectral hardness. The X-ray emission is dominated by a power-law spectrum, indicating the presence of a hot plasma (geometrically thick: $h/r \sim 1$, see Figure 1.2) around the compact object. The low hard state transfers into an intermediate state in the upper right part in the diagram.

2. Hard-intermediate state: The intermediate state is characterized by an increase in X-ray intensity due to a rising accretion rate and a decrease in spectral hardness compared to the low/hard state. This state is associated with the presence of a thermal component in addition to the power-law spectrum. The jets undergo a notable transformation, transitioning from a consistent flow to a temporary state characterized by brighter, discrete ejecta. This change occurs at a specific location commonly known as jet line.

3. High/Soft state: The high/soft state is characterized by a high X-ray intensity and low spectral hardness. The X-ray emission is dominated by thermal radiation from an optically thick $\tau \gg 1$ accretion disk surrounding the compact object.

4. Soft-intermediate state: The emission of radio and infrared synchrotron radiation diminishes, and the source transitions toward the left side of the diagram. It enters a soft thermal state where the dominance of the accretion disk becomes prominent. The emission in this state is mainly attributed to a multi-temperature black body.

The transitions between these states can occur due to various physical processes, such as changes in the accretion rate, the geometry of the accretion flow, or the properties of the companion star (Homan et al., 2001).

Quasars are very distant and luminous AGN that emit intense radiation across a broad range of wavelengths, from radio waves to X-rays. They are powered by the accretion of matter onto supermassive black holes (SMBHs), which can have masses ranging from millions to billions of times that of the Sun. Quasars are some of the brightest objects in the universe and are thought to be powered by the release of gravitational potential energy as matter falls into the BH.

Despite their differences, microquasars and quasars are connected by their common physical processes. Both types of compact objects are powered by the accretion of matter onto a BH, which can cause emission of intense radiation and the formation of jetted material. Studying the behavior of microquasars can therefore provide insights into the physics of quasars and other distant AGN, and help astronomers better understand the processes that drive the evolution of active galaxies across the universe (Belloni, 2010).

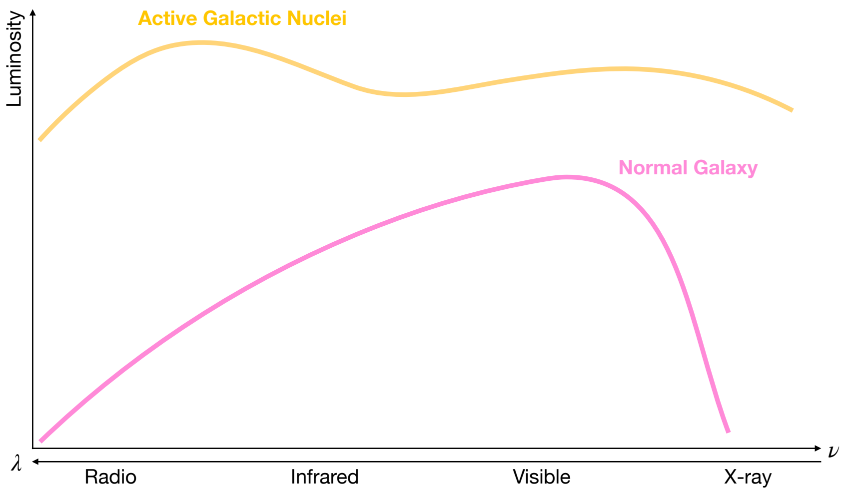

Figure 1.3: Schematic difference between a normal galaxy (rose) and an active galaxy (yellow) in terms of intensity as a function of frequency/wavelength. A major difference is visible in the low-frequency radio regime.

1.3 Active galactic nuclei

The discovery of the radio galaxies Cygnus A (Hey et al., 1946), Centaurus A (Cen A; Bolton et al., 1949), and Virgo A (Bolton et al., 1949) opened a new field of radio astronomy focused on the study of the release of energy from matter accreting onto compact singularities, such as supermassive black holes. These objects, hosting a central engine, are commonly referred to as AGN. Only a small percentage of these show activity in the radio regime, i.e., AGN with high jetted activity account for 1 % of the population whereas low activity galaxies are found in 10 % of AGN (Padovani et al., 2017). AGN can emit light over the whole electromagnetic spectrum, much broader than normal galaxies (Figure 1.3). AGN continuum emission extends across more than a dozen orders of magnitude in frequency (see Figure 1.4) and is up to four orders of magnitude more luminous than non-active galaxies. Their excessive emission is observed from a small region ($\lesssim 1\,\mathrm{pc}^3$; pc≡parsec). Their spectrum from radio to gamma-rays is directly linked to the emitted energy which is limited by the Eddington limit[1]. The Eddington limit places a limit on the maximum luminosity of the central engine when accreting matter, $L_{\mathrm{Edd}} \leq 3.8 \cdot 10^4\, {}^{M_{\mathrm{SMBH}}}/{}_{M_\odot}\, L_\odot^{14}$, from which the SMBH mass M_{SMBH} can be inferred. The total energy released by this compact object can reach therefore 10^{41} W, supposing that the driving mechanism must be different from nuclear fusion, and is balanced by gravitational versus radiation pressure.

[1]The Eddington Limit is derived by setting the gravitational force $F_{\mathrm{G}} = GM{}^{m}/{}_{r^2}$ equal to the radiation force $F_{\mathrm{rad}} = L{}^{\sigma_T}/{}_{4\pi r^2 c}$.

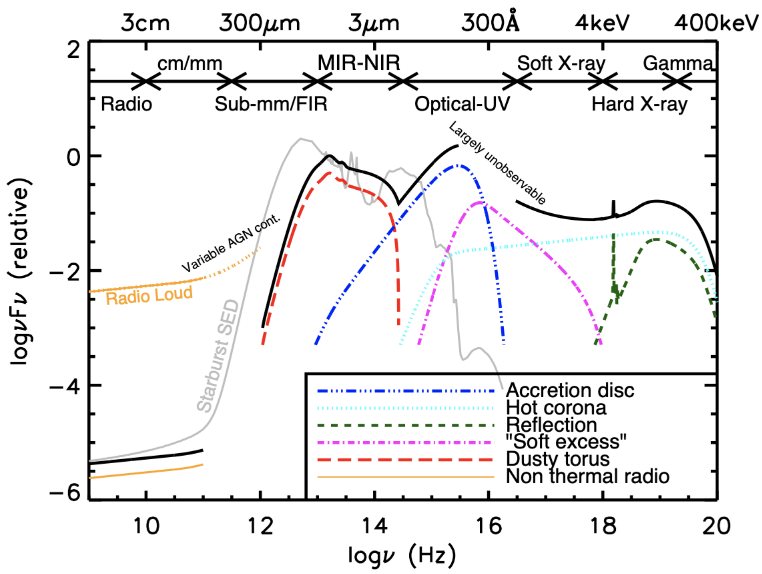

Figure 1.4: A schematic total spectral energy distribution (SED) of an AGN is represented by a black solid curve, while the individual components from AGN ingredients are shown by colored curves. The primary emission from the AGN accretion disk peaks in the UV region, and radio-loud AGN exhibit significantly higher radio emission compared to radio-quiet AGN. The non-thermal emission in radio (yellow) is associated with the synchrotron radiation from relativistic jets. Figure taken from Harrison (2014).

1.3.1 Ingredients to form an AGN

The central engine is believed to be located at the very center of the AGN and is powered by a SMBH. The SMBH is surrounded by an accretion disk of gas and dust that is in the process of spiraling toward the BH. As the material in the disk falls toward the BH, it releases gravitational potential energy, which is converted into radiation (for more details, see jet launching in Section 3.2.1). This process produces the intense luminosity that characterizes AGN. The central engine of an AGN is responsible for producing a wide range of phenomena, including the broad emission lines that are observed in the spectra of these objects, as well as the outflows of gas and dust that are observed to be moving away from the nucleus of the galaxy at high speeds. All ingredients contribute to the spectral energy distribution (SED) of the AGN. From radio to gamma-rays, from non-thermal radiation to thermal radiation, and from physical scales ranging from the SMBH to the accretion disk, and the outer jets/winds (Figure 1.4).

The supermassive black hole

The supermassive black hole forms the innermost part of the central engine in AGN. The vast amounts of energy that are released in these objects can only be explained by the presence of a strong gravitational potential, which is a characteristic of SMBHs.

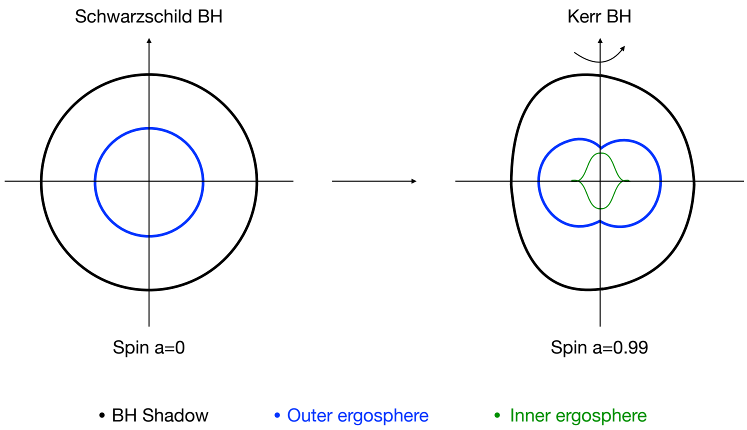

Figure 1.5: Black Hole (BH) shadow and ergosphere (inner/outer green/blue) for a non-rotating (Schwarzschild) BH with spin $a = 0$ and a rotating (Kerr) BH with spin close to unity. The sketch shows the deprojection of the shadow and the north-south reduction of the ergosphere, while forming an inner ergosphere in the rotating black hole system. The non-rotating BH is point-symmetric.

The event horizon is a critical concept related to BHs, as it defines the radius at which the gravitational pull is so strong that not even light can escape. The shape and radius of an event horizon in a compact object depends on whether the BH is non-spinning (Schwarzschild BH, left sketch in Figure 1.5) or spinning (Kerr, right sketch in Figure 1.5).

Schwarzschild black hole The Schwarzschild metric describes a non-rotating BH, with the event horizon defined as the Schwarzschild radius

$$R_\mathrm{S} = \frac{2GM_\mathrm{BH}}{c^2} \equiv 3\frac{M_\mathrm{BH}}{M_\odot} \equiv 0.02\,\mathrm{AU}\frac{M_\mathrm{BH}}{M_\odot}, \tag{1.1}$$

with the solar mass $M_\odot = 1.9891 \cdot 10^{30}$ kg and the astronomical unit AU$= 1.5 \cdot 10^{11}$ m. Within the Schwarzschild radius, a spin-independent gravitational radius R_G can be defined as $R_\mathrm{G} = {}^{GM_\mathrm{BH}}/_{c^2}$.

Kerr black hole A rotating Kerr black hole (Kerr, 1963) enlarges the equator of the event horizon, an effect which is described as Lense-Thirring effect (Thirring, 1918). The presence of the ergosphere is a characteristic feature that distinguishes a rotating BH from a static one, as this region has an elliptical shape (Figure 1.5). The Kerr radius R_K is dependent on the BH spin $a = {}^{Jc}/_{GM_\mathrm{BH}^2}$, with J being the angular momentum:

$$R_\mathrm{K} = R_\mathrm{G}\left(1 - \sqrt{1 - a^2}\right). \tag{1.2}$$

The ergosphere, outside of the event horizon, has a radius of

$$R_\mathrm{e} = R_\mathrm{G}\left(1 - \sqrt{1 - a^2 \cos\theta}\right), \tag{1.3}$$

where θ is the rotation angle. The Event Horizon Telescope (EHT) recently captured the first-ever direct image of the immediate vicinity surrounding the SMBH in M87, at the scale of its event horizon (Event Horizon Telescope Collaboration et al., 2019a). The resulting image depicts an asymmetric ring with a diameter of (42 ± 3) µas, which aligns with the expected characteristics of a Kerr black hole.

Accretion flow

The accretion disk forms as matter from the surrounding region, such as interstellar gas and captured stars, spirals inwards due to the immense gravitational pull of the BH. As the material moves closer to the BH, it gains gravitational potential energy and forms a rapidly rotating disk structure. The disk itself forms around the BH because of matter friction and angular momentum conservation (see Section 1.2). The gas in the disk is heated through various processes, such as friction and viscous forces, which convert gravitational potential energy into thermal energy. This heating causes the gas to emit intense radiation across a wide range of wavelengths, from ultraviolet to X-rays (see Figure 1.4). The accretion disk provides an energy source for AGN. As matter falls onto the disk and spirals inward, it releases a tremendous amount of gravitational potential energy. This energy release in form of the accretion flow powers the relativistic jets in AGN (Lyndel-Bell, 1969; Salpeter, 1964).

The efficiency of the accretion, which is one of the most efficient process of energy extraction in the universe (Tchekhovskoy et al., 2011), can be derived by having an equality of the kinetic and potential energy of the plasma and further assuming a luminosity dependency on the accretion rate ${}^{\mathrm{d}m}/_{\mathrm{d}t}$ as

$$L = \frac{1}{2}\frac{\mathrm{d}m}{\mathrm{d}t}v^2 = \frac{GM}{R}\frac{\mathrm{d}m}{\mathrm{d}t}, \tag{1.4}$$

with v being the free fall velocity and R the location of the matter around the BH. The luminosity L relates to the efficiency η as

$$L = \eta\frac{\mathrm{d}m}{\mathrm{d}t}v^2. \tag{1.5}$$

Using the Schwarzschild radius R_S (see Equation 1.1), the efficiency becomes:

$$\eta = \frac{GM}{v^2 R} = \frac{1}{2}\frac{R_\mathrm{S}}{R}. \tag{1.6}$$

Typical efficiencies range around $\eta \sim 10\,\%$ (Massi, 2018, and references within).

The broad and narrow emission line regions

The ionized gas in the vicinity of the SMBH, within a few parsecs, is excited by the intense radiation and produces characteristic emission lines that can be observed in the optical and ultraviolet spectra of the AGN.

The gas emitting the spectral lines in AGN is usually divided into two distinct regions based on the widths of the observed lines - the narrow line region (NLR) and the broad line region (BLR; see Figure 1.6). The NLR typically exhibits narrow emission lines with a full width at half-maximum (FWHM) of a few hundred $\mathrm{km\,s^{-1}}$, while the BLR shows broad emission lines with FWHM of several thousand $\mathrm{km\,s^{-1}}$.

The physical origin of the different line widths can be attributed to the location of the gas and the nature of its motion. The narrow emission lines are thought to arise from gas that is located farther away from the SMBH and is less affected by its gravitational potential. In contrast, the broad emission lines originate from gas that is in close proximity to the SMBH, where the gravitational potential is much stronger. The high velocities observed in the BLR lines can be explained by the gas orbiting the SMBH at high speeds, which produces a Doppler broadening of the emission lines. By assuming Keplerian motion of the gas, the SMBH mass M_{BH} can be estimated from the time difference τ between the broad line luminosity variability and the variability of the disk. In detail, the mass is calculated by applying the Virial theorem $M_{\mathrm{BH}} = {}^{\tau c}\!/_{G}(f\Delta\nu)$, where f denotes a geometry scaling factor, G is the gravity constant, c is the speed of light, and $\Delta\nu$ represents the FWHM.

The properties of the NLR and BLR regions in AGN provide important clues about the physical conditions and processes taking place in the vicinity of the SMBH. For example, the presence or absence of the BLR in a given AGN can be used to classify it as either a Type 1 or Type 2 Seyfert galaxy (see Section 1.3.2). The BLR is believed to be obscured by a dusty torus in Type 2 AGN, while it is visible in Type 1 AGN.

The dusty torus

Surrounding the inner accretion disk is a denser torus composed of cooler, dusty material that is opaque enough to obscure the thin accretion disk and BLR when viewed edge-on in the optical regime (see Figure 1.6). To directly observe this torus in a typical AGN, an angular resolution of approximately one milliarcsecond is required. Fortunately, this level of resolution is achievable using very-long-baseline interferometry (VLBI). It is worth highlighting that the internal structure of the torus can be intricate. Various observational indications, such as the existence of cold dust at relatively close distances to the central engine, the isotropic infrared emission originating from the torus, and distinctive X-ray absorption characteristics, imply that the distribution of dust and gas within the torus may be clumpy (Schartmann et al., 2008, see Figure 1.6).

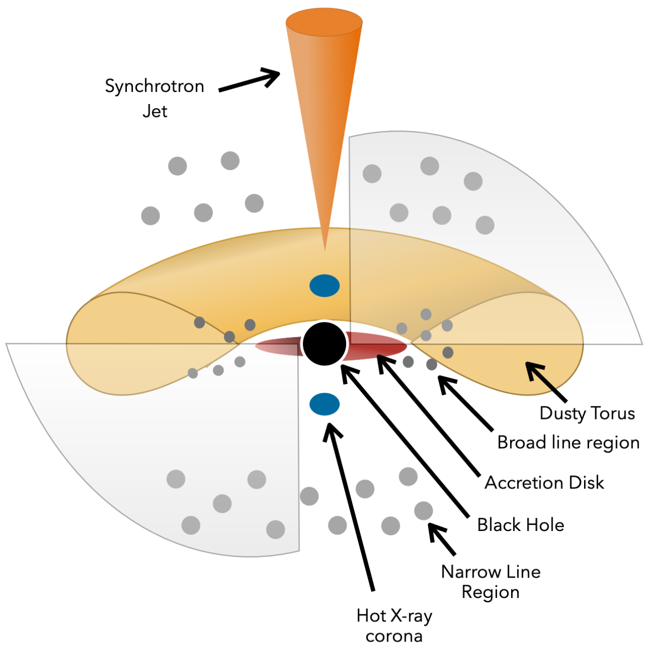

Figure 1.6: AGN torus model including the broad line region within the dusty torus and the narrow line region outside of it. The geometry of the broad and narrow line emission regions within the torus around the central engine may include a clumpy medium (grey circles) or a homogeneous disk (grey continuum) or as a combination. Figure adapted from Thorne (2023).

The relativistic jet

The jets in AGN are collimated, highly energetic outflows composed of plasma and magnetic fields. These bipolar outflow phenomena are similar to outflows observed in a wide range of compact astrophysical systems with varying central masses. These systems include young and protostellar objects, evolved stellar binaries, massive stars associated with gamma-ray bursts, and the centers of active galaxies. Although these systems differ in several aspects, they share a common feature: the involvement of mass accretion onto a central compact object, leading to an (relativistic) outflow. These correlations suggest a tight connection between the BH, accretion disk, and relativistic jet, implying that the underlying physics governing jet phenomena might universal across all compact objects.

AGN jets are known to propagate at relativistic speeds, with bulk Lorentz factors reaching values of tens or even higher (e.g., Zensus et al., 1995; Lister et al., 2013). The power of AGN jets can vary widely, typically ranging from 10^{43} to $10^{48}\,\mathrm{erg\,s^{-1}}$ (Ghisellini, Gabriele, 2013). They exhibit an impressive diversity in size, spanning from sub-parsec to kiloparsec and, in some cases, even reaching megaparsec scales (Mack et al., 1997). Our understanding of these jets is largely based on high-resolution interferometric observations in the radio band, facilitated by techniques such as VLBI,

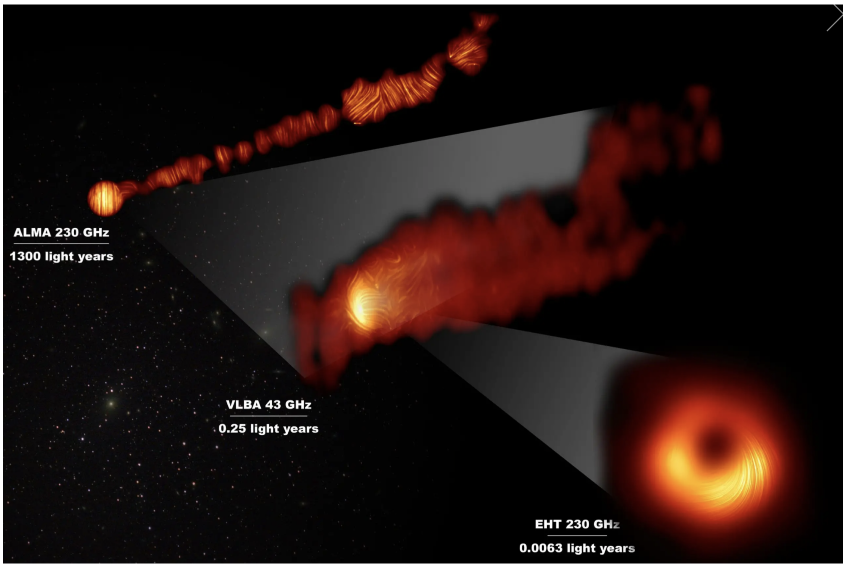

Figure 1.7: Multi-wavelength radio perspectives of the central region of Messier 87 (M87). **Top**: polarized-light image obtained by ALMA. **Middle**: VLBA image at 7 mm wavelength, and **Bottom**: the most detailed view by the EHT at 1.3 mm wavelength including polarized emission wind lines. Credits to: Event Horizon Telescope Collaboration et al. (2021), Goddi et al. (2019), Kravchenko et al. (2020), and Algaba et al. (2016).

for details see Section 2.2.2. The inner parsec scales of jets down to the BH can be revealed by: (i) increasing the observed frequency, or (ii) adding more radio telescopes at longer baselines. The effect of increasing both the observed frequency and the length of the interferometric baselines on the example of M87 is illustrated in Figure 1.7.

Studying relativistic outflows in AGN provides valuable insights into the underlying physics of BH accretion, particle acceleration, and magnetic field interactions at extreme scales. A detailed description of jets can be found in Chapter 3.

Relativistic beaming effects In some AGN sources, especially with jets oriented toward the observer, it occurs that observable features are apparently moving faster than the speed of light. The light-travel time effect causing this is a geometrical effect where projected material on the sky is moving over a smaller range in the same time as it really is, for reference see Figure 1.8. Two effects have to be considered: the relativistic beaming along the direction of motion, focussed within a critical angle $\theta_{\text{crit}} = {}^1/_\Gamma$ considering the bulk Lorentz factor $\Gamma = {}^1/\sqrt{1-\beta^2}$ with the speed of the plasma defined as $\beta = {}^v/_c$; and the relativistic Doppler boosting affecting the frequency and observed flux. The Doppler factor

$$\delta = \frac{\nu_\text{r}}{\nu_\text{s}} = \frac{1}{\Gamma + (1 \pm \beta \cos\theta)} \tag{1.7}$$

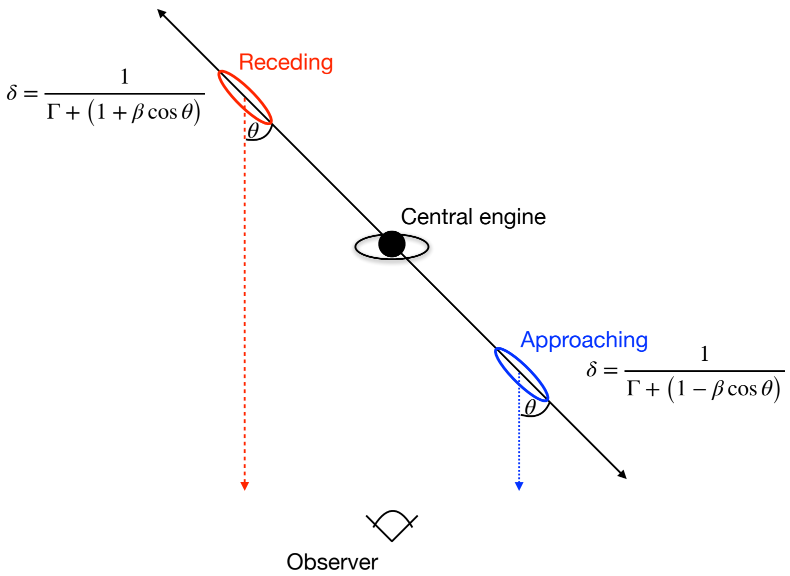

Figure 1.8: Geometrical effects in relativistic systems. Doppler factor as a function of the inclination θ and speed β for both receding and approaching jet flow. Sketch adapted from Boettcher et al. (2012).

defines how the observed frequency ν_r depends on the emitted frequency ν_s. The relativistic effects are greatly amplified on small angles to our line of sight (LoS) θ and plasma flows moving with a velocity close to the speed of light. Depending on whether the observed jet stream is approaching or receding, Equation 1.7 is resulting in a boosted or de-boosted shift in frequency (see Figure 1.8). The fact that the approaching jet appears to move faster than the speed of light is defined as superluminal motion (Rees, 1966).

1.3.2 The unification of AGN

Urry and Padovani, 1995, introduced a classification attempt to connect various observational sub classes of AGN by their optical emission profile or their morphology. They proposed a common model in which a SMBH is present at the center of each AGN, which is surrounded by an accretion disk and an obscuring dusty torus.

Figure 1.9 illustrates this model and shows the central engine (a BH), an accretion disk, a dusty torus, the broad and narrow line regions, as well as the relativistic jet, which occurs in only a small percentage of AGN (i.e., radio-loud AGN). In the unification model, AGN are categorized based on three primary criteria:

1. The viewing angle (inclination), which defines the amount of observable light received from the inner region of the AGN relative to the amount of light obscured by the dusty torus in our LoS.

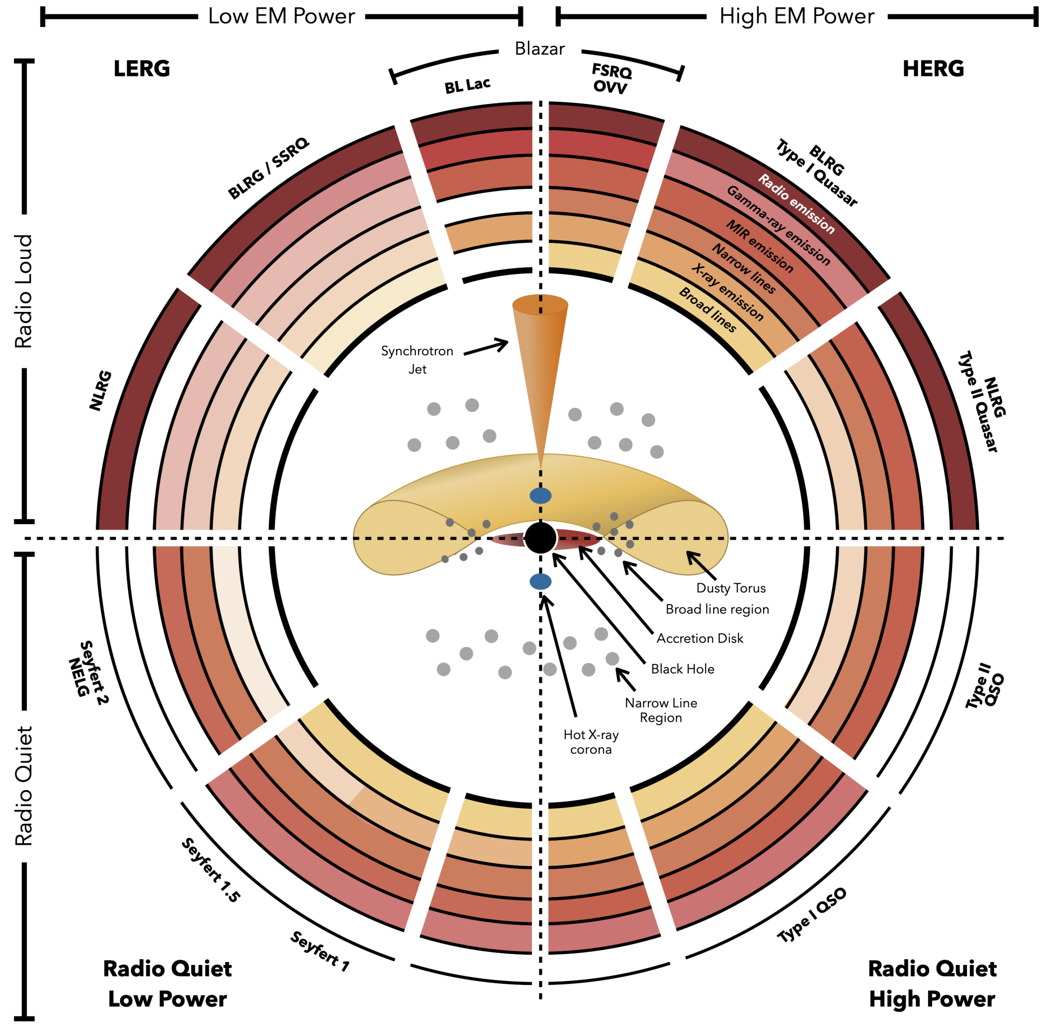

Figure 1.9: An illustrative summary depicting the fundamental components and geometry of an AGN, showcasing the radio quiet (bottom) and radio loud (i.e., significant jet emission; top) case. Making further distinction in the rate of accretion (low emission power versus high emission power). The transparent yellow to red color-code corresponds to the emission type and strength in a particular viewed AGN. The model also considers the role of different components, such as an accretion disk, broad emission lines, and obscuring material, which can give rise to distinct observational features depending on the line of sight to the AGN. Figure taken from Thorne (2023).

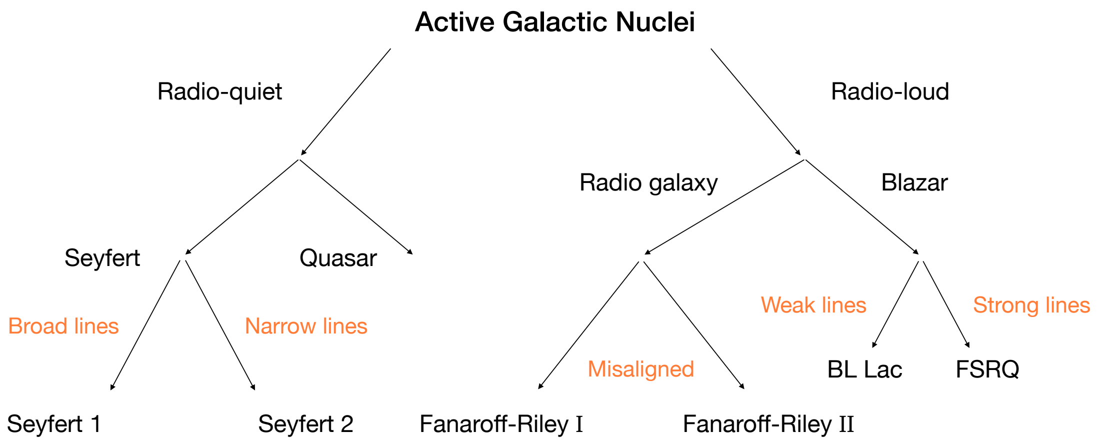

Figure 1.10: Classification of AGN types based on observational criteria: radio loudness (**top row**), viewing angle (**second row**), and strength of emission line or morphology of the AGN (**bottom row**). Figure adapted from Burke and Graham-Smith (1997).

2. The Eddington ratio $\lambda = L/L_{\mathrm{Edd}}$, which effectively distinguishes between different mass accretion rates and accretion flow geometries.

3. The radio loudness R, which is the ratio of the bolometric luminosity of radio and optical emissions. It divides AGN into radio-loud ($\mathrm{R} \geq 10-100$) and radio-quiet ($\mathrm{R} \leq 0.1-1.0$) classes. Therefore, the radio loudness also serves as a measure of the jet's emission.

The asymmetry in Figure 1.10 reflects the possibility of an AGN jet in the radio band to be either present or not. Hence, the first classification is radio-quiet versus radio-loud.

A radio-quiet AGN would be even fainter in the radio regime, by means of approximately a factor of thousand less than a radio-loud one. Further, radio-quiet is defined by the absence of an AGN jet. Seyfert galaxies and low-ionization nuclear emission line region (LINER) spirals are associated with radio-quiet types. The former are divided into Seyfert 1 and Seyfert 2 depending on the presence or absence of broad emission lines while both exhibit narrow emission lines (see Section 1.3.1). However, NGC 1068, classified as a Seyfert 2 galaxy, exhibits broad emission lines in polarized light (Antonucci and Miller, 1985), indicating that the observational effect might be indeed only an orientation effect. LINERs are weaker than Seyferts and host by definition a low-luminosity AGN. Lastly, Quasi-Stellar Objects (QSO), also known as radio-quiet quasars, are essentially Seyfert 1 galaxies observed from a smaller viewing angle. They emit optical and X-ray continuum radiation and display both narrow and broad emission lines.

On the other side, radio-loud AGN ($L_{1.4\,\mathrm{GHz}} > 10^{23}\,\mathrm{Ws}$) are further classified into distinct observable AGN types (see Figure 1.10). Three main classes and their sub classes of radio-loud AGN are recognized (Burke and Graham-Smith, 1997), while radio-loud defines jetted AGN:

- **Radio galaxies** are generally more extended with strong radio components, steep spectra, and larger viewing angle with jets oriented at large angles to our LoS.

- **Radio-loud Quasars** are bright continuum emitters with strong emission lines at ultraviolet and optical wavelengths, and with a small viewing angle (jet aligned to the LoS which leads to Doppler boosting effects). **Blazars** are also referred to as boosted Quasars and are dominated by compact radio components. Their continuum ranges until gamma-ray wavelengths and their SED is dominated by non-thermal jet emission. Mostly, they show strong variability.

Radio galaxies can be divided by emission profiles or morphology while radio-loud Quasars are classified by the characteristics of their SED:

- Low emission radio galaxies (**LERG**) show optical and X-ray emission from the jet region and no emission lines at all.

- High emission radio galaxies (**HERG**) may be identified with Seyfert 2 types and exhibit narrow line emission.

- Fanaroff-Riley **FR I** galaxies are defined by their core-brightened radio jet with dark radio lobes (LERG). They tend to show strong double-sided jets.

- Fanaroff-Riley **FR II** galaxies are, in contrast, edge-brightened radio galaxies with strong radio lobes associated with hotpots due to particle acceleration. They often appear one-sided.

- Flat-spectrum radio quasars (**FSRQ**) galaxies show broad emission lines. They identify as blazars which are on average more powerful and can be detected at higher redshifts.

- **BL Lacs** are identified by a hard spectrum, being less powerful, and showing weak or no emission nor absorption lines.

Blazars and radio galaxies are expected to be the same intrinsic object, rotated in inclination. FR I type sources may be associated with BL Lac objects, while FR II galaxies might be re-directed FSRQs. Summarized, all differences, being morphological, observational, or by differences in emission lines can be summarized by the schematic presentation in Figure 1.11. The summary is, among other data, distinguished by an analytical result that indicates jets are frequently observed when the Eddington ratio is low, and furthermore, when exhibiting a dual distribution of jet power based on the morphology of the source (Figure 1.12).

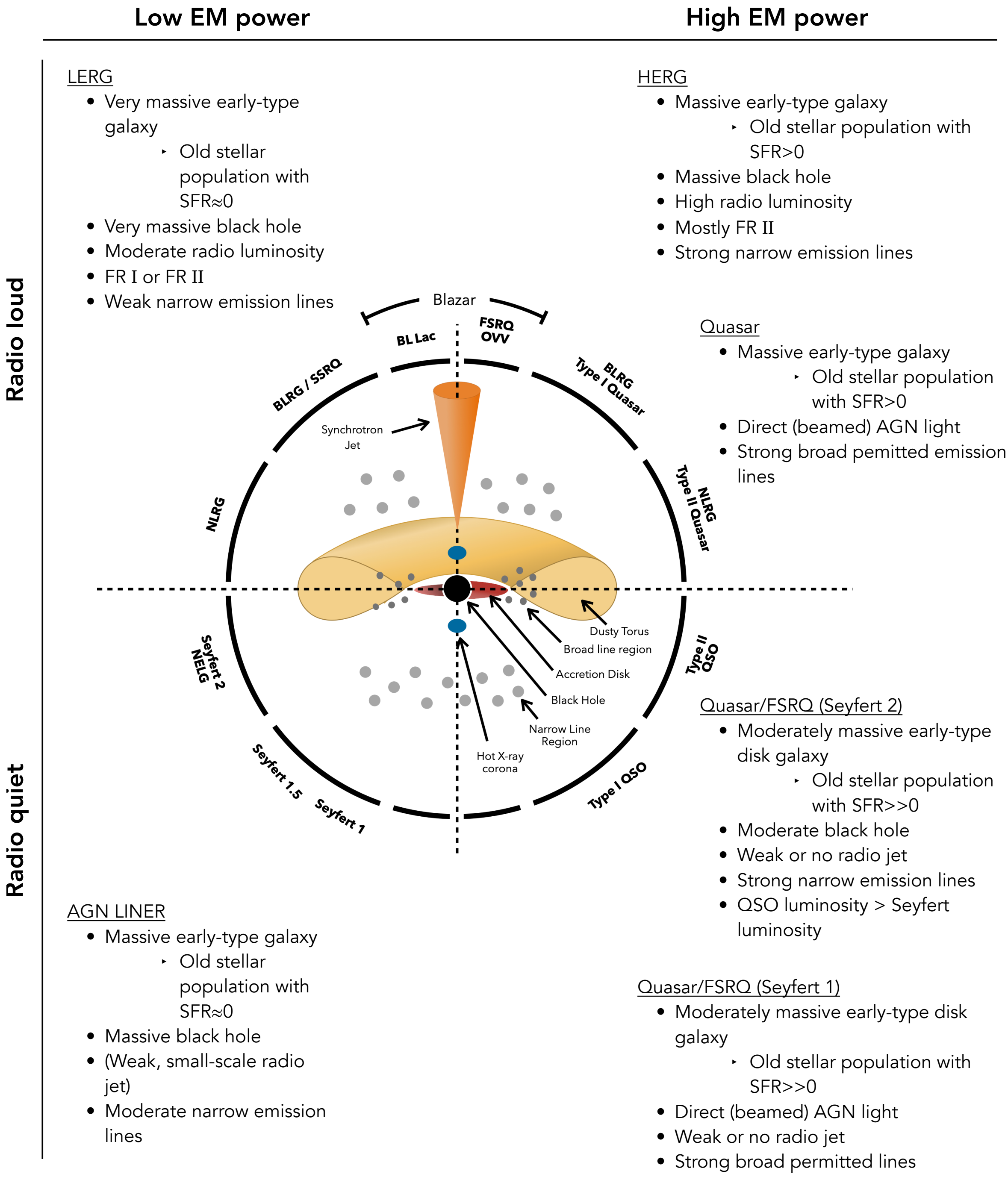

Figure 1.11: The physical classification of the AGN population is reviewed in this schematic sketch. The characteristics associated with each AGN class are listed. Distinction of radio-loud AGN (top) and quiet AGN (bottom), as well as weaker jets (left), and strong jets (right) is also made. This schematic unification model highlights the characteristics each type carries as a system, e.g., considering the type of host galaxy, star formation rate, luminosity, and emission lines. Figure adapted from Thorne (2023) and Heckman and Best (2014).

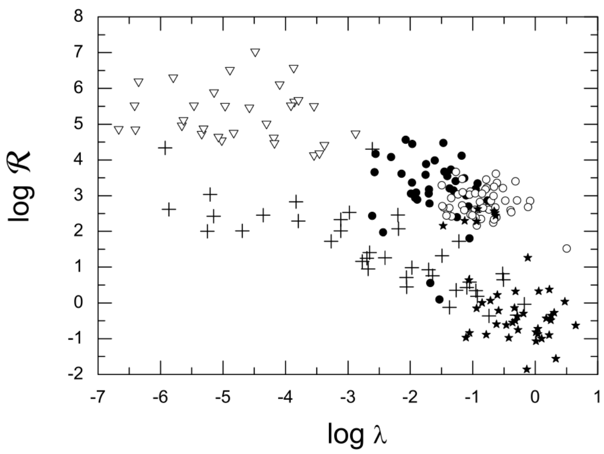

Figure 1.12: The logarithmic radio loudness $\mathcal{R}$ as function of the Eddington accretion ratio λ. The analytical study is fulfilled for different types of AGN. Figure taken from Sikora et al. (2007).

Blazars

Blazars, in general, exhibit a flat radio spectrum and display strong continuum emission spanning from radio to high-energy gamma-rays. They demonstrate a strong variable component at all frequencies and timescales. Blazars are classified as face-on AGN, indicating the presence of a relativistic jet closely aligned with our LoS. This alignment results in highly focused and Doppler boosted emission, which explains various phenomena associated with blazars. Notably, blazars show a high level of linear polarization (LP; up to 50 %) in the optical and radio ranges. They are recognized as the most variable and luminous type of AGN. The components of their jets exhibit superluminal motion (Rees, 1966) with bulk Lorentz factors typically ranging from $\Gamma = 5 - 15$ (Lister et al., 2019). Depending on the presence or absence of (optical) emission lines, blazars can be further distinguished into FSRQ or BL Lac objects, respectively.

The spectral energy distribution of blazars displays two peaks with an anti-correlation between luminosity and frequency (see Figure 1.13). The first peak is attributed to synchrotron radiation emitted by a single population of electrons (Angel and Stockman, 1980; Scarpa and Falomo, 1997). The second peak is divided into two hypothetical models: the leptonic model (Maraschi et al., 1992), describing emission produced by Compton scattering of low-energy photons, and the hadronic model (Mannheim, 1993; Mücke and Protheroe, 2001), which involves synchrotron radiation emitted by relativistic protons themselves.

However, there have been numerous contradictory sources observed, displaying both high luminosity and high peak frequencies (Padovani et al., 2003; Padovani et al., 2012). These contradictions are considered to be intrinsic factors, leading to the association of blazar types with FR I and II (Meyer et al., 2011). Recent studies have shown the

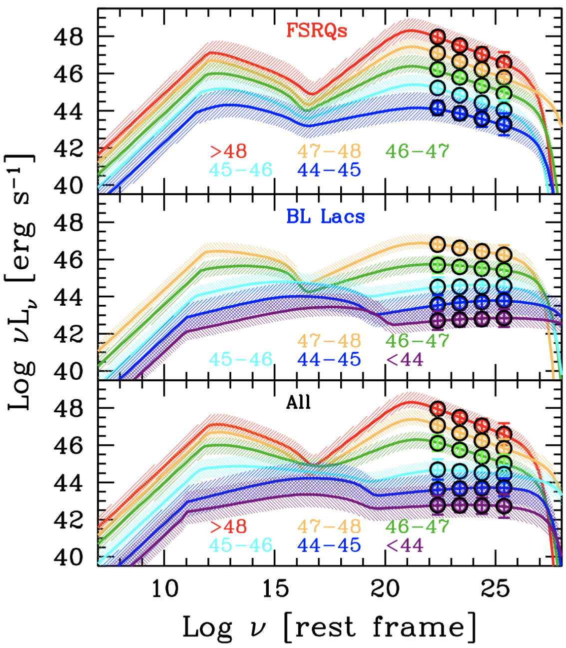

Figure 1.13: The Fermi blazar sequence showing the luminosity as function of the frequency. FSRQs of various luminosity classes exhibit an upward trend in Compton dominance as luminosity increases (**top panel**). However, there is no observed trend of decreasing peak frequencies. Similar behavior is observed when examining BL Lac objects (**central panel**). When considering all blazars as a whole, without distinguishing between FSRQs and BL Lacs, the same patterns persist (**bottom panel**). Figure taken from Ghisellini et al. (2017)

existence of a proposed blazar sequence for BL Lac objects, but no strong correlation has been found for FSRQs (Ghisellini et al., 2017). This discrepancy is interpreted as a result of the difference in the dominance of radiative cooling (see Chapter 6).

Magnetic fields play a significant role in the launching process and collimation of relativistic jets in blazars (see Section 3.2). Additionally, they contribute to particle acceleration and flaring phenomena. Therefore, understanding the magnetic field structure in the observed jets is essential, both on large scales to reveal the launching and collimation region and on small scales to study particle acceleration. The study of polarized signals, specifically focusing on the electric vector position angles (EVPAs) and circular polarization (CP), allows for the investigation of magnetic fields in blazars (Lyutikov et al., 2005, see Section 2.1.5). Circular polarization is particularly useful for probing the magnetic field structure and studying the particle composition in blazars. The emission can arise intrinsically from synchrotron radiation or extrinsically through Faraday conversion of linear to circular polarization (Komesaroff et al., 1984). The latter is predominantly influenced by the low-energy particles in the jet, enabling the study of properties such as the low-energy cut off of the electron spectrum and the particle composition (Homan and Wardle, 1999; Beckert and Falcke, 2002).

Observational evidence for structured jets in blazars on the parsec scale was first discovered through polarimetric Very Long Baseline Array (VLBA) observations of the FSRQ 1055+018 by Attridge et al. (1999). They observed a distinct difference in polarization direction between the inner jet (predominantly parallel to the jet) and the outer layer (perpendicular to the jet). Similar polarization structures have been observed in various other sources as well (e.g., Pushkarev et al., 2005; Gabuzda et al., 2014). The limb brightening of the jet, where the edges appear brighter than the core region, is another indication of spine-sheath structures. These structures have also been observed in high-resolution observations of radio galaxies and blazars on parsec scales (e.g., Giroletti et al., 2004; Piner et al., 2009; Nagai et al., 2014; Giovannini et al., 2018).

Theoretical models of blazars have demonstrated that both the polarization feature and the structure of the spine and sheath of the jet heavily depend on the morphology of the magnetic field (Kramer and MacDonald, 2021, see Chapter 5).

It is worth noting that in order to spatially resolve the emission in the blazar zone on parsec scales, which corresponds to an angular resolution of milliseconds, very-long-baseline interferometry (see Section 2.2.2) is required. A significant breakthrough has been made by observations with the Event Horizon Telescope (EHT; Event Horizon Telescope Collaboration et al., 2019a; Janssen et al., 2021; Kim et al., 2020). The EHT's high frequencies offer the advantage of reduced opacity in the jets. Most blazars are observed to become optically thin at approximately 100 GHz (Planck Collaboration et al., 2011). Hence, the EHT makes it possible to observe the innermost regions of blazars at a frequency of 230 GHz, where the emission originates. Extensive research has been conducted over the past few decades, particularly utilizing millimeter-wave (mm) very-long-baseline interferometry techniques. This approach offers exceptionally high angular resolution and the ability to probe regions that remain opaque at longer wavelengths (Kim et al., 2020). The EHT analysis of the blazar NRAO 530 provides a distinctive understanding of the subparsec scale configuration, utilizing microarcsecond precision (Jorstad et al., 2023). This insight holds significance for comprehending blazar physics on a broader scale. The discovery of an immensely massive supermassive black hole just around 900 million years after the occurrence of the Big Bang poses a challenge to prevailing models of early (supermassive) black hole growth (Belladitta et al., 2022). For a more comprehensive summary of the blazar sequence the reader is referred to Ghisellini et al. (2017), Hovatta and Lindfors (2019), Blandford et al. (2019), and Prandini and Ghisellini (2022).

1.4 Thesis motivation

Studying AGN jets, particularly in their most powerful form known as blazars (AGN jets viewed from a small angle to the LoS), has become an area of intense interest in unraveling the mysteries of AGN behavior. Observations across the entire electromagnetic spectrum of AGN revealed polarized emission explained by relativistic electrons spiraling around magnetic field lines. Hence, The observed high level of linear polarization, reaching up to 60−70 %, can be explained by the physical process of synchrotron radiation. On larger scales, jets are believed to be dominated by kinetic energy and consequently contain relatively weak magnetic fields. However, within the region of collimation, the jets are believed to be magnetically dominated. Theoretical investigations of jet formation propose that strong magnetic fields play a crucial role in initiating and launching jets. Further, theoretical models of AGN jets suggest that the jet plasma is likely to be magnetized with a large-scale helical morphology. Among these studies, those involving magnetohydrodynamic flows have been successful in explaining fundamental jet characteristics observed on scales from parsecs and beyond.

Comparisons between numerical (relativistic) magnetohydrodynamic jet simulations and the observed polarization of relativistic jets are essential for the examination on how the synchrotron emission morphology of the jet is influenced by the intrinsic magnetic characteristics of its relativistic plasma.

The main focus of this thesis centers on polarized synchrotron emission. The comprehensive analysis offered by this work provides valuable insights and results from numerical jet simulations compared to interferometric observations in the radio regime. The full Stokes view of blazar jets presented in this thesis highlights the observational discrepancies resulting from different magnetic field morphologies, particularly in circular polarization, and provides indications on the magnetic field's characteristics, by studying the electric vector position angles. Moreover, the conducted studies in this work highlight the necessity of considering radiative losses in numerical methods for a more precise treatment of jet simulations.

The first part of this manuscript summarizes the variety of active galactic nuclei observed in the centers of galaxies. The postulated theories of general relativity and BHs as a singularity in space-time form a base for the distinction of BHs of different sizes in mass: an view on stellar mass black holes up to supermassive black holes. The introduction to supermassive black holes is followed by an overview of various ingredients to form an AGN. Starting with the central engine, the supermassive black hole, and moving to what powers relativistic outflow: the accretion disk. The SMBH is surrounded by various components. The accretion disk building the innermost structure is surrounded by the broad and narrow line region, and a dense torus builds the outermost structure of the AGN consisting of either a homogeneous plasma or clumpy distinct clouds of matter. Radio-loud AGN exhibit jet emission, i.e., a collimated, highly energetic and fast outflow launched from the central region of the galaxy. Depending on the viewing angle of the jet to the LoS, these AGN classify in different types.

The remainder of this thesis is organized in the following manner:

- Chapter 2 explains details on the process of observational data. The physical mechanisms behind the observed emission are explained. It follows an overview on polarization. The chapter introduces radio astronomy as a concept, i.e., single-dish observations, interferometric mechanisms, and both the algorithms and methods used to analyze observational data, providing detailed information on the calibration and imaging steps performed.

- Chapter 3 outlines the past and present research on relativistic jets. The chapter forms an extensive overview of observational features in multi-wavelengths observations of jets interpreted by numerous theories.

- Chapter 4 describes the numerical implementation of relativistic jets. The chapter starts with numerical results of the past and present on different scales and features of AGN jets. The principles of plasma physics, diving into the heart of relativistic magnetohydrodynamics is presented. The numerical codes for the thermal jet simulations and the radiative transfer codes to calculate the non-thermal synchrotron emission are forming the end of this chapter.

- Chapter 5 includes the first publication of the dissertation. It shows how the synthetic polarized synchrotron emission depends on the intrinsic magnetic field morphology, as well as on the chosen electron scaling relation to map non-thermal variables from thermal parameters. The paper results in a sheath-brightened jet for a purely toroidal magnetic field, and a spine-brightened jet for a purely poloidal magnetic field in total intensity.

- Chapter 6 presents a submitted manuscript on the study of observational features in polarized synchrotron emission. The study focuses on 15 GHz observational results to compare the resultant emission maps with archival MOJAVE data and levels of circular polarization, and on 23 GHz observations for a sensitivity check. The robustness of electric vector position angles over the past years in comparison with archival MOJAVE data is confirmed. Consequently, this proves that the intrinsic structure of VLBI radio cores remains constant. The structure and sign in CP are in agreement with previous studies, revealing a switch in sign indicating a opacity change from 15 GHz to 23 GHz.

- Chapter 7 includes a manuscript on the hybrid fluid-particle approach of jet simulations, i.e., including Lagrangian particles, which are macro-particles consisting of numerous non-thermal micro-particles, in RMHD codes. The inclusion of radiative losses is ensured and results in an unobscured view on the simulated synchrotron jet emission. The comparison to Centaurus A stresses the presence of a toroidal component in its intrinsic magnetic field field configuration.
- Chapter 8 concludes the findings, explains those in the framework of the introductory chapters within this thesis and provides an prospective view on the future work and progress that is needed in the research on AGN jets.

2 | Processing the radio signal

Radio astronomy involves the exploration of natural radio emission originating from astrophysical objects. The radio frequency range covers an extensive range from 10 MHz to 1 THz, spanning five decades within the low-frequency domain of the electromagnetic spectrum. This wide frequency range allows for the observation of various astronomical sources, emitting both thermal and non-thermal radiation, as well as the study of propagation phenomena. Effectively covering this expansive radio window necessitates various radio telescopes and observation methods.

In its early stages, radio astronomy, using initial ground-based radio antennas, was a field driven by chance discoveries on a completely new window to the universe. These findings unveiled unforeseen sources, such as non-thermal radiation from our own galaxy (Reber, 1940), the dynamic realm of powerful radio galaxies and quasi stellar radio sources (quasars) (Hazard et al., 1963; Schmidt, 1963), the cosmic microwave background radiation resulting from the hot Big Bang (Penzias and Wilson, 1965), pulsars and neutron stars (Hewish et al., 1968), the supermassive black hole at our galaxy's core (Balick and Brown, 1974), and pronounced gravitational lensing effects (Walsh et al., 1979). Presently, radio astronomy has become an inclusive component of multi-wavelength astronomy, no longer existing as a distinct and separate discipline.

Radio waves can emerge from various physical processes (see Section 2.1), encompassing thermal mechanisms like Bremsstrahlung, non-thermal radiation like synchrotron (see Section 2.1.3), and inverse Compton scattering (see Section 2.1.4). Synchrotron radiation is produced when charged particles, such as electrons, spiral around magnetic field lines due to the Lorentz force in the presence of a strong magnetic field.

Radio astronomers directly measure incoming waves, a departure from the practice in the rest of the electromagnetic spectrum, where the photon-attribute of the light is predominantly measured. Measuring frequency holds two practical advantages: firstly, frequency measurement is more precise than wavelength measurement, and secondly, frequency remains constant when radiation passes through a refractive medium, whereas wavelength undergoes alteration.

The emitted signals are captured and processed by radio telescopes, specifically engineered to detect and amplify faint radio waves (see Section 2.2.1). Achieving high diffraction-limited angular resolution $\theta \simeq \lambda/D$ at radio wavelengths λ requires radio telescopes with substantial aperture diameters D. For imaging intricate and faint sources, optimal angular resolution is paradoxically achievable at the long-wavelength radio (mm to cm) end of the electromagnetic spectrum using extensive multi-element interferometers (see Section 2.2.2).

2.1 Radiation mechanisms

The polarized emission of AGN can provide important information about the physical mechanisms in the emitting region. For example, synchrotron radiation (see Section 2.1.3) typically produces polarized radiation that is aligned with the magnetic field direction (see Section 2.1.5). The degree of polarization can also provide information about the magnetic field strength and orientation in the emitting region, see, e.g., Chapter 5 or Kramer and MacDonald (2021). Overall, the polarization of radio waves can provide valuable insights into the physical mechanisms and environments where radiation was originated, as well as the properties of the intervening material.

2.1.1 Brightness temperature

By applying the Rayleigh-Jeans law to calculate the brightness temperature T_{B}, it becomes apparent that the jet emission is non-thermal due to the high values observed. The following equation defines the brightness temperature T_{B},

$$T_{\mathrm{B}} = \frac{I_\nu c^2}{2k\nu^2}, \tag{2.1}$$

and links, mathematically, both frequency ν and observed intensity I_ν to the temperature of the emitting region by considering the Boltzmann constant k. The brightness temperature can be interpreted as the temperature of a hypothetical blackbody that would produce the same amount of radiation as the observed object at a given frequency. In other words, the brightness temperature is a way of quantifying the amount of radiation emitted by an object on the sky, regardless of the physical mechanism that produced the radiation (Kirchhoff, 1860). For example, thermal radiation from an object at a certain physical temperature can produce the same brightness temperature as non-thermal radiation from an object at a much higher temperature. Non-thermal radiation, such as synchrotron radiation from high-energy electrons, could therefore produce a different brightness temperature, which is not related to the temperature of the emitting material. This thesis focuses on physical processes involving the non-thermal jet emission.

2.1.2 Radiative transfer

The theory of radiative transfer deals with the interaction between radiation and intervening matter, based on the quantum description of light. In most astrophysical scenarios, this particle description is adequate for comprehending the production and transfer of radiation within and through an astrophysical medium, particularly at the macroscopic level. Radiative transfer defines the specific emissivity j_ν as the power $\mathrm{d}E/\mathrm{d}t$ emitted per unit volume $\mathrm{d}V$, per unit frequency interval $\mathrm{d}\nu$, and per solid angle $\mathrm{d}\Omega$:

$$j_\nu = \frac{\mathrm{d}E}{\mathrm{d}\Omega \mathrm{d}\nu \mathrm{d}t \mathrm{d}V}. \tag{2.2}$$

In other words, Equation 2.2 (Rybicki and Lightman, 1979) equals the specific intensity added per unit distance through the medium. Absorption and emission is then simply associated with the power added or removed within a solid angle $\mathrm{d}\Omega$. The latter scales with the absorption coefficient κ_ν. The power removed is specified as $\kappa_\nu I_\nu \, \mathrm{d}\nu \, \mathrm{d}\sigma \, \mathrm{d}s \, \mathrm{d}\Omega$, with $\mathrm{d}V = \mathrm{d}\sigma \mathrm{d}s$, where $\mathrm{d}s$ defines the path length through the absorbing medium over a cross-sectional area $\mathrm{d}\sigma$. The power equation of radiative transfer is

$$\frac{\mathrm{d}I_\nu}{\mathrm{d}s} = j_\nu - \kappa_\nu I_\nu, \tag{2.3}$$

which describes the behavior of the specific intensity along a specific sight line. One solution to Equation 2.3 depends on the opacity of the medium. The intensity of a ray can be split into its components in emission $I_{\nu,e}$ and absorption $I_{\nu,a}$:

$$I_{\nu,e} = I_\nu^0 + \int_0^s j_\nu \, \mathrm{d}s \quad \text{and} \quad I_{\nu,a} = I_\nu^0 e^{\left(-\int_0^s \kappa_\nu \, \mathrm{d}s\right)}. \tag{2.4}$$

The integral in the exponential term defines the optical depth τ_ν, which reduces to

$$I_\nu = -I_\nu^0 e^{-\tau_\nu}, \tag{2.5}$$

assuming homogeneous absorption through the plasma. With strong attenuation and an optically thick medium the optical depth becomes large ($\tau_\nu \gg 1$) while for a transparent medium, being optically thin, the optical depth decreases with a lower limit of zero. The transition between these is exactly at $\tau_\nu = 1$.

2.1.3 Synchrotron radiation

It is thought that the source of non-thermal synchrotron radiation in AGN comes from relativistic jets, which are typically composed of charged particles, such as high-energy electrons, and magnetized plasma. The magnetic field strength in these jets varies, being higher closer to the central engine and especially in the radio cores of

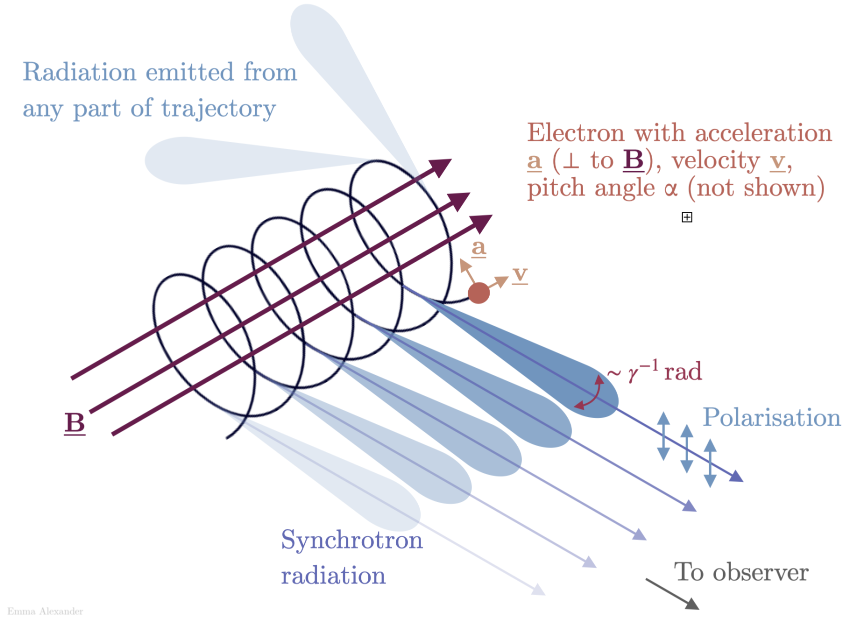

Figure 2.1: Description of synchrotron radiation generated by an electron following a helical trajectory around a structured magnetic field. Credits: Wikimedia; Emma Alexander.

blazars, while being lower in the extended structure of relativistic jets (Ricci et al., 2022). For more information on the magnetic field morphology along jets, the reader is referred to Chapter 5 or Kramer and MacDonald (2021). In observational terms is synchrotron radiation directly linked, among others, to radio emission. The low-energy radio component in the SED spectrum of radio-loud AGN can be attributed to synchrotron emission (see Figure 1.4).

Energy in the form of synchrotron radiation is emitted by (charged) particles spiraling around a magnetic field due to the Lorentz force, i.e., gyration (see Figure 2.1). In the case of non-relativistic particles, the cyclotron frequency ν_{cyc} as a function of the electron charge e is independent on the angle between the velocity $\beta = v/c$ and the magnetic field B and is defined by

$$\nu_{\mathrm{cyc}} = \frac{eB}{2\pi mc}. \tag{2.6}$$

For relativistic particles with energy $E = \gamma mc^2$, with a Lorentz factor of $\gamma \gg 1$, the frequency is reduced due to the increase in effective mass. The resulting energy-dependent *synchrotron* frequency ν_{S}[1] is written as

$$\nu_{\mathrm{S}} = \frac{\nu_{\mathrm{cyc}}}{\gamma}. \tag{2.7}$$

[1]The gyration, hence, the synchrotron radiation would stop if the relativistic velocity would be in parallel direction to the magnetic field.

The emitted energy over a time frame by a particle orbiting in arbitrary direction in reference to the magnetic field $\mathbf{B}\beta = B\beta\cos\phi$ is given by the laws of electrodynamics (see Dermer and Menon, 2009; Jackson, 1975; Griffith and Ruppeiner, 1981):

$$\left(\frac{\mathrm{d}E}{\mathrm{d}t}\right)_{\mathrm{S}}(\phi) = -\frac{16\pi c}{3}\left(\frac{q^2}{mc^2}\right)^2 u_{\mathrm{B}}\beta^2\sin^2\phi. \tag{2.8}$$

The magnetic energy density $u_{\mathrm{B}} = {}^{B^2}/_{8\pi}$ is included in Equation 2.8. If the radiation direction, i.e., the pitch angle distribution terminates in a largely shorter timescale than the elapsed time for the energy losses, Equation 2.8 can be averaged over ϕ:

$$\left(\frac{\mathrm{d}E}{\mathrm{d}t}\right)_{\mathrm{S}} = \frac{1}{4\pi}\int_{4\pi}\mathrm{d}\Omega\left(\frac{\mathrm{d}E}{\mathrm{d}t}\right)_{\mathrm{S}}(\phi) = -\frac{32\pi c}{9}\left(\frac{q^2}{mc^2}\right)^2 u_{\mathrm{B}}\beta^2\gamma^2, \tag{2.9}$$

assuming a particle charge q. Introducing the Thomson cross-section σ_{T} as

$$\sigma_{\mathrm{T}} = \frac{8\pi}{3}\left(\frac{q^2}{mc^2}\right)^2, \tag{2.10}$$

and rewriting energy E in terms of γ, Equation 2.9 reads

$$\left(\frac{\mathrm{d}\gamma}{\mathrm{d}t}\right)_S = -\frac{4}{3}c\sigma_T\frac{u_B}{mc^2}\beta^2\gamma^2 \equiv -P, \tag{2.11}$$

which applies for the total energy loss per unit time of a single relativistic particle due to synchrotron radiation or the inverse of the total power P of the emitted synchrotron radiation. Further, the energy per unit area per unit frequency equals the spectrum of the synchrotron radiation ${}^{\mathrm{d}W}/_{\mathrm{d}\omega\mathrm{d}\Omega}$. Integrating over a solid angle and dividing by orbital period yields

$$\frac{\mathrm{d}W}{\mathrm{d}\omega\mathrm{d}t} \equiv P\left(W\right) \propto F\left(\frac{\omega}{\omega_c}\right), \tag{2.12}$$

where ω_c is the critical frequency of the spectrum $\omega_c = \frac{3}{2}\gamma^3\omega_B\sin\phi$. With Equation 2.6, Equation 2.7, and $\omega = 2\pi\nu$ the critical frequency becomes

$$\omega_c = \frac{3\gamma^2 qB\sin\phi}{2mc}. \tag{2.13}$$

The total power P of the synchrotron radiation averaged in time per unit frequency is given by

$$P = \int_0^\infty P(\omega\phi)\mathrm{d}\omega \propto \int_0^\infty F\left(\frac{\omega}{\omega_c}\right)\mathrm{d}\omega, \tag{2.14}$$

where the final dimensionless function $F\left({}^{\omega}/_{\omega_c}\right)$, which defines the shape of the spectrum, is not pre-defined.[2] The relativistic ($\beta \approx 1$) synchrotron power is finally derived:

$$P(\omega) = \frac{\sqrt{3}}{2\pi} \frac{q^3 B \sin\phi}{mc^2} F\left(\frac{\omega}{\omega_c}\right). \tag{2.15}$$

Power spectra can usually be approximated by a power-law in a given range of frequency:

$$P(\omega) \propto \omega^{-s} \quad \text{or equivalently} \quad P(\nu) \propto \nu^{-s}, \tag{2.16}$$

where the power-law index s defines the steepness (see Figure 2.2). Analogously, an approximation of a power law holds for particle distributions of relativistic electrons. The number density of particles with energies between E and $E + \mathrm{d}E$ and $E_{\text{min}} \leq E \leq E_{\text{max}}$ can be written as

$$N(E)\mathrm{d}E \propto E^{-s}\mathrm{d}E \quad \text{or} \quad N(\gamma)\mathrm{d}\gamma \propto \gamma^{-s}\mathrm{d}\gamma, \quad \left(E = \gamma m_e c^2\right). \tag{2.17}$$

Applying this to the total power Equation 2.14 and substituting $x \equiv {}^{\omega}/_{\omega_c}$ yields

$$P(\omega) \propto \omega^{-(s-1)/2} \int_{x_{\text{min}}}^{x_{\text{max}}} F(x) x^{(s-3)/2} \mathrm{d}x. \tag{2.18}$$

For an approximately constant integral from $x_{\text{min}} \approx 0$ to $x_{\text{max}} \approx \infty$, the total power reduces to

$$P(\omega) \propto \omega^{-(s-1)/2}. \tag{2.19}$$

Finally, we conclude that the synchrotron spectral index α and energy distribution power-law index s connect via

$$\alpha = \frac{s-1}{2}. \tag{2.20}$$

The spectrum in Figure 2.2 shows the emitted synchrotron intensity as a function of the frequency in a logarithmic plot. The shape of the spectrum is showing the superposition of individual contributions of relativistic particles (electrons). The left-hand side of the spectrum shows an increase that assigns to optically thick areas, such as the radio core (see Section 1.3 for more information), until the turnover frequency is reached. The position of the turnover frequency depends on the magnetic field strength and the energy density. During the rising part, the slope is described by $P(\nu) \propto \nu^{5/2}$. The optically thickness is associated with a synchrotron self absorption region, where

[2] The function $F(\omega)$ might involve, for instance, an integral of a modified Bessel function of second kind (Ginzburg and Syrovatskii, 1969).

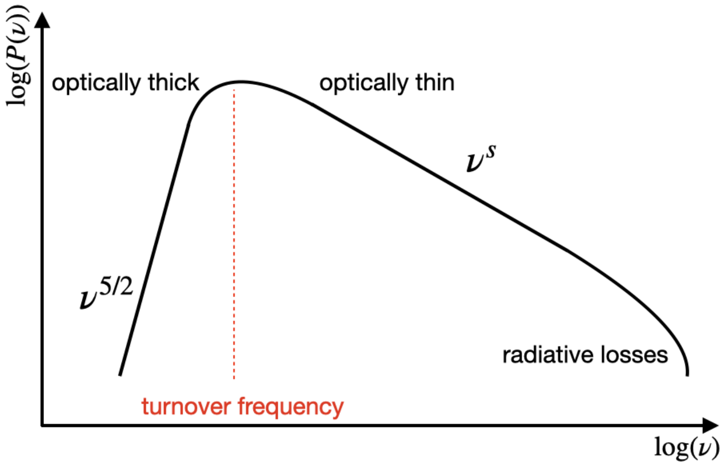

Figure 2.2: Diagram showing a synchrotron spectrum as a power function of frequency, as commonly observed in active galactic nuclei (AGN). The rising slope corresponds to an optically thick region, whereas the falling slope illustrates optically thin synchrotron radiation with a tail of radiative losses. The slope s of the spectrum is directly linked to the spectral index α in observational emission maps of AGN.

some of the synchrotron photons are absorbed by the spiraling electrons. This thesis, however, focuses on the right-hand optically thin part of the spectrum. In this region, observations of extended components are expected. The slope is described as a power-law of the form $P(\nu) \propto \nu^{-s}$, where the synchrotron spectral index falls roughly in the range $0.6 \leq \alpha \leq 2.5$. Higher values are commonly found at higher frequencies due to radiative losses and a resultant steepening of the spectral energy distribution. In particular, the synchrotron spectrum shows a cut off at the highest frequencies for highly relativistic particles, resulting in a rapid decrease of the synchrotron power. This phenomenon occurs because the electron power-law distribution experiences time evolution and will be depleted without a process of re-energizing. Particles re-gain energy through Fermi acceleration, also known as diffusive shock acceleration. The concept states that particles undergo acceleration by gaining velocity or equivalent energy after each reflection (such as in shocks, turbulence or cosmic shear effects) during their movement. There are two types of Fermi acceleration mechanisms: first order, which is more significant in the environments of AGN, and second order. In first-order Fermi acceleration, particles gain energy by continuously crossing (upstream and downstream) through a shock wave, which leads to acceleration of the particles. However, with a lack of re-energizing, the emissivity of the synchrotron plasma decreases over time. The radiative losses, here specifically synchrotron, which refer to the cooling or aging of the spectrum, are proportional to the magnetic energy density, which can be calculated from the rate of energy losses due to synchrotron radiation of a single relativistic electron. As the electrons age, the break in the spectrum shifts to lower frequencies. This is further studied in Chapter 7.

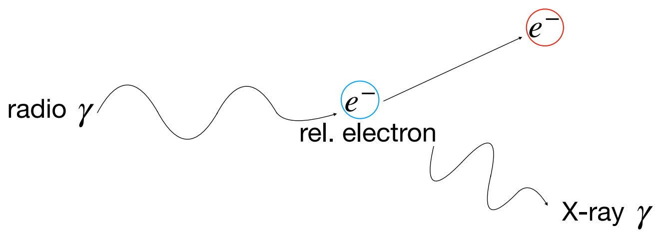

Figure 2.3: Illustration of the inverse Compton effect. The low-energetic radio photon is up-scattered by an electron at rest to be emitting in X-ray afterwards.

Relativistic particles described by a power-law energy distribution and an isotropic pitch angle distribution will produce (linearly) polarized light to a degree of

$$\Pi = \frac{p+1}{p+\frac{7}{3}}. \tag{2.21}$$

Equation 2.21 is the fraction of two Bessel functions to contribute to the shape of spectrum. However, the degree of polarization can be lower for a given distribution due to superposition effects along and across the LoS than for a single non-thermal particle. Polarization is further described in detail in Section 2.1.5.

2.1.4 Inverse Compton scattering

Compton scattering refers to a phenomenon in which the energy of a photon is transferred to a particle during a collision (see Figure 2.3). In the classical case, a high-energy X-ray photon interacts with a low-energy electron, resulting in a decrease in the energy of the photon. However, in inverse scenarios, the opposite can occur with a relativistic non-thermal particle transferring energy to a low-energy photon, which is known as inverse Compton scattering. This process boosts the frequency of the scattered photon by a factor of γ^2, allowing radio photons to be boosted to higher energies up to the ultraviolet and X-ray bands.

Inverse Compton scattering can be further classified based on the origin of the seed photons. If the seed photons come from synchrotron radiation, the process is called synchrotron-self Compton. If the photon field is of external origin, such as from the broadline region or cosmic microwave background, it is referred to as external Compton. The total power for inverse Compton scattering can be expressed mathematically. The high-frequency emission ($10^{16} - 10^{26}$ Hz) observed in astrophysical scenarios is typically a result of inverse Compton scattering (see Figure 1.4 and Figure 2.3).

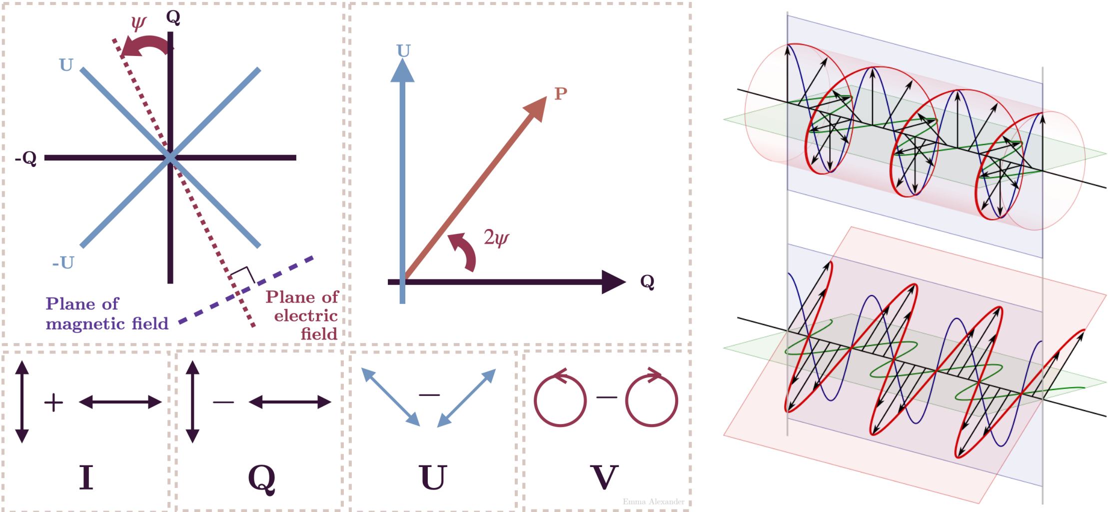

Figure 2.4: **Left:** Representations of the Stokes parameters in relation to the planes of the electric and magnetic fields. Credits: Github, Emma Alexander. **Right:** Top figure shows circular polarization, bottom figure shows linear polarization. Both with underlying magnetic field lines. Figure taken from Wikimedia.

2.1.5 Polarization

Linear polarization

The linear polarization of synchrotron emission is caused by the perpendicular acceleration of relativistic electrons to the magnetic field, as described by the mechanism of synchrotron radiation. However, due to randomized orientation of the electrons over microscopic scales, the pitch angles are also arbitrarily distributed and the resulting synchrotron emission is incoherent. The polarized properties of synchrotron emission can be described using Stokes parameters (Stokes, 1851):

$$\begin{aligned} I &= E_1^2 + E_2^2, \\ Q &= E_1^2 - E_2^2, \\ U &= 2E_1E_2 \cos\left(\varphi_1 - \varphi_2\right), \\ V &= 2E_1E_2 \sin\left(\varphi_1 - \varphi_2\right). \end{aligned} \tag{2.22}$$

Figure 2.4 and Equation 2.22 describe the Stokes parameters. Stokes I is the total intensity: $I \geq \sqrt{Q^2 + U^2 + V^2}$. Stokes Q defines the linear polarization at 0° and 90°, respectively, while Stokes U rotates the linear polarization component to −45° and 45°, respectively. The last component, Stokes V, describes the CP, which is positive for right-handed circular polarization and negative for left-handed circular polarization. It is evident that the Stokes parameters rely on the electric field components $\mathbf{E}$, which

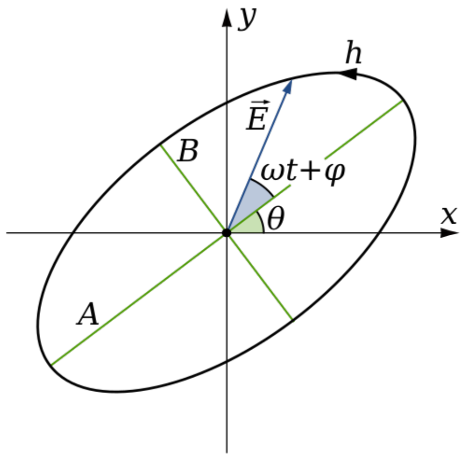

Figure 2.5: Polarization ellipse. The electric field component E in x-,y-direction, representing the amplitude of the electromagnetic wave, is directly linked to the phase in time $\omega t - \varphi$ of the polarization. The parameter h denotes the direction of circular polarization. Figure taken from Wikimedia.

correspond to the electromagnetic wave projected on to the sky (see Figure 2.5):

$$E_{z,y} = E_{1,2} \cos\left(\omega t + \varphi_{1,2}\right), \tag{2.23}$$

with $E_{1,2}$ being the complex amplitudes of the electric field.

Further, EVPAs (χ from now on; Ψ in Figure 2.5, respectively) are a function of the linear polarized Stokes parameters Q and U:

$$\chi = \frac{1}{2} \arctan\left(\frac{U}{Q}\right). \tag{2.24}$$

The fraction of linear polarization m_l is calculated in relation to the total intensity:

$$m_l = \frac{\sqrt{Q^2 + U^2}}{I}. \tag{2.25}$$

Circular polarization

When light is emitted, it can be either linearly polarized, where the electric vector vibrates in a straight line, or circularly polarized, where the electric vector rotates around the direction of propagation. This type of polarization is achieved by combining two linearly polarized waves that are orthogonal to each other and have a phase difference of 90 degrees.

In general, CP in AGN can be produced by synchrotron radiation, which is emitted by relativistic electrons spiraling around magnetic field lines, or by Faraday conversion, which is a birefringent effect converting LP into CP as the wave passes through a magnetized plasma. The rotation of the polarization angle depends on the strength and orientation of the magnetic field, and can be used to probe the magnetic field structure in the AGN.

The amount of CP produced by these mechanisms is of very low levels (less than 1 %), while LP is significantly more pronounced (up to 70 %). The specific amount of CP produced by an AGN depends on various factors, such as the strength and configuration of the magnetic field, the energy and distribution of the emitting particles, and the viewing angle of the observer. Therefore, the amount of circularly polarized light produced by AGN can vary widely. In blazars, the CP mechanism is commonly attributed to linear birefringence. The degree of fractional circular polarization m_c is evaluated using the Stokes parameters I and V, i.e.,

$$m_c = -\frac{V}{I}. \tag{2.26}$$

Circular polarization can serve as a valuable probe between observations and numerical simulations of jets, allowing for a deeper understanding of the characteristics of the plasma within the jet (Wardle et al., 1998). When circularly polarized light passes through plasma, it can interact with the plasma's electrons, which can respond to the magnetic component of the electromagnetic wave. The way that the electrons respond to the wave depends on their energy and density, as well as on the magnetic field composition. Hence, observational data of CP in blazars can be used to study the composition and magnetic field properties of the plasma in the jets. The degree and orientation of the CP can provide information about the density and energy distribution of the plasma electrons, and the strength and orientation of the magnetic field.

2.2 Radio astronomy

In 1933, Karl Jansky discovered a radio signal at 21 GHz from an extraterrestrial origin (Jansky, 1933). Remarkably, the emitted signal corresponded to one particular area in the sky: the central region of our host galaxy, the Milky Way. Jansky's pioneering work in radio astronomy ignited a lasting sense of awe among astronomers, as the radio sky has remained an unceasing origin of newly discovered wonder. Acknowledging his discovery, radio astronomy defines the Jansky unit [$1\ \mathrm{Jy} = 10^{-26}\,\mathrm{W\,m^{-2}\,Hz^{-1}}$], which is now commonly used for the flux density $P(\nu)$. It defines the flux per unit frequency or unit bandwidth. The total flux P is obtained by

$$P = \int_0^\infty P(\nu)\,\mathrm{d}\nu. \tag{2.27}$$

The pursuit of scientific advancements has necessitated heightened sensitivity and precision to characterize instruments, a particularly challenging endeavor within the radio frequency range. Notably, the angular resolution of a telescope operates in an inverse relationship with the wavelength of the radiation. This implies that despite the substantial size of telescopes, achieving noteworthy angular resolution remains a challenging task. Regardless of these challenges, the primary and substantial benefit lies in the fact that radio waves, along with optical waves, possess the unique ability to permeate the Earth's atmosphere. However, beyond 1 cm ($\sim$ 30 GHz), the radiation experiences partial absorption by the atmosphere. This absorption arises from the molecular vibrational and rotational transitions of substances like water, oxygen, and carbon dioxide. Furthermore, the atmosphere emits radio waves itself, occasionally constraining the feasibility of conducting delicate observations, particularly near the water vapor line around 22 GHz. Consequently, observations at high(er) frequencies become attainable only from elevated and/or dry regions on earth, for instance, like the Institut de Radioastronomie Millimétrique (IRAM) 30-m telescope on Pico Veleta, Sierra Nevada, near Granada, Spain. The Effelsberg 100-m telescope, which preferentially observes at centimeter wavelengths, is built in a valley in the Eiffel, Germany, to prevent turbulence but also to be isolated from radio-frequency-inference (RFI) produced by modern electronics. The Atacama Large Millimeter/submillimeter Array (ALMA), and the Atacama Pathfinder Experiment (APEX), in the Atacama desert, Chile are located at approximately at height of 5000 m above sea level to overcome limits in high frequency observations.

The challenge concerning advancements in angular resolution limitation has been a focal point in the evolution of aperture synthesis, a concept recognized by the Nobel Prize (Ryle and Hewish, 1960). Aperture synthesis involves the ingenious process of assembling an array of telescopes to create a substantially expanded effective aperture. This sophisticated method finds its richest application in VLBI, building a synthetic telescope dish, comparable to the size of Earth. The Very Long Baseline Array, VLBA, and Event Horizon Telescope (EHT) play an important role in this thesis. The main results of Chapter 6 are conducted by analyzing 15 GHz and 22 GHz observations with the VLBA. The EHT successfully imaged the event horizon of two supermassive black holes: M87* (Event Horizon Telescope Collaboration et al., 2019a) and Sagittarius A* (Event Horizon Telescope Collaboration et al., 2022). Concentrating on AGN jets, the results presented in Chapter 7 focus on a comparison to the EHT observations at 230 GHz of the radio galaxy Centaurus A (Janssen et al., 2021), see further Section 3.6.

2.2.1 Elements of a radio antenna

This thesis chooses a single-dish radio telescope to illustrate the components of a radio antenna: The 100 m radio telescope in Effelsberg.

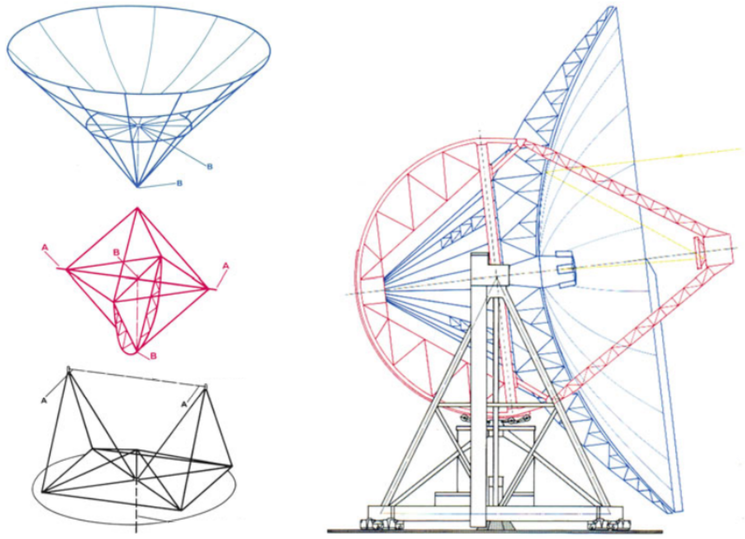

Figure 2.6: Sketch of components of a rotatable radio antenna as the example of Effelsberg. The sketch shows the steerable base, a quadrupod structure, and an umbrella cone. Figure taken from Baars and Kärcher (2018).

Effelsberg

The concept of the Effelsberg telescope was designed in the 1960's, and remains one of the most accurate antenna systems in radio astronomy until today (Wielebinski et al., 2011). The 100 m telescope is one of the biggest, heaviest (at the time when it was constructed) steering telescope dishes worldwide. It takes 16 motors and 32 wheels to move approximately 100 tons in each wheel on the rail track. The motors are powering for- and backwards on the 64 m diameter ring track to stabilize the position and ensure an axis accuracy of 0.2 mm. To transfer this accuracy to the dish and the received signal, the telescope structure is built to prevent astigmatism. To avoid this error, which could be caused by the heavy weight on construction parts, Effelsberg increased the supporting point of the reflector dish from two to four and a quadrupod has been added to stabilize the structure. The desired homology, however, is only ensured if the force will be diverted between these four homogeneously. This results in the umbrella principle (see, e.g., Wielebinski et al., 2011). Further, stabilization in radial direction is an important factor, too. For that, the constructions of the quadrupod and umbrella cone are detached from each other and only linked at a single point (see Figure 2.6).

The dish of the Effelsberg telescope is built in the principle of a Gregorian system. The radio signal - observable from 90 cm to 3.5 mm - is, for instance, passing the primary reflector before being focused in the secondary reflector and finally arrive in the feed horn (secondary focus). However, both is possible: to observe with the primary or secondary focus distinctively (see Figure 2.6, more details in the following paragraphs).

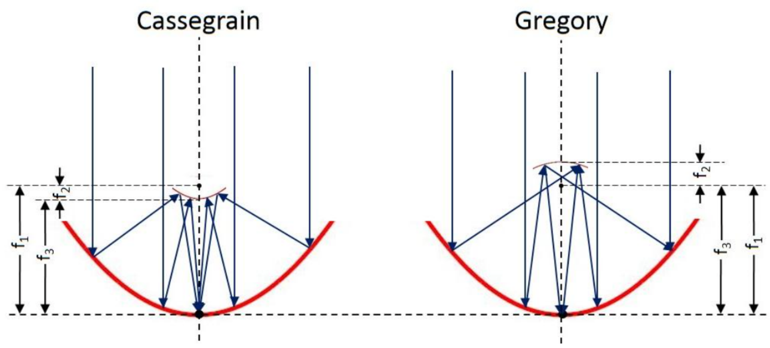

Figure 2.7: Optical paths in Cassegrain (**left**, convex) versus Gregory (**right**, concave) mirror systems. Figure taken from U. Klein, lecture notes.

Primary reflector The fundamental task of the primary reflector in the shape of a paraboloid is to concentrate the incoming wave front into a spherical beam. To gain a strong signal, the mirror preferentially offers a large reflecting surface. The power P then reads

$$P = \frac{1}{2} A_{\text{eff}} \cdot P(\nu) \cdot \Delta\nu, \tag{2.28}$$

with A_{eff} being the effective collecting area and $\Delta\nu$ being the selected receiving the bandwidth.

Secondary reflector The secondary reflector is ideally located close to the central focus of the primary reflector. This is necessary for two reasons: first, to extend the focal plane, i.e., the plane applicable for focused observations, and second, to prevent ground radiation influences. Two systems would be fitting: a Cassegrain or a Gregorian focus. The first one will be a hyperbolic mirror oriented in the same direction as the primary one (see Figure 2.7). The latter is using an elliptically shaped secondary mirror (e.g., as is the case at Effelsberg). The extended focal plane allows to place several receiver systems at once, i.e., as mentioned above for Effelsberg observations within a frequency range of 300 MHz to 90 GHz.

Beam pattern and feed horn The reflected focused incoming wave has to pass the feed horn before the signal is detected by the receiver. The feed horn filters RFI and prevents mixing of polarization. Once the desired polarization is selected, the signal can be detected both on a linear or a circular basis. The latter is provided by a quarter-waveplate situated along the pathway. That way, a delay of half a wavelength in light that is polarized parallel to a specific axis of the component is introduced with respect to light polarized perpendicular to that axis. This optical device is capable of rotating the polarization angle of linearly polarized light by an adjustable amount. The signal, i.e., the incoming focused wave front is transformed into a constant electric

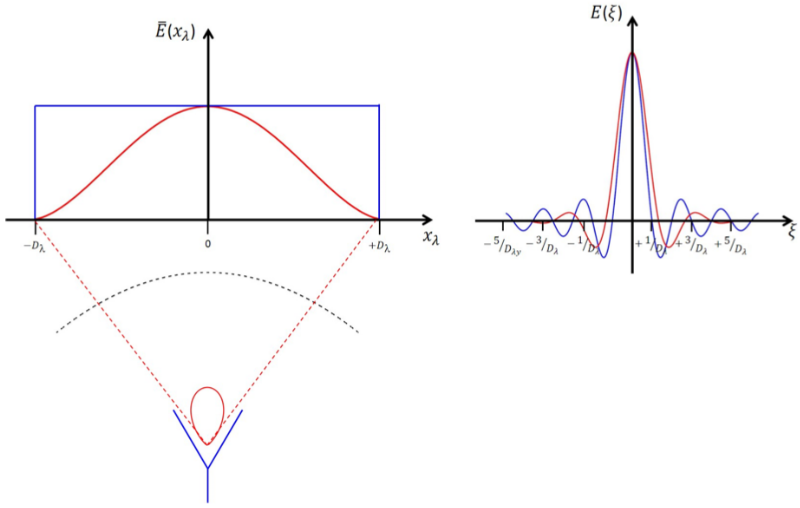

Figure 2.8: Radio signal (**left**) and Fourier transformation (**right**) showing the main beam and side lobes. Reduction of the electric field strength toward the edged to avoid strong side lobes. Figure taken from U. Klein, Radio astronomy: tools, applications and impacts.

field along a finite aperture. However, a constant illumination leads to (relatively) high sidelobes, which are undesirable. If a function with sharp edges is used, it results in high-frequency Fourier components during the transform (see Figure 2.8 in blue lines). To address this, the field strength toward the edge of the dish is reduced, commonly achieved through grading (see Figure 2.8 in red lines). Grading is achieved by designing the feed to have its reception pattern falling to zero toward the edges of the dish. As a result, the feed in the focus plays a crucial role in controlling the illumination of the reflector.

Receiver

The radio signal has to cross several electronic stages from entering the feed horn until it is recorded (see Figure 2.9). The initial radiation undergoes amplification using a high-frequency amplifier (HF amplifier). Subsequently, a mixer is employed to down-convert the HF signal to an intermediate frequency (IF stage) following the heterodyne principle. This principle not only allows for tuning the observing frequency to the desired value by adjusting the local oscillator frequency but also ensures a decoupling between the HF and IF components. This prevents detrimental feedback that would otherwise occur due to the required high amplification. A bandpass filter is then utilized to select the desired frequency band, and further amplification is provided by the IF amplifier, making the voltage detectable by the detector, which consists of a diode that rectifies the incoming voltage (see Figure 2.8). At this stage, power is measured, with the output voltage of the detector being proportional to the power. The

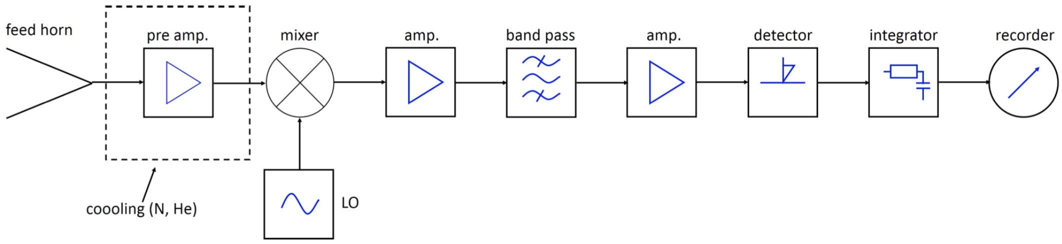

Figure 2.9: Electrical components of catching a radio signal. Figure taken from U. Klein, Radio astronomy: tools, applications and impacts.

signal is integrated with an RC device having a time constant, enabling its transfer to a display, and finally, an analogue-to-digital conversion (A/D conversion) is implemented, allowing the data to be stored and processed in a computer.

However, each added electronic component in the path is a potential liability to the system. Electric devices will inevitably loose tiny fractions of the received signal, resulting in so called leakage. If initial received signal would be amplified without down-conversion, these fractions would be amplified, too, and cause the system to be unstable. To counteract this effect, the signal path can be decoupled in frequency space, for instance, after the first amplification. The heterodyne amplification describes exactly this process.

Antenna resolution

The voltage beam width F as function of the aperture diameter u in one dimension (d= 1) is the Fourier transform of the grating, and is given by (Burke and Graham-Smith, 1997)

$$F_{\mathrm{d}=1}\left(\Theta\right) = \frac{\sin\left(\pi u \Theta\right)}{\pi u \Theta}, \tag{2.29}$$

where Θ marks the angle of the observed object with respect to the point of reference in the dish. In two dimensions (d = 2), for a circular aperture the result in Fourier transform reads

$$F_{\mathrm{d}=2}\left(\Theta\right) = \frac{2J_1\left(\pi u \sin\left(\Theta\right)\right)}{\pi u \sin\left(\Theta\right)}, \tag{2.30}$$

where J_1 is a Bessel function of the first order. Note that ${}^1\!/_u = {}^\lambda\!/_D$ holds for dishes of diameter D taking into consideration that the geometry of a FWHM is quantifiable. The resolving power is expressed by the Rayleigh criterion (Rayleigh, 1879). It describes the limit to resolve two points on the sky separately. Hence, the smallest resolvable angular scale of these objects is given by

$$\Theta = A\frac{\lambda}{D}, \tag{2.31}$$

with the emitted wavelength λ and antenna size D. For a realistic, parabolic (or circular) radio antenna, the factor A in units of u, defining the position of the first minimum in beam power, results in $A = 1.22\,u$.

2.2.2 Radio interferometry

The resolution is limited by the telescope's dish size, see Equation 2.31. This, however, can be virtually extended by using the principle of a Michelson interferometer (Michelson and Morley, 1887; Michelson et al., 1994). In radio interferometry, several smaller radio stations are (electronically) connected and, hence, form one artificial large aperture. This can extend up to the Earth's diameter in size in the case of VLBI. Furthermore, RadioAstron started observations in 2011, a space-based radio observatory, extending VLBI to a space based baseline of 350.000 km (Kardashev et al., 2012). Radio interferometer gather signals from distant telescopes, generate synthetic data through cross-correlation, and produce high-resolution images using Fourier transformation during the appropriate imaging process (see Section 2.3).

Interferometry is based on the physical principle of interference between to (incoming) waves. These can be coherent or incoherent depending on their correlation in phase. If a signal emitted by a point source of small angular size compared to the separation of the interference maxima, is observed by two or more antennas, then the dark and luminous regions in the virtual plane are called fringes. To determine the amplitude of the fringes, the visibility function or complex interferometric visibility is applied.

The van Cittert-Zernike theorem

The Huygens-Fresnel principle defines the electric field E_λ of monochromatic radio waves emitted from a source at a position R, measured at distance r:

$$E_\lambda\,(r) = \int \epsilon_\lambda\,(R)\,\frac{e^{2\pi i|R-r|/\lambda}}{|R-r|}\,\mathrm{d}S. \tag{2.32}$$

Since only a single polarization component is being analyzed, the radiation can be treated as a scalar field. As the source is assumed to be far away ($R \gg r$), the complex electric field on the surface of the source on the celestial sphere $\epsilon_\lambda(R)$ is two-dimensional, and the integration is done over an observed surface area dS. Only by using the most accurate systems, i.e., hydrogen maser or atomic clocks for timing the signal and high precision digitization, the recorded signal can be cross-correlated to

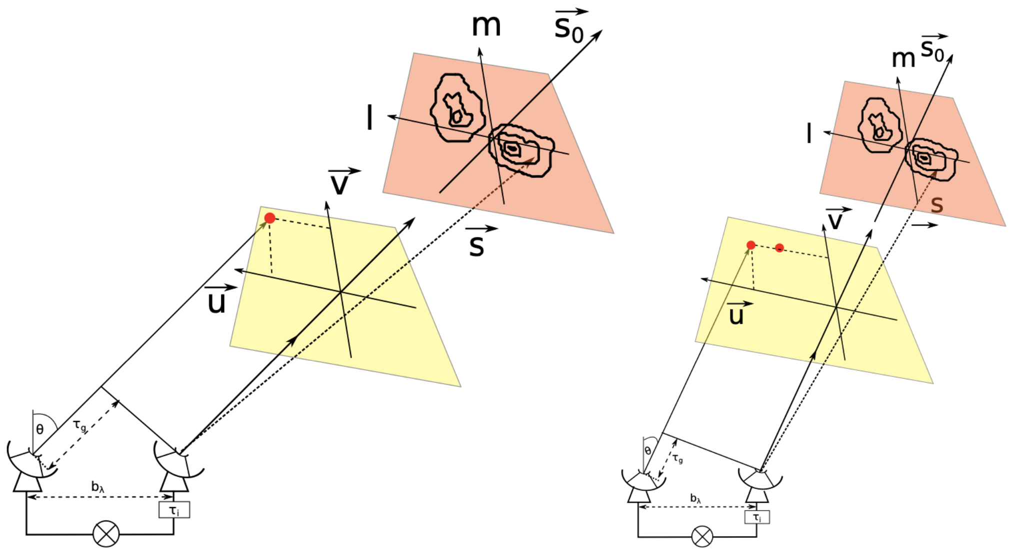

Figure 2.10: On the **left**, a basic two-element interferometer is depicted at time t_1, while on the **right**, the same interferometer is shown at time t_2. The lm-plane represents the distribution of source brightness, and it is linked to the measured visibility in the uv-plane. The rotation of the Earth causes the uv-plane to be filled with data points for reach antenna pair (red dots). Figure taken from Baczko (2020).

form an interference pattern V between sets of two telescopes in the array. The time average over the electric field will yield the following pattern:

$$V_\lambda\left(r_i, r_j\right) = \left\langle E_\lambda\left(r_i\right) E_\lambda^*\left(r_j\right)\right\rangle, \tag{2.33}$$

where $E_\lambda\left(r_i\right)$ and $E_\lambda\left(r_j\right)$ are measured at r_i and r_j, respectively, and $E_\lambda^*\left(r_j\right)$ is the complex conjugate. To link the source brightness $I_\lambda(s)$ (in a solid angle $\mathrm{d}\Omega$) to the response of the interferometer under the assumption of spatially incoherent radiation, it can be shown that

$$V_\lambda\left(r_i, r_j\right) = \int I_\lambda\left(s\right) e^{-2\pi i s\left(r_i - r_j\right)/\lambda}\, \mathrm{d}\Omega. \tag{2.34}$$

Equation 2.34 connects the source brightness to the measured quantities, i.e., the complex visibilities, through a Fourier transform.

In practice, the wavelength can be related to baselines between antennas labeled with i and j, respectively, by $r_i - r_j = (u, v)\lambda$. Further, the unit vector s can be written in three dimensions as $\left(l, m, \sqrt{1 - l^2 - m^2}\right)$ adding a factorization to the complex visibility integral:

$$V_\lambda\left(u, v\right) = \int\int \frac{I_\lambda\left(l, m\right)}{\sqrt{1 - l^2 - m^2}} e^{-2\pi i\left(ul + vm\right)}\, \mathrm{d}l\mathrm{d}m. \tag{2.35}$$

This is illustrated in Figure 2.10.

Telescopes observe polarization states related to the electric field (vector) E separately. Consequently, the polarization is split in right- and left-handed circular polarization states, RCP and LCP, respectively. This is accomplished by using quarter-wave plates in the receivers. RCP and LCP can determine the four Stokes parameters (Stokes, 1851):

$$\begin{aligned}
I_{ij} &= \left(\langle R_i R_j^* \rangle + \langle L_i L_j^* \rangle\right)/2, \\
Q_{ij} &= \left(\langle R_i L_j^* \rangle + \langle L_i R_j^* \rangle\right)/2, \\
U_{ij} &= i\left(\langle L_i R_j^* \rangle + \langle R_i L_j^* \rangle\right)/2, \\
V_{ij} &= \left(\langle R_i R_j^* \rangle - \langle L_i L_j^* \rangle\right)/2.
\end{aligned} \tag{2.36}$$

Full-polarization VLBI measurements have been taken for the purpose of this thesis. However, recovering each Stokes parameter takes more than calculating RCP and LCP. In reality, the visibilities are corrupted by direction independent calibration effects for measurements taken along a baseline $i - j$. These calibration products can be written as V_{ij}. Visibilities along $i - j$ are defined by

$$V_{ij} = V_{ij}^{\text{obs}} = \mathcal{J}_{ij} V_{ij}^{\text{true}} + \text{noise} = g_i g_j^* V_{ij}^{\text{true}} + \text{noise}, \tag{2.37}$$

where $\mathcal{J}_{ij}$ would be the Jones (Jones, 1941) or Mueller (Mueller, H., 1948) matrices. The former one would be applicable to describe the polarization state if the four Stokes parameter could be described by a 2×2 formalism. The latter one applies for a 4×4 formalism and if the light is incoherent and not completely polarized. The Jones metric can be reduced to a diagonal form in a Cartesian coordinate system. The diagonal components, considering linear dipoles and no polarization, can be identified as the baseline-based complex gains g_i (g_j, respectively).

2.2.3 Interferometric arrays

Very Long Baseline Array

The Very Long Baseline Array is comprised of ten antennas distributed over the US territory from the Caribbean to Hawai‘i with baselines measuring up to 8611 km (Napier et al., 1994; NRAO, 2023, see dark blue crosses in Figure 2.11). Each antenna captures the incoming signal, which is then transmitted to the correlator in Socorro, NM, USA. All ten telescopes are identical, featuring 25-meter diameter parabolic disk antennas. The combined signal at the primary focus is amplified, digitized, and recorded using fast and high-capacity devices. The recorded data do not only encompass the signal itself but also includes specific information about the observing conditions. The radio observations conducted by the VLBA span a wavelength range from 3 mm to 90 cm.

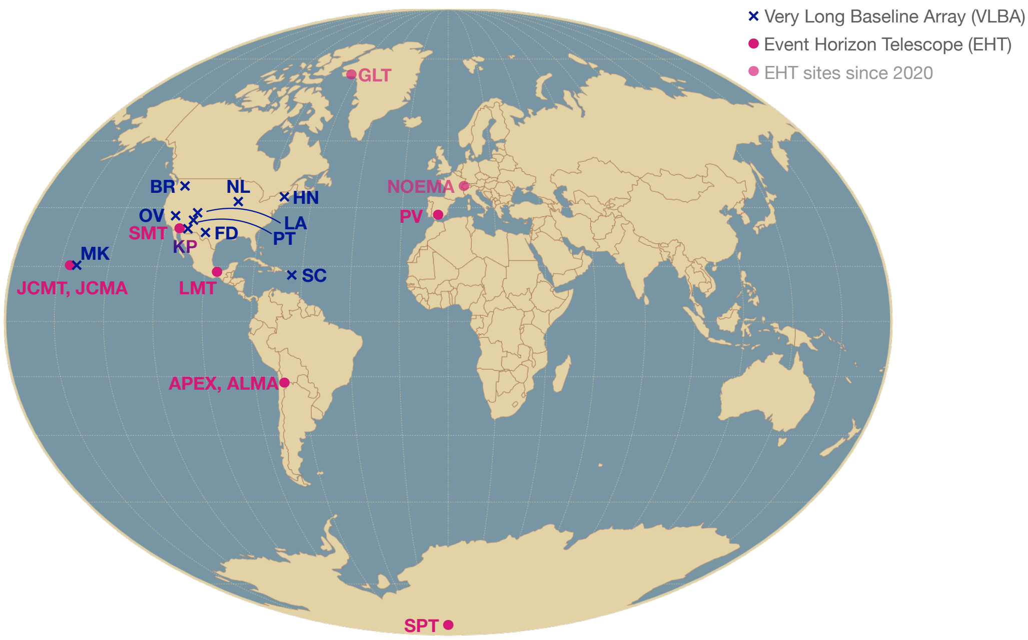

Figure 2.11: Very long baseline interferometric sites for the Very Long Baseline Array (VLBA) in yellow and the Event Horizon Telescope, EHT, in magenta. The VLBA consists of ten single-dish antennas distributed over north America. The EHT sites are shown for the 2017 array including American sites, Pico Veleta (Granada, Spain) as a European site, the South Pole Telescope, as well as interferometric arrays (ALMA). Later on, NOEMA in the french alps, Europe, and the Greenland Telescope (GLT) joined the EHT. Map adapted from a Worldmapgenerator application.

Event Horizon Telescope

The Event Horizon Telescope is a global network of radio telescopes forming an Earth-sized millimeter-wavelength telescope. By combining data from multiple VLBI stations on several continents, the EHT creates an array with high angular resolution capable of observing objects down to the event horizon scales of supermassive black holes (Event Horizon Telescope Collaboration et al., 2019a, see Figure 2.11). Larger dishes are particularly valuable because their collecting area increases with the square of the dish diameter. The Large Millimeter Telescope (LMT) in Mexico, has a diameter of 50 m, making it the largest fully steerable mm/sub-mm wave telescope in the EHT array.

Certain EHT sites, like ALMA, SMA, and NOEMA, consist of smaller antennas grouped together. These sites also function as interferometers but operate on shorter baselines, ranging from tens to hundreds of meters, compared to the thousands of kilometers used by the EHT. The dishes at these sites are connected electronically. This is done in order to utilize these sites as EHT stations, enabling their collecting area to be combined. For instance, phased ALMA can combine up to 64 dishes, each with a 12 m diameter, resulting in a total collecting area of 7200 m^2, which is approximately three times the 2000 m^2 collecting area of LMT.

2.3 Algorithms and methods

Over the last years, first with the formulation of the measurement equation (Smirnov, 2011), and later with the momentum given by the EHT developments, an ever increasing number of algorithms and methods are being established to reduce radio astronomical data. Improvements in that area, as well as in technical devices and VLBI arrays, are necessary to produce emission maps of AGN of higher resolution. These improvements can resolve features closer to the central engine, reduce the signal to noise ratio, and allow further comparison between different imaging techniques (e.g., Janssen et al., 2022). Similarly, this thesis uses several well-documented open-source software packages in the testing phase and arrives at a combination of calibration and imaging pipelines. Details are outlined in Section 2.3.1 and Section 2.3.2.

2.3.1 Calibration of very-long-baseline data

In radio interferometry, the process of combining recorded signals at different telescope sites is called correlation. The Max Planck Institute for Radio Astronomy is one institute hosting a super computer for this specific process, i.e., a correlator. After the hard drives with the observational data are shipped to the correlator, the information of each site are read in upon arrival, including site coordinates, frequency setups of the receivers used, clock information, spectral resolution, and weather conditions. The output data are typically converted into a common visibility data set, for example, `FITS-IDI` for calibration in the Astronomical Image Processing System (`AIPS`, see Greisen, 2003, for details). Polarization complicates the procedure, namely, before being processed further by the scientist, the different polarization modes are converted into a solely circular polarized structure using, e.g., `PolConvert` (Martí-Vidal, I. et al., 2016). A more detailed calibration pipeline for the data analysis in this thesis is described in Chapter 7. However, the calibration principles within `AIPS` remain similar to Figure 2.12, which shows a (generic) pipeline for VLBA data calibration. The data can be pre-flagged to remove statistical outliers before starting the process: the gains per frequency sub-band and the correction of sampler threshold errors are provided by an autocorrelation and flux density calibration. Afterwards, each data set has to be corrected for atmospheric phase-delays before, further, accounting for delays in electric devices as well as correcting the digital phase in voltage. In the same step, one can calibrate the complex bandpass response, i.e., fixing the delays between frequency bands and polarization channels.[3] The last residual delays to be accounted for in a perfectly well calibrated data set are for the baselines, which is corrected by applying fringe fitting. If the data are recorded in polarimetric mode and are used

[3]The analysis of this thesis did not apply bandpass corrections.

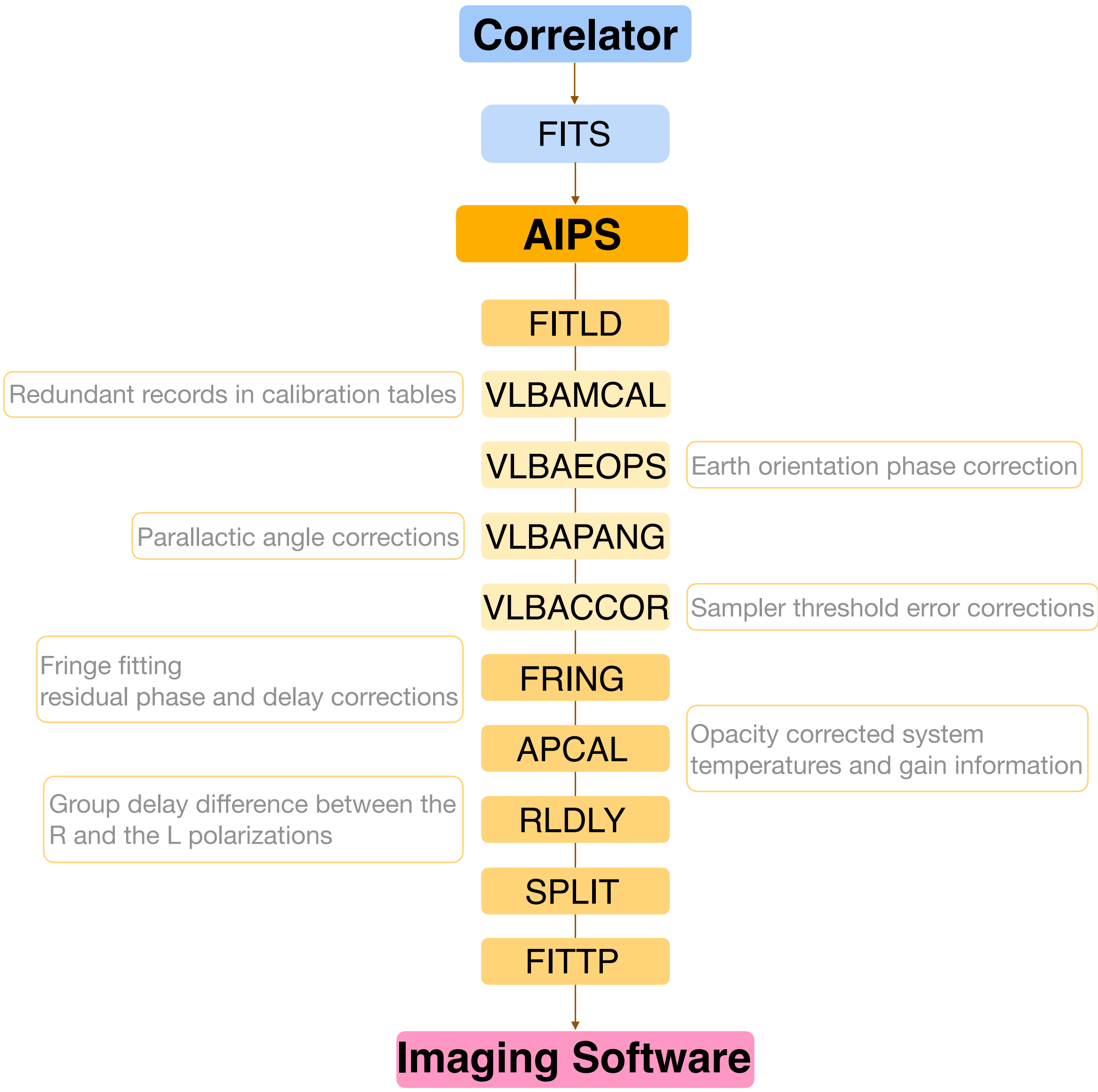

Figure 2.12: Flow chart of common steps involved in processing continuum VLBI. The data are collected at the correlator (blue) and processed into a single `FITS` file, which is read into `AIPS`. The distinct steps performed within `AIPS` to calibrate for *(i)* the phase and *(ii)* the amplitude are illustrated in yellow. The light yellow steps are representing VLBA specific pipelines within `AIPS`, which perform multiple tasks. Finally the data is transferred to an imaging software (in light rose; CLEAN, `DoG-HiT`, respectively).

for analysis in polarized emission, they have to be accounted for delays in the right-handed and left-handed polarization channels. Details on these steps are explained in, e.g., Chapter 6 within this thesis, Janssen et al. (2022) and Homan and Lister (2006).

As elaborated in Section 2.2.2 and outlined in Equation 2.37, the visibility function generated by the correlator encompasses a wide range of corruptions introduced by atmospheric and instrumental factors. In essence, the calibration process involves deducing the amplitude and phase of these distorting components.

AIPS

AIPS is one of the most commonly used softwares for data calibration. AIPS specifies its own VLBA reduction pipeline consisting of basic AIPS tasks (see light yellow steps in Figure 2.12). Data reduction within AIPS relies on the principle of keeping as much data as possible, which should remain unaltered until the final stages. Consequently, the corrections computed during each calibration step are not immediately implemented. Each calibration step is preserved within distinct calibration tables after applying solutions of individual steps.

As a consequence of Equation 2.37, the observed correlated phase ϕ_{ij}^{obs} deviates from the true correlated phase $\phi_{ij}^{\mathrm{true}}$ in the following manner:

$$\phi_{ij}^{\mathrm{obs}} = \phi_{ij}^{\mathrm{true}} + \phi_{ij}^{\mathrm{noise}}. \tag{2.38}$$

Here, $\phi_{ij}^{\mathrm{noise}}$ accounts for various residual phase errors introduced by atmospheric and positional effects. Cotton, 1997, expressed each phase as a function of time-dependent delays τ_{ij} via

$$\phi_{ij} = 2\pi\nu\tau_{ij}. \tag{2.39}$$

The process of fringe-fitting serves as a calibration technique aimed at estimating these diverse phase errors. Once the delays and delay rates are determined, appropriate adjustments can be applied to the visibilities, which are coherently integrated across frequency and time domains. Over the years, several algorithms have been developed for performing these operations, with the latest ones leveraging the fast Fourier transform (FFT) fringe search method. In the process of fringe fitting, a crucial aspect involves the meticulous selection of reference antennas (controlled by the REFANT parameter in the AIPS task FRING). It is advisable to choose antennas that perform well and are ideally positioned at a central location in the array.

The initial amplitude visibilities provided by the correlator (i.e., cross-correlation coefficients) signify the extent of correlated noise, quantified in arbitrary correlator units. To assign them a physical unit, namely Jansky (see Section 2.2), it is customary to introduce the concept of the system equivalent flux density (SEFD) for each antenna i. The SEFD is defined as

$$\mathrm{SEFD}_i = \frac{2k_\mathrm{B}T_{\mathrm{sys},i}}{A_\mathrm{eff}}, \tag{2.40}$$

where $T_{\mathrm{sys},i}$ is the system temperature of each antenna. Similar to single-dish observations, the amplitude of a baseline connecting stations i and j can be calibrated using

$$S_{i,j} = \rho_{i,j} d \sqrt{\mathrm{SEFD}_i \mathrm{SEFD}_j}, \tag{2.41}$$

with $\rho_{i,j}$ representing initial cross-correlation coefficient of the baseline $i - j$, and d as correction factor of digital sampling effects (Thompson et al., 2017). Hence, utilizing the accessible data on T_sys and A_eff values allows for the execution of the conversion process through the `AIPS` task APCAL (see Figure 2.12). At high(er) frequencies, however, this correction is not sufficient. Due to atmospheric opacity effects the astronomical signal may experience significant alternations. The `AIPS` task APCAL facilitates the implementation of opacity correction when details about the atmospheric conditions at each station are supplied.

Finally, By utilizing observations of RL and LR correlations, the `AIPS` task RLDLY calculates and applies the disparity in group delay between the right-handed and left-handed polarization gains (see Figure 2.12, and details in Chapter 6).

2.3.2 Imaging of very-long-baseline interferometric data

In order to get a satisfactory (true) image, multiple imaging approaches are compared. This thesis focuses on images generated in two ways. First, `Difmap` (Shepherd, 1997), which based on the inverse problem and using the CLEAN algorithm. Second, `DoG-HiT` (Müller and Lobanov, 2022), which is based on the regularized maximum likelihood method.

Inverse/Forward modeling

A generic form for any forward problem in radio interferometry would be by an operator F and noise ϵ of size δ,

$$g^\delta = FI + \epsilon_\delta, \tag{2.42}$$

that goes from measured visibilities g^δ to the sky brightness distribution I. The inverse problem describes the opposite.

In any modeling a fitting description of the reduced χ^2, i.e., the deviation of measured $F(M)$ and expected $F(E)$ parameters, $|F(E) - F(M)|^2$, is valuable. Further, the reduced χ^2 is dependent on the degrees of freedom c (N_c is the number of degrees of freedom, respectively). In radio astronomy and in imaging algorithms, these are equivalent to visibility, amplitude (neglecting the phase) and closure traces (including the complex amplitude and phase). The fit quality of the reduced χ^2 is written as (Burke and Graham-Smith, 1997)

$$S_i = \chi^2 = \frac{1}{N_c} \sum_{i=1}^{N} \frac{|F(E) - F(M)|^2}{\sigma_i^2}, \tag{2.43}$$

which describes a weighted sum of squared deviations and includes the variance σ_i (Event Horizon Telescope Collaboration et al., 2019b).

Visibility

Visibility is the most valuable parameter in imaging VLBI data. The expected parameter for the forwarded visibility is substituted by $F(E) = \tilde{F} f$, where f would be the current guess. The function is aiming to get f as close to the expected visibility as possible by solving for the most accurate fit $\tilde{F}$. The visibility in a VLBI data set is a complex parameter, which consists of amplitude and phase, both of which would have different functions and solutions.

Closure quantities

Within a comprehensive uv-coverage scenario, the true image connects to the true visibilities via Fourier transformation. Nevertheless, the captured visibilities differ from their true counterparts due to factors of noise and errors originating from antennas (including atmospheric influences). These calibration-related (unconsidered) effects, which are not tied to a specific direction, can be incorporated by applying complex gains $g_{i,j}$ at the level of individual antennas (see Equation 2.37). Closure phases or amplitudes are the solution to gain corrupted visibilities. By considering closure quantities of visibilities, i.e., phase and amplitudes gain-independent values are defined. Closure phase is added over a triangle of antennas in an array i, j, k by which the systematical errors can be reduced. Closure amplitudes are measured over four antennas i, j, k, l accordingly. Both closure quantities are independent of station based gains. In forward modeling, closure phase and amplitude can be expressed in forms of χ^2.

CLEAN The CLEAN algorithm applied in `Difmap` was defined by Högbom (1974). In Figure 2.8 the side lobes of the Fourier transformed signal are illustrated. Aim of the CLEAN algorithm is to deconvolve the dirty map to yield an image reflecting only the true brightness convolved with a Gaussian beam (see Figure 2.13). This is ideally represented by the half power beam width (HPBW), which corresponds to the

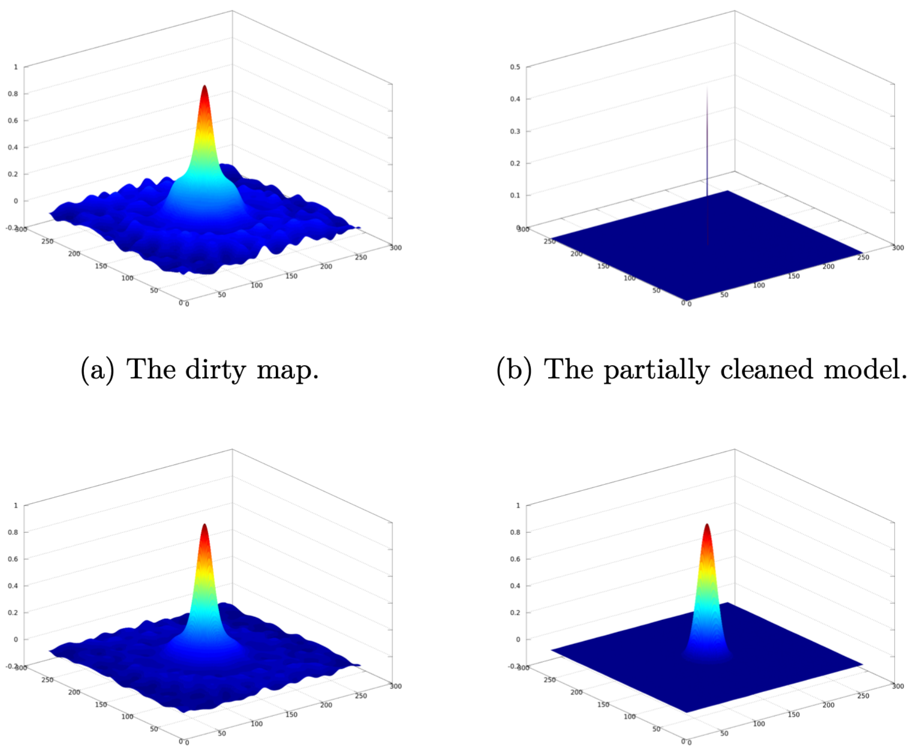

(a) The dirty map.

(b) The partially cleaned model.

(c) The partially cleaned map.

(d) The final cleaned map.

Figure 2.13: Stages of the CLEAN algorithm as it performs deconvolution on a Gaussian source. The horizontal (x) and vertical (y) dimensions are presented in pixel units, while the vertical (z) dimension corresponds to the Stokes I flux, measured in Jy. Figure taken from Coughlan (2014).

largest spacing D and thus removes the small side lobes. The angular resolution of the brightness along the image can be described by HPBW $\simeq \lambda/D$.

Modern CLEAN algorithms work in both the visibility and aperture plane to fill the missing spacing between measured peak intensities. This is in general conducted by selecting manually the brightest regions on the dirty image and proceed from there. The steps performed within CLEAN following Högbom, 1974, are:

(i) Select manually CLEAN windows on the brightest spot on the dirty map (residual; see Figure 2.13 panel a).

(ii) Record the position and intensity in relation to the dirty image in delta-components (see Figure 2.13 panel b). The differences are the observed gains.

(iii) Move the dirty beam to the location of the highest peak within the residual and adjust its scale to a fraction of the intensity of the most recent peak identified.

(iv) A new re-scaled maximum appears on the map and the procedure begins from step (i) again.

(v) The complete roster of CLEAN components undergoes convolution with the CLEAN beam, which is represented by a Gaussian approximation of the main lobe of the dirty beam. This Gaussian approximation closely matches the correct shape and resolution while not including of any sidelobes (see difference between panel c and d in Figure 2.13).

The process of cleaning, i.e., choosing the maximum in a specified window, wraps up in a combination of point sources on an otherwise CLEANed field of view. However, the CLEAN algorithm encounters some limitations: the reconstructed (true) image is performed on subjective steps, which adds human biases, and the final convolved image, depending on re-weighted visibilities, barely fits the observed visibilities. Further, it is missing reasonable regularization as well as solutions for gaps in the uv-plane (Müller and Lobanov, 2023b). CLEAN's Ansatz shows a too conservative resolution while considering only the instrumental image solution (Lobanov, 2005; Honma et al., 2014; Müller and Lobanov, 2023b). However, it is sensible to use prior, minor assumptions, for instance, selecting the total intensity to be greater than zero or that the image should appear intrinsically consistent and without side lobes. Modern forward modeling techniques, like Bayesian methods (see Appendix A; within the posterior evaluation Ansatz) and regularized maximum likelihood (RML) approaches are superior in performing accuracy, dynamic range, and resolution (Event Horizon Telescope Collaboration et al., 2019b; Arras et al., 2021; Müller and Lobanov, 2022; Roelofs et al., 2023).

Regularized maximum likelihood

Regularized maximum likelihood techniques reformulate the Ansatz in Equation 2.42 to solve for an optimization problem, i.e., minimizing the noise (ultimately minimizing the χ^2) via convex optimizations. RML techniques are structured within the overarching framework of the 'general Tikhonov regularization' approach. This involves the minimization of a weighted combination of terms representing data fidelity and regularization (Müller and Lobanov, 2022):

$$I(f) \in \underset{f \in X}{\arg\min} \sum_i \alpha_i S_i \left(g^\delta, Ff\right) + \sum_j \beta_j R_j\left(f\right). \tag{2.44}$$

In this context, S_i represents the data fidelity component, which accounts for an approximated guess solution Ff applied to the observed data g^δ. While doing this, F signifies the translation of image intensity into visibilities, implying a deliberate and weighted transformation of the discrete Fourier transform. R_j signifies the regularization component, assessing the physical plausibility of the final estimated guess, $I(f)$. The regularization is necessary to be added to the initial problem in order to account for overfitting problems within the noise and sidelobes of the recorded signal. The parameter α_i and β_i, respectively, regulate the bias or offset between the two terms. In total, the optimization problem is a function of the specific data fidelity terms for visibilities S_{vis}, amplitude S_{amp}, closure phase S_{cph}, and closure amplitude S_{camp}. Further, the regularization terms include the sparsity of the resolution R_{l^0} applied on a convex approximation R_{l^1} and favouring simplicity instead R_{l^2}. The regularization terms also describe the total variation R_{TV} and its total squared variation R_{TSV}, and finally the total flux constraints as a function of the compact flux R_{flux}. By appropriately tuning the weighting parameters α_i and β_i, the resulting reconstructions exhibit superior resolution compared to CLEAN (as stated in the quote). Not only are these reconstructions more accurate, but they also resolve the issue of ambiguity between the model and the image that is introduced by the CLEAN method. Additionally, they enable the incorporation of terms that are independent of (self-)calibration procedures (Event Horizon Telescope Collaboration et al., 2019b; Arras et al., 2021; Müller and Lobanov, 2022; Roelofs et al., 2023).

Commonly used regularization terms within the sparsity promoting, smoothness, and simplicity terms in RML are entropy functionals (Maximum Entropy Method, MEM; ehtim or SMILI Chael et al., 2019; Akiyama et al., 2017a; Akiyama et al., 2017b), plug-and-play neural networks (AI based imaging), or sparse representation by a dictionary of basis functions(compressed sensing; `DoG-HiT` Müller and Lobanov, 2022).

`DoG-HiT` The `DoG-HiT` algorithm (Müller and Lobanov, 2022) ensures that the retrieved model conforms to the observed visibilities, thereby minimizing a sensible data-fidelity component within the objective function. To reduce reliance solely on phase and amplitude calibration, this approach incorporates closure phases and closure amplitudes as discussed above. The model obtained should adhere to physical realism, devoid of secondary sidelobes and noise. Consequently, the interpolation in the Fourier domain must satisfy the same criteria, with the algorithm seamlessly interpolating the optimal fit to gaps in the uv-coverage. Furthermore, the model's simplicity is emphasized, aiming to reasonably match the observed data. Specifically, `DoG-HiT` avoids generating image features that are predominantly influenced by Fourier frequencies within the unmeasured visibilities, effectively preventing over-compression. To achieve these objectives, `DoG-HiT` employs a custom-designed dictionary that employs specially crafted wavelets as fundamental building blocks. These wavelets facilitate data decomposition within the image domain, analogous to multiplication by their Fourier transforms in the Fourier domain.

3 Relativistic jets: theory and observation

Astrophysical jets are defined as a collimated beam of partly relativistic, i.e., high velocity plasma. Besides jets observed in AGN, these phenomena are found in a wide range of objects, such as, young stars, microquasars, and pulsars. They all have in common that an accretion disk (see Section 1.3.1) is required to launch a jet close to the central engine (see Section 1.3.1). Whether they are launched by a dipolar magnetosphere or the disk magnetic field is unsure, however, the estimated strength of the magnetic field is constant throughout several theories. Focusing on that and discovering the mystery of the launching mechanism in these sources is not enough to explain the nature of the jet phenomenon. There are many open questions to answer: what is the nature of the jet launching mechanisms, i.e., which (general relativistic) magnetohydrodynamic (GRMHD) process launches the jet? What types of particles does the jet consist of? How are jets collimated? How does the intrinsic magnetic field evolve and affect the polarized emission?

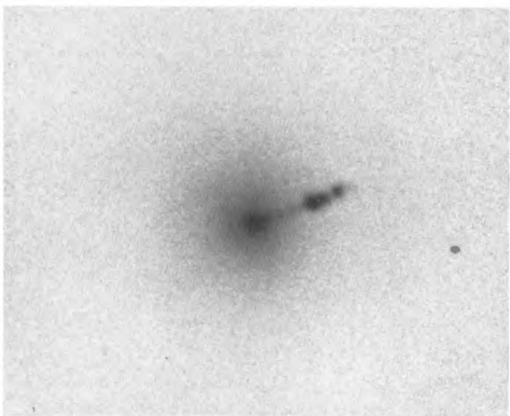

Figure 3.1: Linearly polarized optical-ultraviolet image of the M87 galaxy in the Virgo cluster, showing the center bright part of the galaxy and the extragalatic jet emitting from the core (1mm $= 0.8''$). Figure adapted from Baade and Minkowski (1954).

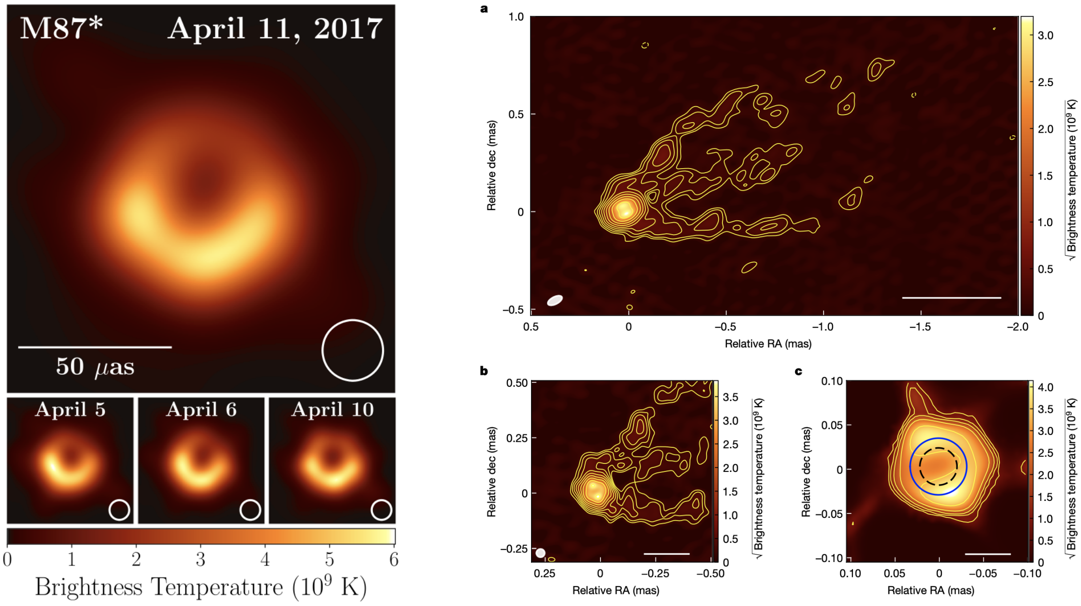

Figure 3.2: **Left**: First image taken of a supermassive black hole in the center of the active galaxy M87 by the Event Horizon Telescope Collaboration at 1 mm, showing the photon ring structure and shadow of M87* for four observational nights. Figure taken from Event Horizon Telescope Collaboration et al. (2019a). **Right**: First observation of the jet-launching region in M87. Images show both the jet base and the center black hole shadow. Data taken by the GMVA+ALMA at 3.5 mm. Figure taken from Lu et al. (2023).

3.1 Pioneering observations of AGN jets

The first discovered jet is hosted by the radio galaxy Messier 87. Curtis, 1918, observed a first stray of matter as a thin line in optical-ultraviolet observations that streams away from the inner nucleus. Later, the term 'jet' was first used for an optical-ultraviolet counterpart of the strong radio source (Baade and Minkowski, 1954). Linearly polarized observations of the optical light stressed the theory that the emitted radiation is synchrotron radiation and further gave a hint on the underlying magnetic field (Figure 3.1). More recently, in 1999, this magnetic field was proven to be highly ordered and that the jet in M87 is highly polarized (up to 50 %). The Event Horizon Telescope Collaboration has further confirmed that result by images of M87*, the central black hole (Event Horizon Telescope Collaboration et al., 2019a), see Figure 3.2 left. Global millimeter VLBI array (GMVA) observations revealed the disk-jet connection for the first time (Lu et al., 2023), see Figure 3.2 right.

Further, the jet velocity can be measured by observations over several epochs and identifying jet knots, e.g., as it was done for M87 (Biretta et al., 1991) in the optical band. For blazars, the speed appears to be higher because of Doppler boosting effects, e.g., for PKS 1510 − 089 in Figure 3.3 (Marscher et al., 2010).

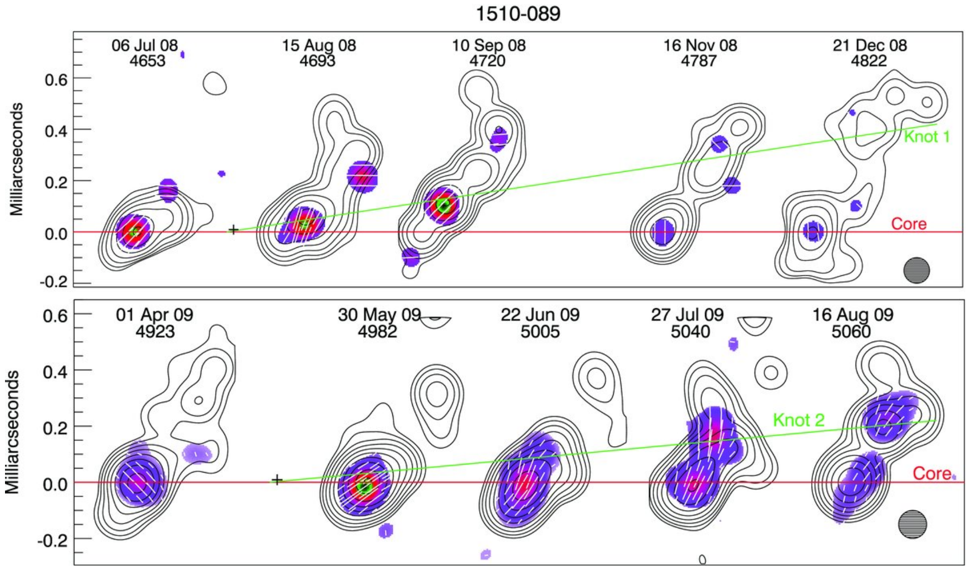

Figure 3.3: Observations of jet features apparently moving at relativistic speed away from the radio core in the blazar PKS 1510 − 089 for multi-epochs, covering more than a year. The projected moving knots are associated with superluminal motion. Knot 1 and 2 move with an estimated speed of $v = 22c$. Figure taken from Marscher et al. (2010).

3.2 Jets: from the central engine to parsec scales

The jet *launching* mechanism from an accretion disk is related to the presence of magnetic fields. It is postulated that plasma from the innermost region is accelerated away from the BH along magnetic field lines. The plasma is pulled away from the rotating BH and disk by MHD forces and propagates along the magnetic field. The outflow is magnetocentrifugally *accelerated* and finally *collimated* (see, e.g., Ferreira, 1997). However, a theoretical model matching the observations of AGN jets has yet to be finalized. This section will focus on the magnetocentrifugally acceleration in contrast to "thermal" acceleration, as this model is favoured (For an advanced description the reader is referred to Guthmann et al., 2002).

3.2.1 Jet launching

The process of electrodynamics (McKinney, 2006) as a main driver of AGN jets has been proven wrong and, hence, the field of astrophysics is left with two big theories: Blandford & Znajek (BZ; Blandford and Znajek, 1977) and Blandford & Payne (BP; Blandford and Payne, 1982). Both require a spinning BH environment and the presence of a magnetic field. BP relies on the presence of an accretion disk whereas BZ launches a jet from the magnetic field anchored directly into the BH magnetosphere. The BZ mechanism explains the fast rotation of magnetized plasma in the vicinity of the BH and the BH rotation itself, advecting the magnetic field inwards and causing a number of magnetic loops around the BH. Finally, a magnetosphere is built up. In parallel, plasma is pulled up via, e.g., the Penrose mechanism (Penrose and Floyd, 1971) and is captured by the magnetosphere (Tchekhovskoy, 2015). The BP mechanism would result in less relativistic jet plasma being launched from the accretion disk due to the lack of additional power from BH rotation. The magnetocentrifugal acceleration of the disks leads to disk winds (Camenzind, 1986) as well as twisted magnetic flux tubes (Lyndel-Bell, 1969; Hawley et al., 2015).

One potential distinction between the BP and BZ mechanisms lies in the composition of the resulting jets. A jet originating from the accretion disk may have a greater tendency to carry protons and ions alongside electrons e^- and positrons e^+, whereas material emitted from the BH's ergosphere is more likely to consist solely of lighter particles (e.g., e^+, e^-). These lighter particles are believed to be generated through the interactions of high-energy photons from the accretion disk within the BH's magnetosphere. The mass loading of the jets, in both scenarios, is expected to be influenced by the physical conditions of the disk and the inclination of the magnetic field lines, as field lines that are too close to the axis may be less effective at capturing material.

The jet-disk environment results in a twofold: (i) jet collimation (Koide et al., 2000; De Villiers et al., 2003; McKinney, 2006), and (ii) jet-wind mixing that forms a jet sheath region (Chatterjee et al., 2019), which is the underlying phenomenon of edge-brightening in jet observations such as revealed in the radio galaxy Centaurus A (Section 3.6) or 3C 84 (Paraschos et al., 2022, and G.-F. Paraschos et al. in prep.).

3.2.2 Jet acceleration

The magnetocentrifugal acceleration from the disk overcomes the initial transient phase, the Alfvén radius, that is, until the velocity of the flow becomes slower than the Alfvén speed, and forces the plasma to be accelerated (BP process). The initial poloidal magnetic field converts to a toroidal magnetic field, showing strong helical components (see Figure 3.4). The outflowing plasma in this case is mostly thought to consist of electrons/protons. In the co-rotating frame of the plasma and magnetic field, a centrifugal potential accelerates the plasma (Guthmann et al., 2002).

On the other hand, the same mechanism driven by the BH magnetosphere (BZ) drives wind outflows. Here, the flow consists of an electron-positron pair plasma. Enough energy in the magnetosphere, driven by the BH, is extracted and would help to produce leptonic ejection. Ultimately, in both cases, the Poynting flux accelerates the plasma (for details on various mechanisms visit Guthmann et al., 2002).

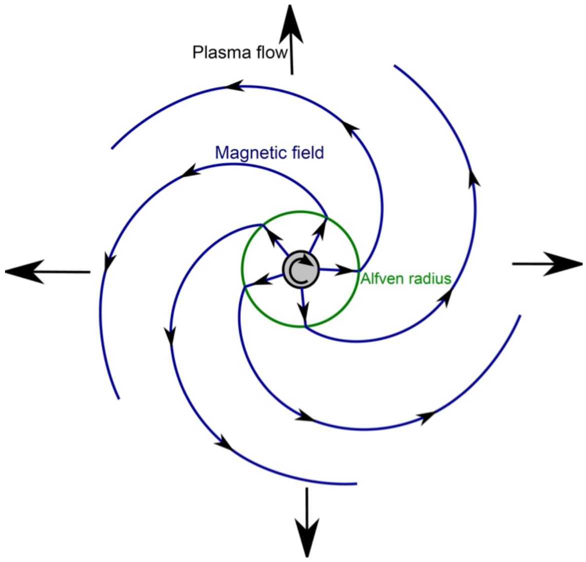

Figure 3.4: Sketch of the transition from a poloidal magnetic field structure to a toroidal magnetic field at the Alvén radius of a central rotating black hole. The jet is moving out of the plane and would exhibit a helix in three dimensions. Figure taken from Clausen-Brown (2012).

3.2.3 Jet collimation

Different kinds of instabilities apply depending on whether the jet is magnetically dominated or kinetically dominated. Magnetically dominated jets are causing a magnetically unstable jet if the jet carries a strong toroidal component. On the other hand, kinetically dominated jets may disrupt or form instabilities followed by the jet-ambient medium interference (Perucho et al., 2012). The former one might be connected to current-driven kink instabilities (Bateman, 1978) while the latter one corresponds to Kelvin Helmholtz instabilities (Ferrari et al., 1978).

However, jets can evolve with strong parameters collimating the flow. In contrast to the toroidal component, a strong poloidal or ordered magnetic field will help to maintain the jet stability over large scales. The velocity gradient within the jet may be decreased by high Lorentz factors (Perucho et al., 2012).

The toroidal magnetic component is important for the self-collimation of jets though. It exerts a force on the charged particles within the jet, guiding, and confining their motion along the jet's central axis. The confinement prevents the jet from rapidly dispersing and widening as it travels away from the BH. Further away from the BH occurs a break point of the collimation profile. The former parabolic shape is commonly believed to transform to a conical shape. This was proposed to happen at the Bondi radius (Pushkarev et al., 2017; Kovalev et al., 2020; Boccardi et al., 2021; Ricci et al., 2022). However, this cannot be generalized, e.g., in the case of Centaurus A where the transition happens closer to the central engine (Müller et al., 2011).

3.3 VLBI observations of jets

During the 1960s and 1970s, single-dish telescopes advanced further, enabling radio imaging of AGN jets at kiloparsec scales. Notable instruments such as the Green Bank Telescope and the Parkes Radio Telescope played significant roles in studying the morphology and intensity distribution of AGN jets (Roberts, 1970; Bolton et al., 1971). Scientific achievements in single dish observations have contributed to characterizing the radio emission of relativistic jets. These include determining flux densities, spectral characteristics, and identifying different types of AGN based on their radio properties (Kellermann et al., 1989; Becker et al., 1995). Single dish observations have also aided in the discovery and classification of various AGN sub-types, such as radio galaxies and blazars (Fanaroff and Riley, 1974; Padovani et al., 2017).

VLBI observations have yielded remarkable scientific discoveries. The technique has revealed fine-scale structures, kinematics, and dynamics within AGN jets. Key breakthroughs include the discovery of superluminal motion, where apparent jet components move faster than the speed of light due to relativistic effects (Blandford and Königl, 1979). VLBI has also unveiled jet collimation mechanisms, jet precession, and detailed structures such as shocks, knots, and jet-cloud interactions (Zensus et al., 1995; Lobanov, Andrei, 2015; Boccardi et al., 2017).

Recent advancements in VLBI include space-based telescopes, such as the RadioAstron mission, which have improved resolution and enabled even more detailed studies of AGN jets (Kardashev et al., 2013; Gurvits, 2018).

3.4 Multi-frequency observations of jets

Different observing bands of electromagnetic radiation provide valuable insights into the physical processes occurring within AGN jets. By observing AGN jets across a broad range of frequencies, from radio to gamma-ray wavelengths, astronomers can probe various aspects of the jet emission and dynamics. Unveiling the heart of the BH/central engine requires multi-wavelength observations as illustrated in Figure 3.5. VLBI observations enable to zoom into the hearts of AGN (Boccardi et al., 2017; Blandford et al., 2019; Janssen et al., 2019; Lu et al., 2023), as it has been proven with the black hole shadow in M87 (Event Horizon Telescope Collaboration et al., 2019a).

Radio frequencies

Radio observations reveal a large range of features, depending on the amount of antennas used and the observed frequency range. The EHT collaboration succeeded in the first image of a black hole shadow by increasing the frequency and adding VLBI

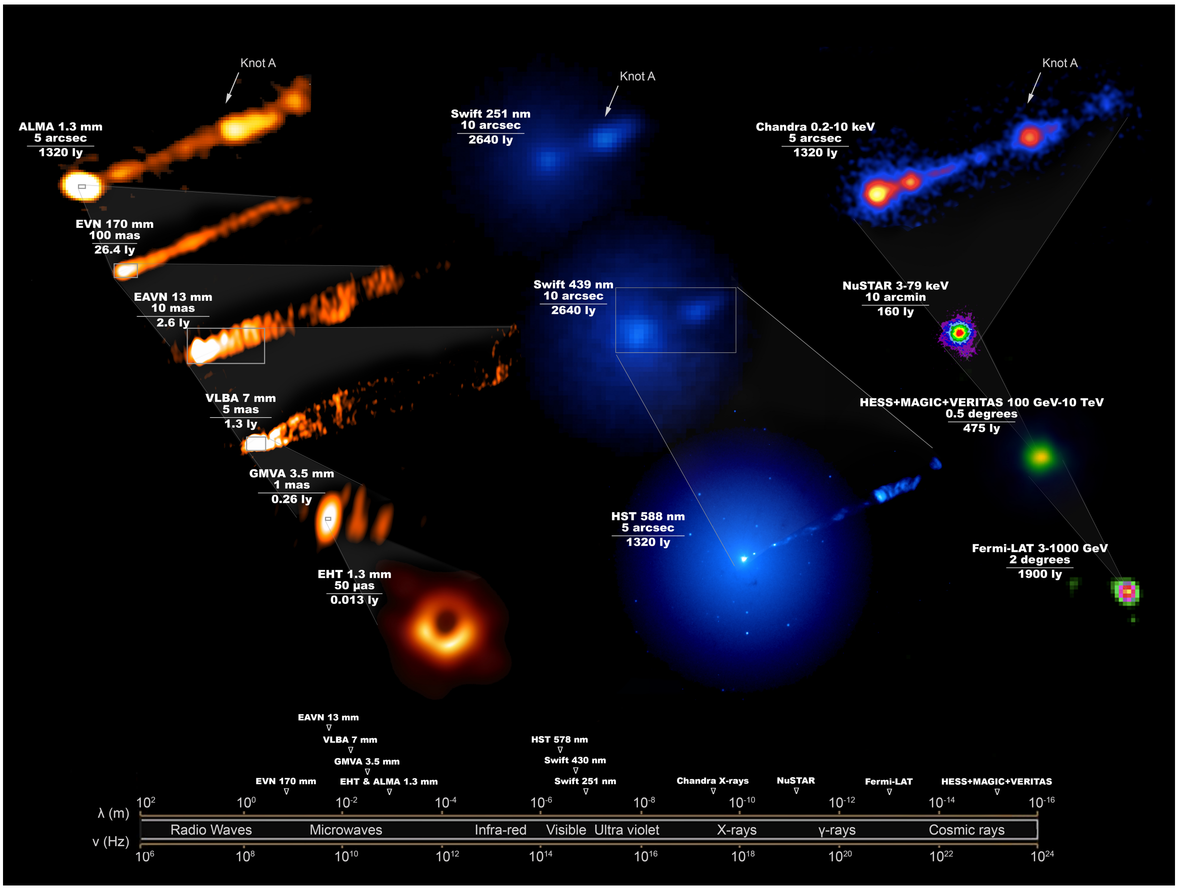

Figure 3.5: The active galaxy M87 as seen at different wavelengths. Observational data from radio to gamma-rays taken during a (quasi-) simultaneous campaign in 2017 to the EHT observing campaign. Courtesy of the EHT Multi-Wavelength Science Working Group; the EHT Collaboration; ALMA (ESO/NAOJ/NRAO); the EVN; the EAVN Collaboration; VLBA (NRAO); the GMVA; the Hubble Space Telescope, the Neil Gehrels Swift Observatory; the Chandra X-ray Observatory; the Nuclear Spectroscopic Telescope Array; the Fermi-LAT Collaboration; the H.E.S.S. collaboration; the MAGIC collaboration; the VERITAS collaboration; NASA and ESA. Figure composed by J. C. Algaba, visit ALMA homepage.

stations to their telescope survey, i.e., they increased the angular resolution to be able to image the inner most center of AGN. Figure 3.5 shows the progress in imaging M87 when moving from 1.3 mm with ALMA down to 1.3 mm with the EHT. The observed jet reveals a collimated structure on parsec scales, followed by an edge-brightened jet on sub-parsec scales and shows finally the light bending around a compact object. The observed synchrotron radiation in radio frequencies is of non-thermal origin and related to the interaction of moving plasma with the magnetized ambient medium.

Optical and infrared frequencies

Observations in the optical and infrared wavelengths provide insights into the thermal (and non-thermal) emission from AGN jets. These frequencies are sensitive to the emission from ionized gas, and they help identify features such as emission lines and shocks within the jets. The shocks are highlighted in radio and X-rays, too (see Figure 3.5). Optical and infrared observations can also probe the interaction between the jet and its surrounding environment, such as the host galaxy or nearby interstellar medium. By studying the line ratios and spectral features, astronomers can infer physical conditions, such as electron densities, temperatures, and chemical compositions in the jets (see Antonucci, 2012).

X-ray frequencies

X-ray observations complement radio observations. A comparison between ALMA and Chandra data can strengthen the identification of knots (standing or moving features, hot spots, recollimation shocks), as is visible in Figure 3.5 (Marscher, 1998; Weaver et al., 2022). The combination helps to unveil the origin and strength of particle acceleration in jets. Although synchrotron self-Compton emission is supposed to not be able to produce powerful bright AGN jet features, the observed knots fit the synchrotron spectrum well (Marshall et al., 2002). It is postulated that the bactrian shape of the two-peaked X-ray SED would be explained by synchrotron emission, at least partly (Blandford et al., 2019). X-rays are also observed further down the jet. The hot gas surrounding the BH as well as the BLR and NLR (Section 1.3.1) are strong X-ray emitters. Therefore, X-ray observations can probe the accretion mechanisms in AGN.

Gamma-ray frequencies

High-energy telescopes are trying to connect the high energy neutrinos with their origin in the universe. The Energetic Gamma Ray Experiment Telescope (EGRET) successfully managed to analyze upper limits on the high-energy gamma-ray emission in galaxy clusters (Reimer et al., 2003), globular clusters (Michelson et al., 1994), and to contribute to the overall picture of the extragalactic gamma-ray background (Völk, 2000). Further, The Fermi Gamma-ray Space Telescope, a space-borne observatory dedicated to conducting gamma-ray astronomy observations while positioned in a low-Earth orbit, has helped to identify new high-energy gamma-ray candidates (e.g., black holes, neutron-star mergers, pulsars, see Ajello et al., 2021). The IceCube telescope observed a correlation between several AGN and high energy neutrinos, and found a percentage of about 20 % high-energy detections in radio-loud AGN (Karouzos et al., 2011). The overlap between radio and gamma-rays is postulated to be a spine-sheath model. The faster inner spine of the AGN jet emits in gamma-rays while the slower bulk velocity in the sheath emits predominantly radio waves (Sol et al., 1989; Laing, 1996; Blandford et al., 2019). Further studies revealed rapid variability stressing that these AGN might be blazar types. Gamma-ray observations further help to understand processes in the universe, such as, estimations on the extragalactic background light, shedding light on the highest redshifts and cosmology studies, or on gravitationally lensed systems (Blandford et al., 2019).

Neutrino emission

AGN have been regarded as promising sites for potential high-energy neutrino production, as they rank among the most powerful emitters of radiation in the known universe (Abbasi et al., 2022, and references therein). Their relativistic jets are plausible locations for generating both high-energy (PeV−EeV) and ultrahigh-energy cosmic rays ($\approx (1-200)$ EeV, Matthews et al., 2018). The explanation for this lies in the fact that the radiating electrons in these phenomena can be secondary particles resulting from inelastic collisions involving primary hadrons, leading to the emission of neutrinos in parallel with gamma-rays. Hence, neutrinos can serve as indicators to differentiate between purely leptonic models and those involving high-energy hadrons as primary particles.

In the case of blazar sources, the production of neutrinos is intensified due to the relativistic motion of the jet. The most recent all-sky search for the sources of high-energy neutrinos using 10 years of IceCube data has hinted at a potential contribution of AGN cores to the flux of high-energy neutrinos. Specifically, there has been a reported possible identification of a single neutrino emitted with an energy of approximately 400 TeV from the flaring blazar TXS $0506+056$ (IceCube Collaboration et al., 2018). However, the absence of a correlation in the arrival directions of other neutrinos with known blazars suggests that no more than a quarter of these neutrinos can be attributed to Fermi blazars (Aartsen et al., 2017).

3.5 Polarized light from jets

Magnetic reconnection events, turbulences in plasma, compression in shocks, and polarized light are tools to investigate magnetic fields on all scales in the universe. However, magnetic reconnection evens appear on microscopic scales that are very hard to observe. Hence, polarization is most useful to reveal the magnetic field morphology on larger scales. VLBI observations make it possible to reveal this from galactic scales (Cygnus A, see Sebokolodi et al., 2020) down to event-horizon scales (Event Horizon Telescope Collaboration et al., 2019a; Event Horizon Telescope Collaboration et al., 2022). In case of OJ 287, BL Lac, and PKS 0735+17, the degree of observed polarization di-

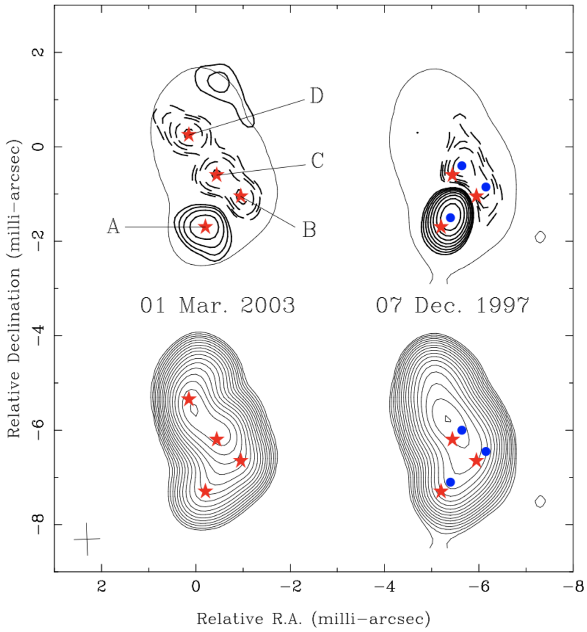

Figure 3.6: 3C 84 observational data in circular polarization (**top**) and total intensity (**bottom**). Dashed lines illustrate a negative sign in circular polarization. Figure taken from Homan and Lister (2006).

minishes toward lower frequencies (Rudnick et al., 1978). For 3C 84, only the high resolution observations revealed high polarization (see, e.g., Homan and Lister, 2006; Lister et al., 2018; Kim et al., 2019; Hovatta and Lindfors, 2019; Gabuzda, 2021, and G.-F. Paraschos et al. in prep.). As a direct measurement between the polarization and magnetic field orientation, astronomers define the EVPA. Electric vector position angles have been observed to be constant over a wide range in the electromagnetic spectrum, i.e., from optical to cm-radio observations for OJ 287 (Rudnick et al., 1978). At longer wavelengths a rotation of EVPA might happen due to opacity changes (i.e., optical depth transition). In general, EVPA are assumed to change rapidly over frequencies, indicating a Faraday screen within the LoS (Park and Algaba, 2022).

Recent observational studies at higher frequencies and higher angular resolution have reported LP in the jet launching and acceleration region, despite the very low observable polarization fraction in AGN jets (Lister et al., 2018). EHT observations have revealed linearly polarized images of the innermost photon-ring structures near the BH shadow in M87 (Event Horizon Telescope Collaboration et al., 2021), and ALMA on parsec jet scales (Goddi et al., 2019) in M87 (see Figure 1.7). The light bending around the ring-like structure explains a special behaviour of EVPAs, i.e., nearly azimuthal orientation. However, this postulates that the electric field vectors do not need to be perpendicular to the magnetic field orientation (Event Horizon Telescope Collaboration et al., 2021; Narayan et al., 2021).

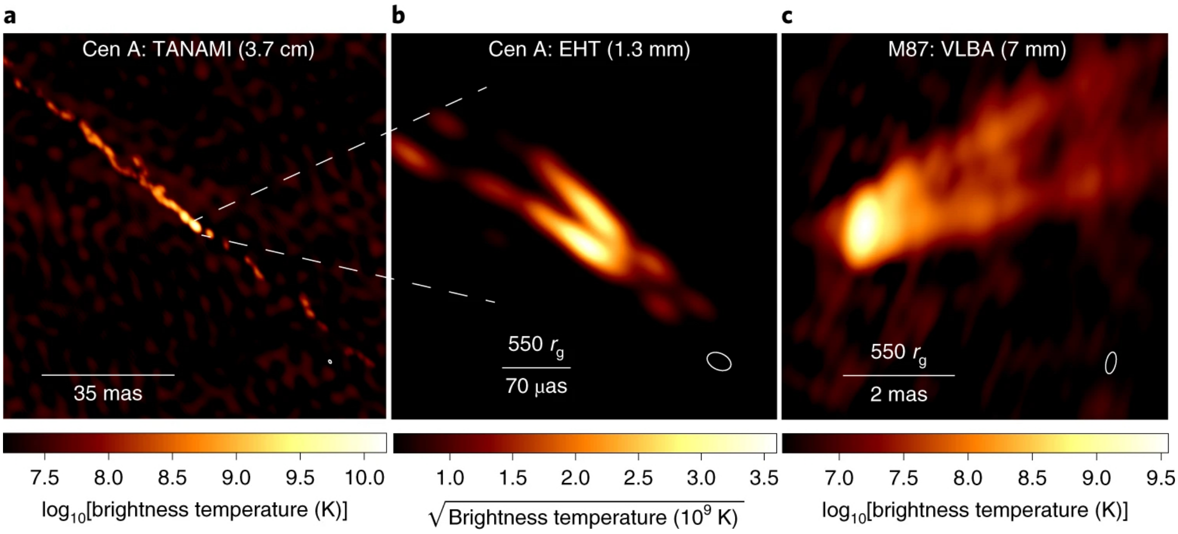

Figure 3.7: Zooming into the sub-parsec scales of the radio galaxy Centaurus A (Cen A). From left to right: Cen A observed with the TANAMI program, the EHT, and the VLBA. The relativistic jet is zoomed in by a field of view of 2 parsec (pc) for TANAMI, 0.007 pc for the EHT, and 0.6 pc for the VLBA. The EHT and VLBA images highlight an edge-brightened jet. Figure taken from Janssen et al. (2021).

Linear polarization is significantly higher than circular polarization and is therefore the first choice to study the polarized properties of relativistic jets. Circular polarization can, however, probe the magnetic field robustness as well as the particle composition. The former needs an underlying synchrotron spectrum, whereas the latter one can be produced by Faraday conversion. The direction of the magnetic field and electromagnetic wave accelerating charged particles can probe an electron population as well as the orientation of the dominant field component. In the framework of the MOJAVE project, Homan and Lister, 2006, published an extensive study of circular polarization on multiple AGN. They detected a level of fractional circular polarization between 0.25 % and 0.70 % with one exception: 3C 84 is showing 3 % (see an example figure in Figure 3.6). They observed circular polarization with a stable sign over several epochs (Homan and Lister, 2006). The Faraday conversion in AGN was underlined by an anti-correlation between linear and circular polarized light in PKS 2126 − 158, strongly suggesting that this is the main driver of CP (O'Sullivan et al., 2013).

3.6 The case of the nearby galaxy Centaurus A

Centaurus A was one of the first detected radio galaxies (Clarke et al., 1992) due to its nearby location $(3.8 \pm 0.1) \times 10^6$ pc (Harris et al., 2010). The SMBH in the center of Cen A has an estimated mass of $(5.5 \pm 3) \times 10^7\,M_\odot$ (Neumayer, 2010). Similar to M87, Cen A is an exciting source for multi-wavelength studies. However, this thesis and herein publications will focus on the characteristics of Cen A in the radio regime.

A multi-epoch VLBI monitoring study over 12 years at $(2-22)$ GHz highlights a relativistic jet (0.1 c), a strong collimation profile, and a stranding feature close to the jet core (Tingay et al., 2001). The jet in Cen A is observed to appear at an inclination of $12° - 45°$ (Müller et al., 2014). The edge-brightening observed in Cen A (Janssen et al., 2021), shown in the middle panel in Figure 3.7, strengthens the postulated spine-sheath structure of the jet (Laing et al., 1999). Limits on the X-ray polarization of the core in Cen A have been estimated by the Imaging X-ray Polarimetry Explorer (IXPE) (Ehlert et al., 2022). These observational features build an ideal laboratory to study Cen A as a primary AGN target in numerical simulations. Chapter 7 will mimic the details presented here to use Cen A as an example to prove the necessity of the inclusion of synchrotron losses in relativistic jet simulations.

4 Numerical simulations in relativistic jets

Numerical studies of relativistic jets started with stationary flows and moved to time-dependent high-resolution techniques (Gomez et al., 1995; Martí and Müller, 1999; Gabuzda et al., 2000). Hydrodynamics revealed observational features in jets, such as shocks or bulk flow velocities. However, moving to three dimensions (Aloy et al., 2000, and references therein) or including magnetic fields (Komissarov, 1999), as well as considering general relativistic effects closer to the jet launching and BH region, are active areas of research since the early 2000s (Koide et al., 2000; Meier et al., 2001, and references therein). For a proper treatment of relativistic jets, which include Faraday screens, opacity, or geometrical effects, the calculated emission has to be compared with actual observational data. This includes relativistic processes and radiative transfer effects (a detailed review can be found in Gómez et al., 1997).

Relativistic hydrodynamical (RHD) codes simulate plasma flows that follow the mathematical description of thermal particle distributions. However, as we have seen, the non-thermal emission originates in synchrotron radiation from relativistic, charged particles spiraling around a magnetic field. Circular (and linear) polarization has been detected, for instance, in 3C 279, 3C 84, and 3C 273 (Larionov et al., 2020; Homan and Lister, 2006; Hovatta, T. et al., 2019). This polarization is synchrotron in nature and is an indication of the presence of both non-thermal electron distributions of electrons and magnetic fields (Wardle et al., 1998; Homan and Lister, 2006). The non-thermal emission is, e.g., explained by the inclusion of shock physics and magnetic fields. This could happen, for instance, in the VLBI core (recollimation shock) that particles would encounter (Daly and Marscher, 1988; Lister et al., 1998; Marscher, 1998). To calculate the emission, a relationship between the fluid variables and the non-thermal emission is needed in numerical modeling as described in Kramer and MacDonald, 2021, and Chapter 5 within this thesis. Alternatively, a non-thermal particle population is assumed to follow the dynamics of the underlying fluid. Details on that are described and applied in Chapter 7. Relativistic astrophysical jets can be thoroughly studied by means of numerical studies, which address distinct regions of these phenomena. Notwithstanding this challenge, remarkable progress has been achieved in the imple-

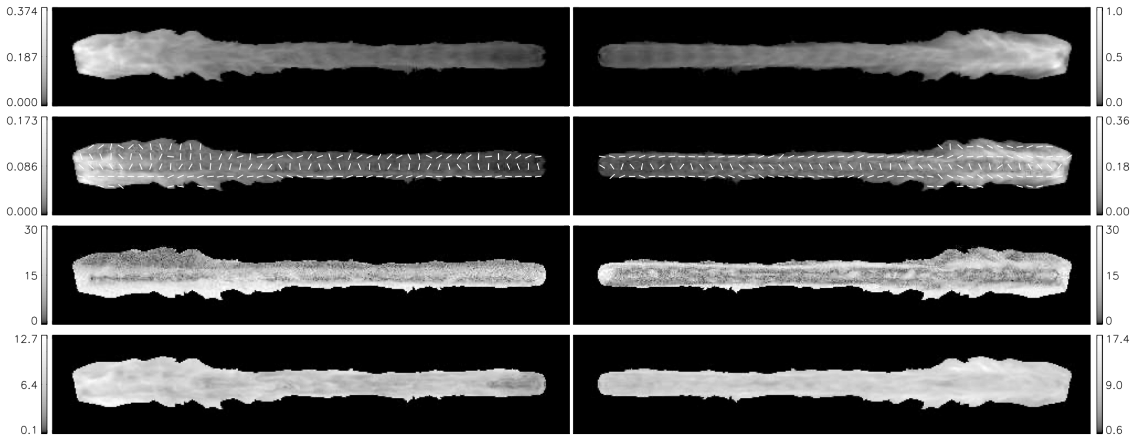

Figure 4.1: The panels display different properties of the jet and its counter jet when viewed at an angle of 50°. From top to bottom, the panels represent the total intensity, polarized intensity, degree of polarization, and mean Doppler factor. The total and polarized intensities are presented on a square root scale, normalized to the maximum intensity of the main jet. Figure taken from Aloy et al. (2000).

mentation and development of numerical algorithms for tackling the complexities of solving relativistic hydrodynamics and magnetohydrodynamics (RMHD; Mignone et al., 2007; Font, 2008; Martí and Müller, 2015).

4.1 Large scale jets

Special relativistic hydrodynamical codes are focused on the highly collimated and stable plasma flows in the first few parsecs or kiloparsecs away from the central BH. On these scales, the effects of GR are negligible. A relatively small step was successful in moving from high-resolution shock capturing to two dimensional axis-symmetric time-dependent RHD simulations (Duncan and Hughes, 1994; Martí et al., 1997; Rosen et al., 1999). The next natural step was to implement the magnetic force and expand these simulations to three dimensions (Nishikawa et al., 1998). A great base of modern RMHD simulations is given by the first three dimensional axis-symmetric relativistic jet propagating through a homogeneous ambient medium on a Cartesian grid (Aloy et al., 1999). Until today, simulations use a similar parameter setup, for example, specific Mach numbers in each simulation, relativistic speeds, that is, $v \leq c$, and (ideal) equations of state. Further, modern simulations implement similar approaches for the jet injection by assuming a circular jet nozzle at the inner numerical boundary.

To ensure a more sophisticated and realistic treatment of the synchrotron emission of the jet post-process ray-tracing/radiative transfer is applied (MacDonald and Marscher, 2018). This allows for more direct comparisons to be made between jet

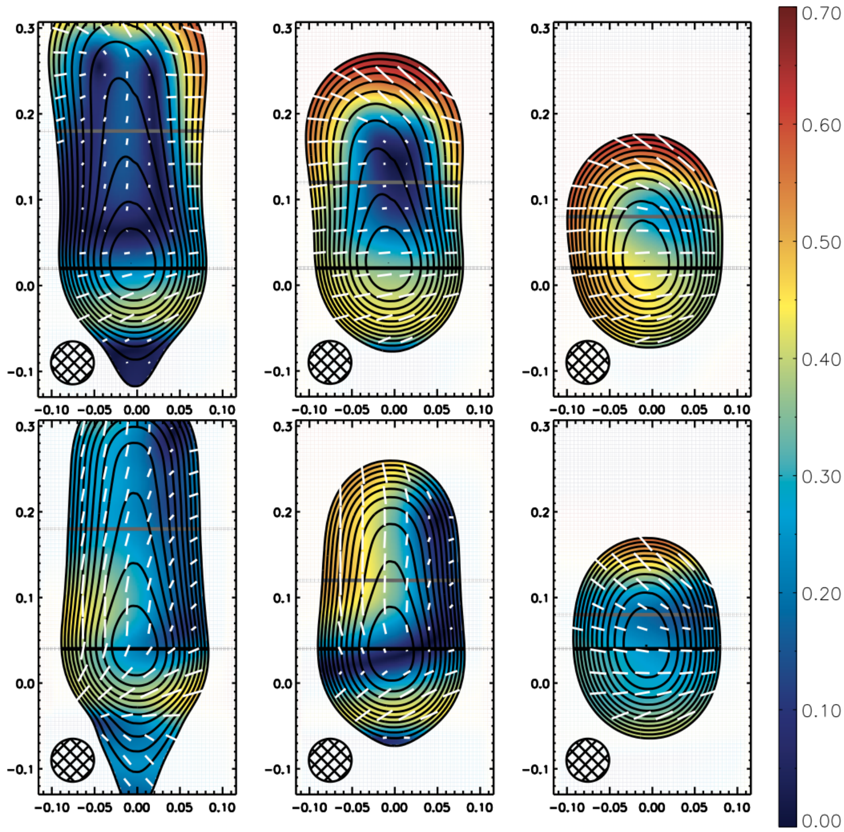

Figure 4.2: The figure shows modeled emission in jets as a post-process ray-traced radiation from MHD numerical simulations of a relativistic outflow. From left to right: Polarization for different inclinations, i.e., $i = 30°, 20°, 10°$. Picturing polarization angles along the cuts along core (black) and jet (gray). Figure taken from Porth et al. (2011).

simulations and observations. A big breakthrough was achieved in three dimensional RMHD emission models (see Figure 4.1, Aloy et al., 2000). The emission was calculated explicitly by integrating the equations of radiative transfer. A great advantage is the inclusion of relativistic effects by this approach. RMHD simulations that studied the synchrotron emission have been added or applied post-process. RMHD simulations that studied the synchrotron emission stressed the dependence of polarization on the inclination and bulk Lorentz factor of the jet, among others, see Figure 4.2 (Porth et al., 2011; Kramer and MacDonald, 2021). Studies on the recollimation shock shifted the focus on features within the jet and revealed a strong correlation between the characteristics of the observed feature (e.g., intensity, morphology) and the choice of the magnetic field topology, e.g., poloidal, helical, or toroidal (Kramer and MacDonald, 2021; Mizuno et al., 2015). Further, these simulations included optically thin total intensity and LP calculations (Fuentes et al., 2018).

4.2 Microphysics in astrophysical jets

Although the hydrodynamic approach effectively captures a significant portion of the fluid dynamics within the jet, it falls short in simulating the intricate physics at the kinetic scale (below the ion inertial length[1], Viall et al., 2021), which directly contributes to the production of synchrotron radiation detected by VLBI arrays. To overcome this limitations, it is necessary to implement microphysics considering (non-thermal) particles encountering radiative losses and shock acceleration. Modern numerical schemes aim to bridge the gap between kinetic scales and large scales (see Figure 4.3) by incorporating hybrid models (see Chapter 7) that account for the emission in AGN sources generated by non-thermal particles (NTPs) accelerated at shocks or in magnetic reconnection events (Sironi et al., 2013). Notably, RMHD simulations have a distinct advantage in creating self-consistent jet models, simplifying the integration of approaches to describe the behavior of NTPs. To incorporate NTPs, their energy density is typically linked to the pressure of the thermal plasma or the magnetic energy density (Porth et al., 2011; Fromm et al., 2016; Kramer and MacDonald, 2021, and Chapter 5). In the latter case, the acceleration of particles is also accounted for. Earlier implementations involved transport algorithms for the advection of NTPs encompassing physical phenomena such as synchrotron losses. To bridge the gap between the macroscopic scales inherent in the RMHD approximation and the micro-scale kinetic effects, various hybrid numerical frameworks have been developed. These approaches include methods such as incorporating sub-grid electron physics using Lagrangian particles or additional fluid tracers (Mimica et al., 2009; Ressler et al., 2015; Vaidya et al., 2018). These hybrid frameworks aim to account for the microscale phenomena while still capturing the macroscopic behavior of the system.

However, the most accurate model for particle behavior is the Particle-in-Cell (PIC) method, which accurately mimics the kinetic dynamics of the plasma constituting the jet in a self-consistent manner by solving Maxwell's equation directly. This method represents the plasma as a collection of charged macroparticles that are moved about on a numerical grid by the integration of the resultant Lorentz force. PIC comprehensively incorporates all the microphysical processes mentioned earlier (Sironi et al., 2015; Kagan et al., 2015; Duţan et al., 2016). A recent study represented the observational differences in plasma compositions in synthetic polarized maps of jet (MacDonald and Marscher, 2018).

[1]The ion inertial length refers to the scale at which ions disengage from electrons, and the magnetic field becomes frozen into the electron fluid rather than the entire plasma bulk.

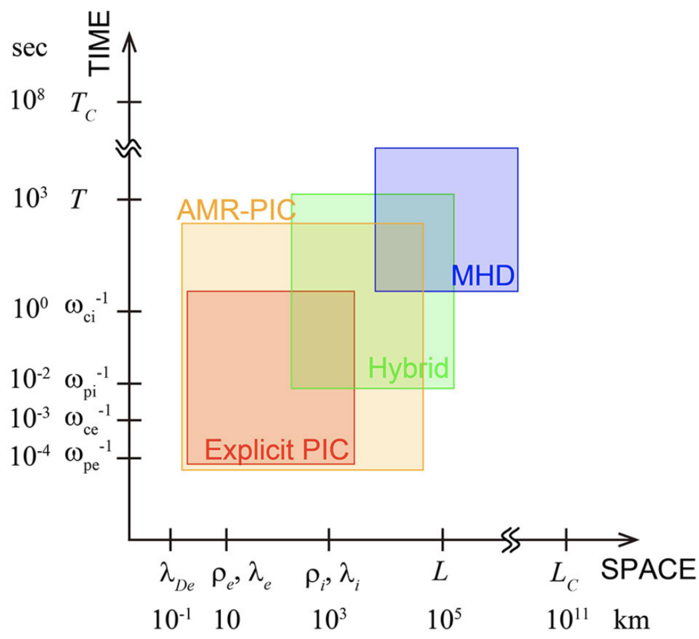

Figure 4.3: The diagram illustrates the ranges covered by each simulation model. Specifically, setting the focus on the electron Debye length λ_{De}, and $\rho_{\mathrm{s}} = v_{\mathrm{th,s}}/\omega_{\mathrm{cs}}$ denoting the gyro radius of either the ion or electron. Figure taken from Fujimoto (2018).

4.3 Principles

The fundamentals of plasma physics are crucial for the understanding of jet physics. *Plasma* itself is distinguished from the three other physical states of matter: solid, liquid, gaseous. For a description of the plasma, single particles can be neglected on scales proportional to the Debye length

$$\lambda_{\mathrm{D}} = \sqrt{\frac{kT}{4\pi e^2 n_{\mathrm{e}}}}, \tag{4.1}$$

with the Boltzmann constant k, temperature T, particle charge e, and particle number density n_{e}. The Debye length holds significant importance as a physical parameter in plasma physics, serving as a metric to determine the distance over which the electric field of a single charged particle affects other charged particles within the plasma. Due to the typically small value of the Debye length and the significantly large plasma frequency, plasma can effectively be treated as neutral fluid with negligible electric fields. This approach aligns with the principles of (magneto-) hydrodynamics.

4.3.1 Special relativistic magnetohydodynamics

The time-dependent, non-linear system of special relativistic conservation laws are addressed by solving a set of hyperbolic equations, following a covariant formulation (Landau et al., 1953). The RMHD equations encompass the conservation of energy, momentum, and mass, interlinked with the evolution of the magnetic field as dictated by the homogeneous Maxwell equation. When formulating the conservation laws as a covariant set of equations, a flat Minkowski metric is assumed, i.e., $\eta^{\alpha\beta} = \mathrm{diag}\,(-1,1,1,1)$. The normalization of the four-velocity and covariant magnetic field vector are[2]

$$u^\alpha u_\alpha = -1, \tag{4.2}$$

$$u^\alpha b_\alpha = 0, \tag{4.3}$$

$$|b|^2 = b^\alpha b_\alpha = \frac{\mathbf{B}^2}{\gamma^2} + (\mathbf{v}\cdot\mathbf{B})^2\,. \tag{4.4}$$

The four-velocity and covariant magnetic field vector are defined as

$$u^\alpha = \gamma\,(1,\mathbf{v})^{\mathrm{T}}\,, \tag{4.5}$$

$$b^\alpha = \gamma\left(\mathbf{v}\cdot\mathbf{B}, \frac{\mathbf{B}}{\gamma^2} + \mathbf{v}\,(\mathbf{v}\cdot\mathbf{B})\right)^{\mathrm{T}}\,. \tag{4.6}$$

The spatial components of the fluid's velocity $\mathbf{v} = (v_x, v_y, v_z)^T$, magnetic field $\mathbf{B} = (B_x, B_y, B_z)^T$, and the Lorentz factor γ are utilized. The relativistic continuity equation describes the conservation of energy; momentum conservation, accounting for the magnetic forces, is upheld through the Euler's equation; and the spatial components of the homogeneous Maxwell equation result in the induction equation

$$\begin{aligned} \partial_\alpha\left(\rho u^\alpha\right) &= 0, \\ \partial_\alpha\left[\left(\rho h + |b|^2\right)u^\alpha u^\beta - b^\alpha b^\beta + p\eta^{\alpha\beta}\right] &= 0, \\ \partial_\alpha\left(u^\alpha b^\beta - u^\beta b^\alpha\right) &= 0, \end{aligned} \tag{4.7}$$

with the co-moving specific enthalpy h, the rest mass density of the fluid ρ, and pressure p. The total pressure p is defined as the sum of thermal pressure p_{th} and magnetic pressure p_{g}, i.e., $p = p_{\mathrm{th}} + p_{\mathrm{g}}$.

[2]The convention is adopted wherein Greek indices range from 0 to 4, while Latin indices span from 1 to 3. The Einstein summation convention is employed, where repeated indices imply summation.

Conservation of the state vector

The solution to Equation 4.7, as well as the corresponding conservative variables and fluxes for RMHD, can be expressed as follows:

$$U^k = (D, m_x, m_y, m_z, B_x, B_y, B_z, E)^{\mathrm{T}} = (D, \mathbf{m}, \mathbf{B}, E)^{\mathrm{T}},$$
$$T^{ik} = \Big(D\mathbf{v} \quad p\mathbf{e}_x - \frac{b_x}{\gamma}\mathbf{B} + m_x\mathbf{v} \quad p\mathbf{e}_y - \frac{b_y}{\gamma}\mathbf{B} + m_y\mathbf{v} \quad p\mathbf{e}_z - \frac{b_z}{\gamma}\mathbf{B} + m_z\mathbf{v}$$
$$B_x\mathbf{v} - v_x\mathbf{B} \quad B_y\mathbf{v} - v_y\mathbf{B} \quad B_z\mathbf{v} - v_z\mathbf{B} \quad \mathbf{m} \Big), \tag{4.8}$$

where $\mathbf{e}_i$ ($i \in \{x, y, z\}$) is the unit vector in the direction of the ith axes of a three dimensional Cartesian coordinate system. The laboratory density D, momentum and magnetic field vector, $\mathbf{m}$ and $\mathbf{B}$, respectively, and the total energy density E are:

$$D = \rho\gamma, \tag{4.9}$$
$$\mathbf{m} = \left(\rho h\gamma^2 + \mathbf{B}^2\right)\mathbf{v} - (\mathbf{v}\cdot\mathbf{B})\,\mathbf{B}, \tag{4.10}$$
$$E = \rho h\gamma^2 - p_g + \frac{\mathbf{B}^2}{2} + \frac{\mathbf{v}^2\mathbf{B}^2 - (\mathbf{v}\cdot\mathbf{B})^2}{2}. \tag{4.11}$$

The summary of the equations for special relativistic MHD is

$$\partial_t U^k + \partial_i T^{ik} = 0. \tag{4.12}$$

This represents a conservation equation for the state vector U, where the variables are commonly referred to as conservative variables. However, the variables that typically hold significance for the physical application are the primitive variables

$$\mathbf{V} = (p, \rho, \mathbf{v}, \mathbf{B})^{\mathrm{T}}. \tag{4.13}$$

The computation of primitive variables from the conserved quantities must be done numerically (Mignone et al., 2007).

Equation of state

To ensure a proper solution, the system of RMHD equations is closed by specifying an appropriate equation of state (EoS) that relates thermodynamic quantities. The specific enthalpy implicitly defines the ideal gas EoS for a given adiabatic index:

$$h = 1 + \frac{\Gamma p}{(\Gamma - 1)\,\rho}, \tag{4.14}$$

while assuming a constant $\Gamma-$law, representing the specific heat ratio.

4.4 Numerical codes

The equations of (R)MHD can be classified as hyperbolic conservation laws, and their solution can be obtained using numerical methods specifically developed for this type of partial differential equation. Modern high-resolution shock-capturing schemes commonly employ finite volume spatial discretization, which solves the integral form of the differential equations and updates the volume averages of the variables. This approach ensures that discontinuities and shocks are treated consistently, allowing for the natural incorporation of the conservative structure of the equations. Furthermore, high-resolution shock-capturing methods maintain robustness and numerical stability, aiding in effectively modeling flows that are strongly supersonic. Most high-resolution shock-capturing schemes rely on the reconstruct-solve-average strategy (RSA). It involves a three-step procedure that helps in accurately evolving the solution over time:

Reconstruct In the first step, the volume averaging of the variables within each computational cell is reconstructed using piecewise monotonic interpolants. This reconstruction is performed to obtain a more accurate representation of the solution within each cell.

Solve In the second step, a Riemann problem[3] is solved at each interface between neighboring cells. It considers the discontinuous left and right states at the interface and computes the numerical flux, which captures the flow of information across the interface. The Riemann solver determines how the solution evolves from one side of the cell to the other.

Average In the final step, the solution is advanced in time by evolving the volume averages of the variables based on the computed numerical fluxes at the interfaces. This step involves updating the solution using appropriate time-stepping methods to ensure accurate time evolution.

A comprehensive examination of the various numerical schemes developed for simulating relativistic astrophysical flows can be found in Martí and Müller, 2003, while Goedbloed et al., 2010, provides a comprehensive introduction to this subject matter. In finite-volume codes based on Godunov-type high-resolution shock-capturing schemes (proposed by Godunov in 1959), the computational domain is discretized into cells. At the interfaces between these cells, a (linearized) Riemann problem is solved to determine the numerical fluxes that represent the flow of information between neighboring cells. These numerical fluxes are then utilized to update the conserved variables in the cell. These codes are specifically designed to solve a set of partial differential equations expressed as conservation laws (see Equation 4.12).

[3] An initial value problem with a conservation equation and piecewise constant initial data containing a single discontinuity in the domain of interest. For details the reader is referred to Roe (2015).

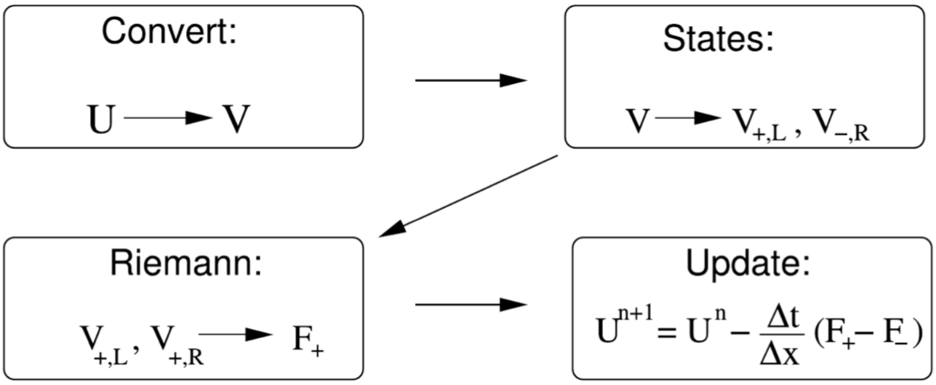

Figure 4.4: The diagram presented illustrates the steps involved in the reconstruct-solve-average strategy (RSA) utilized in the PLUTO code. The first step involves the conversion of the volume-averaged variables $\mathbf{U}$ to primitive quantities represented by $\mathbf{V}$. Subsequently, the primitive variables are divided into two states, specifically the left state $\mathbf{V}_{+,L}$ and the right state $\mathbf{V}_{-,R}$. A Riemann solver is then employed to determine the solution between these states, enabling the computation of the numerical flux functions denoted as $\mathbf{F}_{+}$. Finally, the solution is advanced in time. This schematic diagram has been adapted from Mignone et al. (2007).

4.4.1 PLUTO

In the PLUTO code, a (linearized) Riemann problem is solved to determine the numerical flux that flows between neighboring cells, which are applied in the conservation laws used for RMHD. The conservative variables are updated in time accordingly. The general four-step strategy of the Gudunov-type scheme implemented in the PLUTO code is illustrated in Figure 4.4. The first step involves converting the conservative quantities to primitive quantities to facilitate the subsequent steps (top left corner of Figure 4.4). In cases where the system is relativistic and magnetized, this conversion is carried out numerically due to the significant non-linearity of the equations. The following step is the reconstruction process, which begins with the primitive variables defined at the center of each cell. Through an interpolation routine, the left and right states at the cell faces are computed as part of this step (LeVeque, 1998; Toro et al., 2009), pictured in the top right corner of Figure 4.4. Once the left and right states are computed, the code recovers the numerical fluxes by solving the Riemann problem at the zone interfaces (lower left corner in Figure 4.4). The final step involves temporal evolution, where the set of conservative quantities at a given time t is used to calculate the same set of variables at the subsequent time $t + \delta t$, with δt representing the time step (lower right corner in Figure 4.4). A detailed description of the procedure can be found in Mignone et al. (2007).

Riemann solver

An approximate Riemann solver is a numerical method used to calculate the inter-cell numerical fluxes in a numerical scheme for solving hyperbolic partial differential equations, particularly in the context of finite volume methods. In hyperbolic equations, the inter-cell fluxes are crucial for capturing the propagation of information across cell interfaces. The Riemann problem provides the exact solution at the interface between two cells with different initial states. However, calculating the exact Riemann solution is often computationally expensive and not feasible in practical simulations. The approximate solution to a Riemann problem should, however, have a better accuracy than the one of the finite difference scheme.

Approximate Riemann solvers offer a compromise by providing an efficient and accurate estimation of the inter-cell fluxes. These solvers consider a simplified version of the Riemann problem, typically assuming local equilibrium or utilizing linearized equations. They use this simplified problem to compute an approximate solution that reasonably captures the wave interactions and shock formations at the interface. Various types of approximate Riemann solvers have been developed, such as the Lax-Friedrichs method, the Harten-Lax-van Leer (*hll*) method, and the Harten-Lax-van Leer-Contact (*hllc*) method. These solvers differ in their specific approach to approximating the Riemann solution and have varying degrees of accuracy and computational efficiency. The choice of which solver to use depends on the specific characteristics of the problem being solved (Guthmann et al., 2002).

hll & hlld The lineage of *hll* approximate Riemann solvers can be traced back to the pioneering work of Harten et al. (1983). Since then, the *hll* Riemann solver has gained widespread popularity due to its straightforward implementation, computational efficiency, and robustness (e.g., applied in special and general RMHD by Gammie et al., 2016). Based on the code design and Figure 4.4, obtaining the flux in a specific direction necessitates solving the initial conservation law in Equation 4.12. The volume averages (before converting to conservative values) has to be solved in the left- and right-hand state:

$$\mathbf{U}(x, t_0) = \begin{cases} \mathbf{U}_{+,\mathrm{L}} & \text{if} \quad x < x_+, \\ \mathbf{U}_{+,\mathrm{R}} & \text{if} \quad x > x_+. \end{cases} \tag{4.15}$$

As the flux in a particular direction evolves, the variables $\mathbf{U}$ and $\mathbf{T}(\mathbf{U})$ separate into each seven equations with each seven unknowns, corresponding to an independent conserved variable (it increases to eight variables for *hlld*). The final interface flux is derived by a parametrization of the Rankine-Hugoniot Jump conditions across each intermediate states and fluxes, as well as the two outermost fast magnetotosonic waves.

For a detailed solution for various solvers see (Taub, 1948; Miyoshi et al., 2010; Mignone and Bodo, 2006; Mignone et al., 2007; Mattia, 2022).

RMHD module

In PLUTO, the implementation encompasses the equations of special RMHD, in which the vector of conservative variables and corresponding fluxes are represented by the set of equations in Section 4.3.1. PLUTO follows the approach outlined in Mignone and Bodo, 2006, which has been recently extended to incorporate the constant-Γ ideal-gas law and the specific enthalpy within (see Section 4.3.1). Additional insights can be gained from the works of Mignone et al. (2007).

Lagrangian particle module

In general, the PLUTO code includes a parallel module that supports various types of particles, such as cosmic ray particles, dust grains, and Lagrangian particles. The information related to these particles is stored in sequentially linked node structures. Each node contains the particle itself along with pointers to the previous and next nodes in the sequence. Every particle is assigned a unique identity number upon creation and initialization. There are two available methods for initializing the particles: global initialization or cell-by-cell initialization. The fluid boundary conditions are applicable to the particles, and it is also possible to define custom user-defined boundary conditions. Furthermore, new particles can be injected into specific regions of the computational domain at specified times during the simulation.

The energy distribution of each macro particle is continuously updated over time. In detail, the numerical module keeps track of the particle's attributes at a given position on the Cartesian grid:

$$\frac{\mathrm{d}\mathbf{x}_\mathrm{p}}{\mathrm{d}t} = \mathbf{v}_\mathrm{p} = \mathbf{v}(\mathbf{x} \rightarrow \mathbf{x}_\mathrm{p}). \tag{4.16}$$

The particle attributes are then applied and solved for the energy losses the particle encountered:

$$\frac{\mathrm{d}E}{\mathrm{d}\tau_\mathrm{p}} = -c_1\left(\tau_\mathrm{p}\right)E - c_2\left(\tau_\mathrm{p}\right)E^2 \equiv \dot{E}. \tag{4.17}$$

In Equation 4.17, the first term represents the energy loss resulting from adiabatic expansion, while the second term represents the combined energy loss from synchrotron radiation and inverse Compton scattering off the cosmic microwave background. The physical constants c_1 and c_2 are given by

$$
\begin{aligned}
c_1 &= \frac{\nabla_\mu u^\mu}{3} = \frac{1}{3\rho}\frac{\mathrm{d}\rho}{\mathrm{d}\tau_\mathrm{p}}, \\
c_2 &= \frac{4\sigma_\mathrm{T} c\beta^2}{3m_e^2 c^4}\left[U_\mathrm{B} + U_\mathrm{rad}\left(E_\mathrm{ph}\right)\right]
\end{aligned}
\tag{4.18}
$$

The Thomson cross-section, denoted as σ_T, represents the scattering efficiency. The quantities U_B and U_rad correspond to the energy densities of the magnetic field and the radiation field, respectively. E_ph represents the energy of the incident photon from the cosmic microwave background (Vaidya et al., 2018).

Physical scaling

In PLUTO, the simulations are conducted using dimensionless grid units. As a result, the thermal properties of the RMHD jet flow need to be appropriately converted into physical units as a post-processing step. Utilizing dimensionless quantities offers the advantage of avoiding excessively small or large numbers during the simulation. However, when incorporating specific scales of length, time, and energy into the problem, a physical scaling becomes necessary to ensure accurate representation. Details on this physical scaling and the scaling required in order to model the resultant non-thermal jet emission from our numerical simulations, i.e., initially assuming a power-law distribution of non-thermal particles, is discussed further in Chapter 5 and in Kramer and MacDonald, 2021, respectively.

In order to apply the Lagrangian particle module and account for synchrotron losses, the numerical energy bins of the simulated power-law distribution,

$$
\langle\chi\rangle^0_{\mathrm{p},i} = \frac{N_\mathrm{tot}}{n^0}\left(\frac{1-p}{E_\mathrm{max}^{1-p} - E_\mathrm{min}^{1-p}}\right)E_i^{-p}, \tag{4.19}
$$

with the initial number density of physical particles N_tot, and the initial number density of the fluid n^0, interpolated at the position of the particle (Vaidya et al., 2018), have to be converted to physical units. For both a spectral study as well as the creation of synthetic synchrotron maps, the calculations are dependent on the chosen frequency. Hence, it is important that we ensure the correct frequency range in the emission frame to ensure radio emission in the observer's frame. The spectral index, i.e., the slope of the particle's spectrum is calculated at the desired frequency under the consideration of the Doppler boosting. This single particle's spectral index is interpolated on a Cartesian grid in three dimensions (see further details in Chapter 6).

4.4.2 RADMC-3D

RADMC-3D is an openly available software package designed for conducting astrophysical radiative transfer calculations in one, two, or three dimensions and in Cartesian, spherical, and cylindrical geometries (Dullemond et al., 2012). The code, written in Fortran-90, offers various physical modules, coordinate systems, and grid options, all of which are accompanied by well-written user manuals. In the scope of this thesis, ray-tracing calculations are performed using Cartesian coordinates. The ray-tracing process considers frequency dependence and incorporates intricate radiative physics and opacity effects. The research presented in this thesis makes use of a modified version of RADMC-3D to compute both linear and circular polarization intensity images, taking into account synchrotron emission from a relativistic plasma (MacDonald and Marscher, 2018). This adaptation includes the inclusion of Faraday rotation and the conversion from linear to circular polarization. To achieve this, the PLUTO simulation output is processed, applying the necessary physical scaling (see Chapter 5 and Kramer and MacDonald, 2021). Subsequently, `FITS` images are generated, with the map coordinates adjusted such that the peak total intensity is centered at the origin. This process enables the creation of full Stokes polarization maps from three dimensional simulations, facilitating the comparison of synthetic results with both VLBI emission maps and polarization measurements from individual telescopes (see Chapter 6). An additional benefit of the ray-tracing calculations variation in this thesis is the flexibility to choose different viewing angles for the jet without requiring extensive modifications to the PLUTO data.

Polarized radiative transfer

The radiative transfer of the polarized emission and its interaction with a medium are characterized by the propagation of the four Stokes parameters, representing a full polarized calculation of the emission at a given frequency ν:

$$\mathbf{I}_\nu = (I_\nu, Q_\nu, U_\nu, V_\nu)^{\mathrm{T}} . \tag{4.20}$$

The emitted polarized intensity $\mathbf{I}_{\mathrm{out},\nu}$ after interaction with the medium is related to the intrinsic polarized radiation (Equation 4.20) via an individual 4×4 Mueller matrix M. Combining this, Equation 4.20, and applying it to the equation of radiative transfer (Equation 2.3), it can be solved for an analytical solution for an individual ray along the following vector:

$$\begin{pmatrix} \left(\frac{\mathrm{d}}{\mathrm{d}l}+\kappa_I\right) & \kappa_Q & \kappa_U & \kappa_V \\ \kappa_Q & \left(\frac{\mathrm{d}}{\mathrm{d}l}+\kappa_I\right) & {\kappa^*}_V & -{\kappa^*}_U \\ \kappa_U & -{\kappa^*}_V & \left(\frac{\mathrm{d}}{\mathrm{d}l}+\kappa_I\right) & {\kappa^*}_Q \\ \kappa_V & {\kappa^*}_U & -{\kappa^*}_Q & \left(\frac{\mathrm{d}}{\mathrm{d}l}+\kappa_I\right) \end{pmatrix} \begin{pmatrix} I_{\mathrm{out},\nu} \\ Q_{\mathrm{out},\nu} \\ U_{\mathrm{out},\nu} \\ V_{\mathrm{out},\nu} \end{pmatrix} = \begin{pmatrix} j_I \\ j_Q \\ j_U \\ j_V, \end{pmatrix}. \quad (4.21)$$

The Faraday rotation in Equation 4.21 is quantified by the parameter κ_V^*, while the conversion from linear to circular polarization is represented by the parameters κ_Q^* and κ_U^*. RADMC-3D solves Equation 4.21 under the consideration of optical depth, i.e., $\mathrm{d}\tau = \kappa_{\mathrm{I}}\mathrm{dl}$ by utilizing an analytical solution adapted from (Jones and Odell, 1977). MacDonald and Marscher, 2018, incorporated their analytic solution into the ray-tracing code RADMC-3D, enabling the execution of a full Stokes analysis. A new solution, including a full rotational view of the three dimensional synthetic polarized emission is presented in MacDonald and Nishikawa, 2021, and applied in Chapter 7.

5 Ray-tracing in relativistic jet simulations: A polarimetric study of magnetic field morphology and electron scaling relations

This chapter contains the research published in Kramer and MacDonald (2021).

The jets emanating from the centers of active galactic nuclei rank among the most energetic objects in the universe. Comparisons between numerical simulations of relativistic jets and observed polarized synchrotron emission is essential for understanding how the morphology of the non-thermal synchrotron emission of the jet depends on the magnetic properties of the underlying relativistic plasma. To achieve this, the publication below made use of three dimensional RMHD jet simulations (performed with the PLUTO code[1]) to investigate how the non-thermal synchrotron emission of a relativistic jet is affected by a dominant component in the magnetic field morphology. Precisely, the publication investigates the effects of a purely toroidal, a purely poloidal magnetic field topology, or a mixture of both, i.e., a helical structure of the intrinsic magnetic field. Additionally, the work utilizes polarized radiative transfer and ray-tracing techniques (implemented through the RADMC-3D code[2]) to create the synthetic radio emission maps, encompassing total intensity, linearly polarized intensity, and circularly polarized intensity for the jet simulation. The transition between the thermal properties of the simulation and the non-thermal emission in the synchrotron maps is conducted by applying various electron scaling relations.

[1]For a detailed description on the open-source code see Mignone et al., 2007 and further visit the PLUTO website.

[2]Details on the publicly available code can be found in Dullemond et al., 2012 and on the RAMDC-3D website.

The first part of the following peer-reviewed publication results in a threefold of findings: Helical or toroidal magnetic field structures are suggested to explain the observed increase in total intensity and linear polarization toward the jet edges. Precisely, the outer sheath is edge-brightened and dominates the emission, similar to the jet of 3C 84 (Giovannini et al., 2018; Paraschos et al., 2022), M87 (Walker et al., 2018; Janssen et al., 2019), and Centaurus A (Janssen et al., 2021). In purely poloidal magnetic field simulations, the jet spine or recollimation shock, associated with the radio core in VLBI observations, dominates the emission, resembling observations in, for instance, NGC 1052 (Baczko, 2020; Baczko et al., 2016). Finally, a bi-modal EVPA pattern, where the EVPAs align with the jet axis in the spine and are predominantly perpendicular to the direction of jet motion in the sheath, is observed in the purely toroidal field simulation.

The second part focuses on the dependency of the synchrotron emission on the applied scaling calculations between the thermal variables of the RMHD simulations and non-thermal emission properties. The choice of electron scaling relation (thermal density, pressure, or magnetic energy density) has limited impact on the emission morphology within the shock when arbitrarily excluding the ambient medium in a post-process step. However, when including the ambient medium, the magnetic energy density scaling highlights the jet emission the most through the intervening plasma. The need to exclude the ambient medium from polarized emission calculations in this publication directly implies the importance of particle physics incorporated in relativistic jet simulations to account for radiative losses (see Chapter 7) and shock acceleration.

For this publication, I make use of and adjust the implemented jet description within the RMHD module of the PLUTO code (Mignone et al., 2007). I compile the simulations on the cluster at the Max Planck Institute for Radio Astronomy, Bonn, and generate the published figures of the numerical steps within the paper. I develop a python pipeline for post-processing the simulated data. In detail, the pipeline calculates the non-thermal variables and creates files suited for RADMC-3D. In RADMC-3D, N. MacDonald, as co-author, provided the numerical radiative transfer module to calculate the emission in full Stokes. I combine this module with the open-source software RADMC-3D to create the synthetic (polarized) emission maps of the synchrotron radiation mimicked for an AGN jet. Based on my analysis, the co-author N. MacDonald collaborates with fruitful discussions on the results and comments on the publication of which I am the leading author.

Credit: **Kramer, J. A.** and MacDonald, N. R. (2021), *Ray-tracing in relativistic jet simulations: A polarimetric study of magnetic field morphology and electron scaling relations*, Astronomy and Astrophysics, 656, A143, 15, reproduced with permission ©ESO.

A&A 656, A143 (2021)
https://doi.org/10.1051/0004-6361/202141454

Astronomy & Astrophysics

Ray-tracing in relativistic jet simulations: A polarimetric study of magnetic field morphology and electron scaling relations

Joana A. Kramer and Nicholas R. MacDonald

Max-Planck-Institut für Radioastronomie, Auf dem Hügel 69, 53121 Bonn, Germany
e-mail: jkramer@mpifr-bonn.mpg.de

Received 2 June 2021 / Accepted 4 September 2021

ABSTRACT

Context. The jets emanating from the centers of active galactic nuclei are among the most energetic objects in the Universe. Investigating how the morphology of the jet's synchrotron emission depends on the magnetic nature of the jet's relativistic plasma is fundamental to the comparison between numerical simulations of relativistic jets and their observed polarization.

Aims. Through the use of 3D relativistic magnetohydrodynamic jet simulations (computed using the PLUTO code) we study how the synchrotron emission from a jet depends on the morphology of its magnetic field structure. Through the application of polarized radiative transfer and ray-tracing (via the RADMC-3D code), we create synthetic radio maps of the total intensity of a jet as well as the linearly and circularly polarized intensity for each jet simulation.

Methods. In particular, we create synthetic ray-traced images of the polarized synchrotron emission from a jet when this latter carries a predominantly poloidal, helical, and toroidal magnetic field. We also explore several scaling relations in which the underlying electron power-law distribution is set proportional to: (i) the jet's thermal plasma density, (ii) its internal energy density, and (iii) its magnetic energy density.

Results. We find that: (i) the jet emission is edge-brightened when the magnetic field is toroidal in nature and spine brightened when the magnetic field is poloidal in nature; (ii) the circularly polarized emission exhibits both negative and positive sign for the toroidal magnetic field morphology at an inclination of $i = 45°$ as well as $i = 5°$; and (iii) the relativistic jet's emission is largely independent of different emission scaling relations when the ambient medium is excluded.

Key words. galaxies: jets – magnetic fields – polarization – radiative transfer – relativistic processes – magnetohydrodynamics (MHD)

1. Introduction

Collimated supersonic flows of plasma are characteristic of many astrophysical objects. These phenomena are known as jets and emanate from compact systems (e.g., proto-stars) as well as from supermassive black holes (SMBHs). They are among the most energetic objects in the Universe and commonly emanate from the centers of active galaxies. The class of radio-loud active galactic nuclei (AGN) exhibit jet emission. These objects are mostly embedded in massive elliptical galaxies and only account for less than 10% of observed AGN. Launched from a central engine such as a SMBH, the jets can be accelerated to highly relativistic speeds and remain collimated up to kilo-parsec (kpc) scales. AGN emit radiation across the electromagnetic spectrum, and observations of the jet emission reveal a featureless power-law spectrum. Together with the high level of linear polarization (up to 60−70%), the physical process of synchrotron radiation can explain the emission as well as the optical flux (Troja et al. 2017). From the radio emission, the presence of a magnetic field can be inferred and is commonly thought to play a key role in the launching and collimation process of the jet. AGN jets can extend to hundreds of kiloparsecs even though the jet-launching region occurs on scales of a few gravitational radii from the black hole (BH). On larger scales, jets are thought to be kinetically dominated and therefore contain relatively weak magnetic fields. However, within the collimation region, jets are thought to be magnetically dominated. Theoretical studies of jet formation suggest that strong magnetic fields are an essential mechanism for launching jets (Blandford & Znajek 1977). One of the main conclusions of a number of relativistic jet simulations is that the jet transitions from being magnetically dominated to kinetically dominated as it propagates (e.g., Martí et al. 1997).

Very-long-baseline interferometric (VLBI) imaging of the synchrotron emission emanating from jets commonly reveals a bright central feature (referred to as the radio core) and a series of components that separate from the core over time (i.e., blobs or plasmoids). There are also (in some sources) features downstream of the core that, in contrast to the plasmoids, appear to be stationary relative to the radio core (e.g., Ojha et al. 2010; Fromm et al. 2013). These standing features within the jet are commonly interpreted as recollimation shocks within the jet flow (Daly & Marscher 1988).

A continuum approximation of the plasma nature of the jet (i.e., relativistic magnetohydrodynamics – RMHD) can be implemented based on the assumption that the jet radius, R_j, is much larger than the Debye-Length[1] and gyroradius[2] of the jet's plasma (Hawley et al. 2015). Theoretical models of AGN jets have lead authors to postulate that the jet plasma is likely magnetized with a large-scale helical morphology related to the launching of the jet by the rotation of the central black hole and

[1] The Debye-Length is the length scale in a plasma over which the charge of a plasma is shielded by intervening electrons.
[2] The gyroradius (also referred to as the Larmor radius) is the radius about which an electron rotates about a magnetic field line.

Open Access funding provided by Max Planck Society.

accretion disk (Blandford & Znajek 1977; Blandford & Payne 1982; Hardee et al. 2007). Recent observational evidence indicates that a large fraction of parsec-scale jets do indeed exhibit polarization signatures of helical magnetic field components. This is based on the detection of statistically significant transverse Faraday rotation measure (RM) gradients across the jet on parsec scales (Gabuzda et al. 2008).

The presence of a helical/toroidal magnetic field within the jet can (in theory) produce current-driven instabilities within the jet flow (Kadowaki et al. 2021). These instabilities can then produce sites of magnetic reconnection within the jet plasma which in turn can result in particle acceleration (Singh et al. 2016; Striani et al. 2016). Recent particle-in-cell (PIC) simulations (e.g., Sironi et al. 2021) have indeed shown that magnetic reconnection events within relativistically jetted plasma can efficiently generate power-law distributions of electrons (see also, Sironi & Spitkovsky 2014; Guo et al. 2015; Werner et al. 2016; Guo et al. 2019; Matthews et al. 2020). However, many of these PIC calculations lack sufficient grid sizes to model the length scales of astrophysical jets.

In the present paper, we set about carrying out a systematic study of how the fractional levels and morphology of both linearly and circularly polarized synchrotron emission depend on the underlying magnetic field morphology of the jet as well as various fluid scalings for the underlying electron power-law distribution. This study is executed with fully 3D relativistic magnetohydrodynamic jet simulations coupled with full Stokes polarized radiative transfer via ray-tracing.

RMHD simulations are unable to reproduce the kinetic-scale physics of the jet (i.e., self-consistently generating the non-thermal distribution of electrons responsible for the observed synchrotron emission). We therefore rely on a purely macroscopic model of the jet that simulates the large-scale dynamics of the thermal plasma within the jet flow. We explore various emission recipes for mapping from the thermal fluid variables to the non-thermal distribution of electrons (see, e.g., Porth et al. 2011). This mapping is carried out as a post-process step. In particular, we apply three scaling relations in which the non-thermal distribution of electrons is assumed to be proportional to the (i) density, (ii) thermal pressure, and (iii) magnetic energy density of the plasma. We also examine the effect that different magnetic field morphologies within the jet (namely; poloidal, helical, and toroidal) have on the dynamics of the jet as well as the resultant polarized emission.

Our current jet simulations, while applicable to parsec-scale jets, lack sufficient micro physics (such as magnetic reconnection) to self-consistently generate power-law distributions of electrons. However, our emission calculations provide: (i) an important bridge between the micro physical scales of reconnecting current sheets and parsec-scale jets, and (ii) a valuable point of comparison for the next generation of synthetic synchrotron emission maps to be produced via hybrid fluid particle schemes (see, e.g., Vaidya et al. 2018).

This paper is structured as follows: Sect. 2 gives an introduction to the principles of relativistic magnetohydrodynamics and polarized radiative transfer and introduces the PLUTO (Mignone et al. 2007) and RADMC-3D (Dullemond et al. 2012) codes. We perform a full Stokes analysis with an emphasis on studying the jet's circularly polarized synchrotron emission. For this, the dependence of the jet's polarization on the magnetic field morphology, that is, poloidal, helical, and toroidal, is investigated in Sect. 3. In Sect. 4 we explore the effect that different thermal-fluid-to -non-thermal-electron-emission scaling relations have on the resulting jet emission. Section 5 outlines different numerical approaches, that is, when no jet tracer is included or the lower energy cutoff is computed differently. In Sect. 6 we compare our numerical results to recent observations of jets. Finally, our conclusions are summarized in Sect. 7.

2. Numerical methods

2.1. Principles of the relativistic magnetohydrodynamics in the PLUTO code

To model magnetized fluid flows, the PLUTO code integrates a system of conservation laws which can be expressed in general as:

$$\partial_t U^k + \sum_{i\in\{x,y,z\}} \partial_i T^{ik} = 0, \tag{1}$$

where U^k is a state vector of k conservative quantities and T^{ik} is a rank 2 tensor. Moreover, ∂_i is the four-gradient. The explicit form depends on the physical module selected within the code.

PLUTO solves a time-dependent nonlinear system of special relativistic conservation laws, which in general have the form of Eq. (1). To account for the motion of an ideal relativistic magnetized fluid, that is, in relativistic magnetohydrodynamics, mass and energy-momentum are conserved. The solution to the specified problem of relativistic magnetohydrodynamics and therefore the conservative variables and respective fluxes for RMHD are expressed as:

$$U^k = \begin{pmatrix} D \\ m_x \\ m_y \\ m_z \\ B_x \\ B_y \\ B_z \\ E \end{pmatrix}_k = \begin{pmatrix} D \\ \boldsymbol{m} \\ \boldsymbol{B} \\ E \end{pmatrix}_k, \quad T^{ik} = \begin{pmatrix} Dv_i \\ p\hat{e}_i^x - \frac{b_x}{\gamma} B_i + m_x v_i \\ p\hat{e}_i^y - \frac{b_y}{\gamma} B_i + m_y v_i \\ p\hat{e}_i^z - \frac{b_z}{\gamma} B_i + m_z v_i \\ B_x v_i - v_x B_i \\ B_y v_i - v_y B_i \\ B_z v_i - v_z B_i \\ m_i \end{pmatrix}_k, \tag{2}$$

where $\boldsymbol{v} = \left(v_x, v_y, v_z\right)^{\mathrm{T}}$ is the fluid's velocity, $\hat{\boldsymbol{e}}^j$ ($j \in \{x, y, z\}$) is the unit vector in the direction of the ith axis of a 3D Cartesian coordinate system, and b_i are the spatial components of the covariant magnetic field vector. The quantities in Eq. (2) are defined as follows: (Mignone & Bodo 2006):

$$\begin{aligned} D &= \rho\gamma, \\ \boldsymbol{m} &= \left(\rho h \gamma^2 + \boldsymbol{B}^2\right)\boldsymbol{v} - (\boldsymbol{v}\cdot\boldsymbol{B})\,\boldsymbol{B}, \\ E &= \rho h \gamma^2 - p_g + \frac{\boldsymbol{B}^2}{2} + \frac{\boldsymbol{v}^2\boldsymbol{B}^2 - (\boldsymbol{v}\cdot\boldsymbol{B})^2}{2}. \end{aligned} \tag{3}$$

Hence, the components of U^k resulting from the conservation laws are the laboratory density D, the three components of both momentum $\boldsymbol{m}$ and magnetic field $\boldsymbol{B}$, and the total energy density E, respectively.

For a proper solution of Eq. (1) an additional equation of state (EoS) is specified that defines the specific enthalpy (see Mignone et al. 2005):

$$h = \frac{5}{2}\Theta + \sqrt{\frac{9}{4}\Theta + 1}, \tag{4}$$

which approximates a single-special-relativistic perfect gas. Here, Θ is the ratio of pressure to density, i.e., $\Theta = p/\rho$.

2.2. Scaling

The PLUTO simulations are computed in dimensionless grid units, and therefore the thermal quantities of the RMHD jet flow must be properly scaled into physical units as a post process step. Computing dimensionless quantities has the advantage of avoiding either extremely small or large numbers at run time. A physical scaling is necessary whenever specific scales of length, time, and energy are included in the problem. The physical scaling of our RMHD jet simulations requires the definition of three fundamental units[3]:

$$\begin{aligned}&\text{unit density} && \rho_0\,[\mathrm{g\,cm^{-3}}]\\ &\text{unit length} && L_0\,[\mathrm{cm}]\\ &\text{unit velocity} && v_0\,[\mathrm{cm\,s^{-1}}].\end{aligned} \tag{5}$$

From these unit values, other quantities such as the timescale of the code t_0[s] can be computed: $t_0 = L_O/v_0$. Similarly, the pressure and magnetic field scale factors can be computed from these unit values: $p_0 = \rho_0 v_0^2$ and $B_0 = \sqrt{4\pi\rho_0 v_0^2}$. To then scale the dimensionless fluid variables into cgs units we apply the scale factors:

$$\begin{aligned}\rho_{\mathrm{cgs}} &= \rho\cdot\rho_0,\\ p_{\mathrm{cgs}} &= p\cdot\rho_0 v_0^2,\\ \boldsymbol{B}_{\mathrm{cgs}} &= \boldsymbol{B}\cdot\sqrt{4\pi\rho_0 v_0^2},\end{aligned} \tag{6}$$

where ρ, p, and $\boldsymbol{B}$ are dimensionless grid values. For the simulations presented in this work we specify the following unit values: $\rho_0 \simeq 1.67\times10^{-22}\,\mathrm{g\,cm^{-3}}$, $L_0 \simeq 1.23\times10^{16}$ cm, and $v_0 \simeq 3.0\times10^{10}\,\mathrm{cm\,s^{-1}}$. With this choice of values, the magnetic field strength along the jet will be of the order of gauss (G) to mG.

2.3. Mapping the non-thermal onto the thermal

An additional scaling relation is required in order to model the resultant non-thermal jet emission from our numerical simulations. The non-thermal quantities (i.e., electron number density and power-law energy cutoff) are inferred from the scaled thermal fluid variables of the simulation (i.e., plasma density, pressure, and magnetic field). This thermal to non-thermal mapping of our 3D RMHD jet simulations is used in the calculation of synchrotron emission maps. In particular, we initially assume an energy distribution of non-thermal relativistic electrons (NTEs) n_e which follows a global power-law distribution. This approach is justified by observations as well as theoretical expectations for particle acceleration within jets. In particular, we adopt a power-law distribution in electron energy γ (where $E = \gamma m_e c^2$):

$$n_e(\gamma) = n_0\left(\frac{\gamma}{\gamma_{\min}}\right)^{-s} \quad \text{for} \quad \gamma_{\min}\le\gamma\le\gamma_{\max}, \tag{7}$$

where $n_e(\gamma)$ is the differential number of NTEs and $\gamma_{\min}$, $\gamma_{\max}$ are the power-law cutoffs. The term n_0 is a normalization constant, and the power-law index s is related to the spectral index $\alpha = (s-1)/2$.

To solve for the unknowns of the electron power-law ($\gamma_{\min}$ and n_0), see Eq. (7), we map the total number density of non-thermal electrons (NTEs) onto the thermal fluid variables (similar to Fromm et al. 2016). First, we assume the number density of the injected NTEs is proportional to the thermal fluid number density ρ:

$$\int_{\gamma_{\min}}^{\gamma_{\max}} \mathrm{d}\gamma\, n_e(\gamma) = \zeta_e\frac{\rho}{m_p}, \tag{8}$$

where ζ_e is the ratio of non-thermal to thermal particles (see Mimica 2012). Second, we assume that the total energy density of the NTEs is proportional to the thermal pressure p. Here, we connect the fluid's pressure to the fluid's internal energy density ϵ via the equation of state $p = (\hat{\gamma}-1)\,\epsilon$, where $\hat{\gamma}$ is the adiabatic index. Consequently, the energy density becomes proportional to the internal energy density:

$$\int_{\gamma_{\min}}^{\gamma_{\max}} \mathrm{d}\gamma\, n_e(\gamma) m_e c^2 = \epsilon_e\epsilon = \epsilon_e\,(\hat{\gamma}-1)\,p, \tag{9}$$

where ϵ_e is the ratio between the energy stored in non-thermal particles to that stored in thermal particles. We set the thermal-to-non-thermal conversion factors to $\zeta_e = 1.0$ and $\epsilon_e = 0.5$.

Assuming that $\gamma_{\max} \gg \gamma_{\min}$ and $s > 2$ (we set $s = 2.3$), we solve this system of two equations (Eqs. (8) and (9)) for two unknowns ($\gamma_{\min}$ and n_0), which yields:

$$\begin{aligned}\gamma_{\min} &= \frac{p m_p \epsilon_e (s-2)}{\rho m_e c^2 \zeta_e (s-1)\,(\hat{\gamma}-1)}\\ n_0 &= \frac{\zeta_e^2 \rho^2 m_e c^2 (1-2)^2\,(\hat{\gamma}-1)}{m_p^2 p \epsilon_e (2-s)}.\end{aligned} \tag{10}$$

2.4. Polarized radiative transfer and ray-tracing via RADMC-3D

For our ray-tracing calculations, we use the code RADMC-3D, which is a well-tested and documented ray-tracing software for computing astrophysical radiative transfer in 3D geometries. Our ray-tracing calculations are carried out in Cartesian coordinates and in the co-moving frame of the plasma after which the resultant fluxes are Doppler boosted to obtain the jet flux in the observer's frame. The code reads in PLUTO output files that have been scaled into physical units (namely; the 3D distributions of B, n_e, and $\gamma_{\min}$). RADMC-3D produces 2D Fits images containing full Stokes polarization maps. The radiative transfer is implemented in our plasma simulations through the use of transport coefficients for synchrotron absorption ($\kappa_I, \kappa_Q, \kappa_U, \kappa_V$), synchrotron emissivity ($\eta_I, \eta_Q, \eta_U, \eta_V$), Faraday rotation ($\kappa_V^*$), and Faraday conversion (κ_Q^* and κ_U^*). Along individual rays our modified version of RADMC-3D solves the following transfer matrix:

$$\begin{pmatrix} \frac{\mathrm{d}}{\mathrm{d}l}+\kappa_I & \kappa_Q & \kappa_U & \kappa_V\\ \kappa_Q & \frac{\mathrm{d}}{\mathrm{d}l}+\kappa_I & \kappa_V^* & -\kappa_U^*\\ \kappa_U & -\kappa_V^* & \frac{\mathrm{d}}{\mathrm{d}l}+\kappa_I & \kappa_Q^*\\ \kappa_V & \kappa_U^* & -\kappa_Q^* & \frac{\mathrm{d}}{\mathrm{d}l}+\kappa_I \end{pmatrix}\begin{pmatrix} I_\nu\\ Q_\nu\\ U_\nu\\ V_\nu\end{pmatrix} = \begin{pmatrix}\eta_I\\ \eta_Q\\ \eta_U\\ \eta_V,\end{pmatrix}, \tag{11}$$

to obtain linear and circular polarization as a function of optical depth, i.e., $\mathrm{d}\tau = \kappa_I \mathrm{d}l$. The code applies an analytical solution to Eq. (11) presented in Jones & Odell (1977) and summarized in MacDonald & Marscher (2018). The analytical solution is a function of the normalization constant n_0, the low-energy cutoff $\gamma_{\min}$ of the power-law distribution in Eq. (7), the strength of the magnetic field, and its orientation to our line of sight.

[3] For further details see the PLUTO code (http://plutocode.ph.unito.it).

3. Magnetic field morphology study

3.1. Magnetic field prescriptions

Based on the physical scaling (presented in Sect. 2.2) and our NTE scaling relations (see Eq. (10)), we proceed to study the impact that different magnetic field morphologies within the jet (i.e., poloidal, toroidal, and helical) have on its polarized synchrotron emission. To produce different magnetic field morphologies, we implement (in Cartesian coordinates) expressions for the poloidal and toroidal components of the jet's magnetic field at the jet injection point (i.e., orifice) in our simulations. The jet is oriented along the z-axis in our ray-tracing calculations. The x and y components of the jet's magnetic field's toroidal component are given by Nishikawa et al. (2019):

$$B_x = \frac{\left(\frac{y-y_c}{a}\right)\cdot b_m}{1+\left(\frac{r}{a}\right)^2}, \qquad B_y = -\frac{\left(\frac{x-x_c}{a}\right)\cdot b_m}{1+\left(\frac{r}{a}\right)^2}, \tag{12}$$

where (x_c, y_c) is the location of the center of the jet, which in our simulation is set to $(0, 0)$. The variable r defines the jet's radius while a represents a magnetization radius. The parametrization constant of the magnetic field (b_m) is given by:

$$b_m = \sqrt{\frac{-4p_j\sigma_\phi}{a^2\left(2\sigma_\phi - 1 + 4\log(a)\right)}}, \tag{13}$$

where σ_ϕ is the magnetization parameter for the toroidal component. The constant poloidal term B_z threading the jet is written as:

$$B_z = \sqrt{\sigma_z\left(b_m^2 a^2 + 2p_j\right)}, \tag{14}$$

where σ_z is the magnetization parameter of the poloidal component. We choose $\sigma_z = 1$ for a purely poloidal magnetic field and $\sigma_\phi = 1$ for a purely toroidal field (Nishikawa et al. 2019; Mignone et al. 2009). A helical field is produced by setting $\sigma_z = \sigma_\phi = 0.5$. In Eq. (14) the variable p_j is the jet pressure. In particular, p_j is determined from our simulated jet Mach number $M = 2.7$ and bulk Lorentz factor $\Gamma = 7$ (i.e., $M = v_j \cdot \sqrt{\rho_j/\left(\Gamma p_j\right) + 1/(\Gamma - 1)}$), where ρ_j is the jet density. The sum of both magnetization parameters is set to 1 to enforce an equipartition between the magnetic pressure and thermal pressure within the jet plasma. We point out that the magnetization radius a is equal to the jet radius $r_j = \sqrt{(x-x_c)^2 + (y-y_c)^2}$ as it reaches its maximum value.

Figure 1 illustrates the three different simulated magnetic field morphologies within the jet (from top to bottom: poloidal, helical, toroidal). Here, the poloidal magnetic field vectors are streaming along the jet in the z-direction while the vectors for the toroidal components are predominantly perpendicular to the jet axis. The helical magnetic field vectors are rotated about ~45° in the jet's direction. Two-dimensional slices through the jet are included in Appendix A and illustrate how the injected field morphologies persist down the jet axis.

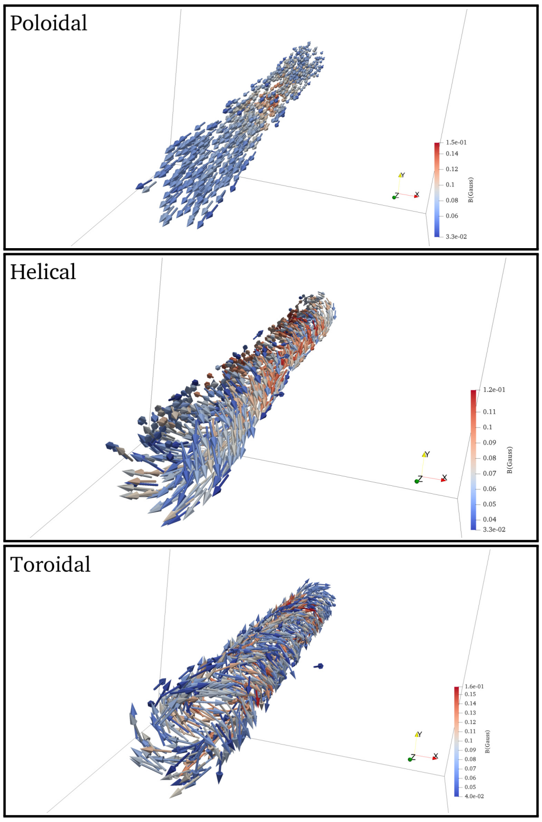

Fig. 1. Illustration of the three different magnetic field morphologies within the 3D RMHD jet simulations. The jet is streaming in the z-direction. The vectors represent the magnetic field strength (and orientation) in gauss (see the color bar) within each computational cell. *From top to bottom*: poloidal, helical, and toroidal magnetic field morphologies.

3.2. Results

Figure 2 presents a summary of the various steps in our synthetic imaging pipeline. In particular, we are interested in studying the polarized properties of the jet's recollimation shock. We image an intermediate epoch of each jet simulation, that is, when the jet's hot spot or terminal shock has not yet propagated off the grid. Through the use of a jet tracer, we extract the region of plasma around the standing shock (demarcated with a purple box in the first panel of Fig. 2) in order to yield an unobscured view of the jet's central spine, thus allowing us to focus on the jet flow upstream of the termination shock. These initial images were created using the poloidal magnetic field simulation. Panel a in Fig. 2 shows a 2D slice through the 3D jet simulation and displays the jet's density in dimensionless grid units. Panels b and c illustrate the zoomed-in ray-traced total intensity maps of the resulting synchrotron emission when the jet is resolved without and with the use of a jet tracer to exclude the ambient medium, respectively. The jet is viewed at an angle to the jet-axis of $i = 45°$ and propagates from top to bottom. In the absence of radiative cooling (i.e., synchrotron losses) and larger simulation sizes, we remove the bow shock from our ray-tracing calculations arbitrarily. Panel d displays the same snapshot but rotated to a viewing angle of $i = 5°$. Finally, panel e is convolved with a Gaussian beam in order to indicate the resolution of the Global Millimeter VLBI Array (GMVA), and with an added Gaussian noise level (to mimic array sensitivity) of 10^{-1} Jy beam^{-1}. These final images show a bright radio core associated with the standing shock in our simulations. In all our RMHD jet simulations (in which each computational box

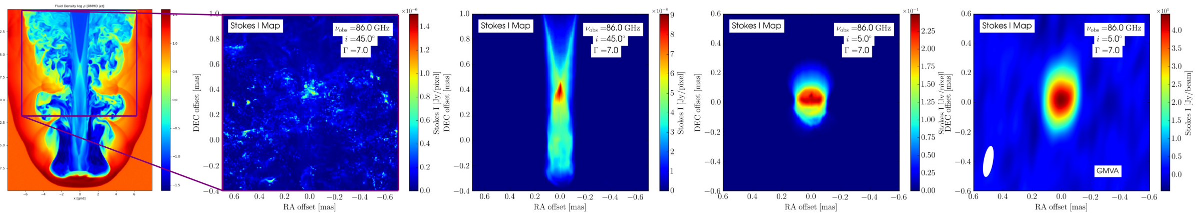

(*a*) (*b*) (*c*) (*d*) (*e*)

Fig. 2. *From left to right*: a demonstration of our synthetic imaging pipeline: *Panel a*: starts with a 2D cut through our 3D RMHD jet colored by thermal density. *Panels b–e*: zoomed into an unobscured region of the jet's standing shock (demarcated with a purple box in panel a) and show: (*b*) the ray-traced synchrotron emission without the use of a jet tracer; (*c*) the ray-traced synchrotron emission with the use of a jet tracer to exclude the ambient medium; (*d*) the same simulation epoch but rotated to a viewing angle of $i = 5°$; and (*e*) the ray-traced image convolved with a Gaussian beam indicative of the resolution of the GMVA and with a Gaussian noise floor (to mimic array sensitivity) of 10^{-1} Jy beam^{-1}.

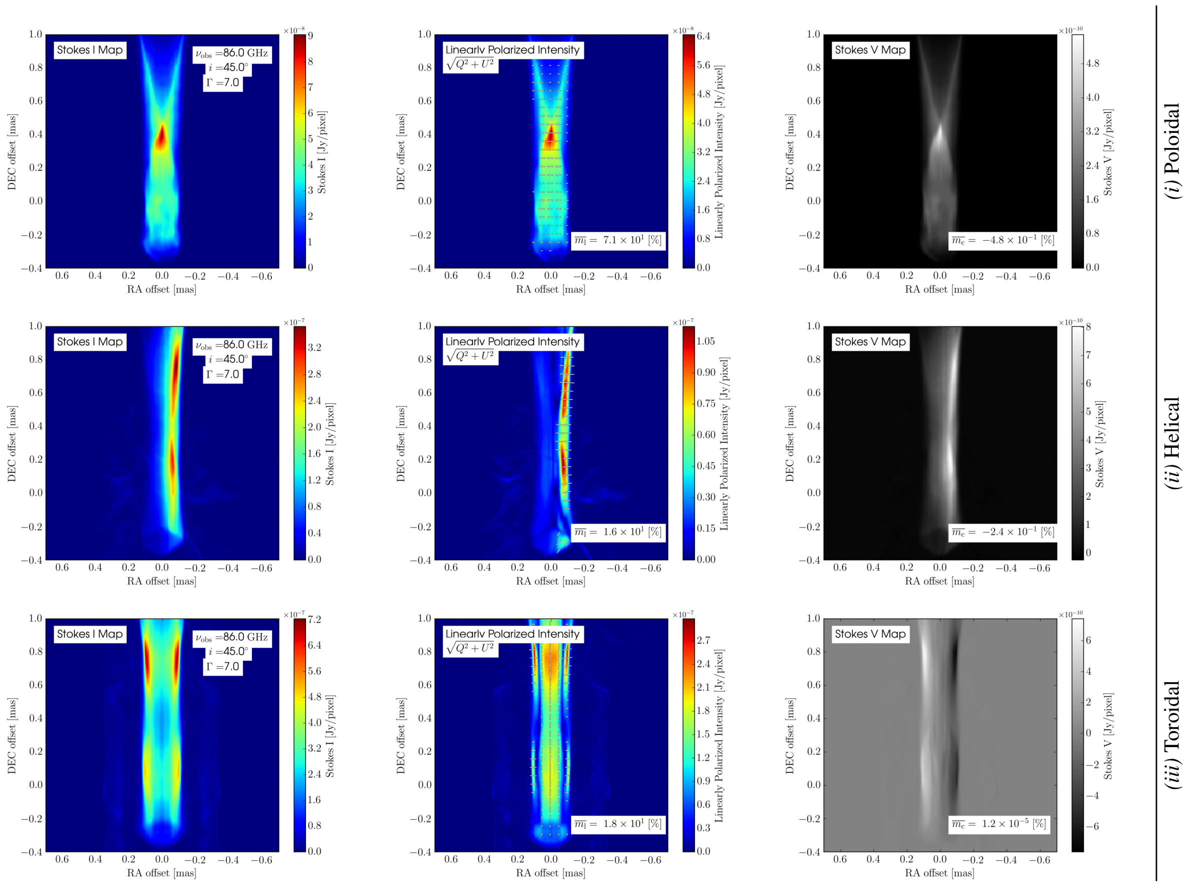

Fig. 3. Ray-traced images of our jet propagating from top to bottom in total intensity (*left column*), in linearly polarized intensity (*middle column*), and circular polarization (*right column*). The pictures illustrate similar epochs in the jet's evolution during each 3D RMHD simulation at 86 GHz. The jet carries a purely poloidal magnetic field (*top row*), a helical magnetic field (*middle row*), and a purely toroidal magnetic field (*bottom row*). Integrated values of the fractional linear and circular polarization are listed to the lower right in the middle and right columns. The purely toroidal field jet appears edge-brightened in contrast to the poloidal jet which is brightest along the spine.

consists of $320 \times 320 \times 400$ zones), we choose to view the source at a luminosity distance of 100 Mpc. The individual scaled cell size is 0.004 pc. All images in this paper are generated at an observing frequency of $\nu_{\rm obs} = 86$ GHz.

We visualize the polarized synchrotron emission of the jet for three different magnetic field morphologies, that is, purely poloidal, helical, and purely toroidal. To begin with, the images in Fig. 3 show the total intensity of the jet's emission in the left column, the linearly polarized intensity ($= \sqrt{Q^2 + U^2}$) including electric vector position angles (EVPAs $= 0.5 \arctan{[U/Q]}$) in the middle column, and the circular polarization in the right column. Moreover, the different rows represent the three magnetic

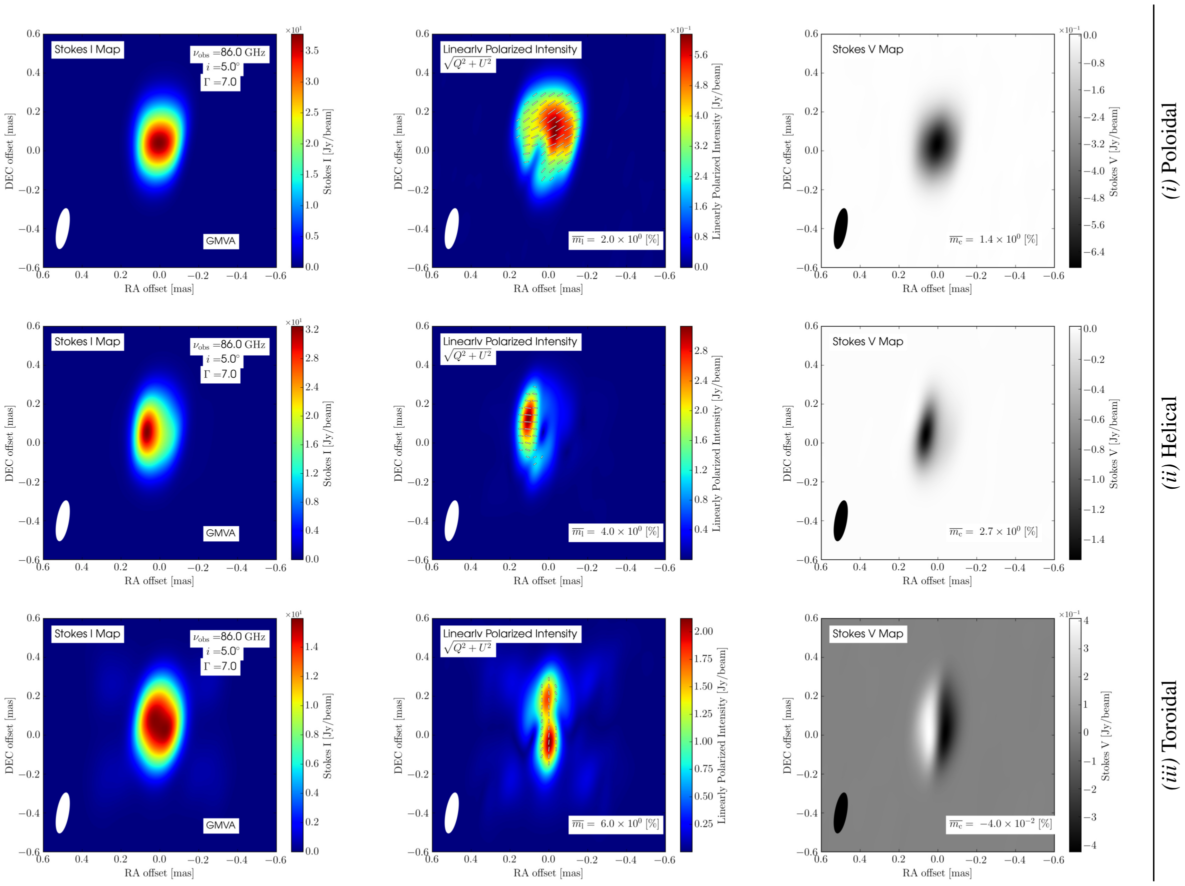

Fig. 4. Ray-traced images of RMHD jet simulations in total intensity (*left*), linearly polarized intensity (*middle*), and circular polarization (*right*) when each jet is viewed edge-on to the jet axis. The images highlight similar epochs in the jet's evolution during each 3D RMHD simulation at 86 GHz. The jet carries a purely poloidal magnetic field (*top row*), a helical magnetic field (*middle row*), and a purely toroidal magnetic field (*bottom row*). The ray-traced images are convolved with a Gaussian beam indicative of the resolution of the GMVA and with a Gaussian noise floor of 10^{-4} Jy beam^{-1}.

field morphologies introduced in Sect. 3.1. The top row depicts the poloidal magnetic field, the middle row the helical field, and the bottom row the purely toroidal magnetic field. All ray-traced images are viewed at 45° to the jet-axis in Fig. 3.

We can see that the emission for the purely poloidal magnetic field is concentrated in the inner part of the jet, and is brightest within the standing recollimation shock. The EVPAs, shown as white line segments in the middle column of Fig. 3, are predominantly perpendicular to the magnetic field orientation, in the ideal case. As the poloidal field is streaming in the direction of the jet, the EVPAs accurately convey the field orientation within our simulations. In addition, the circular polarization has only positive values, unlike the purely toroidal magnetic field.

The toroidal magnetic field (bottom row of Fig. 3) clearly produces emission that is centered along the edges of the jet, as we see an edge-brightened jet in all our images along the bottom row. In addition, we can see both positive and negative circular polarization highlighting the changing orientation of the jet's magnetic field with respect to our line of sight.

The helical magnetic field illustrated in the middle row in Fig. 3 exhibits a mixture of the emission and polarization morphologies present in the toroidal and poloidal cases. The emission is concentrated on the right side of the relativistic jet which stresses the structure of the helical magnetic field lines.

Additionally, we compute integrated levels of fractional polarization. These are flux-weighted averages of the Stokes parameters across the entire jet emission region in each set of images (listed to the lower right in the linearly polarized and circularly polarized images of Fig. 3, $\bar{m}_l \equiv \left(\bar{Q}^2+\bar{U}^2\right)^{1/2}/\bar{I}$ and $\bar{m}_c \equiv -\bar{V}/\bar{I}$). The fractional linear polarization decreases from the poloidal to the toroidal magnetic field model (from ~7.1% to ~1.8%) and drops for the helical magnetic field morphology (~1.6%). The fractional circular polarization also decreases from the poloidal to the helical magnetic field structure. The calculated value for the toroidal field jet changed sign and is several orders of magnitude smaller (from ~−4.8 × 10^{-1}% to ~1.2 × 10^{-5}%).

The images presented in Fig. 3 display a resolved RMHD jet observed at 45°. To further simulate the emission of a blazar radio core we: (i) alter the viewing angle to 5°, (ii) convolve our resultant images with a Gaussian beam indicative of the resolution of the GMVA, and (iii) mimic VLBI array sensitivity by introducing a Gaussian noise floor of 10^{-4} Jy beam^{-1}. This results in a dynamic range of ~1:100 000 in our synthetic

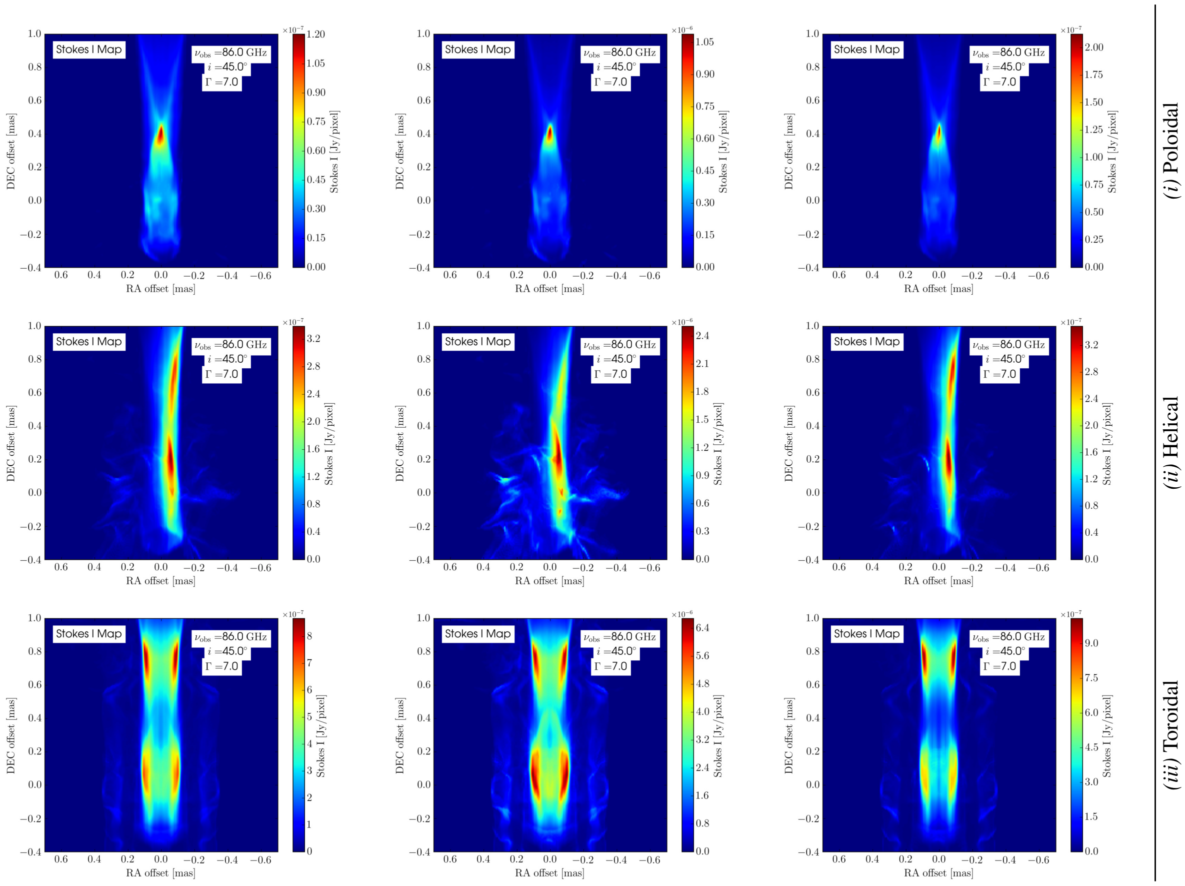

(1) $n_e(\gamma) \propto \rho$ (2) $n_e(\gamma) \propto p$ (3) $n_e(\gamma) \propto B^2$

Fig. 5. Total intensity maps of our 3D RMHD jet simulations using different electron scaling relations. The jet is viewed at $i = 45°$ and propagates from top to bottom in each frame. The images highlight similar epochs in the jet's evolution of each 3D RMHD simulation at 86 GHz. *From left to right*: proportionality of the NTEs to the fluid's density, internal energy density, and magnetic energy density. *From top to bottom*: purely poloidal magnetic field, helical magnetic field, and purely toroidal magnetic field.

images. Figure 4 shows the total intensity of the jet's emission in the left column, the linearly polarized intensity including EVPAs in the middle column, and the circular polarization in the right column. Again, the different rows represent the three magnetic field morphologies. The top row depicts purely poloidal magnetic field, the middle one the helical field, and the bottom one the purely toroidal magnetic field. All simulations are viewed edge-on to the jet axis in Fig. 4.

In total intensity, the poloidal field case exhibits a bright central radio core, whereas in contrast the helical and toroidal field cases exhibit emission peaks offset from the central shock. Also, the helical and toroidal field cases exhibit two signs in circular polarization whereas the poloidal field case exhibits only one. In all cases, the linear polarized emission peaks are offset from the total intensity peaks which is commonly seen in blazars.

Again, we computed integrated levels of fractional linear and circular polarization ($\bar{m}_l$ and $\bar{m}_c$, listed to the lower right in the linear polarization and circular polarization images of Fig. 4). In the case of $i = 5°$ and in contrast to the calculated values at 45°, the fractional linear polarization increases from the poloidal to the helical and then to the toroidal magnetic field model (from ~2.0% to ~6.0%). The fractional circular polarization decreases and changes sign from the poloidal to toroidal magnetic field model (from ~1.5% to ~-3.8×10^{-2}%). The fractional circular polarization peaks for the helical magnetic field at ~2.7%.

Here, the most striking result is that Figs. 3 and 4 demonstrate that resolved circular polarization imaging of relativistic jets can potentially be used to distinguish between a purely poloidal and a purely toroidal magnetic field configuration within standing or recollimation shocks.

4. Emission recipe study

4.1. Emission recipe prescriptions

We now shift our focus to better understanding the impact that different electron scaling relations have on the synchrotron polarization produced in our RMHD jet simulations. In particular, we explore three additional scaling relations to account for the jet's microphysics by adopting the methods presented in Porth et al. (2011). In particular, we set the NTEs energy distribution proportional to: (i) the fluid density, (ii) the thermal

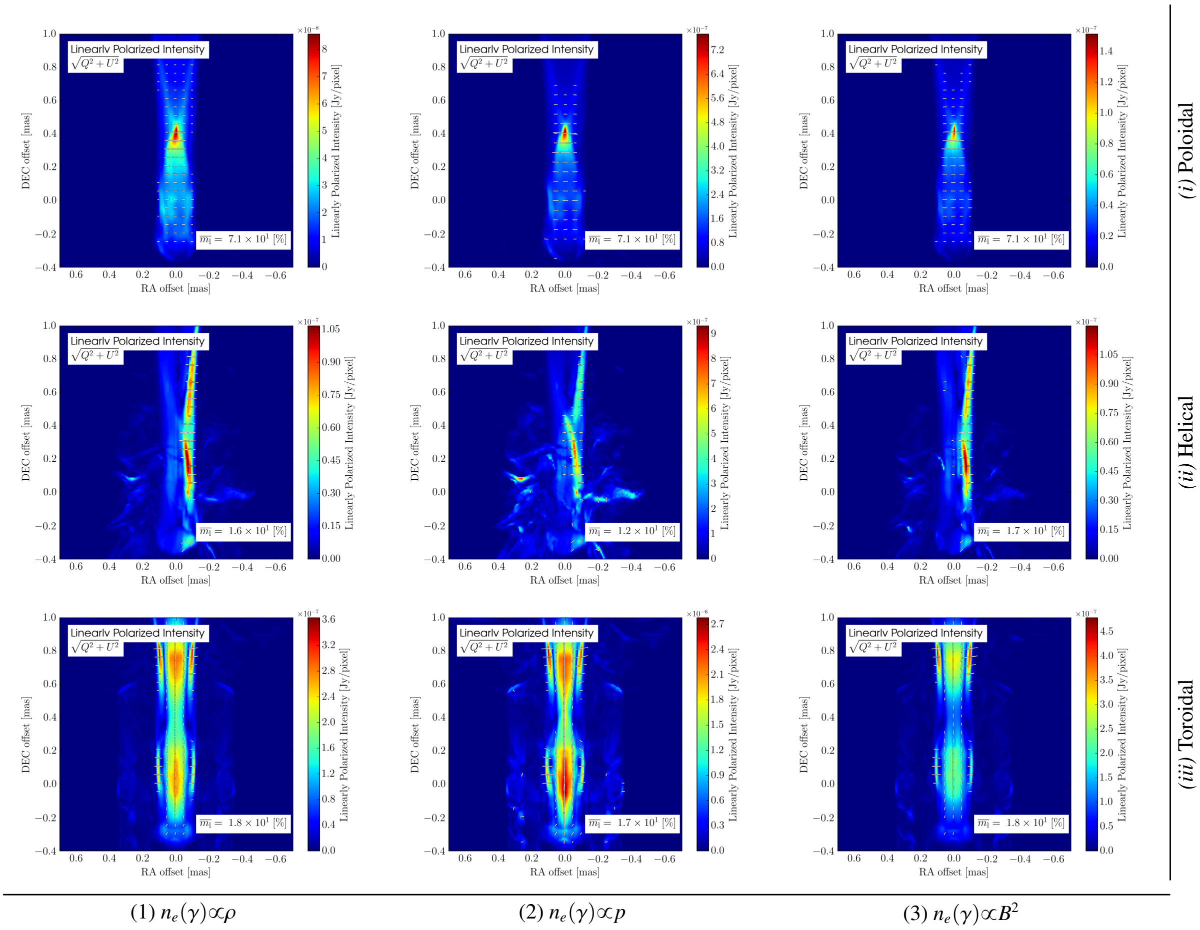

Fig. 6. Linearly polarized emission maps of our 3D RMHD jet simulations using different emission electron scaling relations. The jet is viewed at $i = 45°$ and propagates from top to bottom in each frame. The images highlight similar epochs in the jet's evolution during each 3D RMHD simulation at 86 GHz. *From left to right*: proportionality of the NTEs to the fluid's density, internal energy density, and magnetic energy density. *From top to bottom*: purely poloidal magnetic field, helical magnetic field, and purely toroidal magnetic field.

pressure, and (iii) the magnetic energy density:

$$\int_{\gamma_{\rm min}}^{\gamma_{\rm max}} {\rm d}\gamma n_{\rm e}(\gamma) = \frac{\rho}{m_{\rm p}},$$
$$\int_{\gamma_{\rm min}}^{\gamma_{\rm max}} {\rm d}\gamma n_{\rm e}(\gamma)\gamma m_{\rm e}c^2 = \frac{p}{(\hat{\gamma}-1)},$$
$$\int_{\gamma_{\rm min}}^{\gamma_{\rm max}} {\rm d}\gamma n_{\rm e}(\gamma)\gamma m_{\rm e}c^2 = \epsilon_B \frac{B^2}{8\pi\cdot(\hat{\gamma}-1)}. \quad (15)$$

In this treatment, we set the conversion factors $\zeta_{\rm e} = \epsilon_{\rm e} = \epsilon_B = 1$ (see Sect. 2.3), where ϵ_B is the equipartition fraction. Again, $n_{\rm e}(\gamma)$ takes the form of a power-law, see Eq. (7).

Instead of solving the terms in Eq. (15) for two unknowns, we assume fixed bounds for the electron power-law ($\gamma_{\rm min}$ and $\gamma_{\rm max}$). The lower cutoff for injected NTEs is set to $\gamma_{\rm min} = 10$ and the upper limit to $\gamma_{\rm max} = 10^6 \cdot \gamma_{\rm min}$ (see Eq. (7)).We solve each equation in Eq. (15) for n_0 as a function of either p, ρ, or B:

$$n_0 = \frac{\rho(1-s)}{m_{\rm p}\gamma_{\rm min}\left((10^6)^{1-s}-1\right)},$$
$$n_0 = \frac{p(2-s)}{(\hat{\gamma}-1)\,\gamma_{\rm min}^2 m_{\rm e}c^2\left((10^6)^{2-s}-1\right)},$$
$$n_0 = \frac{\epsilon_B B^2(2-s)}{8\pi\,(\hat{\gamma}-1)\,\gamma_{\rm min}^2 m_{\rm e}c^2\left((10^6)^{2-s}-1\right)}. \quad (16)$$

Again, we set the electron power-law index to $s = 2.3$ (hence $\alpha = 0.65$).

4.2. Results

Based on the solutions presented in Eq. (16) we generate synthetic maps of total intensity, linearly polarized intensity, circular polarization, and calculate integrated fractional levels of polarization. Figure 5 presents resolved total intensity images computed using the three emission recipes (see Eq. (15)). The top row illustrates the poloidal magnetic field, the middle row illustrates the helical field, and the bottom row illustrates the toroidal magnetic field. Here, we analyze the dependence on the electron scaling relations while viewing the jet at $i = 45°$. The left column shows images produced using the density scaling relation, the middle column shows images produced using the pressure scaling relation, and the right column shows images produced

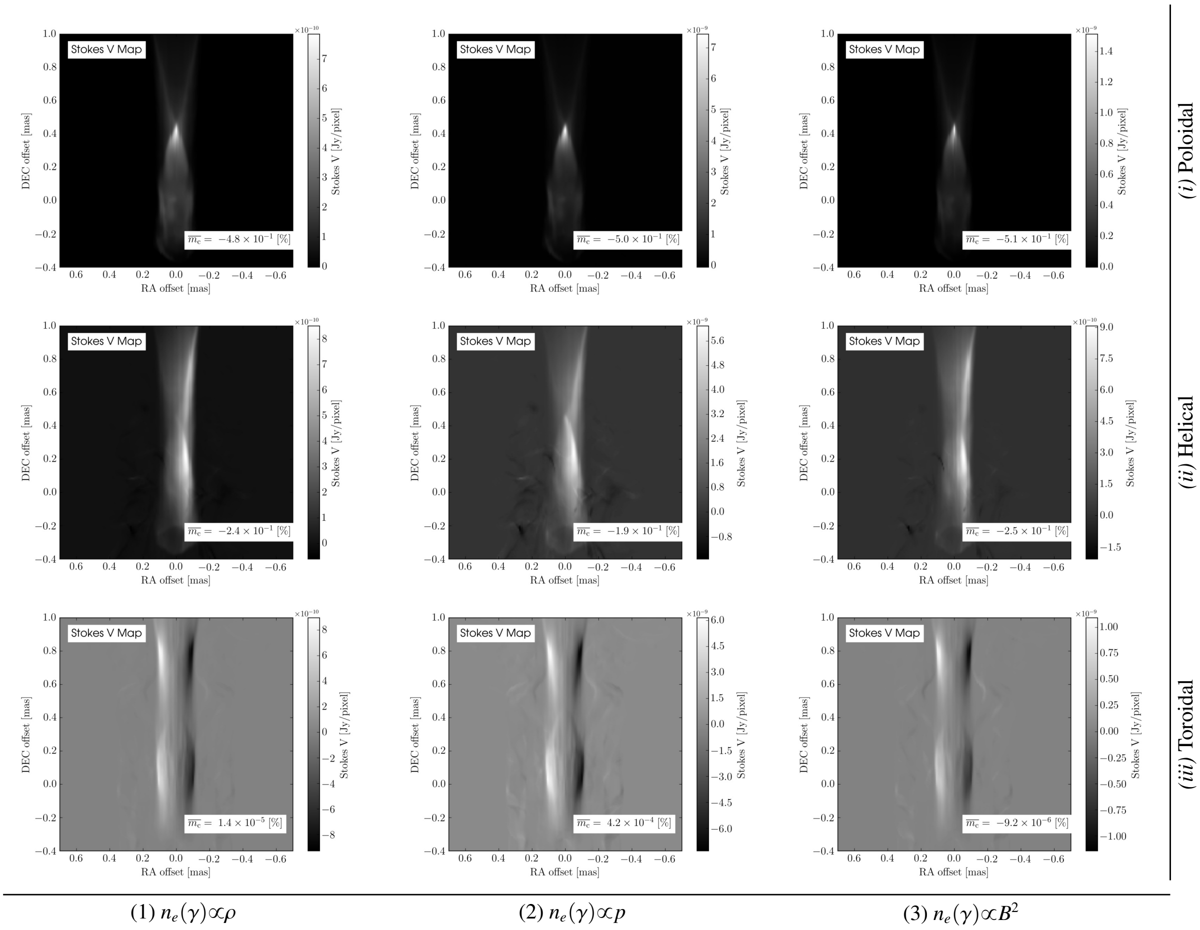

Fig. 7. Circular polarization maps of our 3D RMHD jet simulations using different emission electron scaling relations. The jet is viewed at $i = 45°$ and propagates from top to bottom in each frame. The images highlight similar epochs in the jet's evolution of each 3D RMHD simulation at 86 GHz. *From left to right*: proportionality of the NTEs to the fluid's density, internal energy density, and magnetic energy density. *From top to bottom*: purely poloidal magnetic field, helical magnetic field, and purely toroidal magnetic field.

using the magnetic energy density scaling relation. We see that the three different scaling relations do not have a drastic impact on the resultant jet emission when using a jet tracer to exclude the ambient medium. Similar to our findings in Sect. 3.2, we see an edge-brightened jet in the toroidal field case and a spine- or shock-brightened jet in the poloidal field case for all three electron scaling relations. Figure 6 shows the corresponding linear polarization maps with EVPAs overplotted. The EVPA orientations are similar to the orientations illustrated in Sect. 3.2.

Figure 7 shows the resulting circular polarization maps of the RMHD jet simulations for the three different electron scaling relations. The arrangement is the same as in Fig. 5. All three magnetic field morphologies again show only minor differences. The polarized synchrotron emission is focused in the center of the jet, highlighting the recollimation shock. The helical magnetic field exhibits positive circular polarization on the right side of the jet. For the toroidal magnetic field, the circular polarized emission shows positive values on the left part of the jet and negative values on the right (i.e., left- and right-handed). This is a reflection of the pitch angle present in the helical field case.

Figures 8 through 10 show the same sequence of images for each scaling relation except that the jets are now viewed at an inclination of $i = 5°$ to the jet axis. In particular, the proportionality to the thermal pressure, visible in the middle column of Fig. 9, highlights both the recollimation shock in the central region of the jet and the pressurized regions of the ambient plasma due to interactions with the surrounding medium.

The integrated levels of fractional linear and fractional circular polarization (shown to the lower right in Figs. 6, 7, 9, and 10) exhibit the same level and behavior as discussed in Sect. 3.2 and show no major dependency on the chosen electron scaling relation.

5. Electron emission scaling-relation variations

There are two additional variations of the electron emission scaling relations presented in Sect. 4. In the first variation, we exclude the use of a jet tracer (which is a PLUTO variable) and consider the impact the toroidal magnetic field morphology and various emission scaling relations have on the ray-traced image when including the surrounding ambient medium. In a second variation, we keep the jet tracer but replace the assumption of a constant lower cutoff in the electron power-law spectrum and instead compute $\gamma_{\min}$ as a function related to the thermal pressure and density.

A&A 656, A143 (2021)

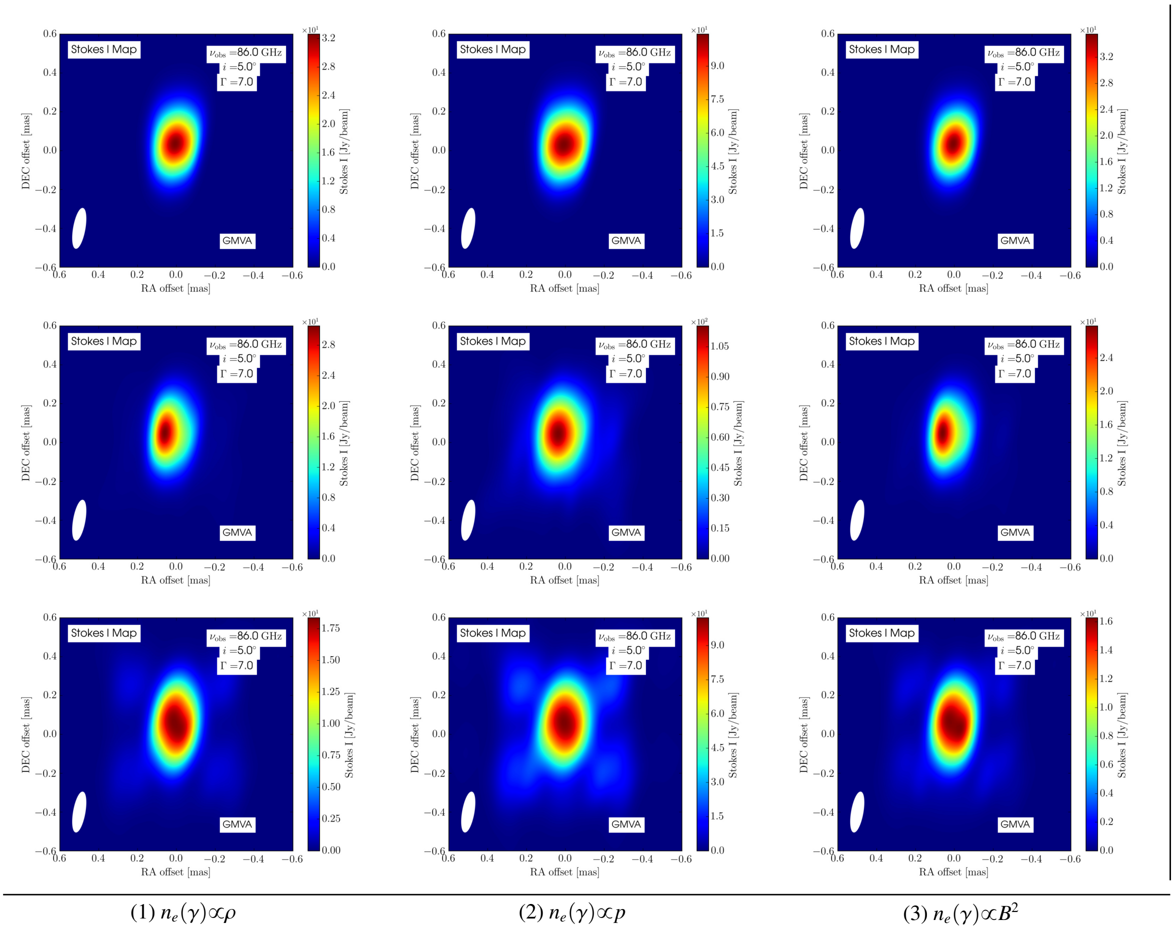

Fig. 8. Ray-tracing images of our jets in total intensity when each jet is viewed edge-on. The images highlight similar epochs in the jet's evolution during each 3D RMHD simulation at 86 GHz. *From left to right*: proportionality of the NTEs to the fluid's density, internal energy density, and magnetic energy density. *From top to bottom*: purely poloidal magnetic field, helical magnetic field, and purely toroidal magnetic field. The ray-traced images are convolved with a Gaussian beam indicative of the resolution of the GMVA and with a Gaussian noise floor of 10^{-4} Jy beam^{-1}.

5.1. No jet tracer

In contrast to Sect. 4.2, we no longer make use of a jet tracer to exclude the surrounding ambient medium in our ray-tracing images. Figure 11 highlights the resultant emission for the toroidal magnetic field case for the three electron scaling relations with the additional component of the ambient medium. For simplicity, we choose to show the total intensity where we see the most striking difference to the results presented in Sect. 4.2. As before, the left column shows images produced using the density scaling relation, the middle column shows images produced using the pressure scaling relation, and the right column shows images produced using the magnetic energy density scaling relation. In contrast to Sect. 4.2, we clearly see the impact of the various emission scaling relations on the jet emission when assuming a toroidal magnetic field morphology and including the ambient medium. The ambient medium is most visible for the density scaling relation and the jet structure itself is largely hidden behind the intervening ambient plasma (which is not radiatively cooled in our simulations). Clearly, the second two recipes (which are proportional to thermal pressure and magnetic energy density) are better at highlighting the jet through the intervening ambient plasma. A solution to the arbitrary use of a jet tracer, moving forward, will be to properly include the effects of synchrotron cooling and diffusive shock acceleration – this is planned for a future paper.

5.2. Lower cutoff for injected NTEs

In the second variation, we keep the jet tracer but instead compute the constant lower cutoff for injected NTEs ($\gamma_{\rm min} = 10$ for Sect. 4) with a prescription based on the ratio between thermal pressure and density (similar to Porth et al. 2011). In particular, we compute (cell-to-cell)

$$\gamma_{\rm min} = 1 + \frac{p}{2\rho c^2}\frac{m_{\rm p}}{m_{\rm c}}. \tag{17}$$

Figure 12 shows the resulting jet emission in total intensity. The arrangement is the same as in Fig. 11. The proportionality to (i) the density, (ii) pressure, and (iii) magnetic energy density does not show any major differences when compared with the lower panels of Fig. 5 (in which we set $\gamma_{\rm min} = 10$). The jet remains edge-brightened for the toroidal magnetic field as seen in Sect. 4.2.

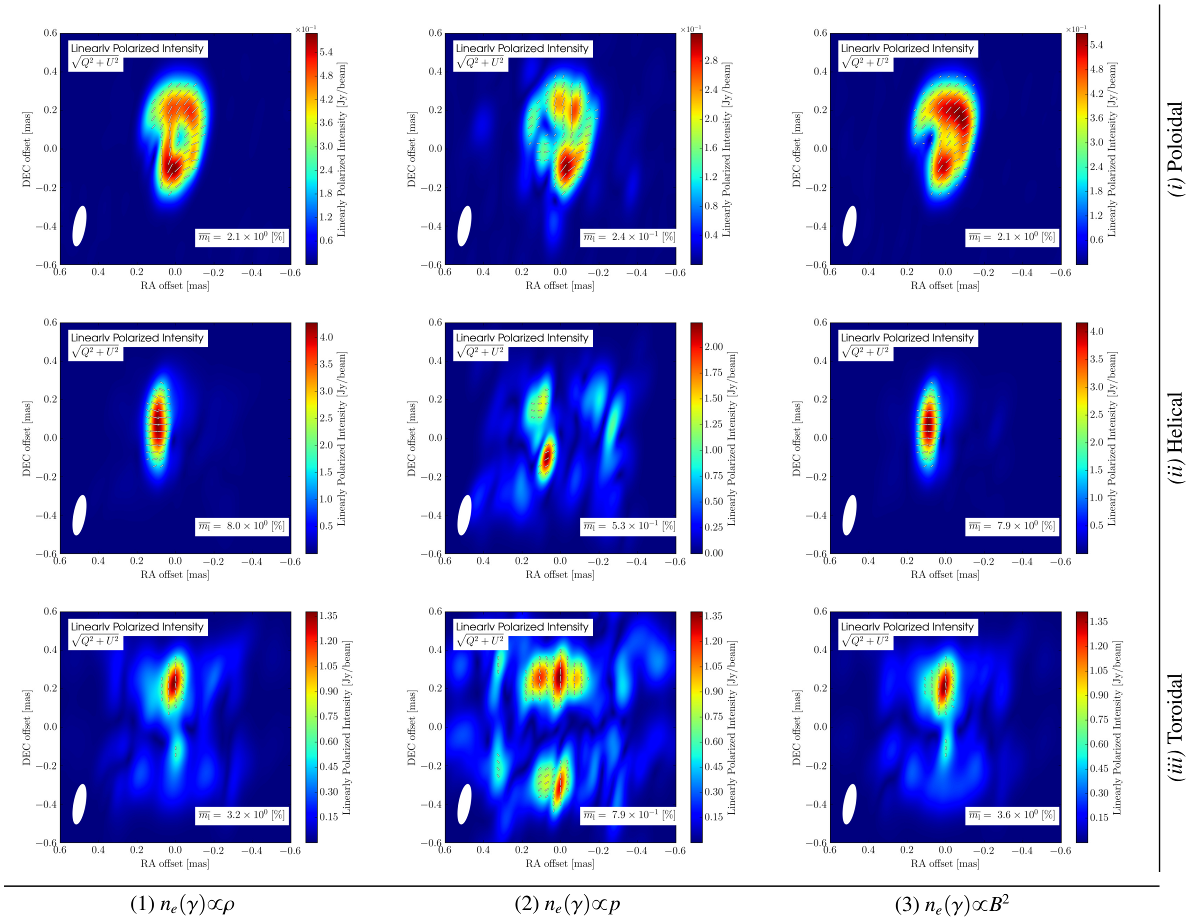

Fig. 9. Ray-tracing images of our jets in linearly polarized intensity when each jet is viewed edge-on. The images highlight similar epochs in the jet's evolution during each 3D RMHD simulation at 86 GHz. *From left to right*: proportionality of the NTEs to the fluid's density, internal energy density, and magnetic energy density. *From top to bottom*: purely poloidal magnetic field, helical magnetic field, and purely toroidal magnetic field. The ray-traced images are convolved with a Gaussian beam indicative of the resolution of the GMVA and with a Gaussian noise floor of 10^{-4} Jy beam^{-1}.

6. Discussion

A wealth of new polarimetric data has been amassed for relativistic jets over the last decade, namely maps of AGN in both linearly polarized intensity and circular polarization, maps of Faraday RM gradients along the jet, and analysis of EVPA orientation along the jet, all of which help to probe the underlying magnetic field geometry. In this section, we make further comparisons between our ray-traced emission maps and observations in order to better understand and interpret the different polarimetric features we observe in our simulations.

Faraday RM gradients observed transverse to the jet axis hint at the existence of helical magnetic fields (e.g., in 0133+479, see Gabuzda 2018; Gabuzda et al. 2018). In a future work, we plan to experiment with generating synthetic RM maps of our three jet simulations to explore the robustness of RM as a metric of the jet's internal magnetic field structure.

Helical or toroidal magnetic field morphologies have been invoked to explain an increase in linear polarization towards the edges of the jet (Pushkarev et al. 2005; Lyutikov et al. 2005). This edge-brightened emission morphology is clearly seen in our simulations.

As discussed in Gabuzda (2018), a purely toroidal magnetic field should result in symmetric edge-brightened emission across the jet, whereas in contrast a helical magnetic field should result in asymmetric emission along the jet edges. These distinct emission morphologies are present within our simulations (see, e.g., Fig. 3).

In our poloidal field simulation the jet spine or shock dominates the emission. This emission morphology has been observed in the jet of NGC 1052 (Baczko 2020). In contrast, in the helical and toroidal field simulations the outer sheath is edge-brightened and dominates the emission. This emission morphology has been observed in the jet of 3C 84 (see, e.g., Giovannini et al. 2018; Kim et al. 2019; Paraschos et al. 2021).

Bi-modal EVPA patterns have been observed in a number of jets (O'Sullivan & Gabuzda 2009) in which the EVPAs preferentially align with the jet axis in the spine and, in contrast, appear predominantly perpendicular to the jet axis in the sheath. We see this bi-modal pattern in our toroidal field simulation (see, e.g., lower middle panel of Fig. 3).

The majority of blazars in which CP is detected tend to exhibit one sign/handedness of circular polarization (see, e.g.,

A&A 656, A143 (2021)

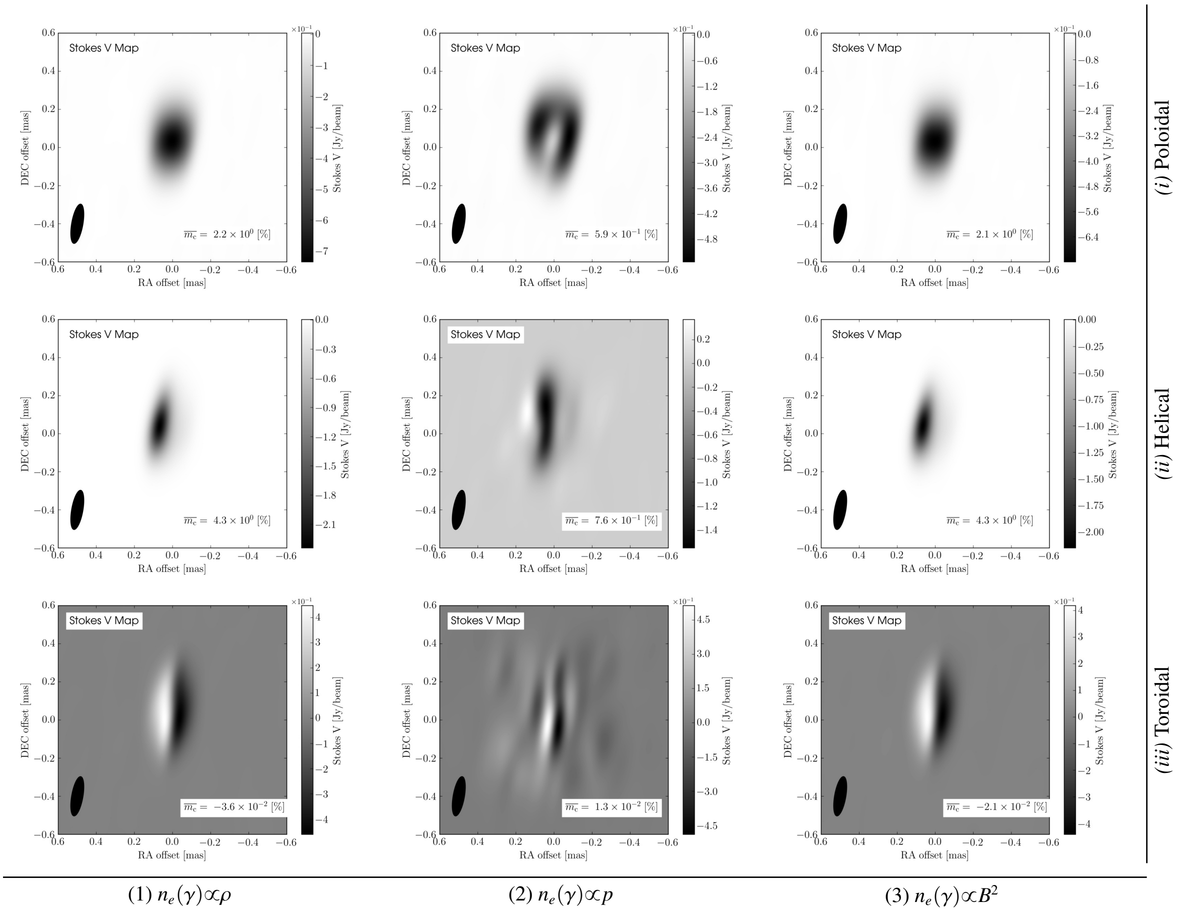

Fig. 10. Ray-tracing images of our jets in circular polarization when each jet is viewed edge-on. The images highlight similar epochs in the jet's evolution during each 3D RMHD simulation at 86 GHz. *From left to right*: proportionality of the NTEs to the fluid's density, internal energy density, and magnetic energy density. *From top to bottom*: purely poloidal magnetic field, helical magnetic field, and purely toroidal magnetic field. The ray-traced images are convolved with a Gaussian beam indicative of the resolution of the GMVA and with a Gaussian noise floor of 10^{-4} Jy beam^{-1}.

Homan & Lister 2006; Homan & Wardle 2004). However, a small number of sources exhibit both negative and positive CP in the radio core region (see, e.g., Vitrishchak et al. 2008). As illustrated in the right column of Fig. 4, we find that a poloidal field produces only one sign of CP in the radio core, whereas in contrast the toroidal field produces both signs of CP in the core. This highlights the potential of combining linear and circular polarization maps to make a more robust determination of the magnetic field orientation within the jet.

7. Conclusion

We carried out a systematic survey of full Stokes radiative transfer calculations, exploring the effects of (i) the jet's magnetic field morphology and (ii) the various electron scaling relations on the resultant linear and circular polarized emission. Our findings can be summarized as follows.

- Resolved circular polarization imaging has the potential to discriminate between a purely poloidal or a purely toroidal magnetic field morphology within the jet.
- When the jet is resolved (i.e., Fig. 3), toroidal magnetic fields result in edge-brightened jets whereas poloidal magnetic fields seem to highlight the jet spine or recollimation shock.
- The integrated levels of fractional linear $\bar{m}_{\rm l}$ and circular polarization $\bar{m}_{\rm c}$ are only mildly sensitive to the choice of electron scaling relation. However, the integrated fractional circular polarization of the toroidal jet is found to be several orders of magnitude smaller than the poloidal and helical jets.
- Scaling the electron number density to the thermal (fluid) density ρ, pressure p, or magnetic energy density B^2 while fixing the bounds of the electron power-law distribution ($\gamma_{\rm min}$ and $\gamma_{\rm max}$) does not seem to have an appreciable effect on the morphology of the linear and circular polarized emission within the shock when the ambient medium is excluded from the ray-tracing. However, when the ambient medium is included, the magnetic energy density recipe best highlights the jet emission through the intervening plasma.

In an effort to further compare simulations to observations, our numerical RMHD jet models have formed the basis of an accepted VLBA proposal to conduct deep full Stokes imaging of a number of blazar jets. This will allow us to make further comparisons between our numerical models and CP observations in an attempt to better understand the nature of the intrinsic

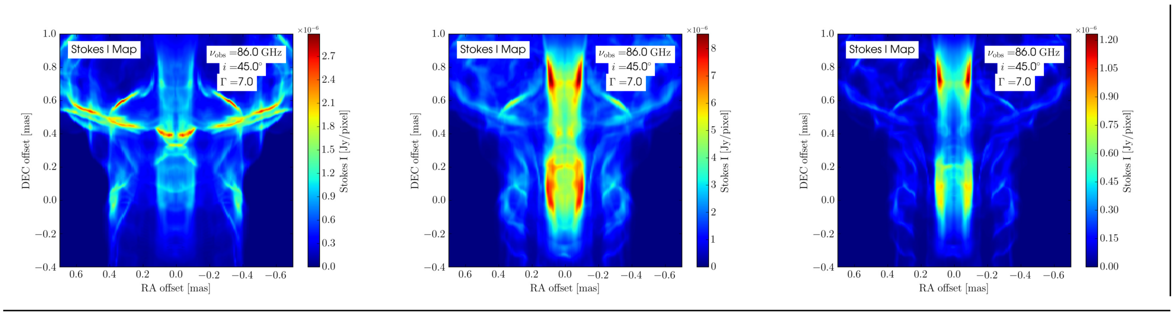

(1) $n\ (\gamma) \propto \rho$ (2) $n\ (\gamma) \propto p$ (3) $n\ (\gamma) \propto B^2$

Fig. 11. Total intensity maps of our 3D RMHD jet simulations using different electron scaling relations and a purely toroidal magnetic field morphology. The images highlight similar epochs in the jet's evolution during each 3D RMHD simulation at 86 GHz. The images, in contrast to Fig. 5, are generated without the use of a jet tracer and illustrate both the emission of the ambient medium and the hidden jet structure. The jet is viewed at $i = 45°$ and propagates from top to bottom in each frame. *From left to right*: proportionality of the NTEs to the fluid's density, internal energy density, and magnetic energy density.

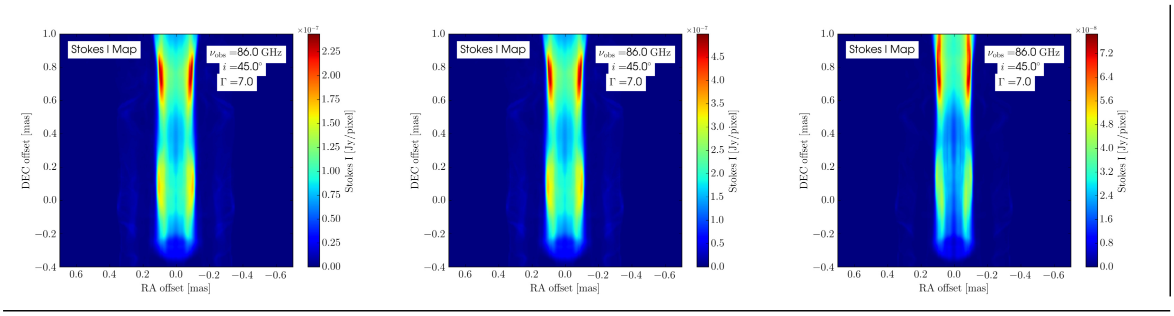

(1) $n_e(\gamma) \propto \rho$ (2) $n_e(\gamma) \propto p$ (3) $n_e(\gamma) \propto B^2$

Fig. 12. Total intensity maps of our 3D RMHD jet simulations using different electron scaling relations and a purely toroidal magnetic field morphology. The images highlight similar epochs in the jet's evolution during each 3D RMHD simulation at 86 GHz. The images are created with a jet tracer which excludes the obscuring ambient medium. The images are comparable to the lower panels of Fig. 5 in which, in contrast to computing $\gamma_{\rm min}$ from the ratio of pressure to density, it is fixed to 10. The jet is viewed at $i = 45°$ and propagates from top to bottom in each frame. *From left to right*: proportionality of the NTEs to the fluid's density, internal energy density, and magnetic energy density. The jet structure does not show considerable differences although the jet is most edge-brightened for the most right proportionality.

magnetic field morphologies of relativistic jets. In the future, we plan to incorporate the effects of synchrotron cooling and diffusive shock acceleration in our ray-tracing calculations (see, e.g., Vaidya et al. 2018).

Acknowledgements. This research was supported through a PhD grant from the International Max Planck Research School (IMPRS) for Astronomy and Astrophysics at the Universities of Bonn and Cologne. The three-dimensional jet simulations presented in this paper are computed with the PLUTO code. The ray-tracing software RADMC-3D produced the polarized images of the synchrotron emission. The authors are grateful to E. Ros for feedback regarding VLBI, M. Perucho for helpful discussions on the physics of RMHD jet simulations, and to the referee, P. Hughes, for a thorough review of this manuscript.

References

Baczko, A. K. 2020, PhD Thesis, Max-Planck-Institute for Radioastronomy, Germany
Blandford, R. D., & Payne, D. G. 1982, MNRAS, 199, 883
Blandford, R. D., & Znajek, R. L. 1977, MNRAS, 179, 433
Daly, R. A., & Marscher, A. P. 1988, ApJ, 334, 539
Dullemond, C. P., Juhasz, A., Pohl, A., et al. 2012, Astrophysics Source Code Library [record ascl:1202.015]
Fromm, C. M., Ros, E., Perucho, M., et al. 2013, A&A, 557, A105
Fromm, C. M., Perucho, M., Mimica, P., & Ros, E. 2016, A&A, 588, A101
Gabuzda, D. 2018, Galaxies, 6, 9
Gabuzda, D. C. 2018, Proc. Int. Astron. Union, 14, 189
Gabuzda, D. C., Vitrishchak, V. M., Mahmud, M., & O'Sullivan, S. 2008, ASP Conf. Ser., 386, 444
Gabuzda, D. C., Nagle, M., & Roche, N. 2018, A&A, 612, A67
Giovannini, G., Savolainen, T., Orienti, M., et al. 2018, Nat. Astron., 2, 472
Guo, F., Liu, Y.-H., Daughton, W., & Li, H. 2015, ApJ, 806, 167
Guo, F., Li, X., Daughton, W., et al. 2019, ApJ, 879, L23
Hardee, P., Mizuno, Y., & Nishikawa, K.-I. 2007, Astrophys. Space Sci., 311, 281
Hawley, J. F., Fendt, C., Hardcastle, M., Nokhrina, E., & Tchekhovskoy, A. 2015, Space Sci. Rev., 191, 441
Homan, D. C., & Lister, M. L. 2006, AJ, 131, 1262
Homan, D. C., & Wardle, J. F. C. 2004, ApJ, 602, L13
Jones, T. W., & Odell, S. L. 1977, A&A, 61, 291
Kadowaki, L. H. S., de Gouveia Dal Pino, E. M., Medina-Torrejón, T. E., Mizuno, Y., & Kushwaha, P. 2021, ApJ, 912, 109
Kim, J. Y., Krichbaum, T. P., Marscher, A. P., et al. 2019, A&A, 622, A196
Lyutikov, M., Pariev, V. I., & Gabuzda, D. C. 2005, MNRAS, 360, 869
MacDonald, N. R., & Marscher, A. P. 2018, ApJ, 862, 58
Martí, J. M., Mueller, E., Font, J. A., Ibánez, J. M., & Marquina, A. 1997, ApJ, 479, 151
Matthews, J. H., Bell, A. R., & Blundell, K. M. 2020, New Astron. Rev., 89, 101543
Mignone, A., & Bodo, G. 2006, MNRAS, 368, 1040
Mignone, A., Plewa, T., & Bodo, G. 2005, ApJS, 160, 199
Mignone, A., Bodo, G., Massaglia, S., et al. 2007, ApJS, 170, 228
Mignone, A., Ugliano, M., & Bodo, G. 2009, MNRAS, 393, 1141

Mimica, P., Giannios, D., Metzger, B., & Aloy, M. A. 2012, EPJ Web Conf., 39, 04003
Nishikawa, K.-I., Mizuno, Y., Gómez, J., et al. 2019, Galaxies, 7, 29
Ojha, R., Kadler, M., Boeck, M., et al. 2010, ArXiv e-prints [arXiv:1006.2097]
O'Sullivan, S. P., & Gabuzda, D. C. 2009, MNRAS, 393, 429
Paraschos, G. F., Kim, J. Y., Krichbaum, T. P., & Zensus, J. A. 2021, A&A, 650, L18
Porth, O., Fendt, C., Meliani, Z., & Vaidya, B. 2011, ApJ, 737, 42
Pushkarev, A. B., Gabuzda, D. C., Vetukhnovskaya, Y. N., & Yakimov, V. E. 2005, MNRAS, 356, 859
Singh, C. B., Mizuno, Y., & de Gouveia Dal Pino, E. M. 2016, ApJ, 824, 48
Sironi, L., & Spitkovsky, A. 2014, ApJ, 783, L21
Sironi, L., Rowan, M. E., & Narayan, R. 2021, ApJ, 907, L44
Striani, E., Mignone, A., Vaidya, B., Bodo, G., & Ferrari, A. 2016, MNRAS, 462, 2970
Troja, E., Lipunov, V. M., Mundell, C. G., et al. 2017, Nature, 547, 425
Vaidya, B., Mignone, A., Bodo, G., Rossi, P., & Massaglia, S. 2018, ApJ, 865, 144
Vitrishchak, V. M., Gabuzda, D. C., Algaba, J. C., et al. 2008, MNRAS, 391, 124
Werner, G. R., Uzdensky, D. A., Cerutti, B., Nalewajko, K., & Begelman, M. C. 2016, ApJ, 816, L8

Appendix A: Persistence of the injected magnetic field morphology

The underlying magnetic field included in the RMHD jet simulations exhibits distinct characteristics for each simulation (i.e., poloidal, helical, toroidal). We implement a poloidal component (B_z, see Eq. 14) and toroidal components (B_x and B_y, see Eq. 12). The magnetization parameters (σ_z and σ_ϕ - see Section 3.1) set the overall morphology of the field (i.e., by varying the ratio between the poloidal and toroidal components).

Figure A.1 illustrates how the magnetic field morphologies injected at the jet orifice persist down the jet. The left column shows 2D slices through the midplane of each simulation with the color scheme highlighting the component of the magnetic field (B_y) which is perpendicular to the jet axis. In contrast, the right column shows 2D slices through the jet's midplane (see dashed line in left column), respectively, with the color scheme highlighting the component of the magnetic field (B_z) which is parallel to the jet direction. The upper, middle, and lower rows correspond to the poloidal, helical, and toroidal field simulations, respectively.

The slices presented in Fig. A.1 are made through the same simulation epochs used in our ray-tracing calculations above. Despite the existence of turbulent eddies and jet shear along each jet axis, the injected magnetic field morphologies largely persist down the jet (be it poloidal, helical, or toroidal).

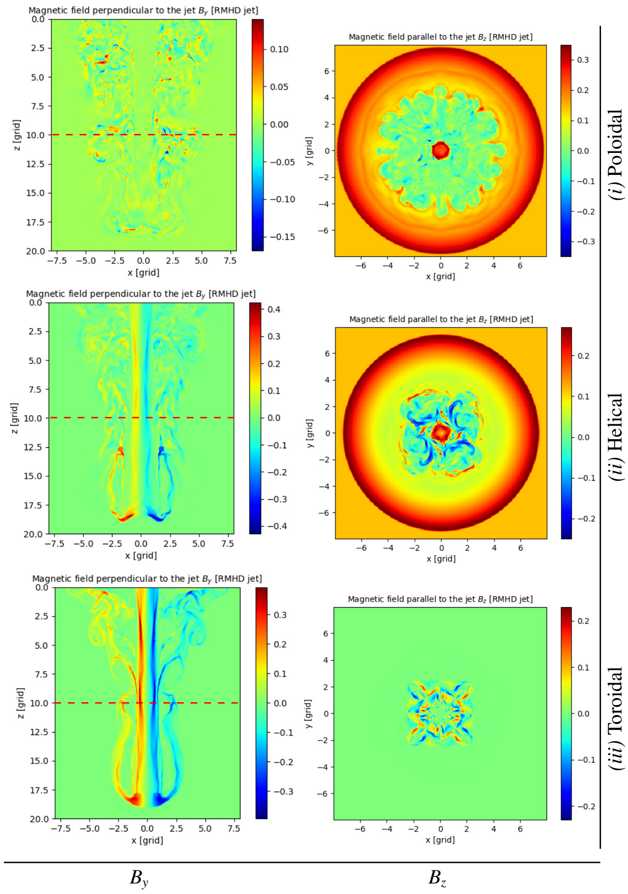

Fig. A.1. 2D slices through our 3D RMHD jets and are color coded according to the magnetic field component perpendicular to the jet axis – B_y (left column), and the field component parallel to the jet axis – B_z (right column) through the jet's midplane (see dashed line in the left column). From top to bottom: Poloidal, helical, and toroidal magnetic field simulations.

6 Probing circular polarization and magnetic field structure in AGN

This chapter contains the manuscript AA/2023/47707 of an observational study submitted to Astronomy and Astrophysics.

The MOJAVE program[1] conducted observations of over four hundred AGN jets using the Very Long Baseline Array from 1996 to 2016. From this extensive dataset, several conclusions were drawn: jets tend to exhibit an increasing fractional polarization with core separation and toward the edges of the jet; about 40 % of jet cores have a preferred and robust electric vector position angle (EVPA) rotation across different epochs; and BL Lac jets (along with their radio cores) exhibit more stable EVPAs than quasars, with the EVPAs tending to align with the initial jet direction (Pushkarev et al., 2017).

Within the MOJAVE program, faint circular polarization was also observed in some jets at levels ranging from 0.3 % to 0.7 % (Homan and Lister, 2006). Notably, quasar like 3C 279 displayed high percent levels of fractional circular polarization in the radio core. A full Stokes analysis of 3C 279 made use of radiative transfer to constrain the magnetic field and particle properties (Homan et al., 2009). Similarly, Kramer and MacDonald, 2021, presented in Chapter 5, conducted simulations of jets with fixed proton-to-positron ratios in the jet plasma and investigated the effects of various magnetic field morphologies within the relativistic jet.

The three dimensional RMHD models within Kramer and MacDonald, 2021, clearly predict that circular polarization serves as a powerful diagnostic of both plasma composition and magnetic field morphology. Specific sources like 0528+134 (negative circular polarization), 1241−072 (positive sign), and 2136+141 (switch in sign for circular polarization) exhibit morphologies consistent with those observed in the RMHD jet simulations. Further observations are required to confirm the persistence of these circular polarization morphologies in the core regions of various sources since 2007 at 15 GHz and to probe the magnetic field morphology of each jet, as demonstrated in studies by, for instance, Thum et al., 2017, on 2506−2520 at 86 GHz.

[1] For information and a detailed listing visit the MOJAVE Website.

For this following submitted manuscript, a 24-hour VLBA observation for nine target source and nine calibrator sources was granted with priority A (ranked with 1.18) and observed in January 2022. The main scientific objective is to examine whether the RMHD models (see Chapter 5 in this thesis) accurately predict a relationship between EVPA orientation and the sign of circular polarization, as indicated in the 15 GHz maps. The analysis within the thesis required observations of nine target sources with the VLBI at two distinct frequencies. The initial frequency of 15 GHz is essential for identifying and testing the resilience of the polarized structures, while the second frequency, 23 GHz, achieves a suitable compromise between sensitivity and resolution. A comparison of the 15 GHz maps reconstructed within the following manuscript and archival data leads to a confirmation of the robustness of EVPAs, indicating a consistent magnetic field morphology in the VLBI radio core over time. A switch in the circular polarization sign, indicating left-handed or right-handed circular polarization, is observed when moving from 15 GHz to 23 GHz. This has been observed in previous studies (Vitrishchak et al., 2008) and is confirmed within the manuscript. A preferred magnetic field orientation for each blazar source is concluded for both the VLBI radio core and the extended jet emission.

I am the principal investigator for the data proposed and observed in this work. The VLBA proposal has been accepted in 2021, and the requested data has been observed in January 2022. I perform the calibration in total intensity (Stokes I) and polarization (Stokes U and Q) with the calibration software `AIPS`. The 15 GHz and 23 GHz maps are created with the automatized pipeline `DoG-Hit` in close collaboration with the developer H. Mueller (Müller and Lobanov, 2022; Müller and Lobanov, 2023a). The writing of the manuscript is shared-work between myself and the co-authors of the manuscript (for the introduction and methodology) of which I am the leading author. The manuscript is finalized with comments and extensive discussions from all co-authors. The manuscript is submitted for publication to Astronomy & Astrophysics.

Astronomy & Astrophysics manuscript no. output
August 11, 2023

Probing circular polarization and magnetic field structure in AGN

Joana A. Kramer[1,*], Hendrik Müller[1], Jan Röder[1], and Eduardo Ros[1]

[1]Max-Planck-Institut für Radioastronomie, Auf dem Hügel 69, D- 53121 Bonn, Germany
*e-mail: jkramer@mpifr-bonn.mpg.de

August 11, 2023

ABSTRACT

Context. The composition and magnetic field morphology of relativistic jets can be studied with circular polarization (CP). Recent 3D relativistic magnetohydrodynamic (RMHD) simulations coupled with radiative transfer calculations make strong predictions about the level (and morphology) of the jet's CP emission. These simulations show that the sign of CP and the electric vector position angle (EVPA) are both sensitive to the jet's magnetic field morphology within the radio core.
Aims. We probe this theory by exploring whether the jet's radio core EVPA orientation is consistent with the observed sign of the core CP in deep full-track polarimetric observations. Based on a selection of sources from earlier MOJAVE observations, we aim to probe the nature of linear polarization and CP in the innermost regions of jets from a small sample of nine blazars. This sample includes sources that have exhibited: (i) positive CP, (ii) negative CP, or (iii) positive & negative CP simultaneously in the radio core region. By coupling deep polarimetric observations of a carefully selected sample of blazars with state-of-the-art RMHD/radiative transfer calculations we hope to gain a deeper understanding of the physics of blazar jets.
Methods. Nine blazar sources were observed using the VLBA at both 15 GHz and 23 GHz. Standard AIPS calibration was applied. Our self-calibration relies on a physically based model applied in `DoG-HiT` resulting in more accurate gains. We consider the compact Stokes *V* structure, too, instead of assuming it to be zero, which is crucial given the significant circular polarization fraction observed at long baselines. To improve imaging quality, we use specialized algorithms like `DoG-HiT` that excel in handling compact emission.
Results. We observe robust, relatively high degrees of fractional circular polarization up to $m_c = 1.8\,\%$ at 15 GHz and $m_c = -3.8\,\%$ at 23 GHz. We observe consistent polarized structure and EVPA orientation over time when comparing our analysis with archival MOJAVE data. Theoretical predictions indicate a clear favored magnetic field orientation within the extended jet emission of the reconstructed signal of the blazar 0149+218. At 23 GHz, the jet structures of 1127–145 and 0528+134, even in superresolution, exhibit characteristics aligned with helical or poloidal magnetic nature. Changes in CP sign as frequency transitions from 15 GHz to 23 GHz suggest the influence of optical depth effects.

Key words. polarization – magnetic field morphology – active galactic nuclei – jets – radio emission - electric vector position angle

1. Introduction

Supermassive black holes (SMBH) in the centers of galaxies are some of the most prominent emitters of high-energy radiation in the universe. Such objects, known as active galactic nuclei (AGN), are driven by the accretion of matter onto their central SMBH. Their emission spans across the entire electromagnetic spectrum, from radio to gamma ray energies, although only about 10 % are referred to as 'radio-loud' AGN (Kellermann et al. 1989).

When matter is accreted onto a BH, highly collimated plasma, called jets, outflows form along its polar axis. Such jets are mostly visible (and studied) at radio wavelengths, identified as non-thermal synchrotron radiation, emitted by charged particles spiralling around magnetic field lines at relativistic speeds. Synchrotron radiation has the potential to be significantly linearly polarized, reaching up to 75 % in the presence of a uniform magnetic field (Pacholczyk 1970; Troja et al. 2017). Linear polarization (LP) observations can provide valuable information about the orientation and morphology of the magnetic field structure within the synchrotron-emitting source. In addition, LP observations provide valuable information about the distribution of thermal electrons and the geometry of the magnetic field in the immediate vicinity of the AGN.

Polarization in AGN was first discovered in the optical regime (e. g. Heeschen 1973) and soon also at millimeter wavelengths (e. g. Kinman & Conklin 1971; Rudnick et al. 1978). In the late 1960s, very long baseline interferometry (VLBI) was applied for high angular resolution studies. The first *polarized* VLBI images were published in the mid-1980s (Cotton et al. 1984; Roberts & Wardle 1986). To this day, VLBI imaging allows us to observe, resolve, and study polarized radiation emitted from both in the innermost regions of AGN (e. g., Event Horizon Telescope Collaboration et al. 2021; Issaoun et al. 2022; Jorstad et al. 2023) and their relativistic jets on the kilo-parsec (kpc) scale (e. g., MacDonald et al. 2017; Hodge et al. 2018; Zobnina et al. 2023; Pushkarev et al. 2023).

LP is commonly expressed in terms of the electric vector position angle (EVPA) in a VLBI image, or as the fractional polarization in some area of the jet with respect to the total intensity peak. Since the EVPA is predicted to be perpendicular to the local magnetic field, polarized images help us to understand the magnetic field geometry in the source. For example, extended jets up to kilo-parsecs tend to show EVPAs perpendicular to the direction of jet motion, indicating a poloidal or helical magnetic field. In turn, if the EVPAs are oriented parallel to the jet, the magnetic field is toroidal, a characteristic of shock compression (Contopoulos et al. 2015). A bi-modal EVPA pattern with a difference between the jet spine and sheath is indicated in theoretical models of 3D RMHD jet simulations (Kramer & MacDonald 2021).

Only the smallest fraction of the observed emission is circularly polarized (CP, Stokes *V*); in fact, the CP fraction only rarely even reaches 1 % and usually falls well below that (Wardle 2021). Nonetheless, the use of the Very-Long-Baseline Array (VLBA) has enabled the analysis of circular polarization in extragalactic jets with exceptional precision, operating at sub-milliarcsecond resolution. Pioneering studies by Wardle et al. (1998) and Homan & Wardle (1999) revealed circular polarization in the central regions of four robust AGN jets, exhibiting local fractional levels ranging from 0.3 % to 1 % of Stokes *I* when observed with the VLBA.

Circular polarization has subsequently been identified in other AGN jets using different instruments, as documented by Rayner et al. (2000), Homan & Lister (2006), and Vitrishchak et al. (2008). The observed CP is thought to originate either from intrinsic synchrotron processes, or from LP converted to CP by Faraday rotation (e. g., MacDonald 2017). CP in AGN jets is a powerful tool for probing the particle composition and magnetic field morphology both at large scales and near the launching site. The first detection of CP in AGN jets was reported in the late 1990s in VLBI observations of the quasar 3C 279 (Wardle et al. 1998). The strongest signal detected in an AGN jet is observed in 3C 84 by Homan & Wardle (2004).

In this work, we present the first comparison of CP maps obtained from VLBI observations with the VLBA and synthetic polarized emission maps produced with the PLUTO Code (Kramer & MacDonald 2021).

The organization of this paper is as follows: In Sect. 2, the methodology is outlined, including details of the 15 GHz and 23 GHz VLBI observations and the calibration procedures employed. This includes polarized calibration with particular emphasis on enhancing Stokes *V* and rectifying compact polarized emission signals using the `DoG-HiT` imaging software. The results are presented in Sect.3, where we showcase polarized intensity maps and delve into the polarized structures and levels within the nine observed blazar sources. A superresolution perspective on 0528+134 is also provided. In Sect. 4, the results are thoroughly dissected and analyzed. This includes a view on archival MOJAVE data. Finally, Sect. 5 summarizes the final conclusions drawn from the resulting maps in the context of physical concepts.

2. Methodology and observations

2.1. Methodology

Over four hundred AGN jets have been observed as a part of the MOJAVE monitoring program with the VLBA from 1996 to 2016[1]

From this long-lasting effort, the following conclusions can be drawn:

- fractional polarization in jets increases with separation from the total intensity peak and towards the jet edges of the VLBI core,
- 40 % of the VLBI cores have a preferred EVPA direction across multiple epochs,
- EVPAs in jets of BL Lac objects, as well as in their radio cores, are more stable than those in quasars. Additionally, the EVPAs tend to be aligned with the initial jet direction (Pushkarev et al. 2017).

Within the MOJAVE program, it was possible to observe CP at very faint levels within some jets (0.3−0.7 % for fractional CP, (Homan et al. 2018). Several sources, including the blazar 3C 279, have shown a few percent levels of CP in the radio core. A full Stokes analysis of 3C 279 was carried out using radiative transfer to constrain the magnetic field and particle properties (Homan et al. 2009). With this approach in mind, we aim to draw our own conclusions by comparing observations and simulations of RMHD jets by

- analyzing the CP dependence on the magnetic field in the VLBI core by applying the predicaments stated in Kramer & MacDonald (2021),
- confirming the robustness of EVPA orientation over multi-epochs by comparison to the MOJAVE archive,
- checking whether the CP exhibits a switch from left-handed to right-handed over frequencies or time,
- and studying the effect of various magnetic field morphologies within the extended relativistic jet emission.

2.2. Observations

We select a sample of AGN blazar sources that have shown the characteristics of the simulations presented in Kramer & MacDonald (2021), i.e., a core-dependent CP for a poloidal magnetic field on the one hand, and a switch in CP sign for a purely toroidal magnetic field morphology on the other hand. The selected target sources are presented in Table 1 along with their monitoring status, optical class, and redshift.

The VLBA experiment BK242 was observed in dual-polarization mode, over a 24-hour period on January 6 and 7, 2022. All ten VLBA antennas were scheduled for observation and were present for most of the allocated time. Technical difficulties at the NL, LA, KP and PT antennas, as well as bad weather at HN and BR resulted in a total of 1599 min of downtime (11.1 % of the total observing time of 14380 min, combined for all antennas).

The data were correlated with a 1 s integration time at the National Radio Astronomy Observatory (NRAO) correlator located in Socorro, NM. The four intermediate frequency (IF) windows are split into 256 channels each, yielding a total bandwidth of 1024 MHz, and contain both linear and cross-hand polarization (i.e., RR, LL, RL, LR). Observations at 15 GHz and 23 GHz were performed simultaneously to check the compatibility of the results to the MOJAVE archival data. Furthermore, a multi-frequency dataset allows us to test the frequency dependence of structures in CP images.

2.3. Calibration[2]

The circular polarization signal is difficult to assess due to the low signal-to-noise ratio and the degeneracy with the total intensity image and the RL-offset calibration. In particular, correct calibration of the gains and the *D*-terms is crucial for robust detection of circular polarization In the past, this problem was solved by CLEAN iterations, alternated with a statistical self-calibration of the gains assuming additionally that the mean Stokes *V* signal should vanish (Homan et al. 2018). This procedure proved good enough to produce significant circular polarization maps presented in Homan et al. (2018). However, a

[1] For a detailed listing visit the MOJAVE 2 cm Survey Data Archive.

[2] All of the following calibration and imaging steps are done for both observational frequencies.

Table 1: Summary of observations

IAU 1950.0	Status[a]	Type[b]	z^c	I^d (Jy/beam)		$\sqrt{Q^2+U^2}^e$ (mJy/beam)		V^f (mJy/beam)		Beam (bpa)[g] (µas)×(µas) (°)	
				15 GHz	23 GHz	15 GHz	23 GHz	15 GHz	23 GHz	15 GHz	23 GHz
0059+581	a	L	0.644	1.8	1.9	50.9	88.5	3.7	3.7	441 × 285 (0.24)	314 × 181 (0.08)
0149+218	b	L	1.320	0.2	0.09	3.4	4.2	0.9	0.8	571 × 269 (2.87)	413 × 277 (2.77)
0241+622	a	L	0.045	1.1	1.4	12.4	7.7	3.8	7.8	450 × 293 (0.52)	328 × 194 (0.31)
0528+134	c	LH	2.070	0.5	0.3	14.9	14.6	2.0	0.9	635 × 260 (2.97)	463 × 168 (2.89)
0748+126	b	LQ	0.889	0.5	0.6	6.9	23.9	0.8	7.9	638 × 267 (3.07)	460 × 168 (2.97)
1127−145	b	LQ	1.184	0.8	1.0	12.3	49.0	1.5	31.6	713 × 260 (3.09)	553 × 167 (2.98)
1243−072	a	LH	1.286	0.6	0.5	20.3	19.6	2.7	2.5	643 × 268 (3.01)	542 × 162 (2.94)
1546+027	c	LH	0.414	1.2	0.8	49.2	49.2	1.5	5.4	631 × 272 (3.10)	469 × 173 (2.98)
2136+141	b	LQ	2.427	0.6	0.3	12.1	21.3	1.8	5.8	596 × 270 (3.01)	439 × 163 (2.90)

Notes. Full source list of science targets. [(a)] MOJAVE status: (a) Not actively monitored. (b) Monitoring resumed. (c) Monitored at irregular cadence between monthly and yearly. [(b)] Types: all sources are classified as L; LSP (low spectral peaked). Q; Quasar. H; HPQ (high polarized quasar); $|m_{\mathrm{optical}}| \geqslant 3\,\%$ on at least one epoch. [(c)] Redshift. [(d)] Total intensity. [(e)] Linearly polarized intensity. [(f)] Circularly polarized intensity. [(g)] Beam size and position angle.

CLEAN-based statistical calibration approach has some limitations: Neither the convolved CLEAN image (which does not fit the data), nor the sample of delta components (which is not a physically reasonable description of the on-sky image) are ideal for self-calibration, as they do not both describe the data and perception of the image structure (Müller & Lobanov 2023b). The latter might introduce systematics that tend to become frozen into the self-calibration (Pashchenko et al. 2023) and hence may affect the much weaker Stokes V signal. Furthermore, due to being an inverse modeling approach, it is not possible to separate the calibration of the RL offset or the amplitudes from the initial phase calibration, and the choices made interactively during the application of the algorithm, in contrast with recent forward modeling techniques that utilize closure quantities (e.g., Akiyama et al. 2017a,b; Chael et al. 2018; Broderick et al. 2020; Müller & Lobanov 2022; Müller et al. 2023).

The assumption of a statistically vanishing circular polarization signal is a well-motivated assumption on short baselines. However, the long baseline structure of the Stokes V signal, caused for example by local turbulence, may be more significant. This requires the inclusion of the Stokes V structure in the calibration process. It has only recently become possible to overcome these issues with the current advances in imaging and polarimetry methods for VLBI (e.g., Akiyama et al. 2017a,b; Chael et al. 2016, 2018; Broderick et al. 2020; Broderick & Pesce 2020; Arras et al. 2022; Tiede 2022; Müller & Lobanov 2022, 2023b,a; Müller et al. 2023; Mus et al. 2023). In the following, we describe the different steps of our calibration methodology.

We follow the basic total intensity calibration procedure using the standard methods described in the AIPS cookbook. In particular, this includes corrections for instrumental delays, Earth orientation parameters, phase corrections for parallactic angles, amplitude corrections for digital sampling effects, fringe fitting, and solving for amplitude gain effects. We used Los Alamos (LA, antenna no. 5) as reference antenna when required. After the cross-hand delay calibration using the task RLDLY, the main D-term calibration takes place during full-Stokes imaging using `DoG-HiT` (Müller & Lobanov 2022, 2023b,a). However, leakage terms (D-terms) are additionally estimated in multiple ways to verify the robustness of the calibration. First, we choose the bright target source 1127−145, which already serves as calibrator in the total intensity calibration to solve for leakage terms in `polsolve` (Martí-Vidal et al. 2021). Second, we use the pipeline `GPCAL` (Park et al. 2021) on three target sources and find that the D-term calibration is consistent across methods. Our typical feed leakage terms (D-terms) have amplitudes of about ± 0.02 with a range of $\sim 0.0005 - 0.0561$.

After the initial calibration with AIPS, we average the data over a 10 s time-span, and identify and mark the data points that deviate significantly from the norm in the imaging software Difmap. In order for `DoG-HiT` to produce a best-fit Stokes I map, we provide total intensity maps a-priori. For five of the nine target sources we use the publicly available MOJAVE data base. We utilize `uvfits`-files for roughly the same observational time (January 2022). For the remaining four target sources, we create a Stokes I model using Difmap.

`DoG-HiT` enhances the Stokes I image, specifically targeting compact emission characteristics. Initially, the approach entails an unpenalized round as detailed in Müller & Lobanov (2022), utilizing the CLEAN image at 15 GHz as the foundation. Subsequently, the `DoG-HiT` technique is employed, resulting in the preservation of multi-resolution support to capture key features across scales. Finally, we self-calibrate the observation to the recently . It is worth mentioning that the `DoG-HiT` procedure produces images by closure-only imaging and in a largely unsupervised way, i. e. independent of the initial self-calibration and human bias. Moreover, `DoG-HiT` produces a physically reasonable super-resolving image that simultaneously fits the observed visibilities, hence alleviating possible biasing effects that may be introduced during the CLEAN self-calibration. The images presented in this work are the results of the `DoG-HiT` reconstruction following the additional calibration steps described below. The image structures are only determined up to a constant re-scaling factor, which is fixed by the initially CLEANed total flux and is totally absorbed in the amplitude calibration. This result is based on closure only imaging. However, it does not affect the relative image structures in any polarization channel, i.e., neither the total intensity contours and the polarized signal, nor the *relative* polarization fractions. This is explained by the fact that this effect is constant on all baselines.

2.3.1. Calibration for compact polarization

The optimal Stokes I model for each source, along with the modified/unself-calibrated data, served as input for `DoG-HiT`. The pipeline involves resolving and fine-tuning compact polarization through the implementation of the `DoG-HiT` algorithm. To initiate the process, a-priori D-term solutions obtained from `polsolve` are applied. Instances of nonphysical high circular polarization are appropriately flagged for attention. Subsequently, both amplitudes and phases are calibrated within a 12-hour time frame. During this calibration, the assumption is made that $\langle \mathrm{RR} - \mathrm{LL} \rangle$ (the difference between right and left circular polarization) is close to zero, indicating a small Stokes V, in consistency with the strategy applied in (Homan & Lister 2006; Homan et al. 2018). The refinement of the Stokes I image is then performed on the flagged dataset with a gradient descent minimization. Following this, the linear polarization image is subjected to the `DoG-HiT` procedure as described in Müller & Lobanov (2023a). Efforts are made to calibrate for any remaining D-term residuals. The process is further extended to address circular polarization using `DoG-HiT` in the same way, i.e., by fitting the Stokes V visibilities, but only varying the parameters in the multiresolution support Müller & Lobanov (following the philosophy in 2023a). An iterative cycle is established, encompassing five rounds of refinement: linear polarization, circular polarization, and residual D-term calibration. This comprehensive approach aims to progressively enhance the precision and quality of the (linear) polarization results.

2.3.2. Refinement of Stokes V calibration

Residual RL offsets are still present in the data, especially on long baselines. We improve the calibration of Stokes V with the de-noised, compact Stokes V. To this end we implement manual procedures in `DoG-HiT`. Based on the 1%-contour of the Stokes I image, a mask is created that delineates a compact and luminous region. This mask is then applied to the Q, U, and V polarization components. Moreover, the Stokes V structures are denoised using a Gaussian filter. A comparative analysis is then performed between the amplitudes of the compact model in Stokes V and the actual observed Stokes V, identifying and flagging anomalies, particularly those due to unrecovered extended emission zones (in total intensity), especially on shorter baselines (mimicking the flagging proposed in Homan et al. (2018) for the circular polarization fractions). Following this, a calibration process targeting both amplitudes and phases, is initiated and performed over a period of one hour. Notably, the calibration enforces the recovery of Stokes V ($\langle \mathrm{RR} - \mathrm{LL} \rangle = V$) using the gain transfer calibration technique. The refinement of the Stokes I image is then conducted exclusively on the data set marked by the previous flags and with all calibration tables present. This approach ensures a focused and controlled improvement in image quality.

Following the adjustment of the R/L antenna gains, the ultimate images were generated for all four Stokes parameters by minimizing the χ^2-metric to the finally calibrated Stokes V visibilities with a gradient descent approach stopped by the discrepancy principle.

3. Results

Full-Stokes maps for all target sources are displayed in Figs. 1–4, each convolved with a Gaussian beam. The beams are shown in the lower right corner of each map, while their sizes can be found in Table 1. The field of view is uniformly applied to the maps, set at a factor of 3 mas as a reference, which varies in scale across different sources. Our records of total intensity and polarization measurements in both 15 GHz and 23 GHz are summarized in Table 1 and the fractional measurements are presented in Table 2. In Table 1, comprehensive data are provided for total intensity (Stokes I), linear polarization (LP, $\sqrt{Q^2 + U^2}$), and circular polarization (CP, Stokes V) at the peak of each map. The total intensity in Jansky (Jy) for all nine observed blazar sources range between $0.5 \leqslant I \leqslant 2.8$ for 15 GHz observational data and $0.5 \leqslant I \leqslant 2.9$ at 23 GHz (see upper left corner in each map in, e.g., Fig. 1 and Fig. 3), where we remind the reader of the uncertainty of the total flux related to closure-only imaging and frozen into the calibration process. In terms of total intensity, 1243−072 results in lower values compared to the archival MOJAVE data observed at 15 GHz, which are used as a reference during the formulation of our observations. The peak value in total intensity remains consistent at both 15 GHz and 23 GHz wavelengths.For comparison to our values presented in Table 1 visit the MOJAVE data archive. Evident jet structures are observed in 0149+218, characterized by a prominent bright spot to the north. An extended jet structure is further observed in 0528+134, 0748+126, 1127−145, and 1243−072. Interestingly, a counter-jet phenomenon becomes apparent in 0241+622 at 23 GHz (see bottom right panel in Fig. 3), contrasting the jet direction observed at 15 GHz (see bottom right panel in Fig. 1). Notably, at both frequencies a counter-jet is newly observed in 0149+218 to the south and in 2136+141 to the east, marking the first occurrence of this phenomenon in these sources.

Table 2: Fractional polarization

IAU	$\bar{m}_l{}^a$ (%)		$\bar{m}_c{}^b$ (%)	
1950.0	15 GHz	23 GHz	15 GHz	23 GHz
0059+581	1.7	2.7	0.4	0.1
0149+218	0.7	0.3	−0.7	−2.2
0241+622	0.7	0.4	0.3	−1.1
0528+134	3.0	2.8	0.8	−0.3
0748+126	1.7	2.7	0.2	1.5
1127−145	0.9	1.4	−0.2	3.1
1243−072	2.9	3.0	0.8	−0.5
1546+027	3.6	3.1	0.1	−0.3
2136+141	0.8	2.6	0.8	−1.5

Notes. Integrated values of polarization fractions for all science targets. [a] Fractional linear polarization. [b] Fractional circular polarization.

3.1. Polarized intensity maps

Figure 1 shows the linear polarization at 15 GHz overplotted with both the contours in total intensity and EVPAs as white ticks. The same plotting scheme is illustrated in Fig. 3 for 23 GHz. The circular polarization maps at 15 GHz and 23 GHz are presented in Fig. 2 and Fig. 4, respectively. In all observed blazars the peak of the Stokes I map corresponds to the compact and resolved VLBI core. Linearly polarized regions consistently coincide with the region of the Stokes I VLBI core. An exception is observed in 0149+218, where the core and map peak in linear polarization are located in different jet components. In this scenario, the polarized peak aligns with a robust

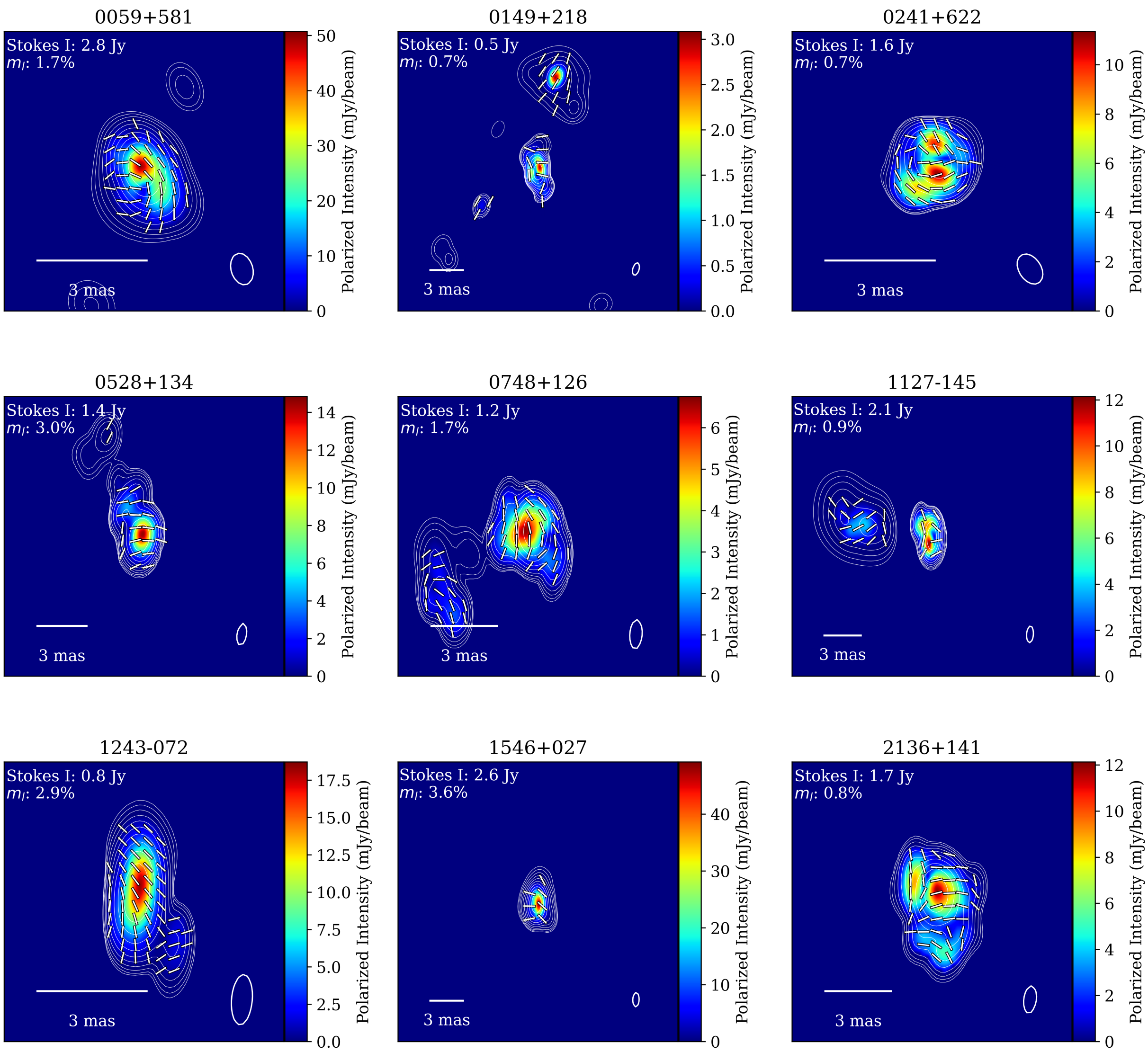

Fig. 1: Reconstruction of data from 6-7 Jan. 2022 for nine target sources: 0059+581, 0149+218, 0241+622, 0528+134, 0748+126, 1127−145, 1243-072, 1546+027, and 2136+141. The figure shows maps for each source in linear polarization at 15 GHz (colorcoding: blue/red low/high). The total intensity is indicated in white contours on each map. The orientation of the linear electric vector position angle is plotted as white ticks, the total polarized intensity by the colormap. An individual convolution beam is shown in the lower right corner of each map. All maps show the same field of view and scale with 3 mas.

component within the jet. Minor discrepancies arise further between circular polarization and the peak in total intensity specifically within the VLBI core (with no impact on the extended jet structure). This discrepancy is likely attributed to the phase calibration process (detailed in Sect. 2.3.2), which could potentially introduce a minor positional shift between the location of circular polarization and the Stokes I peak. Two sources (0149+218 and 1127−145) show strong linear polarization intensity across extended jet structure robustly over both frequencies. The overall values for the fractional linear and fractional circular polarization [%] are in a range of $0.7 \leqslant m_l \leqslant 3.6$ and $0.1 \leqslant m_c \leqslant 0.8$ at 15 GHz, and $0.3 \leqslant m_l \leqslant 3.1$ and $0.1 \leqslant |m_c| \leqslant 3.1$ at 23 GHz. For reference and details see Table 2.

3.1.1. Polarized structure

At 15 GHz, the peak of linear polarization in the target source 0149+218 is located away from the VLBI core in the 15 GHz linear polarization map (see Fig. 1). This behaviour for the circular polarization structure is observed in 0241+622, 0748+126, and 1546+027. Notably, there is a dominant pattern of mostly negative circular polarization (CP) at 23 GHz (Fig. 4), which con-

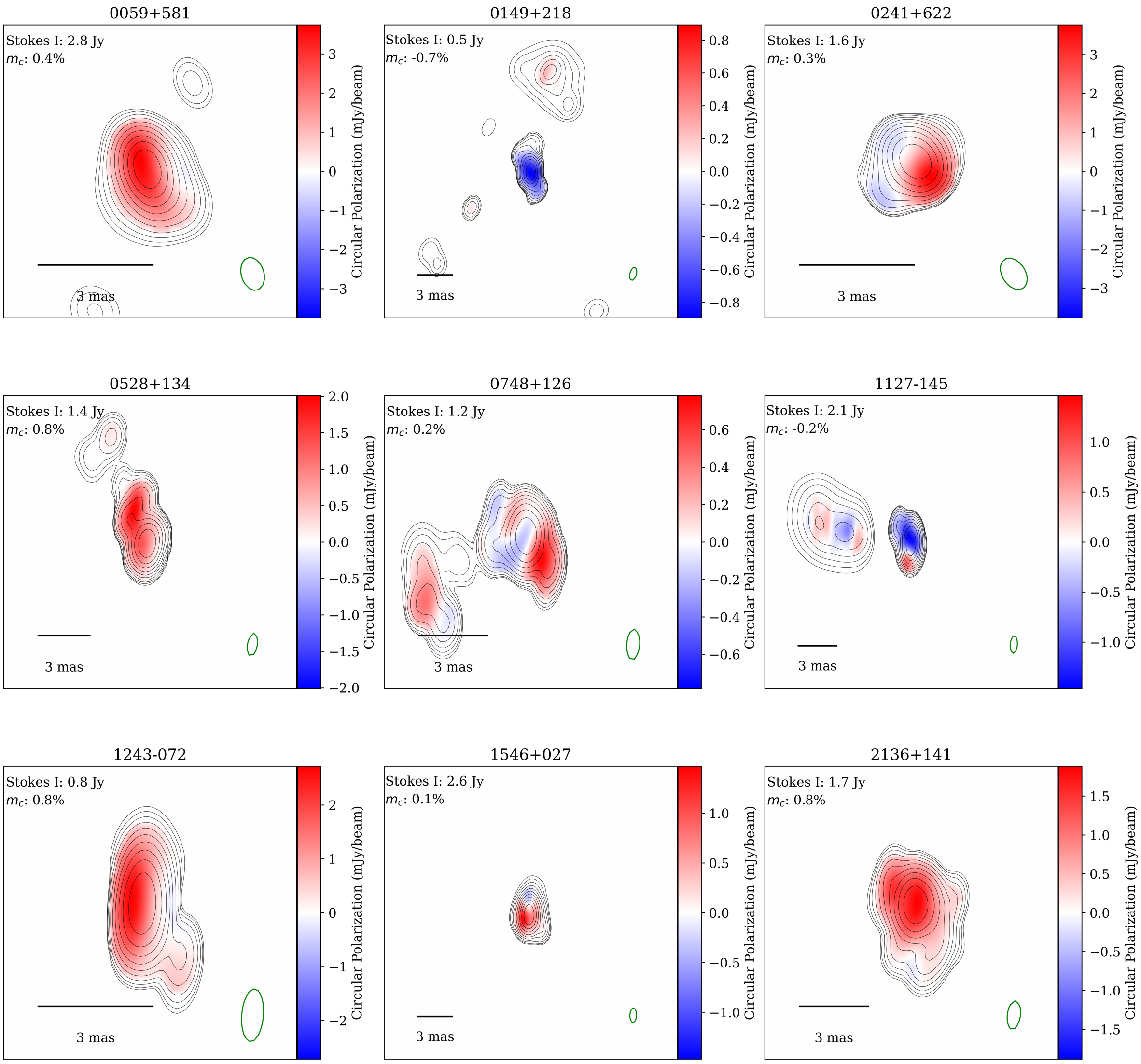

Fig. 2: Circular polarization imaging results from 6-7 Jan. 2022 for nine target sources: 0059+581, 0149+218, 0241+622, 0528+134, 0748+126, 1127−145, 1243−072, 1546+027, and 2136+141. The figure shows maps for each source in circular polarization at 15 GHz (colorcoding: blue/red negative/positive). The total intensity is indicated in white contours on each map. An individual convolution beam is shown in the lower right corner of each map. All maps show the same field of view and scale with 3 mas.

trasts with a positive trend at 15 GHz (Fig. 2). This dominant sign alteration, however, exhibits hints in the sources 0241+622, 1243−072, and 1546+027, where a subtle resemblance to the 23 GHz structure can be discerned in the 15 GHz maps. Notably, a complete shift in sign occurs in 0528+134, 0748+126 and 2136+141 when moving from 15 GHz to 23 GHz. In the case of the blazar 0149+218, a consistent and predominantly negative core is observed across both 15 GHz and 23 GHz. In general, CP tends to be higher at 23 GHz than at 15 GHz (see Table 1), which is rather contradicting to Homan & Wardle (2004). Furthermore, the sources 0059+581, 0149+218, 0748+126, and 1127−145 carry an elongated EVPA structure along the jet direction at 15 GHz (see Fig. 1). For 0528+134 (and 1127−145 to some extent) we observe the EVPAs to be perpendicular to the jet direction at both frequencies (see Fig. 1 and Fig. 3). In 1243−072, observed at 15 GHz, we observe an extended structure to the south (rather than to the west as in previous observational analyzes) with an opening angle of the EVPA towards the edges of the jet. This might be an indication for a helical magnetic field (Kramer & MacDonald 2021).

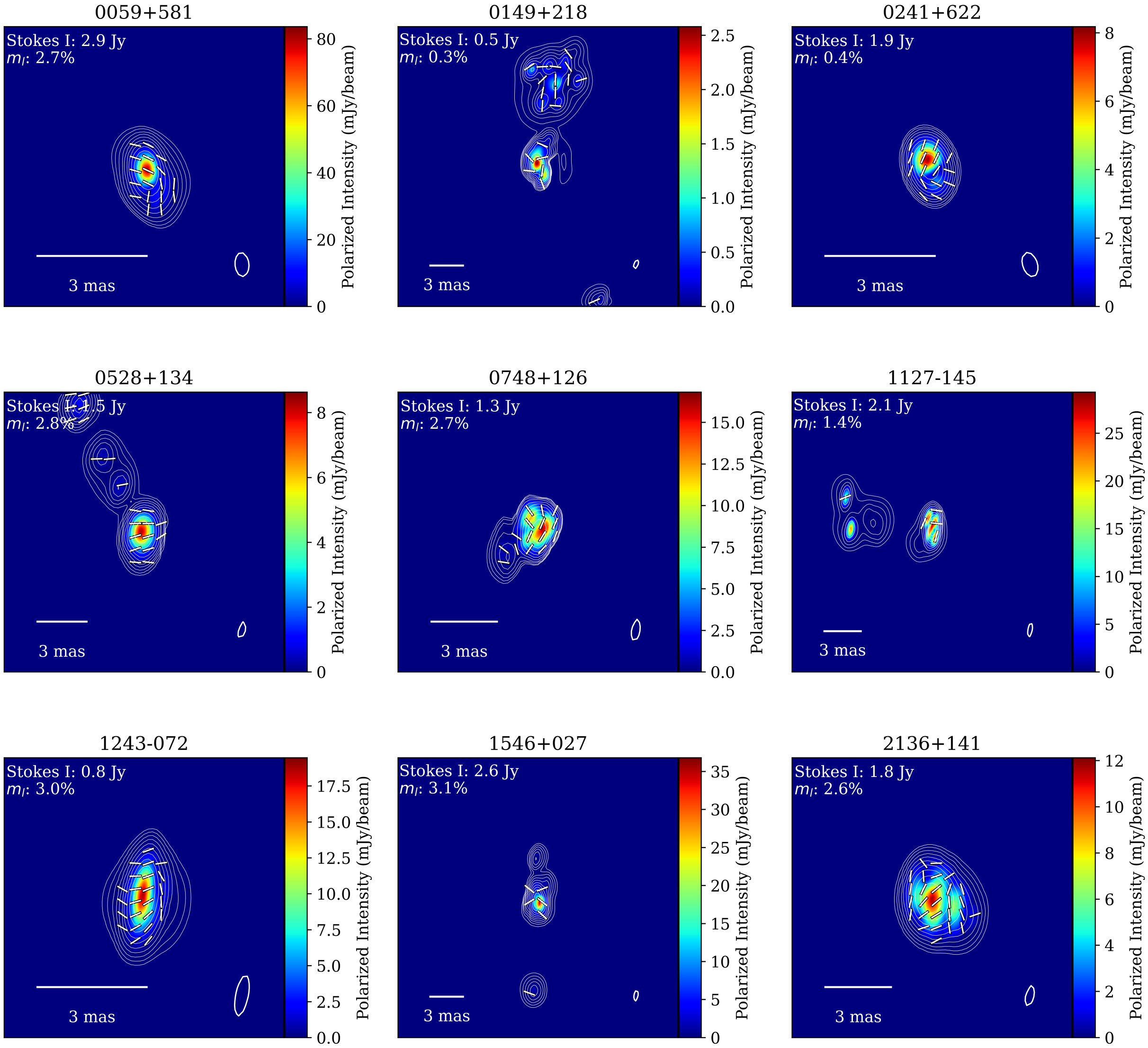

Fig. 3: The same as Fig. 1 but at 23 GHz observational frequency.

3.1.2. Amplitude of polarization

We detect circular polarization (and linear polarization) in all nine target sources. The distribution of the peak values of linear and circular polarization is consistent throughout all sources; specifically, the amplitude in linear polarization (Stokes Q and U) is consistently higher than the circular polarization amplitude (Stokes V). The ratio of the fractional values of linear polarization m_l to circular polarization m_c vary to a greater extent.[3] In the target sources 0149+218, 0241+622, 0528+134, and 1127−145, at 23 GHz, fractional CP surpasses fractional LP (compare Fig. 2 and Fig. 1), which indicates an external Faraday screen (Wardle 1971; Homan et al. 2001). Other sources, namely 1243−072, 1546+027, and 0528+134, have significantly higher m_l values compared to m_c at 15 GHz and 23 GHz. For the remaining sources, m_l and m_c in 15 GHz are quite similar. Overall, there is no clear trend for either frequency nor in the fractional LP when comparing 15 GHz and 23 GHz. When comparing m_l and m_c at 23 GHz, 0059+581 showcases significantly higher fractional LP than CP ($m_l \gg m_c$), a pattern also observed in sources 1243−072, 1546+027 (as seen in 15 GHz).

[3] from this point on we will refer to LP and CP as fractional values.

3.2. Superresolution

`DoG-HiT` achieves superresolution by combining the significant advantages of regularized maximum likelihood reconstructions, which super-resolve structures, with the CLEAN method, which provides high dynamic range sensitivity to extended structures. Without applying a Gaussian beam convolution, we obtain a su-

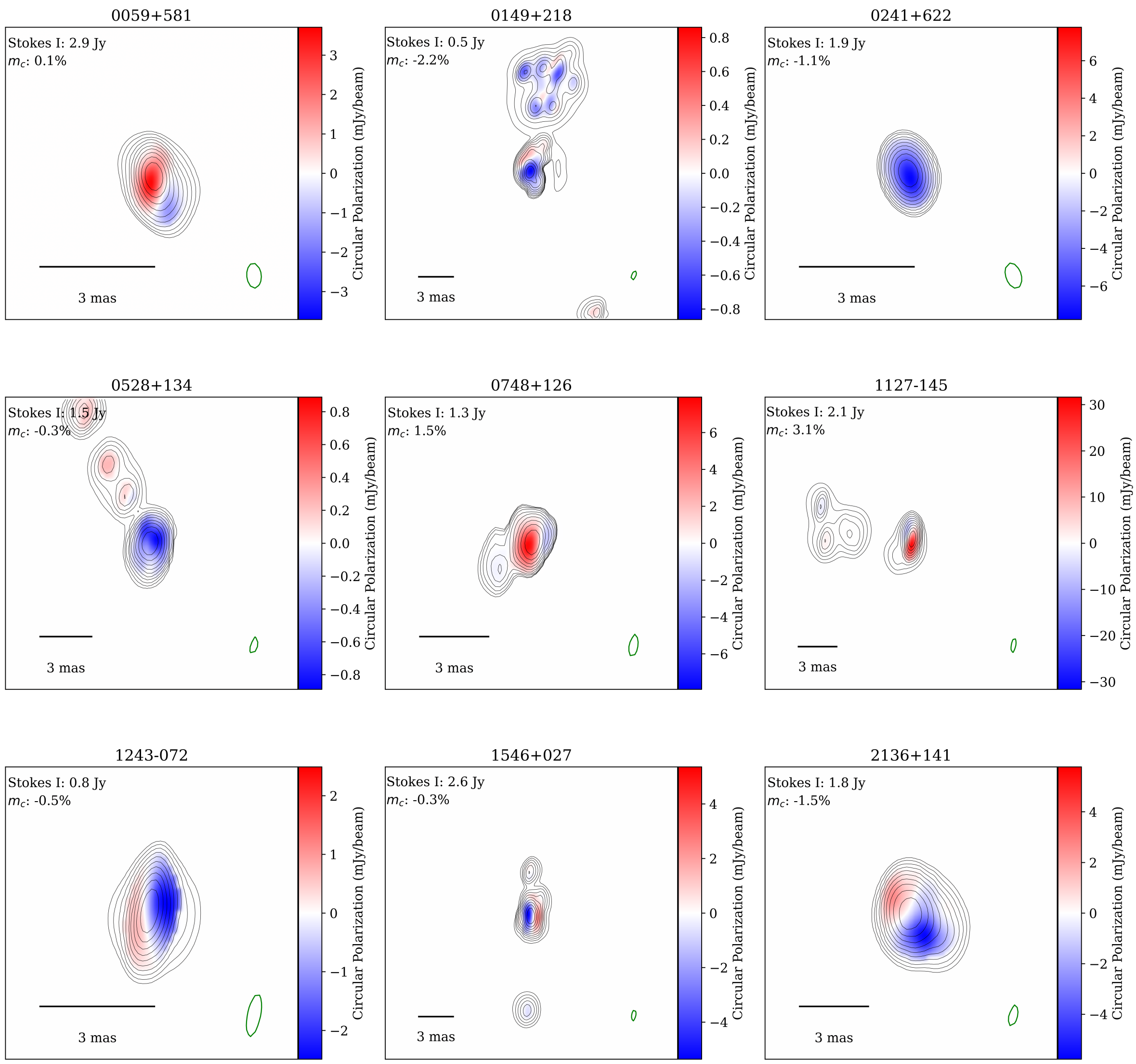

Fig. 4: The same as Fig. 2 but at 23 GHz observational frequency.

perresolved image. We study the blazar 0528+134 at 15 GHz as an exemplary because the source shows the richest structural features along the jet (see Fig. 7). Our resulting map in Fig. 7 matches the reconstructed 43 GHz map published by Jorstad et al. (2017). This suggests that the improvements made to our pipeline allow us to resolve distinct features at lower frequencies. In contrast to the convolved 15 GHz image (Fig. 1), we can also detect a south-east bend jet structure, which is observed for the first time. It could be associated with an additional bend in the northern arm, or as a counter-jet phenomenon.

The jet exhibits two distinct bends, and past analyzes of the trajectories of individual components show that the bend is more pronounced closer to the core and gradually straightens out further away (Britzen et al. 1999). Such curvature on small angular scales has been observed in numerous other sources, suggesting that it is a common phenomenon in AGN (for example, Zensus et al. (1995) for 3C345 and Wagner et al. (1995) for PKS 0420−014).A possible explanation for the observed wiggling of the jet is the ejection of different components along different but straight trajectories, resembling ballistic motion. Jorstad et al. (2017) reported instances of ballistic motion in identified knots.

The EVPAs are oriented perpendicular to the jet's direction, matching an underlying poloidal magnetic field morphology (Kramer & MacDonald 2021) and being consistent with the 43 GHz observations presented in Palma et al. (2011). We find a similar level of fractional polarization, namely, $m_l = 3\,\%$ in the core as (Palma et al. 2011, with $\sim 2\,\%$ at 43 GHz).

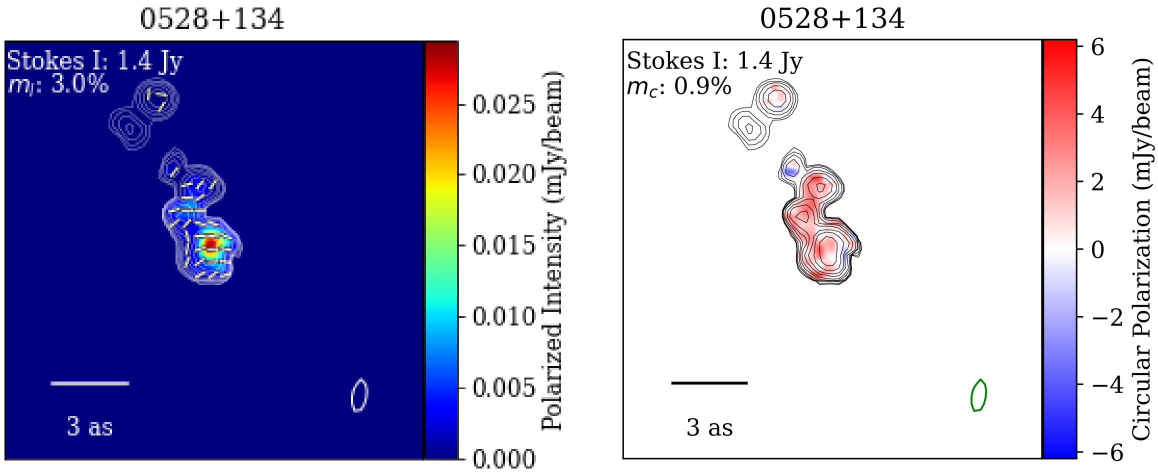

Fig. 5: Reconstruction of data from 6-7 Jan. 2022 for the quasar 0528+134. The images show the resolved maps of: Linear polarization at 15 GHz (color coding: blue/red low/high) in the **left** panel. The total intensity is indicated in white contours. The linear electric vector position angle is plotted as white ticks. **Right:** circular polarization (colorcoding: blue/red negative/positive). The total intensity is indicated in white contours.

4. Discussion

It is imperative to highlight significant improvements that could potentially account for the notable cases of high circular polarization. In particular, the accuracy of Stokes V strongly hinges on meticulous calibration. To be more precise, our self-calibration is anchored in a physical model, as opposed to relying on a potentially non-physical model of CLEAN (delta) components. This adjustment results in more accurate gains. Our method aligns both the linear and cross-hand polarization. The left panel in Fig. 6 ensures that neither component dominates. Our polarization calibration method integrates the compact Stokes V structure (in contrast to previously applied methods assuming $V = 0$), a departure from the conventional assumption of its insignificance. This adaptation is of particular importance in view of the non-negligible circular polarization fraction observed at long baselines. The right panel in Fig. 6 shows the amount of detected circular polarized emission over the uv-distance. Figure 7 stresses that the observed circular polarization is primarily detected on shorter baselines, given the strength of `DoG-HiT`. The observed data (in blue) align well with the reconstructed model (in red). There is no significant trend over the distance, nor are there any major outliers within our calibration method. Our choice of imaging algorithms also plays a key role. We leverage the effectiveness of `DoG-HiT` for compact structures. This integration takes a hierarchical approach, exploiting the unique strengths of each framework to achieve significant improvements in image quality.

While the closure phases for RR and LL remain resilient to variations in antenna gains, they could potentially be affected by instrumental polarimetric leakage. However, the effect of uncertainties in D-terms is significantly more pronounced in cross-hand visibilities compared to parallel-hand visibilities (Smirnov 2011). Consequently, this implies that instrumental polarization exerts a comparatively lesser effect on Stokes V in comparison to its impact on Stokes Q and U. For our data we hence stress again that the Stokes V signal is robust and reliable. The rotation of the EVPAs could slightly change depending on the solution of the leakage terms.

The presence of substantial circular polarization, reaching up to $m_c = 3.1\,\%$ in our dataset at both frequencies, exceeds any previously observed circular polarization rates documented by, e.g., Homan et al. (2001); Homan & Lister (2006)[4] using the VLBA at 5 GHz or by MOJAVE observations with the VLBA at 15 GHz (Homan & Lister 2006, where CP was around 0.3 percent). We agree with their conclusion that the overall circular polarization value tends to increase at higher frequencies. Another case of remarkably high fractional circular polarization was detected in 3C 84, exceeding $m_c = 3\,\%$ (Homan & Wardle 2004).

Most of our sources exhibit stable degrees of fractional linear polarization over the last years (monitored by the MOJAVE program). Six out of nine sources remain consistent in m_l (0059+581, 0528+134, 0748+126, 1127−1245, 1546+027, 2136+141). These six sources plus 0149+218 and 1243−072 also show a stable EVPA degree compared to the archival data collected over several years to decades in the MOJAVE data archive. This is interpreted as an indication for optically thickness (Homan & Wardle 2004).

We detect three sources with a lower linear polarization amplitude than in the past (0149+218, 1127−145, and 1546+027) Two sources show an increase in (fractional) linear polarization since they have been last monitored, i.e., 0241+622[5] in 2013 and 1243−072 in 2010. Solely the source 0149+218 shows a smaller fractional linear polarization alongside a smaller amplitude in linear polarization, and no circular polarization at all in the 15 GHz observations as stated in Sect. 3. At 23 GHz, 0241+622 displays a counter-jet phenomenon, which is consistent with 43 GHz observations Cheng et al. (2020). In the case of 0059+581, the jet structure appears to be oriented further to

[4] Notably, they identified circular polarization exceeding 0.3 % in merely two out of 36 sources.
[5] It is noted that there are no past detections of EVPA.

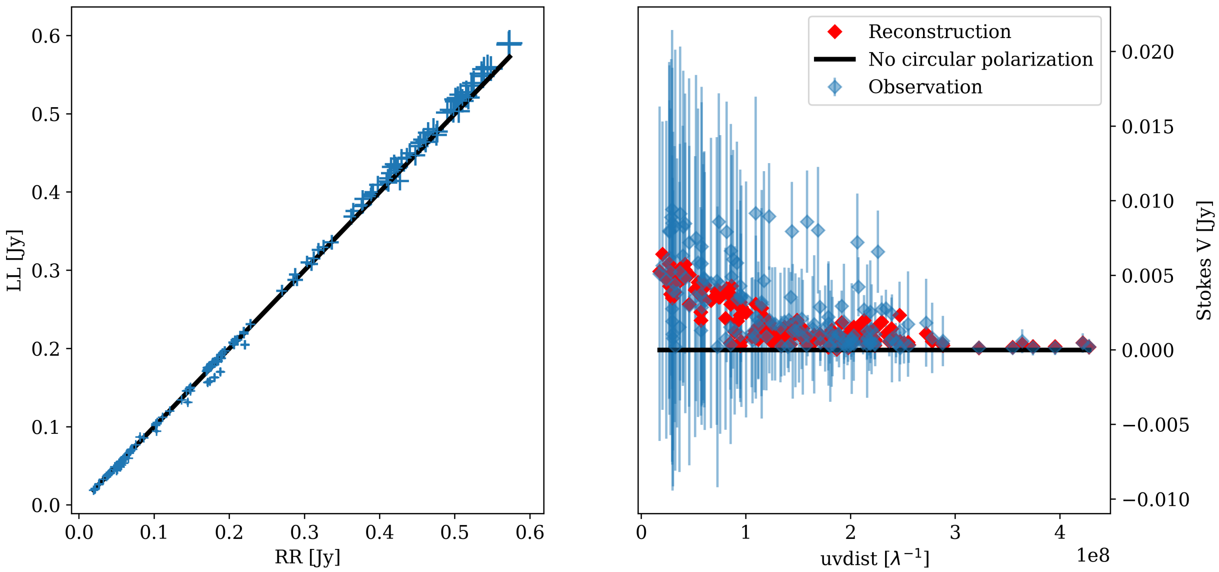

Fig. 6: **Left:** Correlation between right-hand (RR) and left-handed (LL) polarization terms and a model fit for the blazar 0149+218 at 15 GHz observed on 6-7 Jan. 2022. **Right:** Cirular polarization amplitude (Stokes V) as a function of uv-distance. The plot shows data of observed (blue) and reconstructed (red) data in contrast to zero circular polarization (black line).

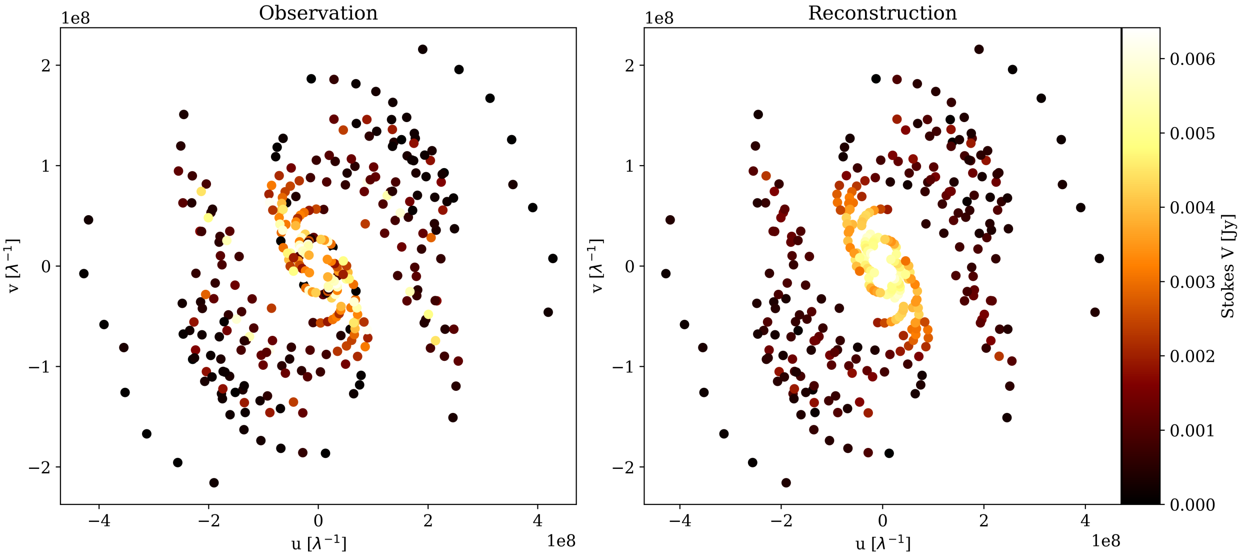

Fig. 7: An example of the observed data points (**left**) and reconstructed data (**right**) from a 24-hour observational run on 6-7 Jan. 2022 for the source 0059+581 at 15 GHz. The diagram shows observational points between antenna pairs plotted as a uv-coverage. The color indicates signal of circular polarization (dark/bright low/high).

the south in 15 GHz compared to its appearance in 2013 (the last monitoring, see 0059+581 in the MOJAVE data archive.

Kramer & MacDonald (2021) provided an analysis on how the magnetic field morphology affects the polarized synchrotron emission within the recollimation shock (VLBI core) and the extended jet structure. They found a centrally highlighted VLBI core and a single sign in CP for a purely poloidal magnetic field. In contrast to that, a purely toroidal magnetic field would result in an edge-brightened jet, a bi-modal pattern of EVPA (however, the EVPAs tend to align with the jet's direction of motion within the spine), and a two-signed CP structure within both the VLBI core and the jet. A helical magnetic field shows various hints of the described characteristics above.

In the context of theoretical forecasts, an explicit magnetic field orientation becomes evident within the extended jet emission of 0149+218: Its polarized structure suggests an underlying toroidal magnetic field structure. This conclusion is supported by two notable observations at 23 GHz, namely, a bi-modal pattern of EVPA (see Fig. 3) and the presence of two signs in CP (see Fig. 4). Its core, however, illustrates a single sign in CP and is, hence, associated with an underlying poloidal magnetic field (see Table 3).

The jet structure in 0528+134 observed at 15 GHz in super-resolution, see Fig. 5, exhibit characteristics that align with a helical or rather poloidal magnetic nature. However, the source exhibits a switch in sign of circular polarization when moving from 15 GHz to 23 GHz. This indicates effects of optical depth of Faraday screens in between that become (in)visible. A poloidal magnetic field is, moreover, favored for the jet structure in the source 2136+141, which is highlighted by a perpendicular EVPA rotation with regards to the jet direction(s).

The blazar sources 0748+126, 1127−145, and 1243−072 are in agreement with a helical magnetic field morphology. The EVPA tend to follow the jets motion (even when bending), however, the central peak of the linear polarization is slightly off-center from the total intensity peak (see, e.g., Fig. 1).

Moving to the radio core, the configuration in 0241+622, 0748+126, 1127−145, and 1546+027, and 2136+141 presents traits indicative of a helical or toroidal magnetic field structure, supported by a double sign in either frequency. Furthermore, one sign in CP tends to be more dominant for 1127−145 and 2136+141, and an offset between the linear polarized intensity peak and the total intensity peak is visible in 0241+622 and 0748+126, which is favored in a helical treatment of the magnetic field. This is stressed by Kramer & MacDonald (2021). When focusing on the radio core of the sources 0059+581, 0149+581, 0528+134, and 1243−072 a distinct emphasis is placed on a purely poloidal magnetic field structure. This is summarized in Table 3.

For quite some time, it has been established that the circular polarization (CP) sign within a specific AGN tends to remain consistent over extended periods, often spanning years or even decades, as highlighted by Homan & Wardle (1999). However, limited information has been available concerning the frequency-dependent behavior of the CP sign. Vitrishchak et al. (2008) findings reveal that out of nine AGN where CP was detected at both 15 GHz and 22 GHz, eight consistently displayed the same sign, with 2251+158 being the exception. Among the six AGN where CP was detected at both 22 GHz and 43 GHz, four exhibited changes in sign between these two frequencies (namely, 0851+202, 1253−055, 1510−089, and 2251+158). We observe the switch in sign for three to five sources as described in Sect. 3.1.1. The occurrence of alterations in the CP sign as the frequency shifts from 15 GHz to 23 GHz implies the influence of optical depth effects. This observation suggests that the sampled regions are likely to be optically thin. This observation is consistent with our verification procedures during data calibration, where we identified the need to correct for opacity effects in the 23 GHz dataset, while no such correction was required for the 15 GHz dataset. Especially, we would like to draw attention to the blazar 1243−072 which experiences a complete switch in sign of CP from 15 GHz to 23 GHz. The interpretation and findings in CP is strongly supported by the offset in EVPA rotation when both frequencies are compared.

5. Conclusion

We employ an advanced imaging algorithm using the imaging software `DoG-HiT`, which shows significant improvements in the reconstruction of compact structures in an unbiased way. Notably, `DoG-HiT` performs polarized gain calibration using the compact Stokes V structure free of biases induced by CLEAN rather than assuming its value to be zero. Our calibration method reveals no misleading trends in the right-or left-handed circular polarization at different distances, and no major outliers, reinforcing the robustness and reliability of the Stokes V signal in our data.

Table 3: Preferred magnetic field morphology

IAU 1950.0	Toroidal[a]	Poloidal[b]	Helical[c]
0059+581 (jet)	(✓)	✓	
0149+218 (jet)	(✓)	✓	
0241+622			✓
0528+134 (jet)		✓(✓)	
0748+126 (jet)			✓(✓)
1127−145 (jet)		✓(✓)	
1243−072 (jet)		✓	(✓)
1546+027	✓		
2136+141 (jet)	(✓)		✓

Notes. [a] Purely toroidal magnetic field configuration. [b] Purely poloidal magnetic field configuration. [c] Helical magnetic field configuration.

Following Gabuzda (2018), we can confidently concur that magnetic fields with a toroidal component or with a helical nature are the most plausible explanations for the extended jet structures (see Table 3). Our analysis leads us to the compelling conclusion that circular polarization serves as a powerful tool for elucidating the intrinsic magnetic field morphology of jetted AGN. Through this approach, we have been able to associate most of the sources with specific intrinsic magnetic field morphology, i.e., whether the magnetic field is poloidal or toroidal in nature and to identify a favored composition within each.

The findings extracted from our study can be summarized as follows:

- The analysis of the linearly polarized emission maps overplotted by electric vector position angles (EVPA, see Fig. 1) reveals a robustness in the polarized structure and EVPA orientation with time compared to archival MOJAVE data.
- Theoretical predictions presented by Kramer & MacDonald (2021) favor an explicit magnetic field orientation within the extended jet structures of the blazar sources.
- The occurrence of changes in the (dominant) CP sign as the frequency transitions from 15 GHz to 23 GHz suggests the influence of optical depth effects (cf. Fig. 2 and Fig. 4).
- Two blazar sources show signs of a newly manifested counter-jet structure in total and linearly polarized intensity: 0149+218 to the south (carrying positive CP) and 2136+141 to the east (negative sign in CP).
- We reconstruct a resolved 15 GHz map of the blazar 0528+134, which shows superresolved components at lower observational frequency than previously observed.
- We avoid relying on a potentially non-physical model of CLEAN components by anchoring our self-calibration to a physical model,
- Our polarization calibration method departs from previously applied methods that assume $V = 0$, we *integrate* the compact Stokes V structure.

In order to strengthen the reliability and authenticity of the observed and reconstructed polarized signal, we intend to compare the VLBI data, accounting for leakage terms of each antenna, with the levels of polarized emission obtained through single-dish measurements. To achieve this validation, we intend to utilize data from the G-GAMMA/QUIVER program (Full-Stokes, multi-frequency radio monitoring of Fermi blazars with the Effelsberg telescope, Angelakis et al. 2019) and the POLAMI program (Polarimetric Monitoring of AGN at Millimeter Wavelengths with the IRAM 30 m telescope, Agudo et al. 2018), focusing on quasi-simultaneous observations that align with our study. This approach will also yield essential information about on the absolute electric vector position angle.

In order to make strong assumptions on a preferred magnetic field, a statistical analysis would be necessary. This could, in principle, be conducted by using the archival MOJAVE data. Besides that, to further test and verify the favored magnetic field morphology for the different sources, we plan to compare synthetic transverse intensity profiles with those obtained from the sources presented in this work. In order to stress the conclusions drawn on the optical depth, a future work will focus on the analysis of the spectral index maps obtained between 15 GHz and 23 GHz.

Acknowledgements. The authors thank J. Livingston for his intense research and fruitful discussion on polarization. We thank J. Kim for his insights on Bayesian imaging techniques on polarized data. We acknowledge I. Myserlis and N.R. MacDonald for their contribution to the observational proposal. We are grateful for D. Pesce's insights on the calibration steps. The analysis was performed with the software MrBeam[6] which is partially based on ehtim [7], regpy[8] and Wise[9]. This research was supported through a PhD grant from the International Max Planck Research School (IMPRS) for Astronomy and Astrophysics at the Universities of Bonn and Cologne. The observations presented are conducted with the Very Long Baseline Array (VLBA) operated by National Radio Astronomy Observatory (NRAO) and correlated at the NRAO correlator in Soccoro. NRAO is a facility of the National Science Foundation operated under cooperative agreement by Associated Universities, Inc. This work is part of the M2FINDERS project which has received funding from the European Research Council (ERC) under the European Union's Horizon 2020 Research and Innovation Program (grant agreement No 101018682).

References

Agudo, I., Thum, C., Molina, S. N., et al. 2018, MNRAS, 474, 1427
Akiyama, K., Ikeda, S., Pleau, M., et al. 2017a, AJ, 153, 159
Akiyama, K., Kuramochi, K., Ikeda, S., et al. 2017b, ApJ, 838, 1
Angelakis, E., Fuhrmann, L., Myserlis, I., et al. 2019, A&A, 626, A60
Arras, P., Frank, P., Haim, P., et al. 2022, Nature Astronomy, 6, 259
Britzen, S., Witzel, A., Krichbaum, T. P., Qian, S. J., & Campbell, R. M. 1999, A&A, 341, 418
Broderick, A. E., Gold, R., Karami, M., et al. 2020, ApJ, 897, 139
Broderick, A. E. & Pesce, D. W. 2020, ApJ, 904, 126
Chael, A. A., Johnson, M. D., Bouman, K. L., et al. 2018, ApJ, 857, 23
Chael, A. A., Johnson, M. D., Narayan, R., et al. 2016, ApJ, 829, 11
Cheng, X. P., An, T., Frey, S., et al. 2020, ApJS, 247, 57
Contopoulos, I., Gabuzda, D., & Kylafis, N. 2015, 414
Cotton, W. D., Geldzahler, B. J., Marcaide, J. M., et al. 1984, ApJ, 286, 503
Event Horizon Telescope Collaboration, Akiyama, K., Algaba, J. C., et al. 2021, The Astrophysical Journal Letters, 910, L12
Gabuzda, D. 2018, Galaxies, 6, 9
Heeschen, D. S. 1973, ApJ, 179, L93
Hodge, M. A., Lister, M. L., Aller, M. F., et al. 2018, ApJ, 862, 151
Homan, D., Hovatta, T., Kovalev, Y., et al. 2018, Galaxies, 6, 17
Homan, D. C., Attridge, J. M., & Wardle, J. F. C. 2001, ApJ, 556, 113
Homan, D. C. & Lister, M. 2006, The Astronomical Journal, 131, 1262
Homan, D. C., Lister, M. L., Aller, H. D., Aller, M. F., & Wardle, J. F. C. 2009, ApJ, 696, 328
Homan, D. C. & Wardle, J. F. C. 1999, AJ, 118, 1942
Homan, D. C. & Wardle, J. F. C. 2004, Astrophys. J. Lett., 602, L13
Issaoun, S., Wielgus, M., Jorstad, S., et al. 2022, ApJ, 934, 145
Jorstad, S., Wielgus, M., Lico, R., et al. 2023, ApJ, 943, 170
Jorstad, S. G., Marscher, A. P., Morozova, D. A., et al. 2017, ApJ, 846, 98
Kellermann, K. I., Sramek, R., Schmidt, M., Shaffer, D. B., & Green, R. 1989, AJ, 98, 1195
Kinman, T. D. & Conklin, E. K. 1971, Astrophys. Lett., 9, 147
Kramer, J. A. & MacDonald, N. R. 2021, A&A, 656, A143
MacDonald, N. 2017, Galaxies, 5, 82
MacDonald, N. R., Jorstad, S. G., & Marscher, A. P. 2017, ApJ, 850, 87
Martí-Vidal, I., Mus, A., Janssen, M., de Vicente, P., & González, J. 2021, A&A, 646, A52
Müller, H. & Lobanov, A. P. 2022, A&A, 666, A137
Müller, H. & Lobanov, A. P. 2023a, A&A, 673, A151
Müller, H. & Lobanov, A. P. 2023b, A&A, 672, A26
Müller, H., Mus, A., & Lobanov, A. 2023, A&A, 675, A60
Mus, A., Müller, H., & Lobanov, A. 2023, in prep.
Pacholczyk, A. 1970, Radio Astrophysics: Nonthermal Processes in Galactic and Extragalactic Sources, Astronomy and Astrophysics Series (W. H. Freeman)
Palma, N. I., Böttcher, M., de la Calle, I., et al. 2011, ApJ, 735, 60
Park, J., Byun, D.-Y., Asada, K., & Yun, Y. 2021, ApJ, 906, 85
Pashchenko, I. N., Kravchenko, E. V., Nokhrina, E. E., & Nikonov, A. S. 2023, MNRAS, 523, 1247
Pushkarev, A., Kovalev, Y., Lister, M., et al. 2017, Galaxies, 5, 93
Pushkarev, A. B., Aller, H. D., Aller, M. F., et al. 2023, MNRAS, 520, 6053
Rayner, D. P., Norris, R. P., & Sault, R. J. 2000, MNRAS, 319, 484
Roberts, D. H. & Wardle, J. F. C. 1986, in Quasars, ed. G. Swarup & V. K. Kapahi, Vol. 119, 141
Rudnick, L., Owen, F. N., Jones, T. W., Puschell, J. J., & Stein, W. A. 1978, ApJ, 225, L5
Smirnov, O. M. 2011, A&A, 527, A106
Tiede, P. 2022, The Journal of Open Source Software, 7, 4457
Troja, E., Lipunov, V. M., Mundell, C. G., et al. 2017, Nature, 547, 425
Vitrishchak, V. M., Gabuzda, D. C., Algaba, J. C., et al. 2008, Monthly Notices of the Royal Astronomical Society, 391, 124
Wagner, S., Camenzind, M., Dreissigacker, O., et al. 1995, Astronomy and Astrophysics, v. 298, p. 688, 298, 688
Wardle, J. 1971, Astrophysical Letters, Vol. 8, p. 183-186, 8, 183
Wardle, J. 2021, Galaxies, 9, 52
Wardle, J. F. C., Homan, D. C., Ojha, R., & Roberts, D. H. 1998, Nature, 395, 457
Zensus, J., Cohen, M., & Unwin, S. 1995, Astrophysical Journal, Part 1 (ISSN 0004-637X), vol. 443, no. 1, p. 35-53, 443, 35
Zobnina, D. I., Aller, H. D., Aller, M. F., et al. 2023, MNRAS, 523, 3615

[6] https://github.com/hmuellergoe/mrbeam
[7] https://github.com/achael/eht-imaging
[8] https://github.com/regpy/regpy
[9] https://github.com/flomertens/wise

7 | Hybrid fluid-particle jet simulations and the importance of synchrotron radiative losses

This chapter contains the manuscript of an extended numerical study soon to be submitted to Astronomy and Astrophysics.

Relativistic jets found in active galactic nuclei are renowned for their remarkable energy output consisting mostly of synchrotron radiation in the radio band. Imaging this emission is crucial to compare its morphology to the exciting physical discoveries from three dimensional relativistic magnetohydrodynamic (RMHD) simulations with observed jet polarization in the radio regime. In the following manuscript, three dimensional hybrid fluid-particle relativistic magnetohydrodynamic (RMHD) jet simulations using the PLUTO code were employed to prove the necessity of the inclusion of particle physics. In detail, by incorporating particle physics, numerical simulations are able to account for diffusive shock acceleration, instabilities, turbulence, and radiative losses. These simulations enable to reduce commonly made assumptions by considering non-thermal particle attributes to account for the resulting non-thermal synchrotron radiation. By using polarized radiative transfer and ray-tracing with the software RADMC-3D, we highlight the differences in total intensity maps when employing various simulation approaches: (i) RMHD approach without the use of jet tracers, which are numerical tools to arbitrarily and numerically exclude the simulated ambient medium around the jet, (ii) RMHD approach with an applied jet tracer, and (iii) hybrid fluid-particle approach.

In particular, the results presented in this manuscript incorporate a new Lagrangian particle module integrated into the latest version of the PLUTO code[1]. Lagrangian particles are macro-particles consisting of numerous non-thermal micro-particles, such as electrons. This advanced module features a state-of-the-art algorithm for modeling diffusive shock acceleration and synchrotron cooling within RMHD jet simulations. By

[1]It is noted that this module is non-public and used under a non-disclosure agreement in collaboration with the main developer team.

utilizing this module, the results provide accuracy in physical components that were previously missing in RMHD jet simulations (Kramer and MacDonald, 2021), such as the consideration of a cooled ambient medium and the enhancement of the distinction between the jet's innermost structure and the backflowing material.

In the investigations of the manuscript, three significant findings are demonstrated: (1) Plugging a purely toroidal magnetic field intrinsically into the relativistic jet results in an edge-brightening, which successfully mimics the radio emission of the Seyfert II galaxy Centaurus A. (2) These results illustrate the need of incorporating synchrotron losses and showcase the improvements achieved by directly accounting for non-thermal radiation through non-thermal particles. (3) Including a variable spectral index into polarized synchrotron emission maps reveals the transition of an optically thick upstream and an optically thin emission downstream of the jet.

In this study, I develop a description of the relativistic jet using the Lagrangian particle module of the PLUTO code (Mignone et al., 2007; Vaidya et al., 2018). The simulations are executed on the The Max Planck Computing and Data Facility (MPCDF)[2], and I generate the figures representing the numerical steps in the paper. Additionally, I design a flexible python pipeline by making use of the python `SciPy` 'interpolate' (griddata) library[3] to post-process the simulated data, which involved calculating non-thermal variables in form of a three dimensional Cartesian grid and generating files suitable for RADMC-3D. For the radiative transfer calculations and emission in full Stokes, co-author N. MacDonald provides the numerical radiative transfer module in RADMC-3D. The final synthetic polarized emission maps are generated by myself. Finally, I compose the text for the manuscript and refine it through discussions and extensive collaboration with D. Mukherjee. The manuscript will be submitted for publication to Astronomy & Astrophysics.

[2]For information visit the MPCDF's website.
[3]A detailed description of `SciPy` interpolate can be found here.

Astronomy & Astrophysics manuscript no. output
August 13, 2023

3D Hybrid fluid-particle jet simulations and the importance of synchrotron radiative losses

Joana A. Kramer[1,*] and Nicholas R. MacDonald[1,2]

[1]Max-Planck-Institut für Radioastronomie, Auf dem Hügel 69, D- 53121 Bonn, Germany
[2]Department of Physics and Astronomy, 108 Lewis Hall, University of Mississippi, Oxford, MS 38677-1848, USA
*e-mail: jkramer@mpifr-bonn.mpg.de

ABSTRACT

Context. Relativistic jets in active galactic nuclei (AGN) are known for their exceptional energy output, and imaging the synthetic synchrotron emission of numerical jet simulations is essential for a comparison with observed jet polarization emission.
Aims. Through the use of three dimensional hybrid fluid-particle jet simulations (with the PLUTO code), we manage to reduce commonly made assumptions in (G)RMHD simulations by using non-thermal particle attributes to account for the resulting synchrotron radiation. Polarized radiative transfer and ray tracing (via the RADMC-3D code) highlight the differences in total intensity maps when (i) the jet is simulated purely with the RMHD approach, (ii) a jet tracer is considered in the RMHD approach, and (iii) a hybrid fluid-particle approach is chosen. The resulting emission maps are compared to the example of the radio galaxy Centaurus A.
Methods. We use the Lagrangian particle module implemented in the latest version of the PLUTO code. This new module contains a state-of-the-art algorithm for modeling diffusive shock acceleration and for accounting for radiative losses in RMHD jet simulations. The module implements the physical postulates missing in RMHD jet simulations by accounting for a cooled ambient medium and strengthening the central jet emission.
Results. We result in a distinction of the innermost structure of the jet and the backflowing material in (1.) mimicking the radio emission of the Seyfert II radio galaxy Centaurus A, when considering an edge-brightened jet with an underlying purely toroidal magnetic field, and (2.) demonstrating the necessity of synchrotron cooling and show the improvements of directly accounting for non-thermal synchrotron radiation via non-thermal particles.

Key words. polarization – magnetic field morphology – active galactic nuclei – jets

1. Introduction

Active galactic nuclei (AGN) are supermassive black holes (SMBH) that actively accrete matter, forming highly energetic, bright, compact objects in the centers of galaxies (Rees 1966). Approximately 10 % of AGN are classified as radio-loud, characterized by the presence of large-scale jets that remain collimated up to kiloparsec scales (Homan et al. 2018). Radio-loud AGN encompass various classes, including radio galaxies and blazars, which differ in orientation with respect to our line of sight. While radio galaxies and blazars are believed to be the same intrinsic object, blazars possess jets that are increasingly aligned with our line of sight (Urry & Padovani 1995).

The magnetic field in AGN can be determined through observations of power-law spectra and polarization signals. The strength of the intrinsic magnetic field is measured using the power-law cut off of the energy distribution of the non-thermal particle, while the field's direction is inferred from polarization measurements, particularly from detection of polarized non-thermal synchrotron emission (Meisenheimer & Roeser 1986; Carilli et al. 1999; Heavens & Meisenheimer 1987; Brunetti et al. 2003).

Astrophysical jets associated with AGN are thought to carry helical magnetic field configurations during their launch. However, the role of these helical fields on the largest scales of the jets, far from the central engine, remains unclear. The synchrotron emission from these jets exhibits high linear polarization (LP; up to 60−70 %, see, e.g., Rybicki & Lightman 1979), and weaker circular polarization (CP; $\sim$ 1 %) providing valuable insights into the intrinsic magnetic field structure (see, e.g., Tsunetoe et al. 2020). Numerical studies reveal that CP has the potential to distinguish between poloidal and toroidal magnetic field morphologies within the relativistic jets (Kramer & MacDonald 2021).

Multi-wavelength observations, spanning from radio to high-energy gamma rays, offer valuable insights on the micro-physical processes occurring within AGN jets and contributing to the observed radiation (EHT MWL Science Working Group et al. 2021). These micro-physical processes (Pontin & Priest 2022) operate at scales several orders of magnitude smaller than the overall jet scales. Bridging the gap between these scales presents a significant challenge for theoretical models of AGN jet emissions.

Due to the inability to reproduce relativistic jets in laboratories, numerical simulations are the primary means of exploring the underlying physics (Bellan 2018). AGN jets can be effectively modeled as plasma since the Larmor radius of the jet particles is much smaller than the spatial scales of the system (Blandford & Rees 1974). Recently, a numerical tool has been developed within the PLUTO code to simulate multi-dimensional flow patterns, incorporating small-scale processes in a sub-grid manner (Mignone et al. 2007; Vaidya et al. 2018).

In general, synchrotron emission signatures from large-scale jets are obtained through time-dependent simulations and post-processing. In relativistic hydrodynamic contexts, transfer functions between thermal and non-thermal electrons are implemented. In the case of relativistic magnetohydrodynamic (RMHD) calculations, the internal magnetic structure of the jet and parameters of the energy distribution are used to compute synchrotron emission maps (Porth et al. 2011; Mizuno et al. 2015; Fromm et al. 2016; Kramer & MacDonald 2021).

To study the micro-physics of particle acceleration at shocks, hybrid implementations that combine particle and grid-based fluid descriptions have been developed, targeting different scales of interest. The Particle in Cell (PIC) approach is often employed to understand shock acceleration at relativistic shocks, particularly at the scales of the *electron* gyro radius. Hybrid MHD-PIC approaches enable the study of shock acceleration phenomena at slightly larger length scales, typically in the order of a few thousand *proton* gyro-scales. These approaches describe the interaction between collisionless cosmic ray particles and a thermal plasma, capturing small-scale kinetic effects in magnetosphere simulations (e.g., Bai et al. 2015; van Marle et al. 2018; Mignone et al. 2018; Daldorff et al. 2014). Recently, Dubey et al. (2023) explored the behavior of the observable emission from particles encountering various shock acceleration mechanisms within the jet stream in hybrid (R)MHD-particle simulations.

For relativistic hydrodynamic flows, the inclusion of non-thermal particle (NTPs) populations allows to study non-thermal emission from internal shocks in blazars (Mimica et al. 2009, 2012; Porth et al. 2011; Fromm et al. 2016). In these models, a simplifying assumption is often made by assuming a constant value for the power-law index governing particle injection at shocks ($N(E) \propto E^{-s}$), with values such as $s = 2.0$ (de la Cita et al. 2016), $s = 2.23$ (Fromm et al. 2016), and $s = 2.3$ (Kramer & MacDonald 2021).

New methods have been developed by Vaidya et al. (2018) to overcome the aforementioned limitations and establish a state-of-the-art hybrid framework for particle transport. This framework aims to model high-energy non-thermal emission by including Lagrangian particles from large-scale 3D RMHD simulations. This is achieved by utilizing the magnetic field from the underlying RMHD simulation to calculate radiative losses, such as synchrotron cooling. The hybrid framework can be compared with observations by incorporating micro-physical aspects of spectral evolution based on local fluid conditions.

The emission from the accelerated charged particles within jets, in various types of AGN, e.g., blazars and Seyfert II radio galaxies such as Centaurus A, is being both beamed and boosted. Relativistic plasma and magnetic fields in AGN jets give rise to incoherent synchrotron emission components spanning from radio to optical, UV, or even X-rays, exhibiting linear and circular polarization. The polarization parameters carry information about the jet's physical conditions, including the magnetic field strength, topology, particle density, and plasma composition (Wardle et al. 1998).

This paper is organized as follows: In Sect. 2, we provide an introduction to the principles of hybrid fluid-particle simulations via the PLUTO code with the focus on Lagrangian particles (i.e., macro-particles consisting of numerous non-thermal micro-particles). We introduce the principles of particle physics within numerical jet simulations, i.e., the inclusion of radiative losses. We further focus on the numerical implementation of our relativistic jet simulations, along with the explanation of the post-process generated three dimensional grid solely from non-thermal particle attributes. We make use of the python interpolation module `SciPy`. Section 3 outlines our applied method for calculating synthetic polarized synchrotron emission maps from particle simulations of jets via the software RADMC-3D. Section 4 explains the investigation of the hybrid-fluid jet simulation, the advantages of particle physics, as well as the polarization characteristics while intrinsically carrying a purely toroidal magnetic field morphology. Our comparison between the numerical outcome of RMHD and hybrid fluid-particle simulations of jets as well as a comparison to observations of the radio galaxy Centaurus A (Janssen et al. 2021) is presented in Sect. 5. Lastly, our findings and conclusions are summarized in Sect. 6.

2. Lagrangian Module

In recent years, researchers have recognized the importance of incorporating Lagrangian particles into (R)MHD simulations to gain deeper insights into the behavior of the jet plasma. Lagrangian particles are individual tracer elements that move with the thermal jet flow, providing valuable information about the fluid's characteristics, such as its velocity, density, and magnetic field strength. By following the trajectories of these particles, we can track the transport and mixing of different plasma components. By this, we examine the impact of magnetic fields on particle dynamics, and study various physical processes occurring within the jet. The use of Lagrangian particles in RMHD jet simulations allows us to perform a more detailed analysis of the complex phenomena taking place in these astrophysical systems. Hence, this approach enables the study of important processes, including particle acceleration mechanisms, the formation and propagation of shocks, and the *effect of radiative losses* within the relativistic jet.

2.1. Cosmic Ray Transport Equation

The reduced cosmic ray transport equation for the relativistic case (Webb 1989) considers particle transport by both convection and diffusion, and the particle's evolution in momentum space, i.e., energy changes due to adiabatic expansion and losses due to radiation. In particular, the time evolution of the non-thermal particle (NTP) is governed by the following expression:

$$\frac{\mathrm{d}n_e(\gamma)}{\mathrm{d}\tau} + \frac{\partial}{\partial E}\left[\left(-\frac{E}{3}\nabla_\mu u^\mu + \dot{E}_l\right) n_e(\gamma)\right] = -n_e(\gamma)\nabla_\mu u^\mu, \quad (1)$$

This paper focuses on the second term ($\dot{E}_l$), to account explicitly for synchrotron losses (Vaidya et al. 2018).

Equation 1 is solved in two steps. In the first step, the particle positions $\mathbf{x}_p$ are evolved in time according to:

$$\frac{\mathrm{d}\mathbf{x}_p}{\mathrm{d}t} = \mathbf{v}_p = \mathbf{v}(\mathbf{x} \rightarrow \mathbf{x}_p), \quad (2)$$

where $\mathbf{v}_p$ is the particle velocity[1]. This velocity is given by the fluid velocity $\mathbf{v}(\mathbf{x} \rightarrow \mathbf{x}_p)$ interpolated at the particle's position. The fluid velocity is computed via the fluid equations:

$$\frac{\partial \mathbf{U}}{\partial t} + \nabla\,\mathbf{F} = 0, \quad (3)$$

where $\mathbf{U}$ represents conservative variables, $\mathbf{F}$ represents the flux terms of a generic problem. The second step, which considers energy losses, updates the particle's energy distribution by solving the energy part of Eq. 1.

[1] The solution is performed using a second-order Runge-Kutta scheme.

2.2. Synchrotron Losses

The energy distribution of each macro particle is continuously updated over time, i.e., the code keeps track of the particle's parameters at a given position on the Cartesian grid (according to Eq. 2). The particle attributes are transferred in each numerical step and solved for the particle's energy losses:

$$\frac{\mathrm{d}E}{\mathrm{d}\tau_{\mathrm{p}}} = -c_1\left(\tau_{\mathrm{p}}\right)E - c_2\left(\tau_{\mathrm{p}}\right)E^2 \equiv \dot{E}. \tag{4}$$

In Eq. 4, the first term represents the energy loss resulting from adiabatic expansion, while the second term represents the combined energy loss from synchrotron radiation and inverse Compton scattering off the cosmic microwave background. The physical constants c_1 and c_2 are given as follows:

$$c_1 = \frac{\nabla_\mu u^\mu}{3} = \frac{1}{3\rho}\frac{\mathrm{d}\rho}{\mathrm{d}\tau_{\mathrm{p}}},$$
$$c_2 = \frac{4\sigma_{\mathrm{T}} c\beta^2}{3m_e^2c^4}\left[U_{\mathrm{B}} + U_{\mathrm{rad}}\left(E_{\mathrm{ph}}\right)\right] \tag{5}$$

The Thomson cross-section, denoted as σ_{T}, represents the scattering efficiency. The quantities U_{B} and U_{rad} correspond to the energy densities of the magnetic field and the radiation field, respectively. E_{ph} represents the energy of the incident photon from the cosmic microwave background (Vaidya et al. 2018).

2.3. Numerical Implementation

To facilitate numerical calculations, it is more convenient to modify Eq. 4 by incorporating the energy-dependent number density ratio $\chi(E)$, which signifies the normalized quantity of electrons relative to the fluid number density. The considered Lagrangian macro-particles represent ensembles of NTPs with finite energy distributions and follow underlying fluid streamlines. The fundamental flow is calculated via the RMHD module within PLUTO. Details on the principles of the RMHD module and physical scaling are provided in Kramer & MacDonald (2021), based on Mignone et al. (2007). The implementation of the magnetic field remains the same as in Kramer & MacDonald (2021), while this paper focuses on a purely toroidal magnetic field prescription ($\sigma_\phi = 1$).

PLUTO stores the number density ratio $\chi(E)$ of the NPTs in logarithmically separated energy bins $E_{\min} \leqslant E_{\mathrm{bin}} \leqslant E_{\max}$. We assume an initial energy distribution $\chi^0(E_{\mathrm{bin}})$ of the NTPs which follows a global power-law distribution

$$\chi^0\left(E_{\mathrm{bin}}\right) = \frac{N_{\mathrm{e}}}{n^0}\left(\frac{1-s}{E_{\max}^{1-s} - E_{\min}^{1-s}}\right)E_{\mathrm{bin}}^{-s}. \tag{6}$$

The spectral index α, which is needed to calculate the resulting synchrotron emission, relates to the power-law index s via $\alpha = (s-1)/2$. N_{e} represents the initial number density of physical particles, and n^0 the initial number density of the fluid (Vaidya et al. 2018). Their ratio equals the total number of micro particles, i.e.,

$$\frac{N_e}{n^0} = \int_{E_{\min}}^{E_{\max}} \chi(E)\,\mathrm{d}E = \sum_{\mathrm{bins}} \chi\left(E_{\mathrm{bin}}\right)\,\delta E_{\mathrm{bin}}, \tag{7}$$

which reads as the sum over the height $\chi(E_{\mathrm{bin}})$ and width $\delta E_{\min}$ of distinct micro-particle bins. In detail, this formulation calculates the total energy/area under the distribution per macro-particle in the spectra illustrated in Fig. 1. The code refers to this as n_{micro}.

To calculate the synthetic non-thermal synchrotron emission from the Lagrangian particle attributes, we rewrite the applied power-law in terms of Lorentz factor γ, i.e., $E = \gamma m_e c^2$. Similar to the second study conducted in Kramer & MacDonald (2021), we fix an initial scale between the lower energy cut-off $\gamma_{\min} = 10$ and the upper limit $\gamma_{\max} = \gamma_{\min} \cdot 10^6$. Equivalent to Kramer & MacDonald (2021), we transfer our three dimensional grid values in units of the magnetic field , the normalization constant of the power-law, and the lower energy cutoff of the power-law, to RADMC-3D. In order to derive the normalization constant we want to mimic the electron power-law distribution $n_e(\gamma) = n_0\left(\frac{\gamma}{\gamma_{\min}}\right)^{-s}$ for $\gamma_{\min} \leqslant \gamma \leqslant \gamma_{\max}$. Together with the continuous equivalent of Eq. 6, we arrive at the normalization constant

$$n_0 = \frac{(1-s)\,n_{\mathrm{micro}}}{\gamma_{\min}^s\left(\gamma_{\max}^{1-s} - \gamma_{\min}^{1-s}\right)}. \tag{8}$$

The particle attributes such as $\chi(E_{\mathrm{bin}})$ are evolved during the code. In a post-process step, we estimate the normalization constant n_0 from the lower energy cut off $\gamma_{\min}(E_{\min})$, and the spectral index α (i.e., power-law index s) between two neighbored energy bins at a certain energy E_{r}. This energy identifies with a desired frequency ν_{r} in the radio regime. The values for n_0, $\gamma_{\min}$, and α for each particle at a specific epoch within the simulation are estimated and interpolated on a three dimensional Cartesian grid (details are described in the following in Sec. 2.4).

At this point, we are applying physical units to the non-dimensional grid units:

$$\rho_{\mathrm{cgs}} = \rho \cdot \rho_0,$$
$$p_{\mathrm{cgs}} = p \cdot \rho_0 v_0^2,$$
$$\mathbf{B}_{\mathrm{cgs}} = \mathbf{B} \cdot \sqrt{4\pi\rho_0 v_0^2}, \tag{9}$$

where ρ, p, and $\mathbf{B}$ define the dimensionless grid values. For all our simulations we specify the following unit values: $\rho_0 \simeq 1.0 \cdot 10^{-21}\,\mathrm{g\,cm^{-3}}$, $L_0 \simeq 3.0857 \cdot 10^{16}\,\mathrm{cm}$, and $v_0 \simeq 2.998 \cdot 10^{10}\,\mathrm{cm\,s^{-1}}$. With this choice of values, the magnetic field strength along the jet will be of the order of gauss (G) to mG. n_{micro} scales in $[\rho_0\, m_{\mathrm{u}}]$, with the atomic mass unit $m_{\mathrm{u,cgs}} \simeq 1.661 \cdot 10^{-24}\,\mathrm{g}$. The jet radius $r_j = \sqrt{(x-x_c)^2 + (y-y_c)^2}$ equals the radius of the particle injection zone. For the injection of the particles we are applying an initial spectral index $\alpha = 2.0$ and an initially considered area within the particle distribution $n_{\mathrm{micro}} = 0.001$ (in code units), before these parameter evolve with the simulation.

2.4. Post-processing

The generation of (polarized) synthetic synchrotron emission maps using the software RADMC-3D requires the normalization constant n_0, the lower-energy cutoff $\gamma_{\min}$, and the spectral index α (i.e., the power-law index s) from the NPTs energy distribution $\chi(E_{\mathrm{bin}})$. However, radiative losses such as synchrotron cooling influence the tail end of the initial power-law distribution.

Figure 1 shows the spectrum over dimensionless energy bins E_{bin} of a Lagrangian macro-particle for different simulated epochs. The spectrum is mimicking the energy loss by synchrotron cooling. The particle starts to appear on the grid at epoch 20 (turquoise, most right) and looses energy while moving within the jet stream and eventually beyond the jet stream. The energy loss is more pronounced when leaving the jet flow

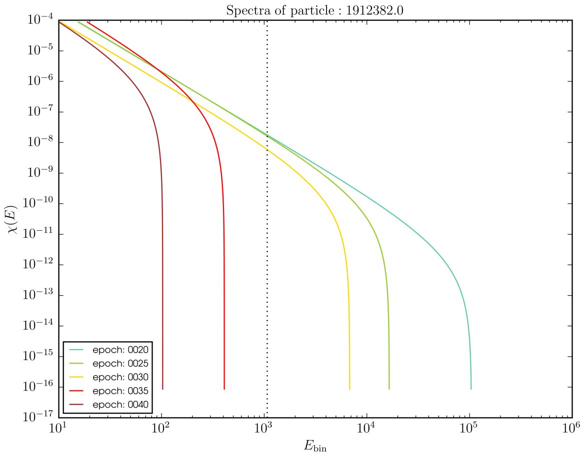

Fig. 1: Normalized spectral distribution in dimensionless grid units of a representative macro-particle of identification number 1912382. The corresponding Lagrangian particle is located in the jet's bulk before entering the back-flow. The initial dimensionless energy bins are chosen to be within $10 \leqslant E_{\text{bin}} \leqslant 10^7$. The particle appears on the grid at epoch 20 carrying an 'energy' at an energy bin of $\sim 10^5$. The radiative losses are visible in moving from higher energy to lower energy in time (or simulated epochs) from right to left. The most left epoch illustrates a 'cooled' particle with an energy corresponding to an energy bin of $\sim 10^2$.

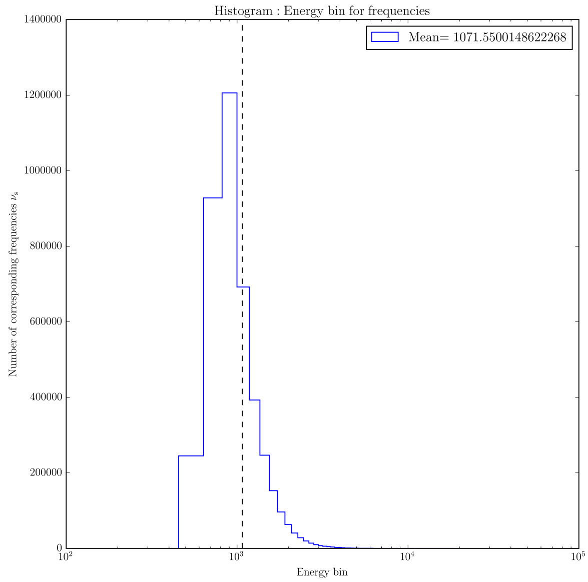

Fig. 2: The histogram represents the number of particles per energy bin with a corresponding frequency of $\nu_{\text{r}} = 86\,\text{GHz}$. The maximum value of particles within the same bin is approximately 1200000 out of 4171200 simulated particles. The mean energy bin, being 1071.55, excludes 1998996 particles from further calculations.

in epoch 35 (red, second from left), after which the particle continues to 'cool' down to simulation epoch 40 (brown, most left). The particle in Fig. 1 represents a Lagrangian particle right after leaving the jet stream, located in the jet bulk before entering the back-flow in epoch 38.

In each distinct time step, the particle encounters the effect of synchrotron cooling, also referred to as synchrotron aging. The left part of the energy distribution can be described by the power-law distribution in Eq. 6. However, the right tail end can not be described by a simple power-law due to radiative losses (compare Fig. 1). We focus our attention in this work on the power-law distribution of the particle by excluding the steep tail end in a post-process step. We achieve this by calculating the spectral index α, i.e., the power-law index s in a given epoch at a given energy $E_{\text{r}} = \gamma_{\text{r}} m_e c^2$ (corresponding to an observational radio frequency) as the slope between two neighboring energy bins around E_{r} (see vertical line in Fig. 1). This procedure ignores macro-particles that cooled away by synchrotron aging.

In order to decide on the energy E_r that removes cooled away macro-particles, we consider the final observational frequency ν_{r} of the synthetic polarized maps in the radio band. To obtain the relativistic energy E_{r} for the estimation of the spectral index α, we consider the critical frequency where most of the synchrotron power is emitted that, as a function of the unit magnetic field B, is given by

$$\nu_{\text{r}} \sim \frac{\gamma_{\text{r}}^2 e B}{2\pi m_e c}, \tag{10}$$

with the electron charge e (Condon & Ransom 2016). Further, we consider Doppler boosting that has to be accounted for when moving from the emitter's frame to the observer's frame. PLUTO simulates the intrinsic emission of the source, i.e., the emitter's frame and corresponding 'frequency'. To convert the intrinsic emission's frequency to the observer's frequency as seen in observations, and as imaged in our ray-traced maps by the RADMC-3D code, we have to account for relativistic effects. The relation between the frequencies reads

$$\nu_{\text{r}} = \frac{\nu_{\text{s}}}{\Gamma\,(1 + \beta \cos\theta_{\text{r}})}, \tag{11}$$

where ν_{r} is the received frequency, and ν_{s} the emitted frequency of the source. Their relation is a function of the relativistic velocity $\beta = {}^{v}\!/_{c} = 1$, and the observed viewing angle θ_{r}. We assume a bulk Lorentz factor of $\Gamma = 7.088$.

Equation 10 depends on the intrinsic magnetic field within the PLUTO simulation at the macro-particle positions. Hence, E_{r} slightly differs for each macro-particle, as depicted in Fig. 2. The histogram represents the number of particles at a corresponding energy bin with a chosen frequency of $\nu_{\text{r}} = 86\,\text{GHz}$. For simplicity, we use the mean value of the energy bins, i.e., $\langle E_{\text{r}} \rangle = 1071.55$, for the estimation of the spectral index α and the decision whether a macro-particle cooled off or not (see vertical line in Figs. 1–2. We checked that individual values E_{r} leave our results unchanged. That way we exclude 1998996 particles that already lost a significant amount of energy, out of 4171200 initially considered particles.

Finally, our post-processing code based on Eq. 10 and Eq. 11 results in values for n_0, γ_{min}, and α at the irregular macro-particle positions within the jet flow of the hybrid fluid-particle simulation. A subsequent interpolation yields the corresponding values on a three dimensional Cartesian grid. This serves as an input

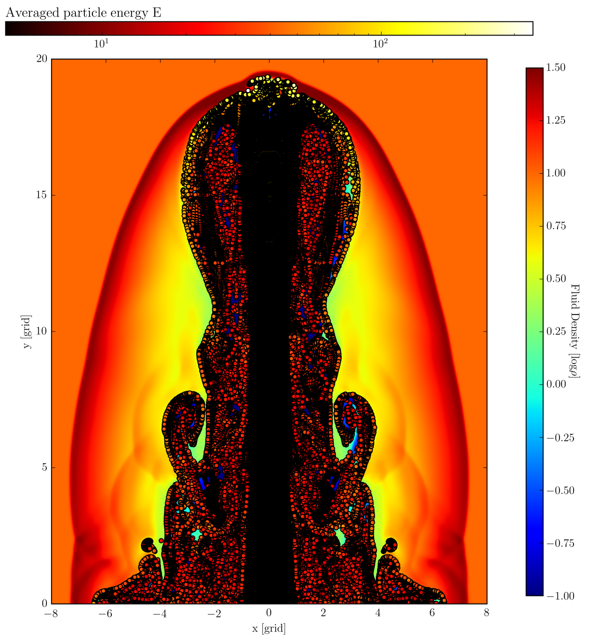

Fig. 3: The figure illustrates a two-dimensional slice of a three-dimensional hybrid fluid-particle simulation. The underlying fluid is colorcoded in density in dimensionless grid units. The overplotted particle population is colorcoded in averaged particle energy in dimensionless grid units, following the underlying jet stream. The figure shows simulation epoch 38, which represents the last epoch before the jet stream would move off-grid.

to RADMC-3D which generates the synthetic synchrotron emission maps. Our post-processing improves our synthetic polarized maps in terms of comparability to observational data. The variable spectral index accounts for opacity effects visible when comparing different observational frequencies. A discussion on that is outlined in App. B. In detail, we will form a variable spectral index cube representing different spectral indices at different regions within the jet (simulation).

We consider the epoch of the jet simulation that is captured in Figure 3 in which the jet's hot spot or terminal shock has not yet propagated off the grid. The figure shows a two dimensional slice through the three dimensional jet simulation and particle population. The particle distribution is color coded in energy on top of the thermal fluid motion color coded in density, both in dimensionless grid units. The particle distribution, injected into the simulation through the jet nozzle, follows the motion and speed of the underlying fluid including the backflow motion of the jet. The particles encountered the influence of the features within the jet stream, for instance, being affected by the recollimation shock.

The detailed steps, following our illustrated pipeline in Fig. 4, are:

1. Panel *(a)*: The particle distribution is separated from the underlying fluid and the position of the macro particle is stored. The distinct particles are illustrated without hard edges. This step highlights the energetic losses of the particles when leaving the jet stream. Additionally, the affect of the recollimation shock, i.e., increasing the particle's energy, can be seen in the depicted image.
2. Panel *(b)*: We interpolate attributes of particles that did not cool off yet at their scattered positions from step 1 on a Cartesian grid. We interpolate the spectral index α (power-law slope s) from the resultant slope of the energy distribution in Fig. 1 at the energy E_r. By setting a spectral index for the strongly cooled particles, which is not considered in the radiative transfer calculations (Jones & Odell 1977), we define subsequently which particles are removed from all interpolations.
3. Panel *(c)*: Similar to step 2, we interpolate the lower energy cut-off $\gamma_{\min}$, that is, the lowest energy bin per particle of the simulated power law distribution in dimensionless units.
4. Panel *(d)*: In a similar manner, we compute the normalization constant n_0 from $\gamma_{\min}$ and the power-law index s (see Eq. 8) of the energy distribution in Eq. 6 at a desired frequency, and therefore at an energy E_r.

Finally, we read out the magnetic field along all directions $B_{x,y,z}$, the lower energy cut-off $\gamma_{\min}$, the normalization constant n_0, and the spectral index α on a full three dimensional Cartesian grid into files adjusted for RADMC-3D. In all our RMHD jet simulations, each computational box consists of $320 \times 320 \times 400$ zones, and we set the viewing distance of the source at a redshift of $z = 0.002$ (Rothschild et al. 2011). The individual scaled cell size is 0.01 parsec (pc). For all the images presented in Sect. 4, we use an observing frequency of $\nu_s = 86\,\mathrm{GHz}$.

3. Synthetic Polarized Emission Calculations

RADMC-3D is a well tested and documented ray-tracing code to solve for astrophysical radiative transfer problems (Dullemond et al. 2012). RADMC-3D solves along each individual ray for the Stokes parameters I, Q, U, V (total intensity, linear polarization, and circular polarization, respectively), while accounting for synchrotron absorption, emissivity, Faraday conversion, as well as Faraday rotation. The solution of the emitted polarized synchrotron radiation is a function of optical depth, the normalization constant n_0, the low-energy cutoff $\gamma_{\min}$ of the power-law distribution in Eq. 6, the strength of the magnetic field, and its orientation to our line of sight. In contrast to Kramer & MacDonald (2021), we make use of the updated implementation of the full Stokes module in RAMDC-3D by MacDonald & Nishikawa (2021). This allows for an additional degree of freedom, i.e., a full rotational view of our three dimensional solution. Finally, we adapted the above described implementation to solve for a variable spectral index. This, in detail, will result in a co-dependence of the Stokes parameters on the spectral index. In detail, the newly implemented solution will apply the radiative transfer calculations along particle geodesics that connect the emitters with the observer. This involves two main steps: *(i)* A relativistic aberration correction is applied cell-by-cell to determine the angle between the local magnetic field vector of each cell and the observer's orientation relative to the jet axis, and *(ii)* a rotation correction is applied the same way to convert the linear polarization ellipse from the local co-moving frame to the plane of the sky. Further details on these corrections are published in MacDonald & Nishikawa (2021).[2]

Once the Stokes parameters are computed for each line of sight (corresponding to each pixel/ray in our synthetic maps), a

[2] Please note that we are not applying a slow-light approach in this work.

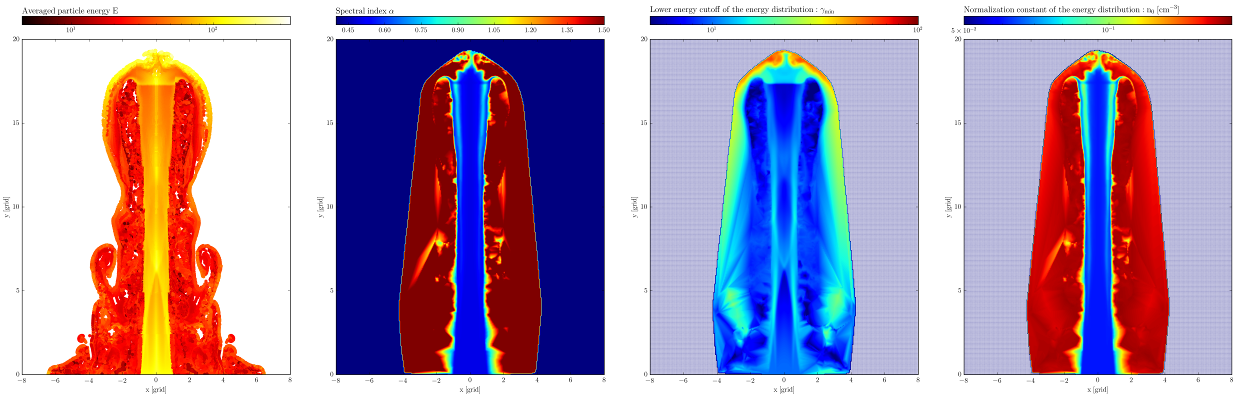

(*a*) (*b*) (*c*) (*d*)

Fig. 4: *From left to right*: a demonstration of our synthetic imaging pipeline. All figures represent a two-dimensional slice through our three-dimensional jet simulations. The pipeline starts to extract the particle population from the underlying fluid (see Fig. 3). The particle population in panel *(a)* is colorcoded in dimensionless averaged particle energy. The brighter color (white, yellow) represents higher energy as it is the case for the inner jet spine. The recollimation shock, i.e., a centralized region of higher energy, is visible in the jet's spine. The particles are 'cooled' by radiative losses (orange, red in color), and cool even more rapidly when leaving the jet flow. Panel *(b)*-(d) illustrate the interpolated particle values to form a grid of particle attributes (highest values in red): panel *(b)* highlights the lower energy cut-off $\gamma_{\rm min}$ of the particle's energy distribution. Panel *(c)* calculates and interpolates the normalization constant n_0 of the energy distribution onto a three-dimensional grid. The last panel *(d)* forms a three-dimensional grid of the spectral index α calculated from the spectrum's slope s of the energetic losses at a given frequency.

Doppler factor is introduced (see Eq. 11). This factor accounts for the velocity and angle variations of the larger jet structure and is used to transform the flux levels into the observer's frame.

4. Hybrid Fluid-Particle Jet Simulation Results

The PLUTO code calculates an optional jet tracer value for each cell in the simulated Eulerian grid, ranging from zero to one. A value close to one indicates that the cell belongs to the jet, while a value close to zero indicates a high presence of ambient medium. By selecting a cut-off value near unity, we can exclude the ambient medium from the input grid that RADMC-3D uses for ray-tracing to create full Stokes emission maps. This exclusion was necessary for the non-hybrid jet simulations presented in Kramer & MacDonald (2021), where we did not account for the effect of synchrotron cooling (specifically, a cut-off value of 0.75 was used, see **middle** panel in Fig. 5)[3]. Consequently, in these initial calculations, the ambient medium does not cool over time and emits as brightly as the jet (i.e., with no tracer: see **top** panel of Fig. 5). An alternative view of this is illustrated in Fig. A.1 and discussed in App. A. As a result, the jet is entirely obscured by the ambient medium in the absence of synchrotron cooling. In contrast, when we incorporate synchrotron cooling and particle acceleration (via our hybrid fluid-particle simulation), we can clearly observe the jet distinctly from the ambient medium (e.g., **bottom** panel of Fig. 5). This is achieved without using any jet tracer to arbitrarily exclude the emission of the ambient medium. The emission calculated solely from particle attributes confirms our findings in Kramer & MacDonald (2021), i.e., that the toroidal magnetic field configuration consistently results in emission concentrated along the edges of the jet. The applied simulations in this work produce an edge-brightened appearance in all presented synthetic synchrotron emission maps. Furthermore, the presence of both positive and negative circular polarization, visible in the jet emission, indicates the changing orientation of the jet's magnetic field relative to our line of sight (see Fig. 6).

4.1. Synthetic Polarized Maps

In our hybrid fluid-particle simulation, we once again investigate a toroidal magnetic field morphology within the jet. We select the toroidal magnetic field configuration to replicate the edge-brightening effect observed in the radio galaxy Centaurus A (Janssen et al. 2021; Kramer & MacDonald 2021). In Fig. 5, we compare the results of the non-particle approach, depicted in the first two panels (**top/middle** with/without a jet tracer), to the corresponding images obtained from the hybrid fluid-particle simulations, illustrated in the **bottom** panel. The figures display the total intensity of the jet's emission at an inclination of $i = 35.5°$, observed at 86 GHz (alternative frequencies are presented in Fig. B.1 and discussed in App. B). The image clearly demonstrates that the use of a tracer is unnecessary if the simulation accounts for radiative losses. This is stressed as we observe a distinct and well-defined jet structure in the hybrid fluid-particle simulation. We can further compare the resultant brightness of the jet (in Jansky per pixel). The difference between the bow shock's luminosity and the rest of the relativistic jet makes a noticeable impact on the resultant brightness. When the bow shock is *not* excluded from the simulation, on the contrary, very present, it outshines the jet structure completely. The bow shock seems to be two orders of magnitudes brighter (i.e., $\sim 2.4 \times 10^{-2}$ Jy/pixel) than the jet structure underneath ($\sim 2.8 \times 10^{-4}$ Jy/pixel). The brightness and structure of the hybrid-fluid particle simulation and the RMHD jet simulation (with an applied jet tracer) seem to be in agreement. The relativistic jet is carrying an underlying purely toroidal magnetic

[3] It is noteworthy that an additional cut of the grid is applied to the data in order to exclude the jet's bulk

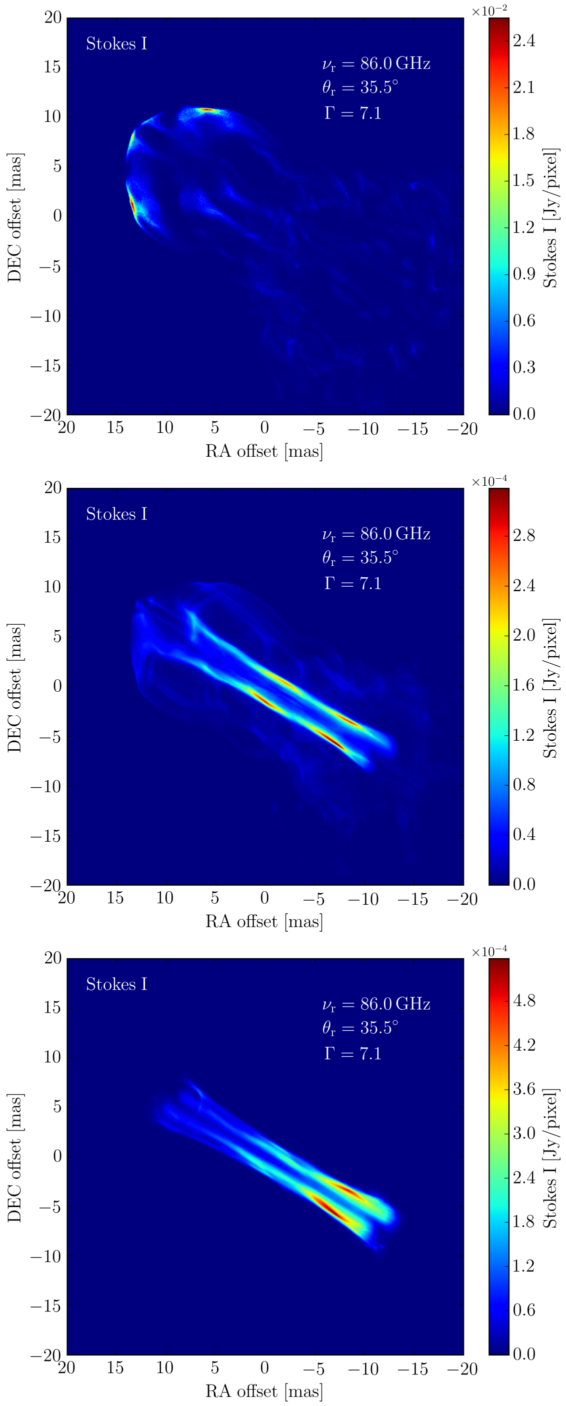

Fig. 5: Synthetic polarized total intensity maps of the 3D RMHD jet simulation generated without the use of a jet tracer illustrating mainly the emission of the ambient medium (**top**). A total intensity map of the 3D RMHD jet simulation applying an arbitrarily chosen jet tracer to exclude the ambient medium and highlight an edge-brightening jet is presented in the **middle** panel. The *final* 3D hybrid fluid-particle jet simulation pictures an edge-brightened jet emission while excluding the ambient medium by including radiative losses (**bottom**). All maps are ray-traced at 86 GHz and viewed at an observational angle of 35.5°.

field in all panels depicted in Fig. 5. The resultant structure resembles the results published in Kramer & MacDonald (2021). When the jet is visible, a sheath highlighting jet structure is observed. Both the hybrid fluid-particle jet and the RMHD jet show the behaviour of maximum luminosity in both edges close to the jet launching in the lower right part of the figures. The hybrid fluid-particle jet excludes more of the upstream-structure of the jet due to opacity effects incorporated into our calculations.

In Fig. 6, the **top** panel displays the linearly polarized intensity, which is calculated as the square root of the sum of the squares of the Stokes parameters Q and U. It also includes the electric vector position angles (EVPAs) represented by EVPAs $= 0.5 \arctan(U/Q)$. The EVPA can be interpreted to stress the intrinsic helix of the magnetic field. As the viewing angle is $i = 35.5°$, the jet is partially boosted/de-boosted to/away from out line of sight. The lower/left edge of the jet carries EVPAs oriented alongside to the jet's direction, highlighting a magnetic field that takes a turn around that edge. The upper/right edge of the jet shows EVPAs perpendicular to the jet's direction in the innermost part and a small rotation towards the edges. This would stress that the magnetic field moves along the jet before taking another turn around the edges. The **bottom** panel shows the circular polarization, i.e., Stokes V.

Furthermore, we compute the integrated levels of fractional polarization, which are flux-weighted averages of the Stokes parameters across the entire jet emission region in each set of images (Kim et al. 2019). These values are listed to the lower right in the linearly polarized and circularly polarized images of Fig. 6. The values are denoted as $\bar{m}_l \equiv \sqrt{\bar{Q}^2 + \bar{U}^2}/\bar{I}$ for linear polarization and $\bar{m}_c \equiv -\bar{V}/\bar{I}$ for circular polarization. The fractional linear polarization reads $m_l = 1.2 \times 10^1$ %, while the fractional circular polarization limits to $m_c = 4.1 \times 10^{-5}$ %. In circularly polarized synchrotron emission, we observe both positive and negative circular polarization, which emphasizes the dynamic changes in the orientation of the jet's magnetic field relative to our line of sight. This finding in our hybrid fluid-particle jet simulation agrees with the RMHD jet simulation presented in Kramer & MacDonald (2021).

5. Discussion

RMHD jet studies such as performed in Kramer & MacDonald (2021), lack a proper treatment of synchrotron losses and shock acceleration within each jet. To address these crucial effects in our ray-tracing analysis, we conduct a study focused on including relativistic macro-particles consisting of numerous micro-particles each carrying a distinct energy distribution, into fully three dimensional jet simulations. The particle distribution follows the underlying fluid stream, hence the definition of hybrid fluid-particle jet simulations. The macro-particle updates its attributes numerically in each time step based on the effects it is encountering by the underlying plasma. These particles track their attributes while concerning radiative synchrotron losses. Our spectral analysis of the particles' energy over time confirms that the particles in the relativistic jet experience synchrotron losses (see Fig. 1). While the particle undergoes evolution in tandem with the fluid, it undergoes a cooling process. Notably, higher-energy electrons within the macro-particle exhibit a more rapid cooling rate compared to their lower-energy counterparts. Consequently, the initial spectrum's high-energy tail experiences decay, leading to a subsequent reduction in the parameter $\gamma_{\max}$ (This finding is confirmed in Dubey et al. 2023).

Furthermore, particles that are impacted by the jet's recollimation shock are gaining energy (see Fig. 4 second image

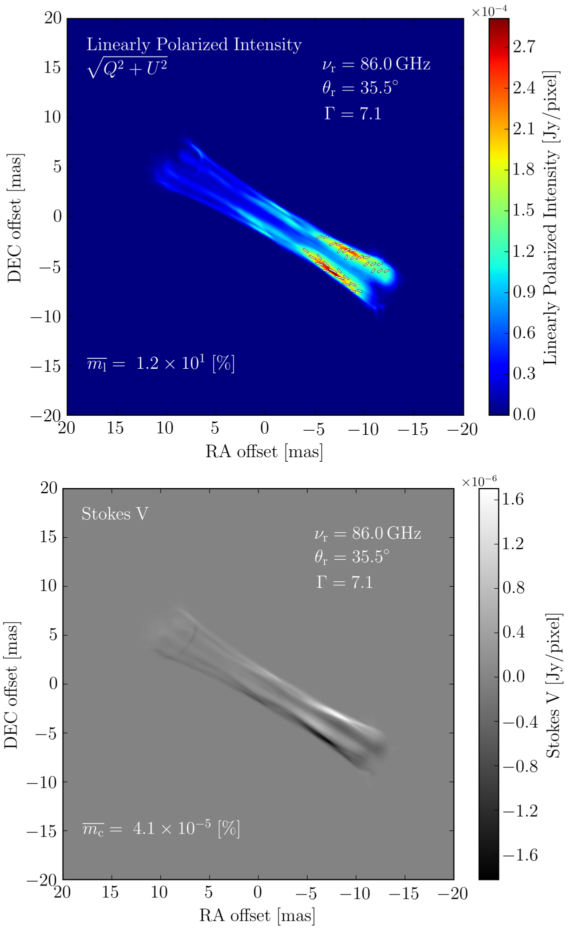

Fig. 6: Ray-traced images of our hybrid fluid-particle jet propagating from bottom right to top left in linearly polarized intensity (**top**), and circular polarization (**bottom**). The pictures illustrate the jet viewed at an observational viewing angle of 35.5° at 86 GHz. The fractional linear (m_l) and circular (m_c) polarization level is stated in the bottom left corner in both maps.

from left). However, we are explicitly choosing a relatively high threshold for particles to encounter shock acceleration in order to focus the study and analysis on the radiative losses. A comprehensive study on the particle shock acceleration mechanisms and results are presented in Dubey et al. (2023).

We continue to compare our synthetic polarized emission maps with observational data. The Event Horizon Telescope observations by Janssen et al. (2021) do not eliminate the prospect of insufficient particle acceleration in the radio galaxy Centaurus A. This uncertainty arises from the absence of a radio core at 230 GHz wavelength, even though a core is evident at the longer wavelength of 8 GHz observed by the TANAMI program earlier (Müller et al. 2014). Their analysis suggests that, in such a situation, the regions of heightened brightness in the jet would likely coincide with a shock within the jet flow. Our perspective, however, diverges. We attribute this phenomenon to the aggregation and amplification of synchrotron emission around the jet edges, driven by the presence of a toroidal magnetic field component. Notably, our numerical model reproduces the observed emission without requiring the introduction of any strong shock acceleration. We stress that a purely toroidal magnetic field configuration would yield symmetric edge-brightened emission spanning the jet, as elaborated in Gabuzda (2018). Conversely, a helical magnetic field configuration would lead to more asymmetric emission along the jet edges. This is confirmed in numerical simulations by Kramer & MacDonald (2021), and in the work presented in this paper. We validate the edge-brightened structure of an underlying toroidal magnetic field configuration when calculating the synthetic polarized synchrotron emission from non-thermal particle attributes directly. We are, moreover, inferring that the intrinsic magnetic field morphology is strongly assumed to be toroidal in nature due to the nearly symmetric brightness profile observed by Janssen et al. (2021).

Our perspective aligns with the interpretation on the total intensity outlined in Janssen et al. (2021), as we also observe a 'core' shift in the peak of Stokes I and linearly polarized intensity as we transition from lower frequencies to higher frequencies (from 15 GHz to 230 GHz, see Fig. B.1 in App. B). We observe that the jet exhibits optical thickness upstream, while downstream, it becomes optically thin. Janssen et al. (2021) identifies the most prominent features within the jet as radio cores, signifying the boundary between regions of upstream synchrotron self-absorption and downstream optically thin regions. They managed to resolve the self-absorbed section between the proposed radio core and the jet apex, a location that coincides with the presence of the supermassive black hole (SMBH) and its accretion disk.[4] The interpretation of the brightest jet feature as radio core, given their data, indeed appears to be the most plausible explanation. According to elementary analytical jet theory, a luminous radio core should be observable in Very Long Baseline Interferometry (VLBI) images. This phenomenon is a common occurrence in sources resembling Centaurus A, and the core shift usually adheres to the standard ν^{-1} relation, consistent with most sources (Sokolovsky et al. 2011).

6. Conclusion

We apply the PLUTO code (Mignone et al. 2007) to conduct three-dimensional RMHD simulations, in an interplay with a Lagrangian particle module incorporated in the PLUTO code (Vaidya et al. 2018). An analysis of the energy distribution of particles over time reveals the impact of synchrotron losses on both the particles within the ambient medium and those within the relativistic jet. To generate ray-traced full Stokes images from these fluid-particle hybrid jet simulations, we perform an interpolation of discrete particle energy and particle number density values across particle positions. Subsequently, these interpolated values are mapped onto continuous Cartesian grids, which are further employed as inputs for the ray-tracing software, RADMC-3D. This process additionally included a variable spectral index cube, which serves to address opacity effects across various frequencies. Importantly, the hybrid fluid-particle jet methodology enables the generation of synthetic emission maps that emphasize the jet's (polarized) synchrotron emission, obviating the need for an arbitrary 'jet tracer' commonly employed in conventional approaches to exclude the ambient medium. This is particularly significant as, in the context of three-dimensional relativistic MHD simulations, the presence of the ambient medium, in the absence of synchrotron losses, can obscure the jet.

[4] It's important to acknowledge that with existing telescopes, the radio core and upstream region typically remain unresolved for the majority of AGN.

The conclusions drawn from our study can be succinctly summarized in the following manner:

- We focus on incorporating relativistic macro-particles composed of numerous micro-particles, each with a distinct energy distribution, into fully three-dimensional jet simulations (see Fig. 3).
- By performing a spectral analysis, we confirm that the particles in the relativistic jet undergo synchrotron losses with time, as evidenced by our study of the energy evolution of the particles (as shown in Fig. 1).
- We calculate the synthetic polarized synchrotron emission directly from non-thermal particle attributes, and verify the presence of the edge-brightened structure, which corresponds to an underlying toroidal magnetic field configuration (Kramer & MacDonald 2021).
- The emission observed in the radio galaxy Centaurus A (Janssen et al. 2021) is faithfully reproduced by our numerical models. This is achieved without the need to introduce any substantial shock acceleration (see, e.g., Fig. B.1).
- We infer that the intrinsic magnetic field morphology in Centaurus A is most likely toroidal in nature by drawing this inference from the nearly symmetric brightness profile observed in the data by Janssen et al. (2021).
- Our observations reveal a variation in the total intensity peak as we move from lower to higher frequencies, indicating a 'core' shift. Meanwhile, we also note that the jet is optically thick upstream, while becoming optically thin downstream (see Fig. B.1).

Acknowledgements. J. Kramer's research was supported through a PhD grant from the International Max Planck Research School (IMPRS) for Astronomy and Astrophysics at the Universities of Bonn and Cologne, Germany. The three-dimensional jet simulations presented in this paper have been performed using the *PLUTO* Code. The calculations were performed on the Raven high performance cluster at the Max Planck Computing and Data Facility. The ray-tracing software *RADMC-3D* was used to generate the polarized images of the synchrotron emission. The authors thank B. Vaidya and D. Mukherjee for important and thoughtful discussions on the results presented in this work. The authors are grateful to E. Ros for comments and M. Janssen for insights on Centaurus A.

References

Bai, X.-N., Caprioli, D., Sironi, L., & Spitkovsky, A. 2015, ApJ, 809, 55
Bellan, P. M. 2018, Physics of Plasmas, 25, 055601
Blandford, R. D. & Rees, M. J. 1974, MNRAS, 169, 395
Brunetti, G., Mack, K. H., Prieto, M. A., & Varano, S. 2003, MNRAS, 345, L40
Carilli, C. L., Kurk, J. D., van der Werf, P. P., Perley, R. A., & Miley, G. K. 1999, AJ, 118, 2581
Condon, J. J. & Ransom, S. M. 2016, Essential Radio Astronomy
Daldorff, L. K. S., Tóth, G., Gombosi, T. I., et al. 2014, Journal of Computational Physics, 268, 236
de la Cita, V. M., Bosch-Ramon, V., Paredes-Fortuny, X., Khangulyan, D., & Perucho, M. 2016, A&A, 591, A15
Dubey, R. P., Fendt, C., & Vaidya, B. 2023, The Astrophysical Journal, 952, 1
Dullemond, C. P., Juhasz, A., Pohl, A., et al. 2012, RADMC-3D: A multi-purpose radiative transfer tool, Astrophysics Source Code Library, record ascl:1202.015
EHT MWL Science Working Group, Algaba, J. C., Anczarski, J., et al. 2021, ApJ, 911, L11
Fromm, C. M., Perucho, M., Mimica, P., & Ros, E. 2016, Astronomy and Astrophysics, 588, A101
Gabuzda, D. 2018, Galaxies, 6, 9
Heavens, A. F. & Meisenheimer, K. 1987, MNRAS, 225, 335
Homan, D., Hovatta, T., Kovalev, Y., et al. 2018, Galaxies, 6, 17
Janssen, M., Falcke, H., Kadler, M., et al. 2021, Nature Astronomy, 5, 1017
Jones, T. W. & Odell, S. L. 1977, Astronomy and Astrophysics, 61, 291
Kim, J.-Y., Krichbaum, T. P., Marscher, A. P., et al. 2019, Astronomy and Astrophysics, 622, A196
Kramer, J. A. & MacDonald, N. R. 2021, A&A, 656, A143
MacDonald, N. R. & Nishikawa, K. I. 2021, A&A, 653, A10
Meisenheimer, K. & Roeser, H. J. 1986, Nature, 319, 459
Mignone, A., Bodo, G., Massaglia, S., et al. 2007, ApJS, 170, 228
Mignone, A., Bodo, G., Vaidya, B., & Mattia, G. 2018, ApJ, 859, 13
Mimica, Giannios, D., Metzger, B., & Aloy, M.A. 2012, EPJ Web of Conferences, 39, 04003
Mimica, P., Aloy, M.-A., Agudo, I., et al. 2009, Astrophysical Journal, 696, 1142
Mizuno, Y., Gómez, J. L., Nishikawa, K.-I., et al. 2015, Astrophysical Journal, 809, 38
Müller, C., Kadler, M., Ojha, R., et al. 2014, A&A, 569, A115
Pontin, D. I. & Priest, E. R. 2022, Living Reviews in Solar Physics, 19, 1
Porth, O., Fendt, C., Meliani, Z., & Vaidya, B. 2011, Astrophysical Journal, 737, 42
Rees, A. I. 1966, Journal of Geology, 74, 856
Rothschild, R. E., Markowitz, A., Rivers, E., et al. 2011, The Astrophysical Journal, 733, 23
Rybicki, G. B. & Lightman, A. P. 1979, Radiative processes in astrophysics, 1st edn. (John Wiley & Sons)
Sokolovsky, K. V., Kovalev, Y. Y., Pushkarev, A. B., & Lobanov, A. P. 2011, A&A, 532, A38
Tsunetoe, Y., Mineshige, S., Ohsuga, K., Kawashima, T., & Akiyama, K. 2020, arXiv e-prints, arXiv:2012.05243
Urry, C. M. & Padovani, P. 1995, Publications of the Astronomical Society of the Pacific, 107, 803
Vaidya, B., Mignone, A., Bodo, G., Rossi, P., & Massaglia, S. 2018, Astrophysical Journal, 865, 144
van Marle, A. J., Casse, F., & Marcowith, A. 2018, MNRAS, 473, 3394
Wardle, J. F. C., Homan, D. C., Ojha, R., & Roberts, D. H. 1998, Nature, 395, 457
Webb, G. M. 1989, ApJ, 340, 1112

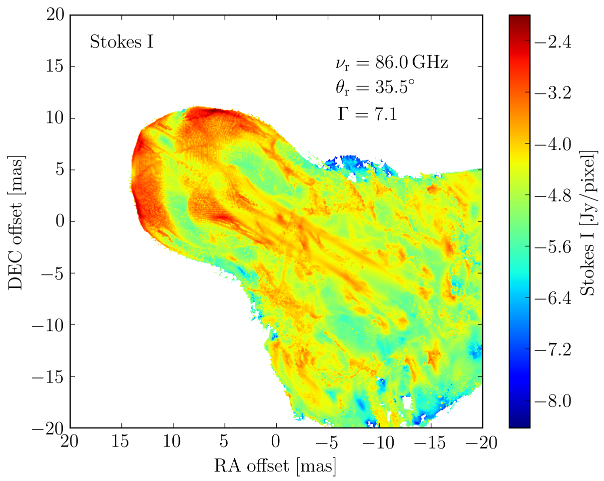

Fig. A.1: Resolved 86 GHz total intensity maps of the 3D RMHD jet simulation presented in Kramer & MacDonald (2021) in logarithmic color-coding. The jet emission is viewed at an observational viewing angle of 35.5°. The logarithmic plot reveals an edge-brightening jet hidden behind the bow shock.

Appendix A: Structure

A fascinating revelation comes to light when employing a logarithmic scale in our analysis: the edge-brightened jet structure emerges from beneath the concealing veil of the ambient medium, as clearly exemplified in Fig. A.1. This figure portrays a comprehensive view of a total intensity map derived from a preceding 3D RMHD jet simulation (Kramer & MacDonald 2021). It is noteworthy that this outcome is achieved without the use of any specialized jet tracer or intricate particle physics mechanisms. One prominent feature depicted in the figure is the bow shock, which, under these circumstances, completely overshadows the jet structure. However, by considering radiative losses, a transformative effect takes place. The bow shock, which comprises particles flowing in reverse, undergoes a cooling process, leading to a reduction in its intensity and overall prominence. This insight stresses the complex interplay between various physical factors that ultimately shape the observable characteristics of the jet and its surrounding environment. Figure A.1 proves that we are, indeed, using the very same numerical setup, and that we can result in an unobscured edge-brightened jet when we choose the hybrid fluid-particle approach.

Appendix B: Frequency

Our observations of the polarized total intensity maps of synthetic synchrotron emission shown in Fig. B.1 reveal several key characteristics of the jet's emission. Firstly, the emission pattern displays edge-brightening, an effect that can be attributed to the presence of a toroidal magnetic field configuration. Notably, this distinctive feature highlights the intricate nature of the jet's magnetic field orientation. Additionally, our analysis displays a core shift phenomenon within the 'radio core'. If we define the radio core as the peak brightness point of the emission, we detect a discernible shift toward the jet launching region when moving to higher frequencies (from 15 GHz to 86 GHz

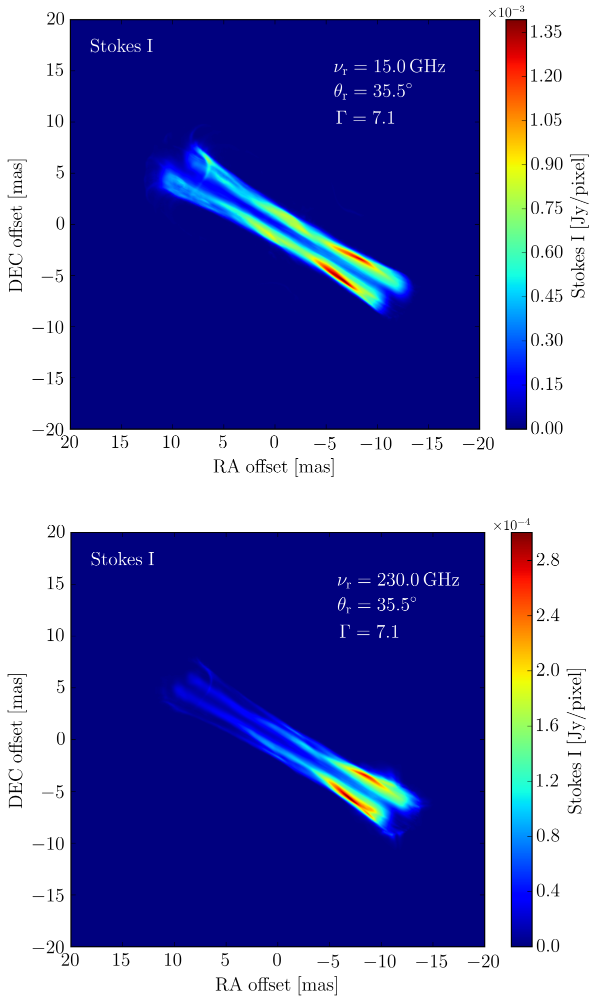

Fig. B.1: Resolved total intensity maps of the final 3D hybrid fluid-particle jet simulation revealing an edge-brightened jet emission in 15 GHz (**top**) and 230 GHz (**bottom**). Both maps are viewed at an observational viewing angle of 35.5°. The figure highlights the affect opacity effects have on resultant synthetic synchrotron emission.

to 230 GHz). Alternatively, if the radio core is considered to denote the boundary between regions of upstream synchrotron self-absorption and downstream optically thin segments, a compelling argument emerges. In this context, identifying the radio core at the location of the recollimation shock becomes a plausible proposition, as visible in the illustrated 2D slice through our 3D hybrid fluid-particle jet in the most left panel in Fig. 4 Furthermore, a noteworthy trend comes to light in our observations: the jet's brightness progressively diminishes as we ascend toward higher frequencies.

8 Conclusions and Prospective Views

Active galactic nuclei (AGN) are among the most energetic, luminous objects in the universe. Their emission can be observed from low energetic radio wave up to high energetic gamma rays, and even neutrino emission. A supermassive black hole (SMBH) accreting thermal matter is supposed to be situated in the center of AGN and functions as the central engine of the system. When matter from the surrounding accretion disk falls onto the SMBH, enforced by its strong gravitational pull, a relativistic outflow can be formed.

The most fundamental quality in classification of AGN is whether they are radio-quiet or radio-loud, i.e., feeding plasma into a highly collimated stream: *the relativistic jet*. The investigation of AGN jets has sparked great fascination. The regions where collimation and acceleration take place in these phenomena can only be accessed through high-resolution observations made possible by very-long-baseline interferometry, complemented by numerical methods. Despite these difficulties, jets provide the ideal laboratory to merge the study of plasma (i.e., macro-) physics and particle (i.e., micro-) physics. To probe theories in multiple fields of physics, among which this thesis focuses on radio astronomy, I *bridge the gap between numerical approaches and observational findings*. In order to achieve this, I focus on *the polarized synchrotron emission* as observed in AGN. Apart from the total intensity emission, both linearly polarized and circularly polarized synchrotron emission offer insights on the intrinsic magnetic field morphology in relativistic jets.

My thesis is divided into three parts, each addressing distinct topics while complementing one another.

To achieve deeper insights on the jet phenomenon, the first study I conduct in the framework of this thesis *focuses on three dimensional relativistic magnetohydrodynamic jet simulations generated using the PLUTO code*. These simulation are used to investigate how the synchrotron emission of a relativistic jet is shaped by its underlying magnetic field structure. Different magnetic field configurations - purely toroidal, purely poloidal, and a mixture of both (helical structure) - are being studied. Advanced radiative transfer techniques implemented within the RADMC-3D code are harnessed to generate synthetic synchrotron emission maps in the radio waveband, encompassing total, linearly polarized, and circularly polarized intensities. The transition from the thermal plasma variables (macro) within the PLUTO code to the observed non-thermal emission (micro) is facilitated by various electron scaling relations. The first part of this comprehensive investigation unfolds three significant results: First, the rise in linear polarization toward jet edges is explained by an underlying toroidal magnetic field configuration. Second, purely poloidal magnetic fields lead to emission dominance by the jet spine or recollimation shock associated with the VLBI core in radio observations. Finally, the simulation carrying the purely toroidal field reveals a distinctive bi-modal electric vector position angle (EVPA) pattern, which mimics the direction of the magnetic field lines. I further discuss the dependence of synchrotron emission on the applied scaling relation between the macro- and micro-physics. While the choice of the electron scaling relation has limited impact on the synchrotron emission morphology when the emission is focused on the innermost jet region, the magnetic energy density scaling stands out when the emission of the ambient medium, including the bow shock of the jet, is considered. The research highlights the need for particle physics, in detail, radiative losses in relativistic jet simulations, which is evident from the need of a numerical tool to arbitrarily exclude the backflowing material from radiative transfer calculations.

My second study *compares archival data from the MOJAVE program to a dedicated own full-polarized 24-hour VLBA observation at 15 GHz and 23 GHz of nine blazar sources* (i.e., jets with a small viewing angle with regard to our line of sight). These observations reveal trends in fractional linear polarization, electric vector position angle alignment, and circular polarized structures in different AGN jets. Focusing on circularly polarized emission in radio galaxy and blazar jets, I examine its diagnostic potential for distinguishing the intrinsic magnetic field morphology in these highly boosted objects. My three dimensional relativistic magnetohydrodynamic jet simulations from the first study within this thesis predict the relationship between the electric vector position angle and left-handed/right-handed circular polarization. This observational study validates these predictions in various sources at 15 GHz and 23 GHz. Nine target sources are observed facilitating the VLBA at both frequencies, demonstrating the consistency of the magnetic field morphology over time, i.e., a robustness in the structure of the electric vector position angles compared to archival data from the MOJAVE team, and revealing a switch in the circular polarization sign between the observed frequencies. I use the advanced technique of combining the significant advantages of regularized maximum likelihood reconstructions, which super-resolve compact structures, and the CLEAN method, which provides high dynamic range sensitivity to extended structures in AGN jets. This is encompassed in the applied `DoG-HiT` software. With this I ensure accuracy in the reconstruction, and achieve superresolution in the final polarized emission maps of the VLBI core and the observed extended jet structure. This results in unprecedented counter-jet/jet-bend observations.

The first study demonstrates the need to include particle physics in order to account for the luminous ambient medium that outshines the innermost jet structure. In the final study, *I introduce the incorporation of a new Lagrangian particle module into the PLUTO code*, which represents macro-particles consisting of multiple non-thermal micro-particles, *in order to arrive at unobscured synchrotron emission maps of AGN jets*. Each of the micro-particles carries a distinct energy distribution that evolves with numerical time steps. I implement this method to consider the effect of radiative losses, in particular, synchrotron cooling in a hybrid fluid-particle approach. This module significantly enriches the physical accuracy of these simulations by improving the differentiation between the jet's inner structure and 'cooled' backflowing material. The study culminates in three noteworthy findings: First, the purely toroidal magnetic field simulation successfully reproduces the radio emission from the edge-brightened jet observed in the nearby radio galaxy Centaurus A. Second, the importance of accounting for synchrotron losses is highlighted and the improvements achieved by incorporating non-thermal particles are demonstrated. Finally, the inclusion of variable spectral indices in polarized synchrotron emission maps reveals the transition between optically thick and thin regions within the simulated jet.

In summary, I provide a laboratory of three dimensional relativistic magnetohydrodynamic numerical jet simulations to unveil the underlying magnetic field topology in observational (polarized) synchrotron maps of AGN jets, such as 3C 84 (G.-F. Paraschos et al. in prep.) or Centaurus A Janssen et al., 2021. This forms an ideal study to compare magnetic characteristics of AGN jets at radio frequencies. In the framework of blazar sources, this work proves the robustness of the electric vector position angles and linearly polarized signals over time. The circular polarization highlights favored magnetic field morphologies in the observed blazar sources at 15 GHz and 23 GHz. For a more precise classification of, e.g., blazar types, a statistical sample would be needed. However, a state-of-the art method for circular polarization calibration and imaging is applied and reveals both higher fractional circular polarization and more resolved features compared to prior studies at higher frequencies in total intensity. Nonetheless, a theoretical model matching the observations of AGN jets has yet to be finalized. My overall treatment is improved by including radiative losses in a hybrid approach. The three dimensional hybrid fluid-particle simulations and the frequency-dependent post processing to generate synchrotron emission maps provide a more sufficient method for unveiling the mystery of AGN jets. I successfully present synthetic polarized synchrotron maps of the radio galaxy Centaurus A to further study its underlying physics and jet features.

'*Mission accomplished? Yes, but not quite yet.*' - A. Zensus, RadioViews 2022.

In the prospective views of this research, I consider several aspects for further investigation. In the field of data analysis, my focus will be on examining the transverse profiles of the extended jet structure in the observational data presented in this thesis as well as using component fitting by using archival data of earlier epochs to study the superluminal motion in blazars. Another crucial aspect involves model fitting to investigate the electric vector position angle behavior and its dependence on the rotation measure, for which data at a third frequency is required (e.g., the Boston University blazar program at 43 GHz). Moreover, I plan to estimate the magnetic field strength in VLBI cores from core shift measurements between frequencies, while I consider to make spectral index maps both from the observational data in the two frequencies provided in this thesis and from the alignment of synthetic emission maps to probe the optical depth.

Regarding the correct treatment of the ambient medium surrounding the jet, efforts will be made to include the particle population or to start with a power-law relationship of the thermal density. Furthermore, I plan to treat instabilities and turbulence within both the ambient medium and the jet itself. It will be necessary to incorporate shock physics in the particle jet to account for diffusive shock acceleration. This way, more turbulent AGN sources can be compared. With the inclusion of shock acceleration, I would aim to conduct a full spectral energy distribution analysis of polarized emission maps up to X-rays. Additionally, there is an emphasis on connecting (special) relativistic magnetohydrodynamic and general relativistic magnetohydrodynamics, which is needed for simulations closer to the central engine, and resolving any discrepancies that may exist between these models. I plan to extend my simulations to mimic jets other than Centaurus A. In detail, efforts are made to stress the bi-modal electric vector position angle pattern observed in 3C 84 (G.-F. Paraschos et al. in prep.)

In terms of imaging, resolving large-scale structures will be a key focus. My data provide an ideal basis for testing and verifying the reconstructed signals with the `resolve` (Junklewitz et al., 2016) or `Comrade` (Tiede, 2022) code based on Bayesian imaging. The implementation of additional tests (e.g., CL-trace) to implement a quantity fully independent on gains, offsets, feed rotation, and leakage is planned for the future. Finally, for single dish polarimetric observations I propose to use data from the QUIVER/F-GAMMA (Angelakis et al., 2019) or POLAMI (Agudo et al., 2018) program to constrain the absolute values of electric vector position angles. A first look at Effelsberg observations of the blazar 0528 + 134 at 4.85 GHz revealed promising similarities in the level of observed fractional linear polarization (Credits: A. Kraus).

A | Bayesian Imaging

Imaging methods in radio astronomy based on Bayes Theorem calculate the reconstructed signal from an optimal algorithm. The theorem links the posterior probability density function $P(f|g^\delta)$ to the likelihood $P(g^\delta|f)$ and the prior distribution $P(f)$:

$$P\left(f|g^\delta\right) = \frac{P\left(g^\delta|f\right) P\left(g^\delta\right)}{P\left(f\right)}. \tag{A.1}$$

$P\left(g^\delta\right)$ is the evidence, or in VLBI, any observational quantity described earlier. In detail, the likelihood would read as

$$P\left(F(M)|f\right) = (2\pi)^{N_c/2} \left[\prod_{i=1}^{N_c} \frac{1}{\sum_i}\right] e^{-N_c/2\chi_c^2}. \tag{A.2}$$

The prior distribution $P(f)$ is feeding the algorithm with information and is providing a first assumption about the prior pixel values. The forwarded model naturally includes the advantage of adding as many prior information to that as available. The first guess is finally derived as an expectation value

$$\hat{f}_{\text{mean}} = \int P(f|g^\delta)\,\mathrm{d}f. \tag{A.3}$$

Another advantages of Bayesian approaches are the hand in hand recovery of an image along with its variance var, derived as:

$$Var = \int (f - \hat{f}_{\text{mean}})^2 P(f|g^\delta)\,\mathrm{d}f. \tag{A.4}$$

Bibliography

Aartsen, M. G. et al. (2017),
The Contribution of Fermi-2Lac Blazars to Diffuse Tev-Pev Neutrino Flux,
Astrophysical Journal, 835, 45 (cit. on p. 60).

Abbasi, R. et al. (2022),
Search for neutrino emission from cores of active galactic nuclei,
Physical Review D, 106, 022005 (cit. on p. 60).

Agudo, I. et al. (2018), *POLAMI: Polarimetric Monitoring of AGN at Millimetre Wavelengths - I. The programme, calibration and calibrator data products*,
Monthly Notices of the Royal Astronomical Society, 474, 1427 (cit. on p. 124).

Ajello, M. et al. (2021),
Fermi Large Area Telescope Performance after 10 Years of Operation,
Astrophysical Journal, Supplement Series, 256, 12 (cit. on p. 59).

Akiyama, K. et al. (2017a), *Imaging the Schwarzschild-radius-scale Structure of M87 with the Event Horizon Telescope Using Sparse Modeling*,
Astrophysical Journal, 838, 1 (cit. on p. 51).

Akiyama, K. et al. (2017b), *Superresolution Full-polarimetric Imaging for Radio Interferometry with Sparse Modeling*, Astronomical Journal, 153, 159 (cit. on p. 51).

Algaba, J. C., K. Asada, and M. Nakamura (2016),
Resolving the Rotation Measure of the M87 Jet on Kiloparsec Scales,
Astrophysical Journal, 823, 86 (cit. on p. 12).

Aloy, M. A., J. M. Ibáñez, J. M. Martí, and E. Müller (1999), *GENESIS: A High-Resolution Code for Three-dimensional Relativistic Hydrodynamics*,
Astrophysical Journal, Supplement, 122, 151 (cit. on p. 65).

Aloy, M.-A., J.-L. Gómez, J.-M. Ibáñez, J.-M. Martí, and E. Müller (2000),
Radio Emission from Three-dimensional Relativistic Hydrodynamic Jets: Observational Evidence of Jet Stratification,
Astrophysical Journal, Letters, 528, L85 (cit. on pp. 64–66).

Angel, J. R. P. and H. S. Stockman (1980),
Optical and infrared polarization of active extragalactic objects,
Annual Review of Astronomy and Astrophysics, 18, 321 (cit. on p. 18).

Angelakis, E. et al. (2019), *F-GAMMA: Multi-frequency radio monitoring of Fermi blazars - The 2.64 to 43 GHz Effelsberg light curves from 2007-2015*, Astronomy and Astrophysics, 626, A60 (cit. on p. 124).

Antonucci, R. (2012), *A panchromatic review of thermal and nonthermal active galactic nuclei*, Astronomical and Astrophysical Transactions, 27, 557 (cit. on p. 59).

Antonucci, R. R. J. and J. S. Miller (1985), *Spectropolarimetry and the nature of NGC 1068.*, Astrophysical Journal, 297, 621 (cit. on p. 15).

Arras, P. et al. (2021), *Comparison of classical and Bayesian imaging in radio interferometry. Cygnus A with CLEAN and resolve*, Astronomy and Astrophysics, 646, A84 (cit. on pp. 50, 51).

Attridge, J. M., D. H. Roberts, and J. F. C. Wardle (1999), *Radio Jet-Ambient Medium Interactions on Parsec Scales in the Blazar 1055+018*, Astrophysical Journal, Letters, 518, L87 (cit. on p. 20).

Baade, W. and R. Minkowski (1954), *On the Identification of Radio Sources.*, Astrophysical Journal, 119, 215 (cit. on pp. 52, 53).

Baars, J. W. M. and H. J. Kärcher (2018), *Radio Telescope Reflectors: Historical Development of Design and Construction*, vol. 447, Astrophysics and Space Science Library, Springer (cit. on p. 36).

Baczko, A. K. et al. (2016), *A highly magnetized twin-jet base pinpoints a supermassive black hole*, Astronomy and Astrophysics, 593, A47 (cit. on p. 79).

Baczko, A.-K. (2020), *Multi-Frequency VLBI Observations of the Active Galaxy NGC 1052*, PhD thesis: Universität zu Köln (cit. on pp. 41, 79).

Balick, B. and R. L. Brown (1974), *Intense sub-arcsecond structure in the galactic center.*, Astrophysical Journal, 194, 265 (cit. on p. 24).

Bateman, G. (1978), *MHD instabilities*, MIT press (cit. on p. 56).

Becker, R. H., R. L. White, and D. J. Helfand (1995), *The FIRST Survey: Faint Images of the Radio Sky at Twenty Centimeters*, Astrophysical Journal, 450, 559 (cit. on p. 57).

Beckert, T. and H. Falcke (2002), *Circular polarization of radio emission from relativistic jets*, Astronomy and Astrophysics, 388, 1106 (cit. on p. 19).

Belladitta, S. et al. (2022), *Central engine of the highest redshift blazar*, Astronomy and Astrophysics, 660, A74 (cit. on p. 20).

Belloni, T. (2010), *The Jet Paradigm*, vol. 794, Springer (cit. on p. 5).

Biretta, J. A., C. P. Stern, and D. E. Harris (1991), *The Radio to X-ray Spectrum of the M87 Jet and Nucleus*, Astronomical Journal, 101, 1632 (cit. on p. 53).

Blandford, R. D. and A. Königl (1979), *Relativistic jets as compact radio sources*, Astrophysical Journal, 232, 34 (cit. on p. 57).

Blandford, R. D. and D. G. Payne (1982), *Hydromagnetic flows from accretion disks and the production of radio jets*, Monthly Notices of the Royal Astronomical Society, 199, 883 (cit. on p. 54).

Blandford, R. D. and R. L. Znajek (1977), *Electromagnetic extraction of energy from Kerr black holes*, Monthly Notices of the Royal Astronomical Society: Letters, 179, 433 (cit. on p. 54).

Blandford, R., D. Meier, and A. Readhead (2019), *Relativistic Jets from Active Galactic Nuclei*, Annual Review of Astronomy and Astrophysics, 57, 467 (cit. on pp. 20, 57, 59, 60).

Boccardi, B., T. P. Krichbaum, E. Ros, and J. A. Zensus (2017), *Radio observations of active galactic nuclei with mm-VLBI*, Astronomy and Astrophysics Reviews, 25, 4 (cit. on p. 57).

Boccardi, B. et al. (2021), *Jet collimation in NGC 315 and other nearby AGN*, Astronomy and Astrophysics, 647, A67 (cit. on p. 56).

Boettcher, M., D. E. Harris, and H. Krawczynski (2012), *Relativistic Jets from Active Galactic Nuclei*, Wiley (cit. on p. 13).

Bolton, J. G., G. J. Stanley, and O. B. Slee (1949), *Positions of Three Discrete Sources of Galactic Radio-Frequency Radiation*, Nature, 164, 101 (cit. on p. 6).

Bolton, J. G., J. V. Wall, and A. J. Shimmins (1971), *Some identifications for weak sources in the Parkes catalogue for declinations +20° to -20°*, Australian Journal of Physics, 24, 889 (cit. on p. 57).

Burke, B. F. and F. Graham-Smith (1997), *An introduction to radio astronomy*, Cambridge University Press (cit. on pp. 15, 16, 39, 48).

Camenzind, M. (1986), *Centrifugally driven MHD-winds in active galactic nuclei*, Astronomy and Astrophysics, 156, 137 (cit. on p. 55).

Chael, A. A. et al. (2019), *ehtim: Imaging, analysis, and simulation software for radio interferometry*, Astrophysics Source Code Library, https://achael.github.io/eht-imaging/ (cit. on p. 51).

Chatterjee, K., M. Liska, A. Tchekhovskoy, and S. B. Markoff (2019), *Accelerating AGN jets to parsec scales using general relativistic MHD simulations*, Monthly Notices of the Royal Astronomical Society, 490, 2200 (cit. on p. 55).

Clarke, D. A., J. O. Burns, and M. L. Norman (1992), *VLA Observations of the Inner Lobes of Centaurus A*, Astrophysical Journal, 395, 444 (cit. on p. 62).

Clausen-Brown, E. R. (2012), *Magnetized relativistic outflows in astrophysics*, PhD thesis: Purdue University, Indiana (cit. on p. 56).

Contopoulos, I., D. Gabuzda, and N. Kylafis (2015), *The Formation and Disruption of Black Hole Jets*, Springer (cit. on p. 4).

Cotton, W. D. (1997), *Very Long Baseline Interferometry*, in: *High Angular Resolution in Astrophysics*, Springer (cit. on p. 46).

Coughlan, C. P. (2014), *The development of new methods for high resolution radio astronomy imaging*, PhD thesis: University College Cork, Ireland (cit. on p. 49).

Curtis, H. D. (1918), *Descriptions of 762 Nebulae and Clusters Photographed with the Crossley Reflector*, Publications of Lick Observatory, 13, 9 (cit. on p. 53).

Daly, R. A. and A. P. Marscher (1988), *The Gasdynamics of Compact Relativistic Jets*, Astrophysical Journal, 334, 539 (cit. on p. 64).

De Villiers, J.-P., J. F. Hawley, and J. H. Krolik (2003), *Magnetically Driven Accretion Flows in the Kerr Metric. I. Models and Overall Structure*, Astrophysical Journal, 599, 1238 (cit. on p. 55).

Dermer, C. D. and G. Menon (2009), *High Energy Radiation from Black Holes: Gamma Rays, Cosmic Rays, and Neutrinos*, Princeton Univeristy Press (cit. on p. 28).

Dullemond, C. P. et al. (2012), *RADMC-3D: A multi-purpose radiative transfer tool*, https://github.com/dullemond/radmc3d-2.0 (cit. on pp. 76, 78).

Duncan, G. C. and P. A. Hughes (1994), *Simulations of Relativistic Extragalactic Jets*, Astrophysical Journal, Letters, 436, L119 (cit. on p. 65).

Duţan, I. et al. (2016), *Particle-in-cell Simulations of Global Relativistic Jets with Helical Magnetic Fields*, Proceedings of the International Astronomical Union, 12, 199–202 (cit. on p. 67).

Ehlert, S. R. et al. (2022), *Limits on X-Ray Polarization at the Core of Centaurus A as Observed with the Imaging X-Ray Polarimetry Explorer*, Astrophysical Journal, 935, 116 (cit. on p. 63).

Einstein, A. (1916), *Die Grundlage der allgemeinen Relativitätstheorie*, Annalen der Physik, 354, 769 (cit. on p. 2).

Esin, A. A., J. E. McClintock, and R. Narayan (1997), *Advection-Dominated Accretion and the Spectral States of Black Hole X-Ray Binaries: Application to Nova Muscae 1991*, Astrophysical Journal, 489, 865 (cit. on p. 5).

Event Horizon Telescope Collaboration et al. (2019a), *First M87 Event Horizon Telescope Results. I. The Shadow of the Supermassive Black Hole*, Astrophysical Journal, Letters, 875, L1 (cit. on pp. 9, 20, 35, 43, 53, 57, 60).

Event Horizon Telescope Collaboration et al. (2019b), *First M87 Event Horizon Telescope Results. IV. Imaging the Central Supermassive Black Hole*, Astrophysical Journal, Letters, 875, L4 (cit. on pp. 48, 50, 51).

Event Horizon Telescope Collaboration et al. (2021), *First M87 Event Horizon Telescope Results. VII. Polarization of the Ring*, Astrophysical Journal, Letters, 910, L12 (cit. on pp. 12, 61).

Event Horizon Telescope Collaboration et al. (2022), *First Sagittarius A* Event Horizon Telescope Results. I. The Shadow of the Supermassive Black Hole in the Center of the Milky Way*, Astrophysical Journal Letters, 930, L12 L12 (cit. on pp. 35, 60).

Falcke, H., E. Körding, and S. Markoff (2004), *A scheme to unify low-power accreting black holes. Jet-dominated accretion flows and the radio/X-ray correlation*, Astronomy and Astrophysics, 414, 895 (cit. on p. 4).

Fanaroff, B. L. and J. M. Riley (1974), *The morphology of extragalactic radio sources of high and low luminosity*, Monthly Notices of the Royal Astronomical Society, 167, 31P (cit. on p. 57).

Ferrari, A., E. Trussoni, and L. Zaninetti (1978), *Relativistic Kelvin-Helmholtz instabilities in extragalactic radio sources*, Astronomy and Astrophysics, 64, 43 (cit. on p. 56).

Ferreira, J. (1997), *Magnetically-driven jets from Keplerian accretion discs*, Astronomy and Astrophysics, 319, 340 (cit. on p. 54).

Font, J. A. (2008), *Numerical Hydrodynamics and Magnetohydrodynamics in General Relativity*, Living Reviews in Relativity, 11, 7 (cit. on p. 65).

Frank, J., A. King, and D. J. Raine (2002), *Accretion Power in Astrophysics: Third Edition*, Cambridge University Press (cit. on p. 3).

Fromm, C. M., M. Perucho, P. Mimica, and E. Ros (2016), *Spectral evolution of flaring blazars from numerical simulations*, Astronomy and Astrophysics, 588, A101 (cit. on p. 67).

Fuentes, A., J. L. Gómez, J. M. Martí, and M. Perucho (2018), *Total and Linearly Polarized Synchrotron Emission from Overpressured Magnetized Relativistic Jets*, Astrophysical Journal, 860, 121 (cit. on p. 66).

Fujimoto, K. (2018), *Multi-scale kinetic simulation of magnetic reconnection with dynamically adaptive meshes*, Frontiers in Physics, 6, 119 (cit. on p. 68).

Gabuzda, D. C., P. Y. Kochenov, R. I. Kollgaard, and T. V. Cawthorne (2000), *VLBI and VLA observations of intraday polarization variability in 0917+624 and 0954+658*, Monthly Notices of the Royal Astronomical Society, 315, 229 (cit. on p. 64).

Gabuzda, D. C., A. R. Reichstein, and E. L. O'Neill (2014), *Are spine-sheath polarization structures in the jets of active galactic nuclei associated with helical magnetic fields?*, Monthly Notices of the Royal Astronomical Society, 444, 172 (cit. on p. 20).

Gabuzda, D. C. (2021), *Inherent and Local Magnetic Field Structures in Jets from Active Galactic Nuclei*, Galaxies, 9, 58 (cit. on p. 61).

Gammie, C. F., W.-T. Liao, and P. M. Ricker (2016), *A Hot Big Bang Theory: Magnetic Fields and the Early Evolution of the Protolunar Disk*, Astrophysical Journal, 828, 58 (cit. on p. 73).

Ghisellini, G., C. Righi, L. Costamante, and F. Tavecchio (2017), *The Fermi blazar sequence*, Monthly Notices of the Royal Astronomical Society, 469, 255 (cit. on pp. 19, 20).

Ghisellini, Gabriele (2013), *Jets, black holes and disks in blazars*, European Physical Journal Web of Conferences, 61, 05001 (cit. on p. 11).

Ginzburg, V. L. and S. I. Syrovatskii (1969), *Developments in the Theory of Synchrotron Radiation and its Reabsorption*, Annual Review of Astronomy and Astrophysics, 7, 375 (cit. on p. 29).

Giovannini, G. et al. (2018), *A wide and collimated radio jet in 3C84 on the scale of a few hundred gravitational radii*, Nature Astronomy, 2, 472 (cit. on pp. 20, 79).

Giroletti, M. et al. (2004), *Parsec-Scale Properties of Markarian 501*, Astrophysical Journal, 600, 127 (cit. on p. 20).

Goddi, C. et al. (2019), *First M87 Event Horizon Telescope Results and the Role of ALMA*, The Messenger, 177, 25 (cit. on pp. 12, 61).

Goedbloed, J. P., R. Keppens, and S. Poedts (2010), *Advanced Magnetohydrodynamics*, Cambridge University Press (cit. on p. 71).

Gómez, J. L., J. M. Martí, A. P. Marscher, J. M. Ibáñez, and A. Alberdi (1997), *Hydrodynamical Models of Superluminal Sources*, Astrophysical Journal, 482, L33 (cit. on p. 64).

Gomez, J. L., J. M. A. Marti, A. P. Marscher, J. M. A. Ibanez, and J. M. Marcaide (1995), *Parsec-Scale Synchrotron Emission from Hydrodynamic Relativistic Jets in Active Galactic Nuclei*, Astrophysical Journal, 449, L19 (cit. on p. 64).

Greisen, E. W. (2003), *AIPS, the VLA, and the VLBA*, in: *Information Handling in Astronomy - Historical Vistas*, Springer (cit. on p. 44).

Griffith, D. J. and G. Ruppeiner (1981), *Introduction to Electrodynamics*, American Journal of Physics, 49, 1188 (cit. on p. 28).

Gurvits, L. I. (2018), *Radio Interferometers Larger than Earth: Lessons Learned and Forward Look of Space VLBI*, arXiv e-prints, (cit. on p. 57).

Guthmann, A. W., M. Georganopoulos, A. Marcowith, and K. Manolakou (2002), *Relativistic Flows in Astrophysics*, vol. 589, Springer (cit. on pp. 54, 55, 73).

Harris, G. L. H., M. Rejkuba, and W. E. Harris (2010), *The Distance to NGC 5128 (Centaurus A)*, Publications of the Astronomical Society of Australia, 27, 457 (cit. on p. 62).

Harrison, C. (2014), *Observational constraints on the influence of active galactic nuclei on the evolution of galaxies*, PhD thesis: Durham University, UK (cit. on p. 7).

Harten, A., P. D. Lax, and B. v. Leer (1983), *On Upstream Differencing and Godunov-Type Schemes for Hyperbolic Conservation Laws*, SIAM Review, 25, 35 (cit. on p. 73).

Hawley, J. F., C. Fendt, M. Hardcastle, E. Nokhrina, and A. Tchekhovskoy (2015), *Disks and Jets. Gravity, Rotation and Magnetic Fields*, Space Science Reviews, 191, 441 (cit. on p. 55).

Hazard, C., M. B. Mackey, and A. J. Shimmins (1963), *Investigation of the Radio Source 3C 273 By The Method of Lunar Occultations*, Nature, 197, 1037 (cit. on p. 24).

Heckman, T. M. and P. N. Best (2014), *The Coevolution of Galaxies and Supermassive Black Holes: Insights from Surveys of the Contemporary Universe*, Annual Review of Astronomy and Astrophysics, 52, 589 (cit. on p. 17).

Hewish, A., S. J. Bell, J. D. H. Pilkington, P. F. Scott, and R. A. Collins (1968), *Observation of a Rapidly Pulsating Radio Source*, Nature, 217, 709 (cit. on p. 24).

Hey, J. S., S. J. Parsons, and J. W. Phillips (1946), *Fluctuations in Cosmic Radiation at Radio-Frequencies*, Nature, 158, 234 (cit. on p. 6).

Högbom, J. A. (1974), *Aperture Synthesis with a Non-Regular Distribution of Interferometer Baselines*, Astronomy and Astrophysics, Supplement, 15, 417 (cit. on pp. 48, 49).

Homan, D. C. and M. L. Lister (2006), *MOJAVE: Monitoring of Jets in Active Galactic Nuclei with VLBA Experiments.*

II. First-Epoch 15 GHz Circular Polarization Results, Astronomical Journal, 131, 1262 (cit. on pp. 46, 61, 62, 64, 95).

Homan, D. C., M. L. Lister, H. D. Aller, M. F. Aller, and J. F. C. Wardle (2009), *Full Polarization Spectra of 3C 279*, Astrophysical Journal, 696, 328 (cit. on p. 95).

Homan, D. C. and J. F. C. Wardle (1999), *Detection and Measurement of Parsec-Scale Circular Polarization in Four AGN*, Astronomical Journal, 118, 1942 (cit. on p. 19).

Homan, J. et al. (2001), *Correlated X-Ray Spectral and Timing Behavior of the Black Hole Candidate XTE J1550-564: A New Interpretation of Black Hole States*, Astrophysical Journal, Supplement, 132, 377 (cit. on p. 5).

Honma, M., K. Akiyama, M. Uemura, and S. Ikeda (2014), *Super-resolution imaging with radio interferometry using sparse modeling*, Publications of the Astronomical Society of Japan, 66, 95 (cit. on p. 50).

Hovatta, T. and E. Lindfors (2019), *Relativistic Jets of Blazars*, New Astronomy Review, 87, 101541 (cit. on pp. 20, 61).

Hovatta, T., O´Sullivan, S., Martí-Vidal, I., Savolainen, T., and Tchekhovskoy, A. (2019), *Magnetic field at a jet base: extreme Faraday rotation in 3C 273 revealed by ALMA*, Astronomy and Astrophysics, 623, A111 (cit. on p. 64).

IceCube Collaboration et al. (2018), *Neutrino emission from the direction of the blazar TXS 0506+056 prior to the IceCube-170922A alert*, Science, 361, 147 (cit. on p. 60).

Jackson, J. D. (1975), *Classical electrodynamics*, Wiley (cit. on p. 28).

Jansky, K. G. (1933), *Radio Waves from Outside the Solar System*, Nature, 132, 66 (cit. on p. 34).

Janssen, M. et al. (2019), *rPICARD: A CASA-based calibration pipeline for VLBI data. Calibration and imaging of 7 mm VLBA observations of the AGN jet in M 87*, Astronomy and Astrophysics, 626, A75 (cit. on pp. 57, 79).

Janssen, M., J. F. Radcliffe, and J. Wagner (2022), *Software and Techniques for VLBI Data Processing and Analysis*, Universe, 8, 527 (cit. on pp. 44, 46).

Janssen, M. et al. (2021), *Event Horizon Telescope observations of the jet launching and collimation in Centaurus A*, Nature Astronomy, 5, 1017 (cit. on pp. 20, 35, 62, 63, 79, 123).

Jones, R. C. (1941), *A New Calculus for the Treatment of Optical SystemsI. Description and Discussion of the Calculus*, Journal of the Optical Society of America, 31, 488 (cit. on p. 42).

Jones, T. W. and S. L. Odell (1977),
Physical conditions in polarized compact radio sources,
Astronomy and Astrophysics, 61, 291 (cit. on p. 77).

Jorstad, S. et al. (2023),
The Event Horizon Telescope Image of the Quasar NRAO 530,
The Astrophysical Journal, 943, 170 (cit. on p. 20).

Junklewitz, H., M. R. Bell, M. Selig, and T. A. Enßlin (2016), *RESOLVE: A new algorithm for aperture synthesis imaging of extended emission in radio astronomy*, Astronomy and Astrophysics, 586, A76 (cit. on p. 124).

Kagan, D., L. Sironi, B. Cerutti, and D. Giannios (2015), *Relativistic Magnetic Reconnection in Pair Plasmas and Its Astrophysical Applications*, Space Science Reviews, 191, 545 (cit. on p. 67).

Kardashev, N. S., Y. Y. Kovalev, and K. I. Kellermann (2012),
RadioAstron: An Earth-Space Radio Interferometer with a 350,000 km Baseline,
The Radio Science Bulletin No 343, 343, 22 (cit. on p. 40).

Kardashev, N. S. et al. (2013), *"RadioAstron"-A telescope with a size of 300 000 km: Main parameters and first observational results*, Astronomy Reports, 57, 153 (cit. on p. 57).

Karouzos, M., S. Britzen, A. Witzel, J. A. Zensus, and A. Eckart (2011), *γ-rays in flat-spectrum AGN: revisiting the fast jet hypothesis with the CJF sample*, Astronomy and Astrophysics, 529, A16 (cit. on p. 59).

Kellermann, K. I., R. Sramek, M. Schmidt, D. B. Shaffer, and R. Green (1989),
VLA Observations of Objects in the Palomar Bright Quasar Survey,
Astronomical Journal, 98, 1195 (cit. on p. 57).

Kerr, R. P. (1963), *Gravitational Field of a Spinning Mass as an Example of Algebraically Special Metrics*, Physical Review Letters, 11, 237 (cit. on pp. 2, 8).

Kim, J.-Y. et al. (2019), *Spatially resolved origin of millimeter-wave linear polarization in the nuclear region of 3C 84*,
Astronomy and Astrophysics, 622, A196 (cit. on p. 61).

Kim, J.-Y. et al. (2020), *Event Horizon Telescope imaging of the archetypal blazar 3C 279 at an extreme 20 microarcsecond resolution*,
Astronomy and Astrophysics, 640, A69 (cit. on p. 20).

Kirchhoff, G. (1860), *Ueber das Verhältniss zwischen dem Emissionsvermögen und dem Absorptionsvermögen der Körper für Wärme und Licht*,
Annalen der Physik, 185, 275 (cit. on p. 25).

Koide, S., D. L. Meier, K. Shibata, and T. Kudoh (2000),
General Relativistic Simulations of Early Jet Formation in a Rapidly Rotating Black Hole Magnetosphere, Astrophysical Journal, 536, 668 (cit. on pp. 55, 64).

Komesaroff, M. M., J. A. Roberts, D. K. Milne, P. T. Rayner, and D. J. Cooke (1984), *Circular and linear polarization variations of compact radio sources.*, Monthly Notices of the Royal Astronomical Society, 208, 409 (cit. on p. 19).

Komissarov, S. S. (1999), *Numerical simulations of relativistic magnetized jets*, Monthly Notices of the Royal Astronomical Society, 308, 1069 (cit. on p. 64).

Körding, E. G., R. P. Fender, and S. Migliari (2006), *Jet-dominated advective systems: radio and X-ray luminosity dependence on the accretion rate*, Monthly Notices of the Royal Astronomical Society, 369, 1451 (cit. on p. 4).

Körding, E. G., S. Jester, and R. Fender (2008), *Measuring the accretion rate and kinetic luminosity functions of supermassive black holes*, Monthly Notices of the Royal Astronomical Society, 383, 277 (cit. on p. 4).

Kovalev, Y. Y. et al. (2020), *A transition from parabolic to conical shape as a common effect in nearby AGN jets*, Monthly Notices of the Royal Astronomical Society, 495, 3576 (cit. on p. 56).

Kramer, J. A. and N. R. MacDonald (2021), *Ray-tracing in relativistic jet simulations: A polarimetric study of magnetic field morphology and electron scaling relations*, Astronomy and Astrophysics, 656, A143 (cit. on pp. 20, 25, 27, 64, 66, 67, 75, 76, 78, 95, 110).

Kravchenko, E. et al. (2020), *Linear polarization in the nucleus of M87 at 7 mm and 1.3 cm*, Astronomy and Astrophysics, 637, L6 (cit. on p. 12).

Laing, R. A. (1996), "Brightness and Polarization Structure of Decelerating Relativistic Jets", in: *Energy Transport in Radio Galaxies and Quasars*, vol. 100, Astronomical Society of the Pacific Conference Series 241 (cit. on p. 60).

Laing, R. A., P. Parma, H. R. d. Ruiter, and R. Fanti (1999), *Asymmetries in the jets of weak radio galaxies*, Monthly Notices of the Royal Astronomical Society, 306, 513 (cit. on p. 63).

Landau, L., E. Lifschitz, and C. Kikuchi (1953), *The Classical Theory of Fields*, American Journal of Physics, 21, 392 (cit. on p. 69).

Larionov, V. M. et al. (2020), *Multiwavelength behaviour of the blazar 3C 279: decade-long study from -ray to radio*, Monthly Notices of the Royal Astronomical Society, 492, 3829 (cit. on p. 64).

LeVeque, R. J. (1998), *Balancing Source Terms and Flux Gradients in High-Resolution Godunov Methods: The Quasi-Steady Wave-Propagation Algorithm*, Journal of Computational Physics, 146, 346 (cit. on p. 72).

Lister, M. L. et al. (2013), *MOJAVE. X. Parsec-scale Jet Orientation Variations and Superluminal Motion in Active Galactic Nuclei*, The Astronomical Journal, 146, 120 (cit. on p. 11).

Lister, M. L. et al. (2018), *MOJAVE. XV. VLBA 15 GHz Total Intensity and Polarization Maps of 437 Parsec-scale AGN Jets from 1996 to 2017*, Astrophysical Journal, Supplement, 234, 12 (cit. on p. 61).

Lister, M. L. et al. (2019), *MOJAVE. XVII. Jet Kinematics and Parent Population Properties of Relativistically Beamed Radio-loud Blazars*, Astrophysical Journal, 874, 43 (cit. on p. 18).

Lister, M. L., A. P. Marscher, and W. K. Gear (1998), *Submilliarcsecond Polarimetric Imaging of Blazar Jets at 43 GHz*, Astrophysical Journal, 504, 702 (cit. on p. 64).

Lobanov, A. P. (2005), *Resolution limits in astronomical images*, arXiv e-prints, (cit. on p. 50).

Lobanov, Andrei (2015), *Brightness temperature constraints from interferometric visibilities*, A&A, 574, A84 (cit. on p. 57).

Lu, R.-S. et al. (2023), *A ring-like accretion structure in M87 connecting its black hole and jet*, Nature, 616, 686 (cit. on pp. 53, 57).

Lyndel-Bell, D. (1969), *Galactic Nuclei as Collapsed Old Quasars.*, Nature, 223, 690 (cit. on pp. 9, 55).

Lyutikov, M., V. Pariev, and D. Gabuzda (2005), *Polarization and energy content of parsec-scale AGN jets*, Memorie della Societa Astronomica Italianasai, 76, 114 (cit. on p. 19).

MacDonald, N. R. and K. I. Nishikawa (2021), *From electrons to Janskys: Full stokes polarized radiative transfer in 3D relativistic particle-in-cell jet simulations*, Astronomy and Astrophysics, 653, A10 (cit. on p. 77).

MacDonald, N. R. and A. P. Marscher (2018), *Faraday Conversion in Turbulent Blazar Jets*, Astrophysical Journal, 862, 58 (cit. on pp. 65, 67, 76, 77).

Mack, K. H., U. Klein, C. P. O'Dea, and A. G. Willis (1997), *Multi-frequency radio continuum mapping of giant radio galaxies*, Astronomy and Astrophysics, Supplement, 123, 423 (cit. on p. 11).

Mannheim, K. (1993), *The proton blazar.*, Astronomy and Astrophysics, 269, 67 (cit. on p. 18).

Maraschi, L., G. Ghisellini, and A. Celotti (1992), *A Jet Model for the Gamma-Ray–emitting Blazar 3C 279*, Astrophysical Journal, Letters, 397, L5 (cit. on p. 18).

Marscher, A. P. (1998),
The Blazar Paradigm: Synchro-Compton Emission from Relativistic Jets,
International Astronomical Union Colloquium, 164, 25–32 (cit. on pp. 59, 64).

Marscher, A. P. et al. (2010), *Probing the Inner Jet of the Quasar PKS 1510-089 with Multi-Waveband Monitoring During Strong Gamma-Ray Activity*,
Astrophysical Journal, Letters, 710, L126 (cit. on pp. 53, 54).

Marshall, H. L. et al. (2002), *A High-Resolution X-Ray Image of the Jet in M87*,
Astrophysical Journal, 564, 683 (cit. on p. 59).

Martí, J. M. and E. Müller (1999), *Numerical Hydrodynamics in Special Relativity*,
Living Reviews in Relativity, 2, 3 (cit. on p. 64).

Martí, J. M. and E. Müller (2003), *Numerical Hydrodynamics in Special Relativity*,
Living Reviews in Relativity, 6, 7 (cit. on p. 71).

Martí-Vidal, I., Roy, A., Conway, J., and Zensus, A. J. (2016), *Calibration of mixed-polarization interferometric observations - Tools for the reduction of interferometric data from elements with linear and circular polarization receivers*,
Astronomy and Astrophysics, 587, A143 (cit. on p. 44).

Martí, J. M., E. Mueller, J. A. Font, J. M. Z. Ibánez, and A. Marquina (1997),
Morphology and Dynamics of Relativistic Jets, Astrophysical Journal, 479, 151
(cit. on p. 65).

Martí, J. and E. Müller (2015),
Grid-based Methods in Relativistic Hydrodynamics and Magnetohydrodynamics,
Living Reviews in Computational Astrophysics, 1, (cit. on p. 65).

Massi, M. (2018), *Max Planck Institut für Radioastronomie Millimeter and Submillimeter Astronomy Group - teaching activity*, (visited on 08/13/2023)
(cit. on p. 9).

Matthews, J. H., A. R. Bell, K. M. Blundell, and A. T. Araudo (2018), *Fornax A, Centaurus A, and other radio galaxies as sources of ultrahigh energy cosmic rays*,
Monthly Notices of the Royal Astronomical Society: Letters, 479, L76,
ISSN: 1745-3925 (cit. on p. 60).

Mattia, G. (2022), *Toward a consistent turbulence model for the origin of jet-launching magnetic fields: theoretical and numerical improvements*,
PhD thesis: Max Planck Institute for Astronomy (cit. on p. 74).

McKinney, J. C. (2006), *General relativistic magnetohydrodynamic simulations of the jet formation and large-scale propagation from black hole accretion systems*,
Monthly Notices of the Royal Astronomical Society, 368, 1561 (cit. on pp. 54, 55).

Meier, D. L., S. Koide, and Y. Uchida (2001),
Magnetohydrodynamic Production of Relativistic Jets, Science, 291, 84
(cit. on p. 64).

Merloni, A., S. Heinz, and T. di Matteo (2003),
A Fundamental Plane of black hole activity,
Monthly Notices of the Royal Astronomical Society, 345, 1057 (cit. on p. 4).

Meyer, E. T., G. Fossati, M. Georganopoulos, and M. L. Lister (2011),
From the Blazar Sequence to the Blazar Envelope: Revisiting the Relativistic Jet Dichotomy in Radio-loud Active Galactic Nuclei, Astrophysical Journal, 740, 98 (cit. on p. 18).

Michelson, A. A. and E. W. Morley (1887),
On the relative motion of the Earth and the luminiferous ether,
American Journal of Science, 3-34, 333 (cit. on p. 40).

Michelson, P. F. et al. (1994), *EGRET Upper Limits to the High-Energy Gamma-Ray Emission from the Millisecond Pulsars in Nearby Globular Clusters*,
Astrophysical Journal, 435, 218 (cit. on pp. 40, 59).

Mignone, A. and G. Bodo (2006),
An HLLC Riemann solver for relativistic flows - II. Magnetohydrodynamics,
Monthly Notices of the Royal Astronomical Society, 368, 1040 (cit. on p. 74).

Mignone, A. et al. (2007),
PLUTO: A Numerical Code for Computational Astrophysics,
Astrophysical Journal, Supplement, 170, 228
(cit. on pp. 65, 70, 72, 74, 78, 79, 110).

Mimica, P. et al. (2009),
Spectral Evolution of Superluminal Components in Parsec-Scale Jets,
Astrophysical Journal, 696, 1142 (cit. on p. 67).

Miyoshi, T. et al. (2010),
The HLLD Approximate Riemann Solver for Magnetospheric Simulation,
IEEE Transactions on Plasma Science, 38, 2236 (cit. on p. 74).

Mizuno, Y. et al. (2015), *Recollimation Shocks in Magnetized Relativistic Jets*,
Astrophysical Journal, 809, 38 (cit. on p. 66).

Montgomery, C., W. Orchiston, and I. Whittingham (2009),
Michell, Laplace and the origin of the black hole concept,
Journal of Astronomical History and Heritage, 12, 90 (cit. on p. 2).

Mücke, A. and R. J. Protheroe (2001),
A proton synchrotron blazar model for flaring in Markarian 501,
Astroparticle Physics, 15, 121 (cit. on p. 18).

Mueller, H. (1948), *The Foundations of Optics*,
Journal of the Optical Society of America, 38, 661 (cit. on p. 42).

Müller, C. et al. (2011), *Dual-frequency VLBI study of Centaurus A on sub-parsec scales. The highest-resolution view of an extragalactic jet*,
Astronomy and Astrophysics, 530, L11 (cit. on p. 56).

Müller, C. et al. (2014), *TANAMI monitoring of Centaurus A: The complex dynamics in the inner parsec of an extragalactic jet*, Astronomy and Astrophysics, 569, A115 (cit. on p. 63).

Müller, H. and A. P. Lobanov (2022), *DoG-HiT: A novel VLBI multiscale imaging approach*, Astronomy and Astrophysics, 666, A137 (cit. on pp. 47, 50, 51, 96).

— (2023a), *Dynamic and Polarimetric VLBI imaging with a multiscalar approach*, Astronomy and Astrophysics, 673, A151 (cit. on p. 96).

— (2023b), *Multiscale and multidirectional very long baseline interferometry imaging with CLEAN*, Astronomy and Astrophysics, 672, A26 (cit. on p. 50).

Nagai, H. et al. (2014), *Limb-brightened Jet of 3C 84 Revealed by the 43 GHz Very-Long-Baseline-Array Observation*, Astrophysical Journal, 785, 53 (cit. on p. 20).

Napier, P. J. et al. (1994), *The Very Long Baseline Array.*, IEEE Proceedings, 82, 658 (cit. on p. 42).

Narayan, R. et al. (2021), *The Polarized Image of a Synchrotron-emitting Ring of Gas Orbiting a Black Hole*, Astrophysical Journal, 912, 35 (cit. on p. 61).

Neumayer, N. (2010), *The Supermassive Black Hole at the Heart of Centaurus A: Revealed by the Kinematics of Gas and Stars*, Publications of the Astronomical Society of Australia, 27, 449 (cit. on p. 62).

Nishikawa, K.-I. et al. (1998), *Three-dimensional Magnetohydrodynamic Simulations of Relativistic Jets Injected into an Oblique Magnetic Field*, Astrophysical Journal, 498, 166 (cit. on p. 65).

NRAO (2023), *Very Long Baseline Array*, https://public.nrao.edu/telescopes/vlba/, Last accessed: 05 August 2023 (cit. on p. 42).

O'Sullivan, S. P., N. M. McClure-Griffiths, I. J. Feain, B. M. Gaensler, and R. J. Sault (2013), *Broad-band radio circular polarization spectrum of the relativistic jet in PKS B2126158*, Monthly Notices of the Royal Astronomical Society, 435, 311 (cit. on p. 62).

Padovani, P., P. Giommi, and A. Rau (2012), *The discovery of high-power high synchrotron peak blazars*, Monthly Notices of the Royal Astronomical Society, 422, L48 (cit. on p. 18).

Padovani, P. et al. (2017), *Active galactic nuclei: what's in a name?*, Astronomy and Astrophysics Reviews, 25, 2 (cit. on pp. 6, 57).

Padovani, P., E. S. Perlman, H. Landt, P. Giommi, and M. Perri (2003), *What Types of Jets Does Nature Make? A New Population of Radio Quasars*, Astrophysical Journal, 588, 128 (cit. on p. 18).

Paraschos, G. F. et al. (2022),
Jet kinematics in the transversely stratified jet of 3C 84. A two-decade overview, Astronomy and Astrophysics, 665, A1 (cit. on pp. 55, 79).

Park, J. and J. C. Algaba (2022),
Polarization Observations of AGN Jets: Past and Future, Galaxies, 10, 102 (cit. on p. 61).

Penrose, R. and R. M. Floyd (1971),
Extraction of Rotational Energy from a Black Hole, Nature Physical Science, 229, 177 (cit. on p. 55).

Penzias, A. A. and R. W. Wilson (1965),
A Measurement of Excess Antenna Temperature at 4080 Mc/s., Astrophysical Journal, 142, 419 (cit. on p. 24).

Perucho, M., I. Martí-Vidal, A. P. Lobanov, and P. E. Hardee (2012),
S5 0836+710: An FRII jet disrupted by the growth of a helical instability?, Astronomy and Astrophysics, 545, A65 (cit. on p. 56).

Piner, B. G., N. Pant, P. G. Edwards, and K. Wiik (2009),
Significant Limb-Brightening in the Inner Parsec of Markarian 501, Astrophysical Journal, Letters, 690, L31 (cit. on p. 20).

Planck Collaboration et al. (2011), *Planck early results. XV. Spectral energy distributions and radio continuum spectra of northern extragalactic radio sources*, Astronomy and Astrophysics, 536, A15 (cit. on p. 20).

Porth, O., C. Fendt, Z. Meliani, and B. Vaidya (2011),
Synchrotron Radiation of Self-collimating Relativistic Magnetohydrodynamic Jets, Astrophysical Journal, 737, 42 (cit. on pp. 66, 67).

Prandini, E. and G. Ghisellini (2022),
The Blazar Sequence and Its Physical Understanding, Galaxies, 10, 35 (cit. on p. 20).

Pushkarev, A. B., D. C. Gabuzda, Y. N. Vetukhnovskaya, and V. E. Yakimov (2005),
Spine-sheath polarization structures in four active galactic nuclei jets, Monthly Notices of the Royal Astronomical Society, 356, 859 (cit. on p. 20).

Pushkarev, A. et al. (2017), *Linear Polarization Properties of Parsec-Scale AGN Jets*, Galaxies, 5, 93 (cit. on pp. 56, 95).

Rayleigh, L. (1879), *On the Capillary Phenomena of Jets*,
Proceedings of the Royal Society of London Series I, 29, 71 (cit. on p. 39).

Reber, G. (1940), *Notes: Cosmic Static*, Astrophysical Journal, 91, 621 (cit. on p. 24).

Rees, A. I. (1966), *The Effect of Depositional Slopes on the Anisotropy of Magnetic Susceptibility of Laboratory Deposited Sands*, Journal of Geology, 74, 856 (cit. on pp. 13, 18).

Reimer, O., M. Pohl, P. Sreekumar, and J. Mattox (2003), *EGRET Upper Limits on the High-Energy Gamma-Ray Emission of Galaxy Clusters*, Astrophysical Journal, 588, (cit. on p. 59).

Ressler, S. M., A. Tchekhovskoy, E. Quataert, M. Chandra, and C. F. Gammie (2015), *Electron thermodynamics in GRMHD simulations of low-luminosity black hole accretion*, Monthly Notices of the Royal Astronomical Society, 454, 1848 (cit. on p. 67).

Ricci, L. et al. (2022), *Exploring the disk-jet connection in NGC 315*, Astronomy and Astrophysics, 664, A166 (cit. on pp. 27, 56).

Roberts, P. H. (1970), *Book Review: Astronomy and Astrophysics. Vol. 1, Literature 1969, Part 1, W. Fricke, U. Güntzel-Lingner, F. Henn, D. Krahn and G. Zech, eds. Springer*, Physics of the Earth and Planetary Interiors, 4, 79 (cit. on p. 57).

Roe, P. L. (2015), *Riemann Problem*, in: *Encyclopedia of Applied and Computational Mathematics*, Springer (cit. on p. 71).

Roelofs, F. et al. (2023), *The ngEHT Analysis Challenges*, Galaxies, 11, 12 (cit. on pp. 50, 51).

Rosen, A., P. A. Hughes, G. C. Duncan, and P. E. Hardee (1999), *A Comparison of the Morphology and Stability of Relativistic and Nonrelativistic Jets*, Astrophysical Journal, 516, 729 (cit. on p. 65).

Rudnick, L., F. N. Owen, T. W. Jones, J. J. Puschell, and W. A. Stein (1978), *Coordinated centimeter, millimeter, infrared, and visual polarimetry of compact nonthermal sources*, Astrophysical Journal, Letters, 225, L5 (cit. on p. 61).

Rybicki, G. B. and A. P. Lightman (1979), *Radiative processes in astrophysics*, Wiley (cit. on p. 26).

Ryle, M. and A. Hewish (1960), *The synthesis of large radio telescopes*, Monthly Notices of the Royal Astronomical Society, 120, 220 (cit. on p. 35).

Salpeter, E. E. (1964), *Accretion of Interstellar Matter by Massive Objects*, Astrophysical Journal, 140, 796 (cit. on p. 9).

Scarpa, R. and R. Falomo (1997), *Are high polarization quasars and BL Lacertae objects really different? A study of the optical spectral properties*, Astronomy and Astrophysics, 325, 109 (cit. on p. 18).

Schartmann, M. et al. (2008), *Three-dimensional radiative transfer models of clumpy tori in Seyfert galaxies*, Astronomy and Astrophysics, 482, 67 (cit. on p. 10).

Schmidt, M. (1963), *3C 273 : A Star-Like Object with Large Red-Shift*, Nature, 197, 1040 (cit. on p. 24).

Schwarzschild, K. (1999), *On the gravitational field of a mass point according to Einstein's theory*, arXiv e-prints, (cit. on p. 2).

Sebokolodi, M. L. L. et al. (2020), *A Wideband Polarization Study of Cygnus A with the Jansky Very Large Array. I. The Observations and Data*, The Astrophysical Journal, 903, 36 (cit. on p. 60).

Shepherd, M. C. (1997), "Difmap: an Interactive Program for Synthesis Imaging", in: *Astronomical Data Analysis Software and Systems VI*, vol. 125, Astronomical Society of the Pacific Conference Series 77 (cit. on p. 47).

Sikora, M., Łukasz Stawarz, and J.-P. Lasota (2007), *Radio Loudness of Active Galactic Nuclei: Observational Facts and Theoretical Implications*, The Astrophysical Journal, 658, 815 (cit. on p. 18).

Sironi, L., U. Keshet, and M. Lemoine (2015), *Relativistic Shocks: Particle Acceleration and Magnetization*, Space Science Reviews, 191, 519 (cit. on p. 67).

Sironi, L., A. Spitkovsky, and J. Arons (2013), *The Maximum Energy of Accelerated Particles in Relativistic Collisionless Shocks*, Astrophysical Journal, 771, 54 (cit. on p. 67).

Smirnov, O. M. (2011), *Revisiting the radio interferometer measurement equation - I. A full-sky Jones formalism*, Astronomy and Astrophysics, 527, A106 (cit. on p. 44).

Sol, H, G Pelletier, and E Asseo (1989), *Two-flow model for extragalactic radio jets*, Monthly Notices of the Royal Astronomical Society, 237, 411 (cit. on p. 60).

Stokes, G. G. (1851), *On the Composition and Resolution of Streams of Polarized Light from different Sources*, Transactions of the Cambridge Philosophical Society, 9, 399 (cit. on pp. 32, 42).

Taub, A. H. (1948), *Relativistic Rankine-Hugoniot Equations*, Physical Review, 74, 328 (cit. on p. 74).

Tchekhovskoy, A. (2015), *Launching of Active Galactic Nuclei Jets*, in: *The Formation and Disruption of Black Hole Jets*, Springer (cit. on p. 55).

Tchekhovskoy, A., R. Narayan, and J. C. McKinney (2011), *Efficient generation of jets from magnetically arrested accretion on a rapidly spinning black hole*, Monthly Notices of the Royal Astronomical Society: Letters, 418, L79–L83 (cit. on p. 9).

Thirring, H. (1918), *Über die Wirkung rotierender ferner Massen in der Einsteinschen Gravitationstheorie*, Physikalische Zeitschrift, 19, 33 (cit. on p. 8).

Thompson, A. R., J. M. Moran, and J. Swenson George W. (2017), *Interferometry and Synthesis in Radio Astronomy, 3rd Edition*, Springer (cit. on p. 47).

Thorne, J. (2023),
Lighting the Night: The Spectral Energy Distributions of Galaxies, English,
PhD thesis: The University of Western Australia (cit. on pp. 11, 14, 17).

Thorne, K. S. (2009),
"John Wheeler, 1952 - 1976: Black Holes and Geometrodynamics",
in: *APS April Meeting Abstracts*, APS Meeting Abstracts B5.002 (cit. on p. 2).

Thum, C. et al. (2017), *POLAMI: Polarimetric Monitoring of Active Galactic Nuclei at Millimetre Wavelengths – II. Widespread circular polarization*,
Monthly Notices of the Royal Astronomical Society, 473, 2506 (cit. on p. 95).

Tiede, P. (2022), *Comrade: Composable Modeling of Radio Emission*,
The Journal of Open Source Software, 7, 4457 (cit. on p. 124).

Tingay, S. J., R. A. Preston, and D. L. Jauncey (2001),
The Subparsec-Scale Structure and Evolution of Centaurus A. II. Continued Very Long Baseline Array Monitoring, The Astronomical Journal, 122, 1697
(cit. on p. 63).

Toro, E. F., A. Hidalgo, and M. Dumbser (2009),
FORCE schemes on unstructured meshes I: Conservative hyperbolic systems,
Journal of Computational Physics, 228, 3368 (cit. on p. 72).

Urry, C. M. and P. Padovani (1995),
Unified Schemes for Radio-Loud Active Galactic Nuclei,
Publications of the Astronomical Society of the Pacific, 107, 803 (cit. on p. 13).

Vaidya, B., A. Mignone, G. Bodo, P. Rossi, and S. Massaglia (2018),
A Particle Module for the PLUTO Code. II. Hybrid Framework for Modeling Nonthermal Emission from Relativistic Magnetized Flows,
Astrophysical Journal, 865, 144 (cit. on pp. 67, 75, 110).

Viall, N. M., C. E. DeForest, and L. Kepko (2021),
Mesoscale Structure in the Solar Wind,
Frontiers in Astronomy and Space Sciences, 8, (cit. on p. 67).

Vitrishchak, V. M. et al. (2008),
The 15–43 GHz parsec-scale circular polarization of 41 active galactic nuclei,
Monthly Notices of the Royal Astronomical Society, 391, 124 (cit. on p. 96).

Völk, H. J. (2000),
"The diffusive galactic GeV/TeV ramma-ray background: Sources vs. transport",
in: *AIP Conference Proceedings*, AIP (cit. on p. 59).

Walker, R. C., P. E. Hardee, F. B. Davies, C. Ly, and W. Junor (2018),
The Structure and Dynamics of the Subparsec Jet in M87 Based on 50 VLBA Observations over 17 Years at 43 GHz, Astrophysical Journal, 855, 128
(cit. on p. 79).

Walsh, D., R. F. Carswell, and R. J. Weymann (1979), *0957+561 A, B: twin quasistellar objects or gravitational lens?*, Nature, 279, 381 (cit. on p. 24).

Wardle, J. F. C., D. C. Homan, R. Ojha, and D. H. Roberts (1998), *Electron-positron jets associated with the quasar 3C279*, Nature (London), 395, 457 (cit. on pp. 34, 64).

Weaver, Z. R. et al. (2022), *Kinematics of Parsec-scale Jets of Gamma-Ray Blazars at 43 GHz during 10 yr of the VLBA-BU-BLAZAR Program*, Astrophysical Journal, Supplement Series, 260, 12 (cit. on p. 59).

Wielebinski, R., N. Junkes, and B. H. Grahl (2011), *The Effelsberg 100-m Radio Telescope: Construction and Forty Years of Radio Astronomy*, Journal of Astronomical History and Heritage, 14, 3 (cit. on p. 36).

Willott, C. J., S. Rawlings, K. M. Blundell, and M. Lacy (1999), *The emission line-radio correlation for radio sources using the 7C Redshift Survey*, Monthly Notices of the Royal Astronomical Society, 309, 1017 (cit. on p. 4).

Zensus, J. A., M. H. Cohen, and S. C. Unwin (1995), *The Parsec-Scale Jet in Quasar 3C 345*, Astrophysical Journal, 443, 35 (cit. on pp. 11, 57).

Acknowledgements

I would like to extend my heartfelt acknowledgments to the remarkable individuals who have played instrumental roles in the fruition of this endeavor. First and foremost, I express my profound gratitude to both of my supervisors. Eduardo, your guidance, expertise, and invaluable feedback have been pivotal in shaping the trajectory of my work. Your unwavering support and commitment to my growth as a researcher since I have been a bachelor student have been truly inspiring. Nick, I am deeply indebted to you for your profound impact on my journey. Your mentorship has not only ignited my passion for numerical work but has also enriched my understanding of its nuances. Your generosity in sharing your knowledge has been a constant source of motivation.

I would like deeply thank Prof. Anton Zensus for his willingness to allow me the privilege of conducting my dissertation within his group. You have provided me with invaluable opportunities for learning, growth, and research. I am particularly grateful for the sympathy extended towards me when my family was in need, as well as for the support I received during the subsequent months.

I also extend my sincere gratitude to the extended members of my thesis advisory committee, Prof. Andreas Eckart and Andrei, and the third member of my examination committee, Prof. Christine Heim. Your commitment to my academic progress and your dedication to evaluating my work have been invaluable. The time and expertise you have shared have been instrumental in shaping the quality of my dissertation.

I extend my heartfelt appreciation to Hendrik for his dedicated efforts in advancing circular polarization imaging. Your commitment to excellence and collaborative spirit have contributed immeasurably to the success of our shared pursuits.

Jan, your contributions deserve special mention. Your assistance in paper writing and an occasional simple act of sharing a croissant have exemplified the spirit of camaraderie that defines our group.

To the entire group, I am profoundly grateful for providing a safe haven for learning, growth, and exchange of ideas. Your collective wisdom and encouragement have been instrumental in shaping my academic journey. I would like to express my heartfelt gratitude to each individual who shared an office space and went on conferences and trips with me throughout my academic journey. Special thanks to Petra for always bringing cookies, Aleksei for planning informative and fun nights, Jongsoe for fruitful discussions on polarization, Hui-Hsuan for game nights under the nightsky in Granada, and George for all our office laughter and ensuring that I would be on the home *straight*. The collaborative and enriching environment that we coexisted in has contributed significantly to my growth, learning, and overall experience.

Vieri and Luca, you have been more than just office neighbors; you have been incredible friends on this academic journey. Thank you for your generosity in allowing me to "borrow" the occasional cup of coffee, which has provided the much-needed fuel to power through challenging days. (No worries - it made up for all the paperwork and non-solutions of riddles). The daily memes that brightened our workspace cannot go unnoticed. Your lightheartedness and ability to find humor even in the midst of academic rigors have made my day.

Laura, you granted me moral support and friendship for over a decade. From coffee breaks to shared experiences as flatmates, your presence has shaped my academic journey and enriched my life in countless ways. Your ability to understand without words, our shared tequila shot before an oral exam, and your warmth in welcoming me into your family are gestures I hold close to my heart. You gifted me my first office-plant and made me addicted. Thank you for showing me the beauty of it.

My gratitude extends to my husband Philipp, whose unwavering love and support have been my constant pillars of strength. Your insights on coding and your unflagging encouragement in professional domains have been a source of immeasurable inspiration. But mostly, I thank you with all my heart for your presence as my home, and your care during times of difficulty, which have been nothing short of extraordinary. You are the family I chose, and your belief in our unbreakable bond has given me immeasurable strength.

I reserve a special place of gratitude for my 95-year-old grandmother, who has endeavored to understand my research through documentaries, and to my late mother, who always believed in me. Your unwavering support, even from afar, has been a driving force behind my pursuit of knowledge and discovery.

In conclusion, I am humbled and blessed to have had the privilege of working alongside these exceptional individuals. Their contributions, both large and small, have left an indelible mark on my journey, and for that, I am truly thankful.